University of Southampton

Faculty of Engineering and the Environment
Smart Electronic Materials and Systems

Water Droplet Impact Energy Harvesting with Lead-free Piezoelectric Structures

by

Samuel Christopher Jack Jellard

ORCID ID 0000-0002-4370-3668

Thesis for the degree of Doctor of Philosophy

June 2019

UNIVERSITY OF SOUTHAMPTON

ABSTRACT

FACULTY OF ENGINEERING AND THE ENVIRONMENT

Smart Electronic Materials and Systems

Thesis for the degree of Doctor of Philosophy

Water Droplet Impact Energy Harvesting with Lead-free Piezoelectric Structures

Samuel Christopher Jack Jellard

Harvesting energy from ambient environmental sources using piezoelectric transducers has seen a tremendous amount of interest from the scientific community in recent times. The practicality of energy scavenging technology looks set to see continued relevance, with decreasing power demands of electrical systems, such as Wireless Sensor Networks (WSN), allowing such technology to progressively act as an energy source to drive and sustain them independently. It has been demonstrated that falling water droplets of millimetric-scale diameter can impart forces of over a thousand times their resting weight upon surface impact, representing an exciting opportunity for further investigation regarding kinetic to electrical energy harvesting. Piezoelectric materials are known to generate electrical energy through applied mechanical strain, and as such are ideally suited for such an application due to their inherently strong electromechanical coupling effect.

The key research aim of this work is to analyse the parameters influencing the energy transfer efficiency of droplet impact harvesting, using this knowledge to produce piezoelectric structures that encourage efficient energy transfer from the mechanical energy of water droplet impact into electrical energy. It was found that careful consideration of both transducer bending stiffness and resonant frequency is required. Fabricated P(VDF-TrFE) on stainless steel foil cantilever beams produced a peak energy output of 28 nJ, from the impact of a 5.5 mm diameter droplet at the beam end, when the transducer bending stiffness was within the range of 0.067 to 0.134 N/m. Energy output was further increased when the beam resonant frequency was close to/at the droplet impact frequency. Whilst this result is intuitive, it has been reliably demonstrated that droplet-surface interactions are not trivial, being proposed elsewhere that energy transfer efficiency is more dependent on the relation between the beam resonant frequency and the natural vibration frequency of the impacting droplet.

Furthermore, an expansive finite element analysis of ideal geometries for droplet impact energy harvesting highlighted the desirable mechanical characteristics of spiral shapes, with double-armed Archimedean spiral transducers composed of P(VDF-TrFE) deposited onto copper foil investigated. In order to drive the spiral

transducers efficiently, a tiered tank system is presented which passively controls the diameter and impact frequency of dispensed droplets from a stored water volume. A total peak output power of 58.9 μW is achieved by a single spiral transducer arm driven by 1 litre of water dispensed as droplets, relating to a power density of 16 mW/cm^3. This power output demonstrates how an array of stacked harvesters could produce a theoretical output power of 0.33 mW for every litre of water which descends through the guttering of a two storey building (estimated 5.7 m vertical height). With a suitable energy accumulation and management system, it is feasible to use this for powering applications such as low-power sensor systems.

List of Contents

List of Figures 5
List of Tables 10
Declaration of Authorship 11
Nomenclature 12
Publication List 15
Acknowledgements 16
1 Introduction 19
1.1 Rainfall Energy Harvesting 19
1.2 Ideal Available Power Estimations 23
1.3 Thesis Structure 25
1.4 Research Contribution 27
2 Literature Review 29
2.1 Droplet Fluid Impact Dynamics 29
2.1.1 Droplet Impact Regimes 33
2.1.2 Ideal Impact for Optimal Energy Transfer 37
2.1.3 Controlling Droplet Impact Frequency and Force 40
2.2 Existing Droplet Impact Energy Harvesters Using Piezoelectric Transducers 45
3 Material Selection 53
3.1 Introduction to Piezoelectricity 53
3.2 Piezoelectric Material Selection 57
3.3 Substrate Material Selection 60
4 Transducer Geometry Investigations 65
4.1 Piezoelectric Cantilever Beam Considerations 68
4.2 Further Geometry and Topology Considerations 75
4.3 Double-Armed Archimedean Spiral Geometry Investigation 81
4.3.1 Key parameter influence on spiral axial stiffness 87
4.3.2 Key parameter influence on spiral first order resonant frequency 91
4.4 Effect of Drainage Holes on Spiral Mechanical Behaviours 95
4.4.1 Electrode Dimension Simulations 97
5 Mechanical Parameters Influencing Energy Transfer Efficiency 101
5.1.1 Transducer Stiffness Variation Experimental Method and Results 101
5.1.2 Droplet Impact Frequency Variation Experimental Method and Results 114
6 Archimedean Spiral Transducer Fabrication and Testing 117
6.1 Sample Fabrication 117
6.2 Spiral Electrode Optimisation and Impedance Matching 120
6.3 Effect of Droplet Impact Location on Energy Output 122
6.3.1 Effect of Droplet Impact Location on Energy Output Result Discussion 128
6.4 Variation of “Gap” Parameter Testing 131
6.5 Fixed-Fixed Beam Comparison Testing 133
7 Tiered Droplet Impact Control System 139
8 Conclusion 145
8.1 Achievement Summary of Research Work 145
8.2 Future Work 148
Appendices 151

List of Figures

Figure 1 Diagram to describe potential harvester positioning to increase output power _____ 22
Figure 2 Diagram displaying water source guidance and stacked harvester array approach _____ 23
Figure 3 Reprinted from [28] (left) graph displaying average number of rain days in Singapore from 1982 to 2015, (right) graph showing the average amount of rainfall per month from 1982 to 2015 _____ 24
Figure 4 Illustration of thesis structure _____ 26
Figure 5 Reprinted from [32], simple diagram to illustrate contact angle between liquid and solid phases, with resulting bottom disc radius_____ 30
Figure 6 Reprinted and edited from [37], diagram to show angles of interest in a three phase system. The red circle illustrates where these three phases meet, otherwise known as the "contact front". "θ s" is equivalent to contact angle "θ" _____ 30
Figure 7 Reprinted from [42], photograph of a leaf demonstrating surface hydrophobicity _____ 31
Figure 8 Reprinted from [43], SEM images to show micro-scale texturing naturally found in lotus leaves. Left side image illustrates micro-texturing, whilst right image highlights superimposed secondary texturing. _____ 32
Figure 9 Reprinted from [45]. Diagram on left, captioned "A", shows an exploded diagram of the piezoelectric energy harvester materials. The series of three pictures to the right show the placement of the mechanical energy harvesters (MEH) in different areas on animal organs__ 32
Figure 10 Left image, reprinted from [46], example of hydrophobic spray product "NeverWet". Right image, reprinted from [47], depicts an Arduino Micro Board circuit in water. This circuit was coated by super-hydrophobic coating "NeverWet" [46], and continued to operate in a submerged environment _____ 33
Figure 11 Reprinted from [49], illustration of a rebounding droplet impact _____ 33
Figure 12 Reprinted from [53] Images of droplet morphology on dry surfaces for a variety of impact scenarios_____ 36
Figure 13 Reprinted from [62] (Left) graph to show the harvested electrical energy (EE) by a piezoelectric cantilever depending on droplet kinetic energy (KE) and whether the cantilever surface is wettable (W) or non-wettable (NW). The two graphs on the right-hand side depict Beam-tip displacement versus time for 80 mm and 140 mm long beams with beam width of 15.5 mm. The dashed line represents zero deflection. Note how wettable beam (top trace) is not centred around the zero deflection line due to additional droplet weight exerted at beam tip._ 38
Figure 14 Reprinted from [62], photographs of droplet impact behaviour for a wettable "W" (left side) and a non-wettable "NW" (right side) beam. Both beams lengths are 80mm. _____ 39
Figure 15 Reprinted from [128]. A series of photographic stills depicting the events of a fragmentation of a 6mm diameter water droplet falling in an ascending stream of air. The images clearly show the "pancake-bag-break up" stages of droplet fragmentation; the flattening of the droplet into a "pancake" shape, the inflation of a "bag-like" shape bordered by a "thicker corrugated rim", before destabilization and fragmentation. The inset picture shows the destabilization of the "bag" rim._____ 40
Figure 16 Reprinted from [66], A measured force vs. time curve for a series of 4 droplet impacts of different diameters. The curve shape reflects inclusion of the compressible nature of water during droplet impacts and the resulting effect on force distribution and magnitude. _____ 42
Figure 17 Reprinted and edited from [10], upper image series depicts the side view of a water drop of radius R = 1.3 mm hitting a piezoelectric quartz at V = 3 m/s. Successive images occur at a 0.5 ms time scale. Lower graph image displays impact force "F" as a function of time for impact measured by the piezoelectric sensor. The curve is not symmetrical between the beginning and the end of the collision. The maximum force F0 is reached after about a tenth of a millisecond. _____ 43
Figure 18 Reprinted from [9], diagram to represent a raindrop energy harvesting system _____ 46
Figure 19 Reprinted from [9], photograph of PVDF band experimental setup _____ 47
Figure 20 Reprinted from [75], voltage output profile of droplet impact illustrating key impact points _____ 48
Figure 21 Reprinted from [23], upper row of diagrams illustrating (left to right) piezoelectric cantilever beam, bridge and floating circle energy harvesting structures. Lower row of images represents corresponding experimental setup of these configurations using MEAS LTD PVDF sensors _____ 49
Figure 22 Reprinted from [23], voltage output across 10 kΩ load resistor produced by a single water droplet impact upon a LDT1-028K MEAS piezoelectric sensor in cantilever configuration. The voltage output for the instances of no rectifying circuit, full bridge rectifier, Greinacher

voltage doubler, Cockcroft Walton Cascade Voltage Doubler (CWCVD) and Karthaus Fisher Cascade Voltage Doubler (KFCVD) rectifying circuits are compared. 49
Figure 23 Reprinted from [76], layer composition of the Midé Volture commercial piezoelectric sensor PZT piezoelectric beam used 50
Figure 24 Reprinted from [84], side-view representation of the electrostatic 53
Figure 25 Reprinted from [87], diagram to show subscript labelling of forces effecting a piezoelectric material in relation to the direction of polarization 56
Figure 26 Reprinted and edited from [89], A simple diagram to illustrate the orientation of groups of dipoles (Weiss domains) (a) before, (b) during and (c) after the poling process. It must be noted that, diagram (b) is a simplified diagram for understanding purposes, with diagram (c) most likely representing the dipole orientation of a piezoelectric material after successful poling. 57
Figure 27 Edited from [93], diagram to show classification of 32 crystal class materials 57
Figure 28 Reprinted from [92], diagram to show relative cost and toxicity of elements 58
Figure 29 Reprinted from [92]. Diagram to show possible candidates for A, B and oxygen sites in perovskite type structured piezoelectric materials 59
Figure 30 Reprinted from [107], illustrations depicting a small elastic floating energy harvester for ocean ripple power harvesting utilising knitted PVDF thin film. Left image depicts knocking structure and beating element, with the PVDF strip labelled "A", whilst right image shows prototype device for experiment in wave maker tank. 60
Figure 31 Reprinted from [134] Diagram illustrating energy flow in a harvester system 65
Figure 32 Diagram to illustrate parameters considered to be necessary to optimise in order to encourage efficiency droplet impact energy harvesting 66
Figure 33 Reprinted from [140], based upon work from [141]–[143] - diagram to show a simple mechanical resonator (left) with the corresponding impedance analogy electrical circuit (right). 67
Figure 34 Reprinted from [134] structure of the cymbal used as a piezoelectric transducer. The presence of cavities in the cymbal allowed the metal end caps to serve as mechanical transformers, which in turn amplified a portion of the incident axial stress. 68
Figure 35 Reprinted from [134] Graph to show output peak voltage of cymbal transducer depending on pre-stress condition. Force of 8 N and 40 N at 100 Hz were applied for zero stress and pre-stress conditions respectively. 68
Figure 36 reprinted from [144], illustration of single fixed end cantilever beam with applied point load force. 69
Figure 37 Reprinted and edited from [146], graph to show the energy transfer characteristics of an impacting droplet upon a substrate depending on the ratio of beam natural frequency to droplet natural frequency. Values displayed here are a) the residual kinetic energy of the droplet after rebound ($Ek1$, green bars), alongside the strain energy of the substrate beam at maximum deflection (Eel, red bars), normalized by the total available energy of the droplet before impact ($Etot$). Vs. fb. Droplets of the same size were used for the impact testing in each case. 72
Figure 38 Illustration of composite piezoelectric transducer beam to highlight key parameters required to optimise piezoelectric layer, depicted in yellow here. The substrate layer is depicted in grey colour. 73
Figure 39 Graph to illustrate optimal piezoelectric layer thickness identification through observation of optimising function maxima for stainless steel and copper substrates 75
Figure 40 A selection of some geometry configurations tested during the 525 geometry variant loading sweep. The colour gradient indicates induced stress, with red highlighting the areas of greatest induced stress, descending to blue to highlight areas of least induced stress. 77
Figure 41 Screenshot of "cross cut" geometry equivalent tensile stress result to illustrate finite element method setup. The colour scale indicates induced stress gradient, with red indicating the areas experiencing the highest induced stress, and blue indicating areas experiencing lower stress levels. 77
Figure 42 Example of geometry tested, "9 Spiral". Main image displays geometry at 20 μs whilst under loading. The induced surface stress is displayed utilising a colour scheme, indicated in the scale. Inset image depicts geometry without loading. 78
Figure 43 Illustrations of design choices under loading which produced the highest von Mises stress. Clockwise from top – 81 Grid Circle, 13 Spiral, 20 Spiral and 30 Cut Hole. 79
Figure 44 Illustration of 30 Cut hole, 0.1 mm radius geometry (left) and 13 spiral turn variation (right). It is proposed that geometries of this nature produce a lower induced stress under loading, as the minimal design features do not encourage areas of high stress to develop throughout the geometry compared to other designs 79
Figure 45 Diagram to demonstrate application pattern of random loading variables upon upper surface of plain geometry 80

Figure 46 Reprinted from [165], diagram to illustrate definition of spiral parameters. Here, a determines the density of spiral turns, with the distance between successive turnings defined using 2πa, represented as *b* in Equation 31 _____ 83
Figure 47 Reprinted from [167], curved beam with co-ordinates notation _____ 83
Figure 48 Diagram to illustrate parameters of interest for the finite element analysis upon a 1-turn spiral _____ 85
Figure 49 Illustration of prescribed displacement axial stiffness testing _____ 88
Figure 50 Illustration of estimated stiffness plotting process for an AF = 30 mm, A1 = 6 mm, 1.5 turn spiral _____ 88
Figure 51 Effect of variation of turn number, spiral final radius and spiral initial radius on estimated axial stiffness _____ 88
Figure 52 Effect of varying spiral gap distance parameter "Gap" on estimated axial stiffness _____ 89
Figure 53 Illustration of spiral design variations for turn number, final and initial radius studies; top row spirals, left to right, 0.5 / 1 / 1.5 turns with AF = 30 mm and A1 = 1 mm. Bottom row, left to right, 0.5 / 1 / 1.5 turns with AF = 30 mm and A1 = 6 mm _____ 89
Figure 54 Illustration of spiral designs for spiral gap distance variation; top row spirals, left to right, 1 mm / 4 mm / 8 mm gap distances with AF = 50 mm and A1 = 1 mm. Bottom row, left to right, 1 mm / 4 mm / 8 mm gap distances with AF = 50 mm and A1 = 6 mm _____ 89
Figure 55 Illustration of geometry changes when increasing the initial spiral radius, "A1", at low spiral turn number _____ 91
Figure 56 Illustration of geometry with varying arm gap thickness _____ 91
Figure 57 Effect of variation of turn number, spiral final radius and spiral initial radius on spiral first order resonant frequency _____ 92
Figure 58 Effect of spiral arm "Gap" distance on spiral first order resonant frequency _____ 92
Figure 59 Images of AF = 20 mm, A1 = 1 mm, Gap = 2 mm sample first order modal shapes, with 0.5 turns (left) and 1.5 turns (right). The colour scale chart indicates total displacement, mm 93
Figure 60 Screenshot of 30 mm spiral final radius Eigenfrequency analysis. Image displays spiral with 1 turn, first order Eigenfrequency of 10.703 Hz. The colour scale indicates surface displacement whilst at resonance. _____ 94
Figure 61 Diagram to illustrate drainage hole configurations analysed _____ 96
Figure 62 Effect of drainage hole configuration on sample resonant frequency _____ 96
Figure 63 Illustration of drainage hole configuration testing on sample mechanical properties using an AF = 35 mm, 1 turn sample _____ 97
Figure 64 Simulated Normalised output power of samples (mixed radius) as a function of electrode length for comparison _____ 98
Figure 65 Simulated normalised output power of samples (AF=35 mm radius) as a function of electrode length _____ 98
Figure 66 Screenshots of AF = 30 mm spiral geometries displaying electrode lengths which produced the greatest power output for a) AF = 30 mm, A1 = 6 mm, 0.75 turns, b) AF = 30 mm, A1 = 6 mm, 1 turn, and c) AF = 30 mm, A1 = 6 mm, 2 turns, d) AF = 40 mm, A1 = 6 mm, 1 turn, e) AF = 50 mm, A1 = 6 mm, 0.75 turns and f) AF = 60 mm, A1 = 6 mm, 0.5 turns _____ 99
Figure 67 Illustration depicting droplet impact testing setup. Droplets are dispensed from a syringe clamped in an extended clamp stand. The voltage response from the piezoelectric transducers is measured across an electrically impedance matched load using an oscilloscope. _____ 102
Figure 68 Cantilever beams with P(VDF-TrFE) deposited on stainless steel and poled, prepared for electrode deposition with foil mask _____ 103
Figure 69 Photograph of a selection of 53 mm length cantilever beam test samples _____ 103
Figure 70 Close up of 53 mm length cantilever beam testing array to highlight mounting/clamping condition _____ 103
Figure 71 Graph displaying results of 3.13 mm diameter droplet impact testing for length = 53 mm samples _____ 105
Figure 72 Graph displaying results of 4.4 mm diameter droplet impact testing for length = 53 mm samples _____ 105
Figure 73 Images to illustrate clamping set-up for 63 mm length samples. (a) depicts a photograph of samples used for testing. (b) illustrates sample dimensions - free beam length is 43 mm, with 10 mm being clamped securely with acrylic supports, and the last 10 mm of the beam reserved for electrode connections. (c) illustrates sample clamping set-up graphically. _____ 106
Figure 74 Images to illustrate progressive trim testing of single sample _____ 108
Figure 75 Graph displaying results of 3.13 mm, 4.4 mm and 5.47 mm diameter droplet impact testing from 0.5 m, 1 m, 1.5 m and 2 m heights onto length = 63 mm samples _____ 110
Figure 76 Graph displaying all droplet release height results from Figure 75 (multiple test samples) averaged to give a single output energy, per beam width, for each droplet diameter tested _ 111

Figure 77 Average output energy per beam width as a function of impacting droplet diameter and release height, progressive trim testing _____ 112
Figure 78 Graph displaying all droplet release height results from Figure 77 (progressive trim testing) averaged to give a single output energy, per beam width, for each droplet diameter tested _____ 113
Figure 79 Photograph to illustrate impact frequency effect on power output test setup _____ 115
Figure 80 Sample output power as a function of droplet impact frequency, simulation and practical test results _____ 115
Figure 81 Diagram to illustrate spiral sample fabrication, characterisation and optimisation process _____ 117
Figure 82 Photograph of custom built surface charge array used to polarize P(VDF-TrFE) on copper foil samples. Samples were positioned underneath the array in order to experience an evenly distributed poling field across the upper surface _____ 119
Figure 83 Photographs to illustrate the effect of NeverWet® superhydrophobic surface treatment on water droplet contact angle, post-treated sample (left) and pre-treated sample (right) _____ 119
Figure 84 Photographs displaying some of the fabricated spirals _____ 120
Figure 85 Varied spiral parameters _____ 120
Figure 86 Actual normalised output power of samples (mixed radius) as a function of electrode length _____ 121
Figure 87 Actual normalised output power of samples (AF=35 mm radius) as a function of electrode length _____ 121
Figure 88 AF = 20 mm, A1 = 6 mm, 0.75 Turns – Output Energy from Blue Arm Connection___ 123
Figure 89 AF = 30 mm, A1 = 6 mm, 0.75 Turns – Output Energy from Yellow Arm Connection 123
Figure 90 AF = 30 mm, A1 = 6 mm, 1 Turns – Output Energy from Blue Arm Connection_____ 123
Figure 91 AF = 30 mm, A1 = 6 mm, 2 Turns – Output Energy from Blue Arm Connection_____ 124
Figure 92 AF = 60 mm, A1 = 6 mm, 0.5 Turns – Output Energy from Blue Arm Connection ___ 124
Figure 93 Laser cut sample (mixed radius) peak energy output data compared to bending stiffness at the impact location (bending stiffness values shown beside trend line)_____ 125
Figure 94 Graph displaying average energy output from all tested impact locations for each sample, giving an overall display of energy output for each sample. _____ 125
Figure 95 AF = 35 mm, A1 = 6 mm, 0.5 Turns – Output Energy from Red Arm Connection____ 125
Figure 96 AF = 35 mm, A1 = 6 mm, 0.75 Turns – Output Energy from Blue Arm Connection __ 126
Figure 97 AF = 35 mm, A1 = 6 mm, 1 Turns – Output Energy from Blue Arm Connection _____ 126
Figure 98 AF = 35 mm, A1 = 6 mm, 1.25 Turns – Output Energy from Red Arm Connection___ 126
Figure 99 AF = 35 mm, A1 = 6 mm, 1.5 Turns – Output Energy from Red Arm Connection____ 126
Figure 100 Graph displaying peak energy output from the tested impact locations for all samples 127
Figure 101 Graph displaying average energy output from all tested impact locations for each sample, giving an overall display of energy output for each sample. _____ 127
Figure 102 Voltage vs. Time for droplet impact upon impact location A for AF = 30 mm, 2 turns sample _____ 128
Figure 103 Voltage vs. Time for droplet impact upon impact location F for AF = 60 mm, 0.5 turns sample _____ 129
Figure 104 Comparison of arm width in regard to energy transfer for AF = 35 mm samples – (left) 0.5 turn sample, (right) 1.5 turn sample _____ 130
Figure 105 Reprinted from [49], image illustrating droplet spreading on impact _____ 130
Figure 106 Photograph to illustrate sample trimming process, AF = 35 mm, 0.5 turns (top) and AF = 35 mm, 1.0 turns (bottom). The 0.5 turn sample had an active electrode length of 35 mm, width 15 mm and thickness 200 nm, with an electrically impedance matched load of 8 MΩ. The 1.0 turn sample had an active electrode length of 59 mm, width 15 mm and thickness 200 nm, with an electrically impedance matched load of 7 MΩ._____ 131
Figure 107 Influence of Gap distance on spiral stiffness for AF = 35 mm, 0.5 turn sample. The line equation for each Gap state is provided to illustrate spiral stiffness variation. _____ 132
Figure 108 Influence of Gap distance on spiral stiffness for AF = 35 mm, 1 turn sample. The line equation for each Gap state is provided to illustrate spiral stiffness variation. _____ 132
Figure 109 Result of progressive arm width trim testing for AF = 35 mm, 0.5 turn sample. Due to sample stiffness, it was not possible to physically test the axial stiffness without damaging the contact electrodes – as such, the simulated stiffness is illustrated here. Error bars illustrate the difference between highest and lowest energy output for each arm width tested. Each gap width configuration was tested with at least 8 droplet impact repetitions, the average energy is displayed here. _____ 133
Figure 110 Result of progressive arm width trim testing for AF = 35 mm, 1.0 turn sample. Error bars illustrate the difference between highest and lowest energy output for each arm width tested.

Each gap width configuration was tested with at least 8 droplet impact repetitions, the average energy is displayed here. 133
Figure 111 Image illustrating the effective length for the 1 turn spiral sample. In this example, the equivalent fixed-fixed beam length is approximately 251.84 mm, with arm width measured as 14 mm. 134
Figure 112 Photograph of AF = 35 mm spiral equivalent length fixed-fixed beams. Beams represent spiral arm width and length in a straight, fixed-fixed beam format. From left to right, fixed-fixed beam equivalent of a 0.25, 0.5, 0.75 and 1 turn samples 134
Figure 113 0.25 turn equivalent fixed-fixed beam energy output depending on droplet impact location, illustrated in upper image 135
Figure 114 0.5 turn equivalent fixed-fixed beam energy output depending on droplet impact location, illustrated in upper image 136
Figure 115 0.75 turn equivalent fixed-fixed beam energy output depending on droplet impact location, illustrated in upper image 136
Figure 116 1.0 turn equivalent fixed-fixed beam energy output depending on droplet impact location, illustrated in upper image 137
Figure 117 Photograph of laser cut acrylic box with dyed water flowing from different sized diameter outlets 140
Figure 118 (left) Photograph of acrylic container with varied bottom outlet diameters, (right) photograph to illustrate variation of Jet-to-drip transition state depending on outlet diameter (6.0 mm to 1.0 mm from left to right, only streams from outlet diameters of 1.0 mm to 4.5 mm are displayed in this image as water would otherwise drain too quickly with all outlets open for reasonable observation to take place). 140
Figure 119 Tiered tank stages to control droplet formation and impact frequency. The tank liquid is de-ionised water dyed with black food colouring. 141
Figure 120 Tiered system drip frequency rates for AF = 60 mm, 0.5 turns sample depending on number of open upper stage 1 mm outlet 142
Figure 121 Power output for the AF = 60 mm, 0.5 turns sample driven with a variety of different upper stage outlets open at a position of 1.0 m beneath the lower 6 mm outlet. Sample power output is derived from voltage signal traces captured at regular time intervals. 142
Figure 122 Dimensions of AF = 60 mm, 0.5 turns sample illustrated 144
Figure 123 Reprinted and edited from [175] FESEM images of the triangular net-like structure of the elastic polyamide film. Image a) shows film before biaxial extension in its superhydrophobic state, with the average side length of the triangle approximately 200 mm. The average size of the polyamide elastic fibre is 20 mm. Image b) shows structure of film in its superhydrophilic state, with applied extension ratio of near to 120%. In this case, average side length of the triangle is around 450 mm. 148
Figure 124 Reprinted [176] from A tank with base aperture containing water 149
Fig. 125 Reprinted from [177], a diagram detailing a basic aquaponic system set-up. Opportunities for implementation of the transducer devices fabricated in this report, to harvest both droplet and air bubble energy, are highlighted with the red squares. 150

List of Tables

Table 1 Estimated impact velocity and force depending on water droplet diameter....44
Table 2 Adapted from [17], a comparison of potential rain droplet energy generators....46
Table 3 Simulated rainfall experiment settings and results....50
Table 4 Comparison of Young's moduli for materials previously used in KNN deposition research.61
Table 5 Relevant material parameters of commonly used electronic device metals....62
Table 6 Parameters used to estimate ideal piezoelectric film thickness....73
Table 7 Simulation sweep material properties, retrieved from COMSOL multiphysics pre-defined material library....77
Table 8 Volume average von Mises stress induced by top ten geometries tested under step loading.78
Table 9 Volume average equivalent tensile stress induced by top ten geometries tested under psuedo-random impulse loading....81
Table 10 Simulation parameters of piezoelectric and substrate materials used....86
Table 11 53 mm length piezoelectric cantilever beam experimental parameters....104
Table 12 53 mm length piezoelectric cantilever beam mechanical parameters....104
Table 13 63 mm length piezoelectric cantilever beam experimental parameters....106
Table 14 63 mm length piezoelectric cantilever beam mechanical parameters....107
Table 15 Progressive trim piezoelectric cantilever beam experimental parameters....108
Table 16 Progressive trim piezoelectric cantilever beam experimental parameters....109
Table 17 Relevant parameters of fabricated spiral sample sets....122
Table 18 Fixed-fixed beam sample parameters....135
Table 19 Results of fixed-fixed beam experimental testing....137
Table 20 Sample output power depending on tiered tank upper to lower outlet ratio....144

UNIVERSITY OF Southampton

Research Thesis: Declaration of Authorship

Print name:	

Title of thesis:	

I declare that this thesis and the work presented in it is my own and has been generated by me as the result of my own original research.

I confirm that:

1. This work was done wholly or mainly while in candidature for a research degree at this University;
2. Where any part of this thesis has previously been submitted for a degree or any other qualification at this University or any other institution, this has been clearly stated;
3. Where I have consulted the published work of others, this is always clearly attributed;
4. Where I have quoted from the work of others, the source is always given. With the exception of such quotations, this thesis is entirely my own work;
5. I have acknowledged all main sources of help;
6. Where the thesis is based on work done by myself jointly with others, I have made clear exactly what was done by others and what I have contributed myself;
7. Either none of this work has been published before submission, or parts of this work have been published as: [please list references below]:

_____

_____

_____

_____

Signature:		Date:	

Nomenclature

General Notation

Symbol	*Value / Unit*	*Description*
$\gamma_{al}, \gamma_{sl}, \gamma_{sa}$	N/m	Water surface tensions / Interface surface tension, with subscript notation depicting interface between solid (s) and liquid (l) and air (a) phases
δ	m	Displacement
ε^T	F/m	Permittivity at constant stress
μ	8.90×10^{-4} Pa.s at approximately 25 °C [1]	Water dynamic viscosity
$\rho, \rho_{air}, \rho_{water}$	1.225kg/m^3(air), 1000 kg/m^3(water)	Density, air density, water density
σ	72 mN/m at approximately 25 °C [2]	Water surface tension
A	m^2	Area/ Cross-sectional area
C_d	0.47 for a sphere, dimensionless	Drag coefficient
d_{ij}	C/N	Piezoelectric charge constant at i – polarisation and j – stress applied direction
d_{ij}^t	C/N	Inverse piezoelectric charge constant at i – polarisation and j – stress applied direction
D	C/m^2	Electrical displacement, or charge density
E	N/C	Electric field
F, F_{ext}	N	Force / Impact Force, externally applied force
F_{air_drag}	N	Resistive force exerted by air pressure
f_b	Hz	Beam resonant frequency
F_0	N	Maximum impact force estimate of falling water droplet
F_{weight}	N	Gravitational force exerted on the droplet
g	9.81 m/s^2	Acceleration due to gravity
h	m	Height

I	m^4	Second moment of area
k_b	N/m	Beam bending stiffness
L	m	Length
L_0	m	Original length of the object
ΔL	m	Change in object length
m	kg	Mass
Oh	Dimensionless	Ohnesorge number
r	m	Radius
$R_{capillary}$	m	Radius of the capillary, or syringe tip opening
$R_{droplet}$	m	Water droplet radius
r_0	m	Initial distance
r_f	m	Final distance
Re	Dimensionless	Reynolds Number
s^E	m^2/N	Material compliance under a zero or constant electrical field
S	Dimensionless	Mechanical strain
t	m	Thickness
T	Pa	Mechanical stress
u	m/s	Flow speed
v	m/s	Velocity
v_0	m/s	Initial velocity
v_f	m/s	Final velocity / Impact velocity
V	m^3	Rain droplet volume
w	m	Width
We	Dimensionless	Weber Number
Y	Pa	Young's modulus

Beam, Curved Beam and Spiral Parameter Notation

Symbol	*Value / Unit*	*Description*
β	rad	Twist angle

θ	rad	Polar angle
Φ	Nm	Twisting moment
a	Dimensionless	Real number constant dictating spiral turns
b	Dimensionless	Real number constant dictating the distance between successive spiral turns
EI_x	N/m	Curved beam bending stiffness
GJ	N/m	Curved beam torsional stiffness
i	$\mathrm{kg \cdot m^2}$	Mass moment of inertia per unit length of the curved beam
k_b	N/m	Bending stiffness
L_{def}	m	Out of plane deflection
M_x	Nm	Curved beam bending moment
M_z	Pa	Curved beam twist torque
n	Dimensionless	Real number constant which determines how tightly a spiral is wrapped around the centre point.
R	m	Radius of curved beam
s	Dimensionless	Position coordinate along the arc

Tiered Tank Droplet Dispenser Notation

Symbol	*Value / Unit*	*Description*
$A_{aperture}$	$\mathrm{m^2}$	Area of the tank bottom aperture
$C_{contraction}$	Value of 0.62 for sharp-edged apertures, Dimensionless	Contraction coefficient, which is a measure of the outlet aperture sharpness
$C_{discharge}$	Dimensionless	Discharge coefficient
C_v	Value of 0.97 for water, Dimensionless	Velocity coefficient
v_{outlet}	Dimensionless	Outlet velocity
V_{flow}	$\mathrm{m^3/s}$	Water volume flow

Publication List

Journal Papers

A) Submitted publications under-going peer review process

1. S.C.J Jellard, S.H. Pu, S. Chen, K. Yao and N. M. White, "Water Droplet Impact Energy Harvesting with P(VDF-TrFE) Piezoelectric Cantilevers on Stainless Steel Substrates" – Submitted to Smart Materials and Structures journal, 19-Feb-2019.

B) Pending publications submitted for peer review process

1. S.C.J Jellard, S.H. Pu, N. M. White, "Archimedes' Water Fountain; A Water Droplet Energy Harvesting System Utilising Piezoelectric Arithmetic Spiral Transducers" – To be submitted to Smart Materials & Structures Journal, Jun-2019.

Conference Papers / Presentations

- Poster Presentation, Singapore, A*STAR IMRE 2017
- Poster Presentation, Singapore, ICMAT 2017
- Oral Presentation, India, ISIF 2017
- Poster Presentation, Energy Harvesting Network, 2018

Acknowledgements

I have been helped by so many individuals throughout my research that writing this acknowledgements section has required an exhaustive search for synonyms of "help" and "thanks", less it become incredibly repetitive!

I will start by sincerely thanking my Southampton and Singaporean supervisory team for their support throughout my PhD candidature. Furthermore, I would like to give praise to the University of Southampton and A*STAR IMRE for the generous support given towards my research project, which has allowed me to attend conferences across the world and learn from the best minds in the field. I would like to particularly extend my gratitude to Dr. Suan Hui Pu and Professor Neil White for facilitating my candidature and giving me the opportunity to carry out research in Singapore. Singapore was very much the adventure of a life time, and has opened doors in my career going forward that I couldn't have ever imagined previously. I have made memories which I will cherish for a life time – thank you.

Research projects wouldn't happen without an extensive technical support base – in light of this, I would like to thank all the Southampton and Singaporean researchers who assisted my work. Specifically, I would like to thank Dr. Yao Kui, Dr Shuting Chen, Dr. Weng Heng Liew, Dr. Meysam Sharifzadeh Mirshekarloo and Dr. Lei Zhang for their help in Singapore. In the UK, I would like to thank Dr. Monika Glanc-Gostkiewicz and Dr. Russel Torah for their helpful guidance regarding the PEM lab, equipment inductions and item procurement; I would have been rather stuck without you! For their unwavering patience, I must give huge credit to the Level 1 Workshop team, in particular Mark and Charlie – how you managed to maintain a welcoming disposition every time I poked my head around the door is beyond me, please let me know your secret! The same goes for Simon Beever from the EDMC workshop, and the level 2 Zepler computer lab team - thank you for always being a friendly, helping hand!

Of course, none of this would have taken place without my family. Words will never adequately convey my appreciation of the love and support that you have given me over the years. Thank you to my Grandmother, Hilary, for the weekly skype calls. I have loved being able to keep in touch with you no matter where I am in the world; our chats have brought much joy to my week. To my sister, Lexi – it has been

wonderful watching you grow up into a strong young woman. I am so excited to see what the future has in store for you. To my parents - thank you for investing in my education, allowing me every opportunity for success.

In particular I want to thank my mother, Andrea. You have shown me the true meaning of courage in the face of adversity, it is no wonder you are truly adored by so many. The privileged position that I find myself in is a direct result of your hard work, and is something I will always be mindful of. You have given me a chance to make a mark upon this world, which however small, is something I am immensely grateful for. You are amazing. Lum!

1 Introduction

"If you want to find the secrets of the universe, think in terms of energy, frequency and vibration."

— Nikola Tesla

The overall aim of this research is to investigate the usage of piezoelectric transducers for converting the kinetic impact energy of falling water droplets into useful electrical energy, as efficiently as possible. With this in mind, the associated objectives of this aim are as follows:

1. Identify the key mechanical parameters which influence the efficiency of energy conversion between the impact droplet and the energy harvesting transducer

2. Investigate how varying the geometry of the energy harvesting transducer influences the energy transfer efficiency

3. Analyse the most ideal method of capturing a high number of droplet impacts in order to produce a useful device energy output

In this introductory chapter, the motivation behind the research problem tackled here is presented, along with the key research contributions made to the field.

1.1 Rainfall Energy Harvesting

"Energy" is derived from the Ancient Greek word "*energia*", which is literally translated as "activity" or "operation". This term likely first appeared in the works of Aristotle, and at the time was a broad, philosophical concept, differing from the scientific term that we recognise today.

It is likely that not even Aristotle could comprehend the context of which this term would come to be used - energy surrounds us at all times, sustaining us and driving our civilization forward. Chemical energy allows our crops to grow, electrical energy powers our cities – at a greater scale, our planet's climate and eco-system are directly influenced by the radiant energy received from the sun, in addition to the geothermal energy contained within the earth's mantle.

Unsurprisingly, the study of energy transfer forms a significant portion of human scientific endeavour, spanning a rich and diverse number of areas. A relatively new area of energy research regards the harvesting of ambient energy sources. The allure of capturing or "scavenging" energy from sources present in nature is captivating. Solar energy, for example, has fostered dramatic research growth in recent times, evolving from a $86 billion industry in 2015, to a projected industry of $422 billion by 2022 [3]. The capture of solar energy is an important source of renewable energy, and looks set to play a significant part in meeting energy demands of the future

The fascination of energy harvesting is arguably related to the diversity of transfer mechanisms which can be explored. At a high energy output level, solar, wind and tidal power sources can be harvested through a variety of photovoltaic and mechanical methods. These mechanisms have been the subject of intensive research for many years, and have seen staggering development in energy transfer efficiency.

The opportunities for development of systems targeting lower energy output sources is no less diverse. With a focus on systems which output electrical energy, research has produced:

- **Thermoelectric devices**, which utilise a thermal gradient between two dissimilar conductors to produce electrical energy [4]

- **Electrostatic energy harvesting devices,** which produce electrical energy through the changing capacitance of vibration-dependent capacitors [5]

- **Triboelectric Generators,** which exploit contact electrification in order to produce electrical output [6]

- **Pyroelectric devices,** which convert a temperature change into electrical energy [7]

- **Metamaterial devices,** which can convert microwave signals into electrical energy [8]

- **Piezoelectric devices,** which convert induced physical stress into electrical energy [9]

It has been demonstrated that falling water droplets can impart forces of over a thousand times their resting weight upon impact with solid objects [10]. Tropical countries such as Colombia, Papua New Guinea and Malaysia experience heavy rainfall throughout the year, with total annual rainfall amounts in the region of 3,000 mm [11].

Such deluges of large droplets impart notable impact forces upon natural and man-made structures, representing an exciting opportunity for further investigation into potential uses of this energy, such as smart city sensor technologies. Previous studies in this field [9–22] are built upon in this research by investigating and demonstrating novel transducer geometries, namely double-armed Archimedean spirals, and passively controlled droplet dispensing tank systems. The key advantages of such a device in comparison to existing energy harvesting technologies include:

Area Efficiency and Harvester "Stack-ability": Although currently incomparable in terms of power output, in order to harvest the available solar energy across a 1 m^2 area, by logic a solar panel must have an active surface area of at least 1 m^2. Conversely, it is not necessary to have a droplet harvester element surface area of 1 m^2 area in order to harvest the equivalent energy; surface run-off from the roof areas of large commercial buildings could be funnelled towards a single harvester device. This idea is illustrated in Figure 1.

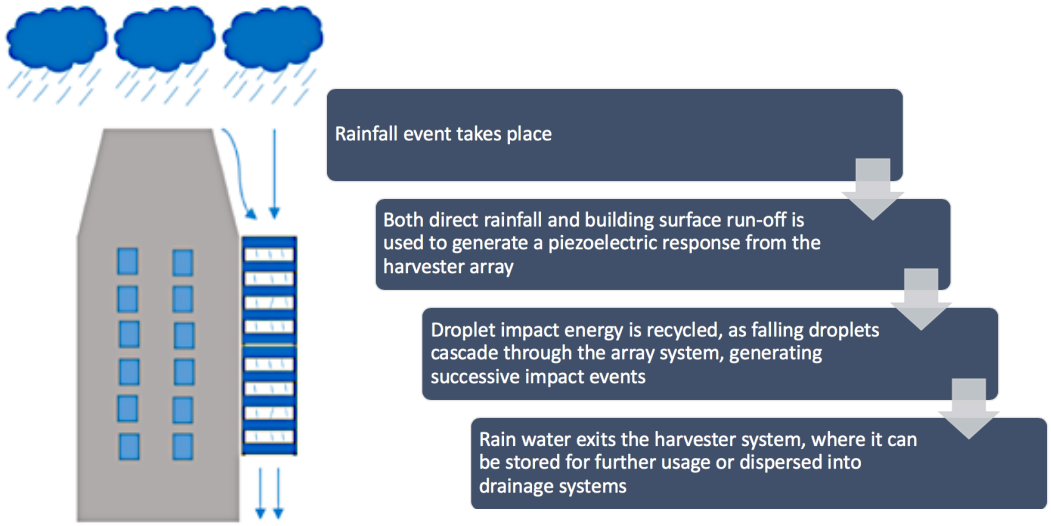

Figure 1 Diagram to describe potential harvester positioning to increase output power

Furthermore, droplet harvesting arrays do not require a "direct-line of sight" to the energy source, and as such can be stacked on top of each other. This allows for droplet impact events to be "recycled" throughout the device, thus increasing power generation efficiency whilst not increasing horizontal space requirements. Moreover, water can be guided from a source before being allowed to fall a certain distance in order to generate kinetic energy once more.

A brief example to outline the potential implementation of this effect:

- Assuming the value of 8 m/s as terminal velocity speed [24], we can estimate that if harvesting array elements are placed a minimum vertical distance of 3.26 metres apart, cascading droplets can accelerate to terminal velocity before a successive impact (assuming they fall from rest and neglecting any external forces).

- This estimation is made using the simplified Equation 1, where v_f is the final velocity, v_0 is the initial velocity, g is the acceleration due to gravity (9.81 m/s), and $(r - r_0)$ is the distance travelled by the droplet throughout its fall. This equation applies to a particle moving linearly in a straight line with constant acceleration [25].

$$v_f{}^2 = v_0^2 + 2g(r_f - r_0)$$

Equation 1

Placement: Many areas which are not currently targeted for energy scavenging can be exploited with successful development of a droplet harvesting technology. For example, pipelines, internal water management and gutter systems/plumbing networks can, with appropriate device tailoring, present useful energy sources.

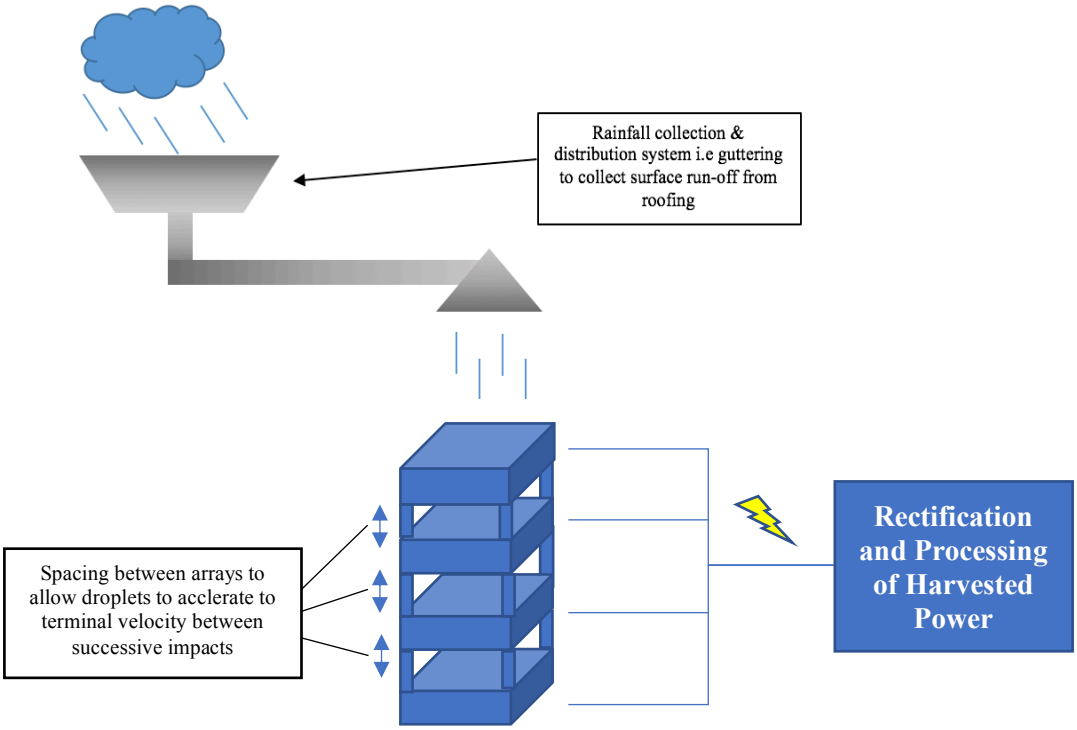

Figure 2 Diagram displaying water source guidance and stacked harvester array approach

Consistent energy transfer efficiency despite sporadic excitation: Whilst classical bladed turbine systems are inappropriate at cm^3 scales and below, due to surface forces and viscosity dominating the energy transfer process over inertial forces, bladeless tesla turbines provide a scaled down alternative. Tesla turbines utilise the boundary layer effect to create shaft rotation. Such turbines have demonstrated 36% peak efficiency at 2 cm^3s^{-1} flow rate, with an unloaded peak power of 45 mW produced at 12 cm^3s^{-1} flow rate [26]. However, efficient turbine operation requires a continuous water volume flow rate, which may not be realistic for the intended application of this research project [27]. Piezoelectric transducers directly harvest the energy of each droplet, presenting an energy-economic solution which does not suffer in terms of energy transfer efficiency from sporadic input stimulus.

1.2 Ideal Available Power Estimations

We may carry out some idealistic calculations to estimate the energy available from

rainfall. If we take the city of Singapore, located in Southeast Asia, for example:

- Figures from the Meteorological Service of Singapore [28] state that it rains on average 178 days of the year, with long-term mean annual rainfall totalling 2331.2 mm (based on records from 1869 to 2015).

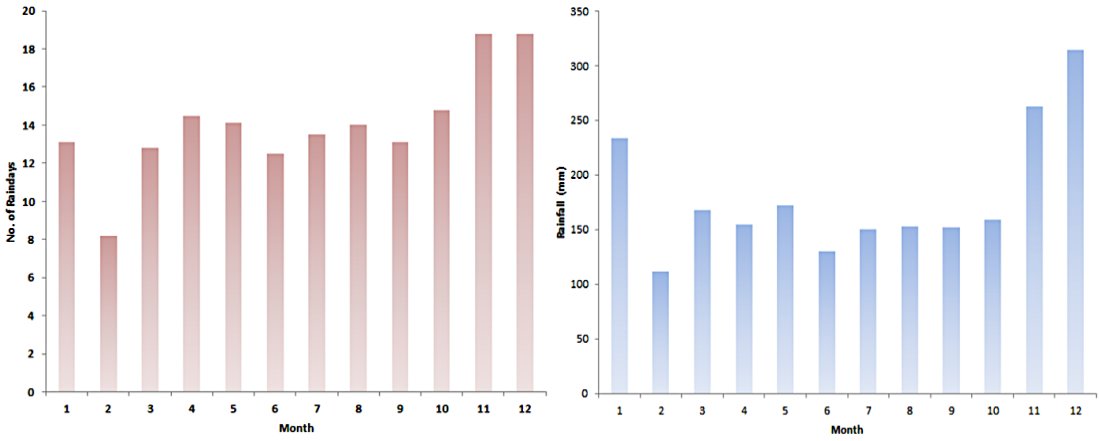

Figure 3 Reprinted from [28] *(left) graph displaying average number of rain days in Singapore from 1982 to 2015, (right) graph showing the average amount of rainfall per month from 1982 to 2015*

- Singapore's land area is estimated to be approximately 719.1 km^2, although as land reclamation activities continue this figure will rise [29]. If we assume that the average rainfall amount of 2331.2 mm (or 2.3312 m) is considered to have fallen per square metre, we can estimate that the total volume of rainfall deposited over the area of Singapore in a year is at least 1,676,366 m^3.

- In terms of recoverable energy, we can produce a theoretical approximation by considering the gravitational potential energy of this total body of water (assuming 1 m^3 of water = 1000 kg mass, therefore 1,676,366 m^3 equates to 1,676,365,920 kg) by using Equation 2.

$$\text{Gravitational Potential Energy} = mgh$$

Equation 2

- If we examine the potential energy of this body positioned in a rain cloud at a height of 2000 m (although tropical rain clouds can extend up to 15000 m above ground level [30]), we find a mean annual potential energy of 3.3×10^{13} J, or 9.2 million kWh. Naturally there is a limit to the energy

calculated as the mass will reach terminal velocity during its fall to earth.

To put this amount of energy into perspective, an iPhone 6 Plus reportedly takes 4.2 kWh to keep charged for a year [31]. Therefore in a perfect situation, rainfall energy could keep 2.2 million iPhone 6 Plus models charged for a year. We optimistically assume that the energy requirements for mobile phone devices will continue to decrease, as advances in energy storage research continue to develop. Translating our estimations into the kinetic energy available, we make an assumption that this body of water is falling at an average speed of 8 m/s. This value represents the anticipated fall speed of a drop with a larger diameter than normally expected, falling through stagnant air conditions [24]. Using Equation 3, where KE is the kinetic energy, m is mass in kg and v is velocity, an estimated 53.6 GJ of kinetic energy is calculated to be available for harvesting.

$$KE = \frac{1}{2}mv^2$$

Equation 3

Naturally, due to the implausibility of covering an area the size of Singapore with rainfall energy harvesting devices, coupled with the impossibility of 100% energy conversion, the amount of potential recoverable energy is significantly less than the values stated here. Furthermore, as this body of water will naturally fall as droplets, we must consider the corresponding effect on mechanical energy transfer. This topic shall be covered in greater detail within this research, in addition to investigating optimal methods of harvesting this energy.

1.3 Thesis Structure

The work contained within this thesis is structured as follows. Firstly, a literature review covering relevant aspects of droplet impact dynamics, in addition to droplet impact energy harvesting research carried out to date, is given in Chapter 2. Chapter 3 briefly analyses piezoelectric materials, before outlining considerations made over the choice of material used to fabricate droplet energy harvesters. Henceforth, the subsequent chapters provide the key contributions of this research work. Chapter 4 outlines how important the shape, or geometry, of the energy harvester is critical to efficient energy harvesting, providing an extensive set of simulation results outlining

which geometries are ideal for droplet impact energy harvesting. Chapter 5 further explores this concept, by investigating how the variation of bending stiffness and resonant frequency of piezoelectric cantilever beams affect the energy transfer efficiency between the impacting droplet and the energy harvester. Chapter 6 builds on previous simulation work, investigating a novel spiral shaped geometry in further detail and producing a series of experimental results outlining the benefits of such a design. Chapter 7 studies the implementation of a tiered tank system in order to control the droplets dispensed onto the spiral samples, highlighting how a previously random excitation method can be converted into a predictable stimulus. Finally, Chapter 8 concludes the work presented here, in addition to offering proposals for future work in this field.

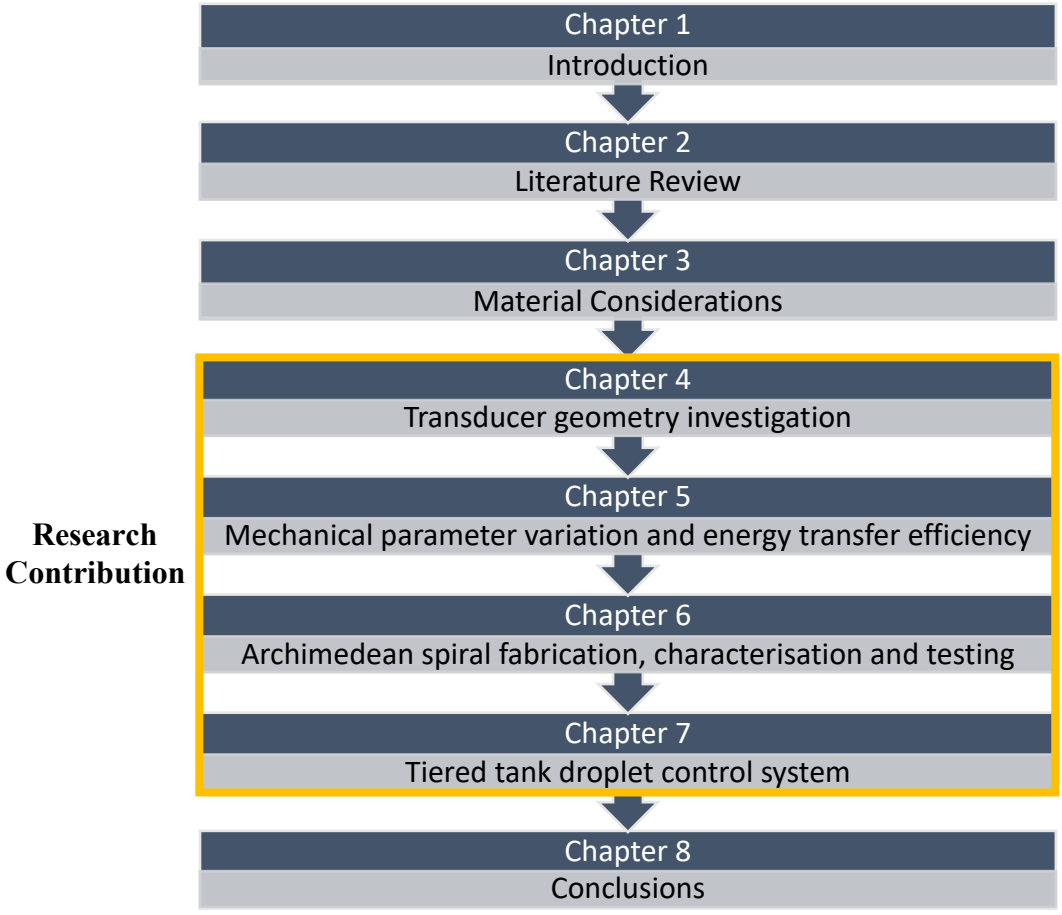

Figure 4 Illustration of thesis structure

1.4 Research Contribution

This research presents novel work in the form of:

1) A thorough analysis of how key transducer parameters, such as bending stiffness and resonant frequency, affect energy transfer efficiency between impacting water droplets and piezoelectric transducers.

2) The simulation, characterisation, fabrication and testing of a unique impact energy harvesting transducer geometry – a double-armed Archimedean spiral. This shape demonstrates inherent design flexibility, as mechanical behaviours can be tailored through variation of parameters such as spiral final/initial radius, turn number and arm thickness. Furthermore, the inherently low resonant frequency and bending stiffness qualities achievable by such geometry designs lend themselves favourably toward water droplet energy harvesting applications.

3) A novel tiered tank system is presented which accepts an input volume of water, before dispensing this water as a series of impact frequency and diameter controlled droplets onto optimal impact locations of the energy harvesting transducers. The achieved output power can be utilised to intermittently drive low power wireless sensor systems, such as ambient humidity and temperature sensors.

The level of research challenge in this project is substantial, requiring competence in finite element modelling, transducer fabrication techniques and testing methodology. It is hoped that the results presented here further inspire work in the field of energy harvesting, presenting an additional option for ambient energy sources to be harnessed in order to power the vast array of electronic devices available on the market today.

To conclude this chapter, the merits of water droplet impact energy harvesting are analysed. It is found that the kinetic energy available from droplets travelling at terminal velocity, such as rainfall, is significant. Furthermore, the nature of the excitation stimulus allows for unique harvester positioning – stacked arrays located in drainage columns, for example.

2 Literature Review

"In the land of splashes, what the scientist knows as Inertia and Surface Tension are the sculptors in liquids, and fashion from them delicate shapes"

— Edgerton and Killian

This chapter will cover the fundamental background literature related to the research problem. Given the importance of understanding both the droplet impact dynamics and subsequent reaction of the energy harvesting transducer, both fields will be briefly covered.

2.1 Droplet Fluid Impact Dynamics

The field of water's interaction with surfaces, otherwise known as "wetting", was first led by Thomas Young and Pierre Simon de Laplace in 1805. It was found that the interface of a material has a specific energy, known as the interfacial energy, which was found to be proportional to the number of molecules present at that interface, and ultimately also proportional to the surface area of this interface [32]–[35]. It is known that, for large bodies of water, the overall force dictating behaviour is gravity. However, at smaller scales, such as rain droplets, we must take surface forces into account. Surface forces produce surprising phenomena, such as droplets 'sticking' to an inclined surface, which seem to defy the laws of physics which constrain larger objects [32]. When a single droplet makes contact with an ideal, solid surface, it naturally spreads from a sphere to one with a flattened bottom in contact with the surface. This flattened bottom makes a disc of radius "*l"* which is referred to as the contact line. We can see that the liquid phase of the droplet joins the solid at an angle of 'θ', known as the contact angle. It is this angle which defines the value of the disc radius "*l*" [32], in addition to parameters such as droplet radius, as illustrated in Figure 5.

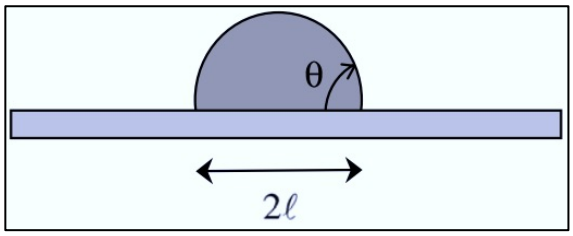

Figure 5 Reprinted from [32]*, simple diagram to illustrate contact angle between liquid and solid phases, with resulting bottom disc radius*

This contact line is where three phases of the system coexist - the solid surface, the liquid droplet and the gaseous atmosphere. Figure 6 shows a more detailed diagram of this three phase system. Consequently, the contact angle between a liquid droplet and a solid surface is used as a measure of the surface's wettability [36]. A relationship giving the value of the contact angle is shown in Equation 4, where "γ" denotes the interface surface tension, with subscript letters "s", "a" and "l" signifying the solid, air and liquid phases accordingly [32].

$$cos\theta = \frac{\gamma_{sa} - \gamma_{ls}}{\gamma_{la}}$$

Equation 4

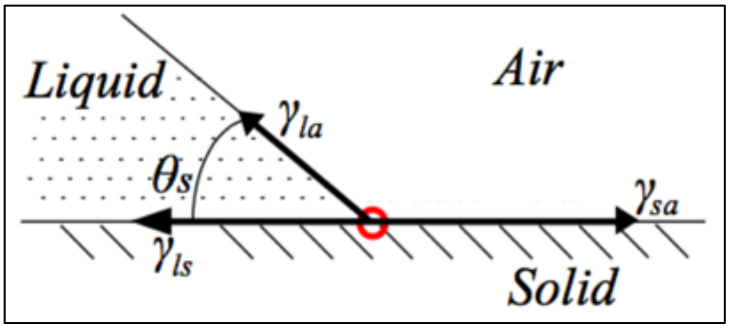

Figure 6 Reprinted and edited from [37]*, diagram to show angles of interest in a three phase system. The red circle illustrates where these three phases meet, otherwise known as the "contact front". "θ s" is equivalent to contact angle "θ"*

In general, a material is considered to be hydrophilic (wettable) if the angle made between liquid and solid is less than 90°. Conversely, if the angle is larger than 90°, the material is considered to be hydrophobic (non-wettable) [38]. Additionally, some surfaces may have contact angles of greater than 150°. These materials are described as superhydrophobic materials, and are very difficult , if not impossible, to wet [39]. There are numerous examples of both hydrophobic and hydrophilic surfaces, with some interesting examples demonstrated in nature. For instance, the leaves of

approximately 200 known plant species are considered hydrophobic [32][40]. One such example is the lotus flower (*Nelumbo*) plant species. The lotus flower has been shown to produce a "lotus effect", referring to the self-cleaning properties of the plant that result from its natural hydrophobicity [41]. This self-cleaning effect can be a useful side-effect of using hydrophobic materials, particularly in outdoor device applications.

Figure 7 Reprinted from [42]*, photograph of a leaf demonstrating surface hydrophobicity*

In nature, hydrophobicity is typically created due to the following three physical properties, composed in a hierarchical structure [32]:

1) Surfaces are typically coated by a waxy epicuticle film, causing the contact angle of droplets to be greater than 90° and thus hydrophobic

2) Such surfaces are "decorated" by micro-textures such as bumps, with scales commonly in the region of 10 μm

3) This micro-textured surface is often accompanied by a superimposed secondary texturing, which is considerably smaller in size (1 μm). This secondary texturing is normally of different morphology, typically hair-like structures.

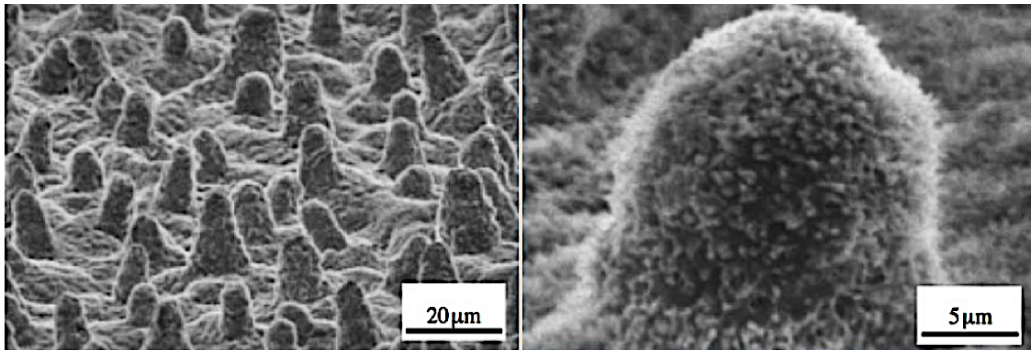

Figure 8 Reprinted from [43]*, SEM images to show micro-scale texturing naturally found in lotus leaves. Left side image illustrates micro-texturing, whilst right image highlights superimposed secondary texturing.*

Given the intended device application, hydrophobic coatings will be required in order to isolate sensitive electronic components from rain water, such as signal processing and storage circuitry. Excessive humidity has been found to generate leakage currents in piezoelectric materials, ultimately resulting in electrical breakdown through ionic migration [44]. There are a variety of commercial methods that are available for isolating materials. Figure 9 demonstrates a bio-compatible polymer, polyimide, being used to successfully isolate an energy harvesting device allowing organic materials, such as a bovine heart, to provide excitation to the device without contamination. [45]

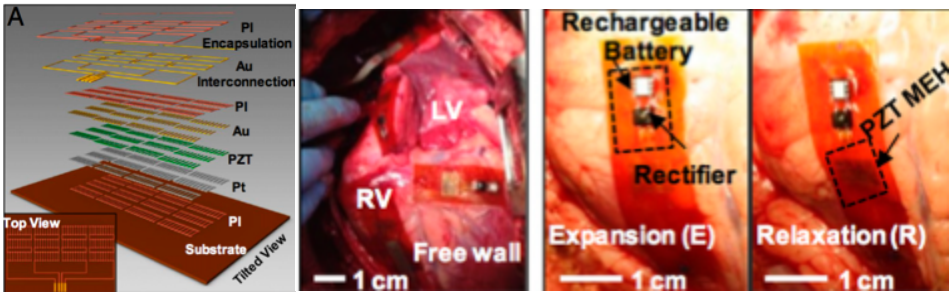

Figure 9 Reprinted from [45]*. Diagram on left, captioned "A", shows an exploded diagram of the piezoelectric energy harvester materials. The series of three pictures to the right show the placement of the mechanical energy harvesters (MEH) in different areas on animal organs*

Whilst natural surface texturing can create hydrophobicity, it is also a highly involved process to reproduce artificially, requiring sophisticated synthesis and etching techniques. Simpler isolation methods are available in the form of hydrophobic spray products, which provide rapid and reliable isolation from water as long as the coating is not subjected to abrasion.

Figure 10 Left image, reprinted from [46]*, example of hydrophobic spray product "NeverWet". Right image, reprinted from* [47]*, depicts an Arduino Micro Board circuit in water. This circuit was coated by super-hydrophobic coating "NeverWet"* [46]*, and continued to operate in a submerged environment*

These products have successfully demonstrated a high level of hydrophobicity in electronic devices after a straight forward application process, and will be utilised in initial device prototyping for this project.

2.1.1 Droplet Impact Regimes

The sheer abundance of phenomena and contributing factors associated with a droplet impact makes it difficult to accurately model droplet impact behaviour without intensive study. It is important, however, to anticipate which impact regimes may be experienced by the energy harvesting transducers, as this will significantly affect the kinetic impact energy transfer efficiency. The type of impact depends upon many factors, with the droplet's size, impact velocity, surface tension and viscosity being among the most critical aspects. The impact surface roughness and the contact angle between the drop and the surface have also been shown to contribute significantly [48]. We begin by considering a single droplet impact onto flat, dry solid.

Figure 11 Reprinted from [49]*, illustration of a rebounding droplet impact*

There are a number of dimensionless relationships, associated with fluid mechanics, that can be used to approximately predict the outcome of a droplet impact in advance.

Equation 5 depicts the Weber number, a dimension-less number often used in the analysis of fluid flows, where there is an interface between two different fluids [50]. In this content, ρ is water density, d is the droplet diameter and v is the droplet speed upon impact. Equation 6 gives the Reynolds number, which is formally defined as the ratio of inertial forces to viscous forces within a fluid, subjected to relative internal movement due to different fluid velocities [51].

In other words, the Reynolds number is used to aid flow pattern prediction in different fluid flow situations. Thirdly, the Ohnesorge number shown in Equation 7 combines both the Weber and Reynolds numbers, providing an equation relating viscous forces to inertial and surface tension forces [52].

$$We = \frac{\rho d v^2}{\sigma}$$

Equation 5

$$Re = \frac{\rho d v}{\mu}$$

Equation 6

$$Oh = \frac{\sqrt{We}}{Re} = \frac{\mu}{\sqrt{\rho \sigma d}}$$

Equation 7

For convenience, we can group the possible outcomes of a dry, rigid surface droplet impact into 6 different classes, illustrated in Figure 12 [82][83][89]:

1) **Deposition –** the impacting droplet spreads on the surface at impact, remaining attached to the surface during the entire impact process without breaking up.

2) **Prompt Splash** – when a droplet impacts upon a rough surface at an increased impact velocity. This scenario is characterized by the generation of droplets at the contact line (where solid, gas, and liquid meet) at the beginning of droplet spreading on the surface, when the liquid has a high outward velocity.

3) **Corona Splash** – occurring when droplets are formed around the rim of the splash corona, remotely from the solid surface. This splash regime is characteristic of droplet impact onto liquid films.

4) **Receding Breakup** – this situation occurs on a wetting surface as the liquid retracts from its maximum spreading radius. During retraction, the droplet contact angle decreases, causing some drops to remain behind the receding droplet. In the case of superhydrophobic surfaces, the retracting drop can break up into a number of fingers, which are each capable of further breakup. This effect is likely due to capillary instability. Such satellite droplets have been observed to break off from the impacting drop both during the spreading and retracting phases.

5) **Partial Rebound** – this situation occurs when a drop recedes after impact. As the drop recedes to the impact point due to elastic effects, the internal kinetic energy of the collapsing drop causes the liquid to squeeze upward, forming a vertical liquid column. Partial rebound occurs when the drop stays partially on the surface, but launches one or more drops at its top. A partial rebound occurs for low values of receding contact angles.

6) **Rebound** - this situation occurs when a drop recedes after impact. As the drop recedes to the impact point due to elastic effects, the internal kinetic energy of the collapsing drop causes the liquid to squeeze upward, forming a vertical liquid column. The case where the entire drop leaves the solid surface, due to this upward motion, is known as complete rebound. A complete rebound occurs for high values of receding contact angle (assuming that the drop recedes with enough kinetic energy).

The above impact scenarios are for a droplet impacting upon a dry surface, with this surface not necessarily being hydrophobic. For superhydrophobic surfaces, it has been found that droplet impact behaviour can become considerably more dynamic. For instance, it has been reported that small liquid droplets can bounce off of solid, superhydrophobic surfaces greater than 20 times before coming to rest [55].

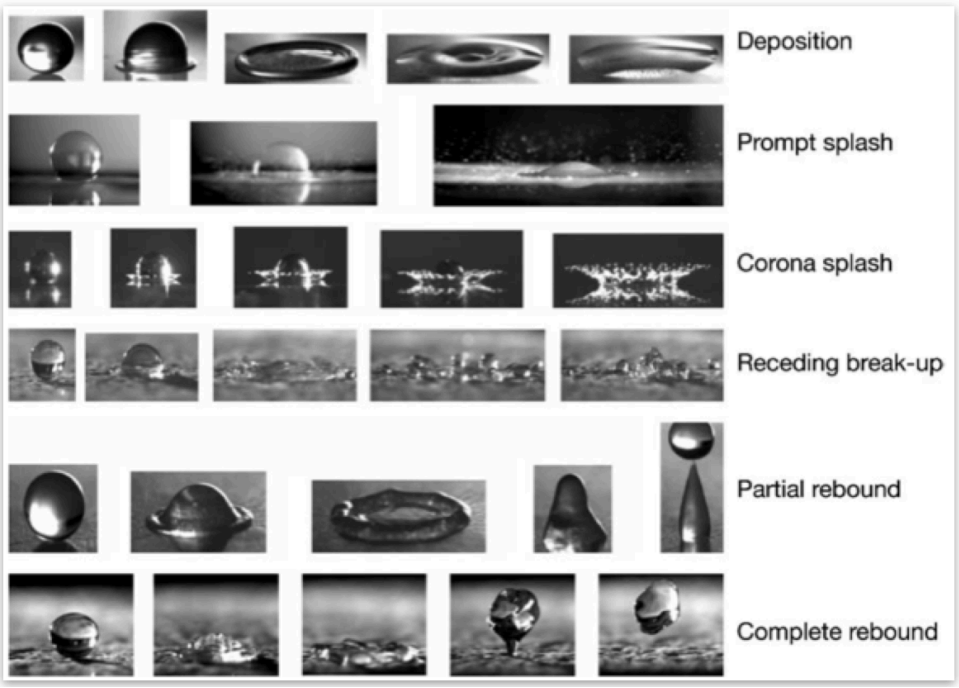

Figure 12 Reprinted from [53] *Images of droplet morphology on dry surfaces for a variety of impact scenarios*

We can reliably predict that, in the case of droplets falling as rainfall at terminal velocity, splashing will occur in most instances. It has been shown that droplets which splash on impact may suffer from energy transfer loss, hence it is advantageous to prevent, or otherwise predict the limit of splashing in order to maximise energy transfer within the droplet harvesting system [9], [12].

It has been demonstrated that splashing impacts occur at higher impact speeds on elastic or "softer" substrates over rigid substrates. This is due to the elasticity of the structure enabling kinetic-to-elastic energy conversion between the droplet and the harvesting structure during the early stages of droplet impact. Consequently, the energy typically dissipated through kinetic-to-surface energy during droplet impact is reduced. This produces a decrease in spreading inertia, resulting in an increased critical splashing speed [56]. Subsequently, it was found that droplets on the "softest" substrates required over 70 % more kinetic energy to splash, in comparison to the same impact on a rigid substrate [57].

Whilst the impact surface will not be "soft" in the conventional sense, we may emulate the cushioning effect of soft materials by utilising flexible transducer elements which bend upon impact. Supporting studies regarding droplet impacts onto elastic membranes found that splashing behaviour was strongly influenced by the tension of the membranes; reducing the tension of the membrane resulting in less splashing,

through conversion of a larger portion of the droplets kinetic impact energy into stored elastic energy [56]. An investigation into the effect of surface elasticity on droplet contact time with superhydrophobic substrates during impact found that [58]:

1. Elastic superhydrophobic surfaces can produce a two-fold reduction in contact time, when compared to the equivalent rigid surfaces. A shorter contact time on impact results in a greater impulse force.

2. Droplet break-up occurs at higher speeds on elastic substrates than on rigid substrates, alluding to an agreement with previous research regarding substrate "softness" [57]

3. For the tested range of droplet sizes before impact, droplet splashing initiated at higher impact speeds on fixed-fixed cantilever beams compared to cantilever beam substrates, due to a more efficient kinetic-to-elastic energy conversion as a result of the mounting condition

Finally, it has been shown that the angle of the surface onto which the droplet impact occurs is an important parameter contributing to splashing behaviour. Experiments observing the impact of perfluorohexane droplets (C_6F_{14}), otherwise known as "FC-72", onto smooth Plexiglas surfaces mounted at variable angles noted that droplet splashing was nearly eliminated when the Plexiglas was inclined at an angle of 45° to the falling droplet. However, it was noted that spreading displacement was higher in general [59]. Although the splashing has been suppressed with increased incline, we must consider the effect this may have on the momentum transfer between the droplet and the harvester element. Given that the force of the droplet is acting at an angle to the impact surface, it may prove undesirable to limit the impulse force of the droplet in pursuit of splash suppression.

2.1.2 Ideal Impact for Optimal Energy Transfer

From a design perspective, it seems unavoidable that hydrophilic surface materials should be neglected as a choice for the transducer element surface. Hydrophilic materials assure maximum contact between water and the deposition surface [60]. As a consequence, droplets deposited on such a surface spread to form thin water films,

or splash. It has been shown that the accumulation of water atop a piezoelectric energy harvester detrimentally affects the energy transfer efficiency [61].

Conversely, it has been demonstrated that impact situations where the droplet remains on a piezoelectric transducer surface after impact – an effect of utilising a hydrophilic surface coating – generate a marginally greater energy than those with non-wettable surfaces, as shown in Figure 13 and Figure 14. It was reported that the beams with superhydrophobic coatings undergo a zero average torque over time, due to the impacting droplets bouncing off of the cantilevers shortly after impact. The usage of the phrase "torque" in this instance is questionable, given that such a term implies a lateral twisting motion of the beam, despite the results focusing on the displacement along the vertical axis. Beams with a hydrophilic surface undergo increased displacement due to the droplet sticking to the cantilever surface [62]. This increases the bending energy of the beam, increasing the amount of energy transfer between the impacting droplet and the piezoelectric transducer. Despite the increase in bending energy generated by hydrophilic materials, it is hypothesised that this effect is only true for the first few impacting droplets, before the transducer becomes mechanically over-damped.

This seems logical when we observe tree leaves. Tree leaves naturally enhance their robustness to rainfall by their ability to shed water droplets. This is due to the leaf's waxy surface layer, which renders the plant structure un-wettable. As such, during rain droplet impact, the torque experienced by the leaf over time is reduced in comparison to a wettable surface. This results in a reduced potential for damage to occur from raindrop impact.

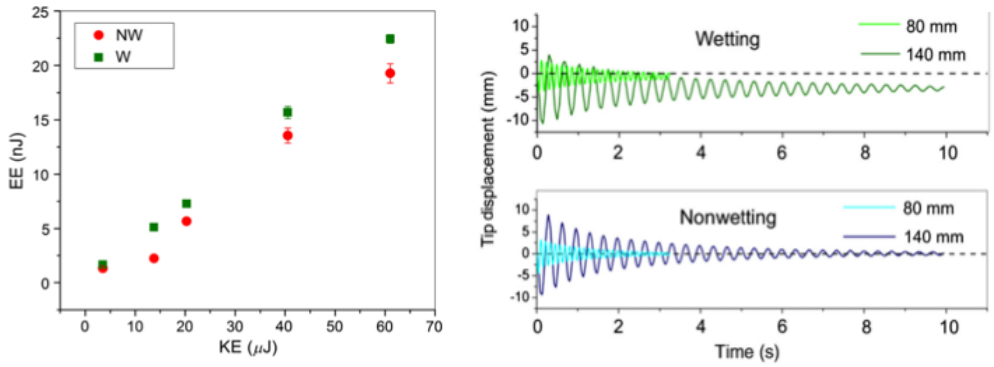

Figure 13 Reprinted from [62] *(Left) graph to show the harvested electrical energy (EE) by a piezoelectric cantilever depending on droplet kinetic energy (KE) and whether the cantilever surface is wettable (W) or non-wettable (NW). The two graphs on the right-hand side depict Beam-tip displacement versus time for 80 mm and*

140 mm long beams with beam width of 15.5 mm. The dashed line represents zero deflection. Note how wettable beam (top trace) is not centred around the zero deflection line due to additional droplet weight exerted at beam tip.

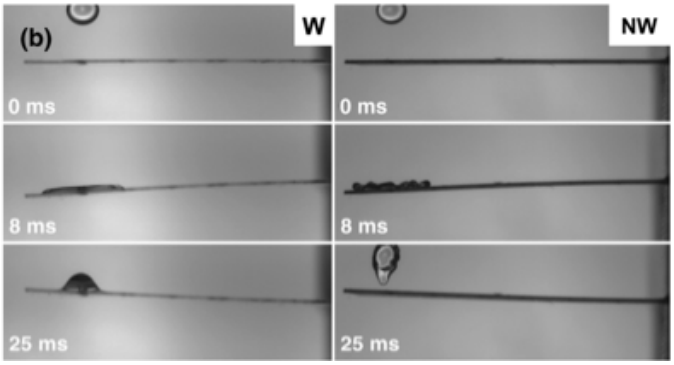

Figure 14 Reprinted from [62]*, photographs of droplet impact behaviour for a wettable "W" (left side) and a non-wettable "NW" (right side) beam. Both beams lengths are 80mm.*

Furthermore, it is proposed that superhydrophobic-coated transducers encourage optimal energy transfer through different mechanisms:

- The transfer of mass, momentum and energy is influenced by the contact time between the droplet and the impact surface. An increased contact time, resulting in an increased impact duration, reduces the impact force by "cushioning". It has been demonstrated that superhydrophobic surfaces can be manipulated to produce a "two-fold" reduction in contact time, thus potentially increasing the impact impulse force through an effect referred to as "spring boarding" [58].

- We compare the impact on a wall between two equivalent balls, one made of clay (perfectly inelastic) and the other of rubber (perfectly elastic). Under Newton's second law, it is dictated that for a body, the rate of change of momentum is directly proportional to the force applied. A perfectly elastic collision will generate twice the impulse compared to the perfectly inelastic equation, if we assume that the clay ball sticks to the wall on impact, whilst the rubber ball rebounds away. Equation 8 and Equation 9 define this, where J_{clay} and J_{rubber} are the kinetic energies of the clay and rubber ball respectively, Δp is the change of momentum, m is the ball mass, v_1 is the ball speed before impact and v_2 is the ball speed post impact. Superhydrophobic coatings reportedly encourage elastic droplet impact behaviour. Investigations

have been carried out which demonstrate that droplets which splash on impact (considered as inelastic impacts) suffer from energy transfer loss [12][9].

$$J_{clay} = \Delta p = mv_2 - mv_1 = 0 - mv_1 = -mv_1$$

Equation 8

$$J_{rubber} = \Delta p = mv_2 - mv_1 = -mv_1 - mv_1 = -2mv_1$$

Equation 9

- Superhydrophobic materials have been reported to induce multiple bouncing of water droplets upon impact, depending on the Weber number of the impacting droplet. This highlights the potential for a single droplet to induce multiple impact events, increasing the energy harvesting capability of the device

2.1.3 Controlling Droplet Impact Frequency and Force

It is useful to estimate the range of impact forces we may expect from incident water droplets. Whether from rain fall or otherwise, droplet diameter studies argue that it is unlikely for a falling rain drop to be larger than 6mm in diameter. At diameters larger than 6mm, the air pressure encountered during falling overcomes the surface tension of the droplet. At this time, the typical spherical shape of the water droplet is deformed, eventually resulting in a rip to the droplet, before disintegration into a group of smaller, spherical droplets. This process can be referred to as a "pancake-bag-break up" routine, referring to the evolving topology of the larger droplet as it undergoes fragmentation [63][64]. This is shown in greater detail in Figure 15.

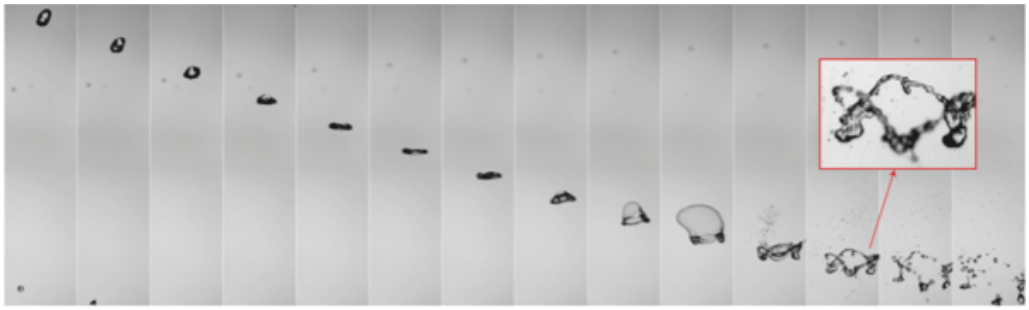

Figure 15 Reprinted from [128]. A series of photographic stills depicting the events of a fragmentation of a 6mm diameter water droplet falling in an ascending stream of air. The images clearly show the "pancake-bag-break up" stages of droplet fragmentation; the flattening of the droplet into a "pancake" shape, the inflation of a "bag-like" shape bordered by a "thicker corrugated rim", before destabilization and fragmentation. The inset picture shows the destabilization of the "bag" rim.

By assuming that the droplet is falling at terminal velocity before impact, we can estimate the impact speed by equating the gravitational force and the opposing resistive force of air pressure imparted on the falling droplet, using a simplified equation of motion [65]. We assume that the droplet is falling as a sphere, and neglect external variables such as the influence of wind, which could either accelerate or decelerate droplet speed depending on its direction. In reality, it is likely that some deformation would occur at such a diameter [63]. We define the gravitational force exerted on the droplet in Equation 10, where F_{weight} is the gravitational force exerted on the droplet, m is the droplet mass, g is the acceleration due to gravity, ρ_{water} is the water density (assumed pure water, 1000kg/m^3), V is the rain droplet volume and r is the rain droplet radius.

$$F_{weight} = mg = \rho_{water} Vg = \frac{\rho_{water} 4\pi r^3 g}{3}$$

Equation 10

We further define the resistive force exerted by air pressure upon the falling droplet in Equation 11, where F_{air_drag} is the resistive force exerted by air pressure, ρ_{air} is the air density (1.225kg/m^3 at 288.15 K and 1 atmospheric pressure), A is the cross sectional surface area of falling object, C_d is the drag coefficient (considered as 0.47 for a sphere and v is the droplet's fall velocity.

$$F_{air\_drag} = \frac{\rho_{air} A C_d v^2}{2} = \frac{\rho_{air} \pi r^2 C_d v^2}{2}$$

Equation 11

Terminal velocity is achieved when the gravitational force exerted on the droplet is equal to the resistive force exerted by air pressure. This is calculated by equating both Equation 10 and Equation 11, then solving for velocity "v", as shown in Equation 12.

$$\frac{\rho_{water} 4\pi r^3 g}{3} = \frac{\rho_{air} \pi r^2 C_d v^2}{2}$$

$$v_t = \left(\frac{8\rho_{water} r g}{3\rho_{air} C_d}\right)^{1/2}$$

Equation 12

With this expression for impact velocity, we may determine an estimate for the impact forces exerted by the anticipated droplet diameter range. In reality, when a water droplet impacts a solid surface it behaves as a compressible, elastic material, due to compressional waves that propagate throughout the body of the droplet from areas contacting the impact surface. These compressional waves constitute an important parameter in determining both the magnitude and distribution of force over the time of impact [66]. By accounting for this behaviour, the force vs. time graph would appear similar to the graph displayed in Figure 16. Furthermore, we see an example of a force vs. time graph for a 2.6 mm diameter droplet impacting upon a piezoelectric quartz impact sensor in Figure 17. In an attempt to emulate this natural effect, we can model impact forces as sharp, pulse loading events.

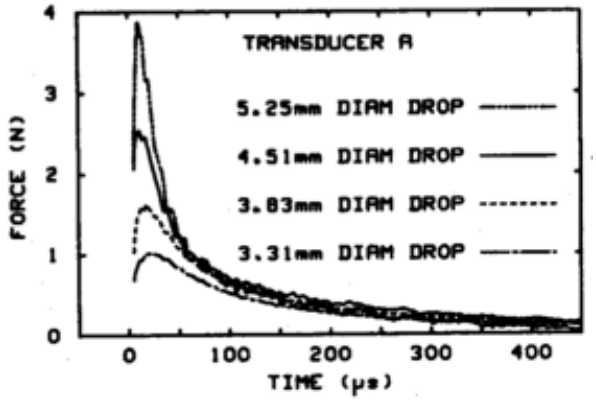

Figure 16 Reprinted from [66]*, A measured force vs. time curve for a series of 4 droplet impacts of different diameters. The curve shape reflects inclusion of the compressible nature of water during droplet impacts and the resulting effect on force distribution and magnitude.*

The impact contact area of the falling droplet as a function of time is considered. Equation 13 describes the basic definition of pressure, with its relationship to force and area.

$$Force\ (N) = Pressure\ (Pa) \times\ Area(m^2)$$

Equation 13

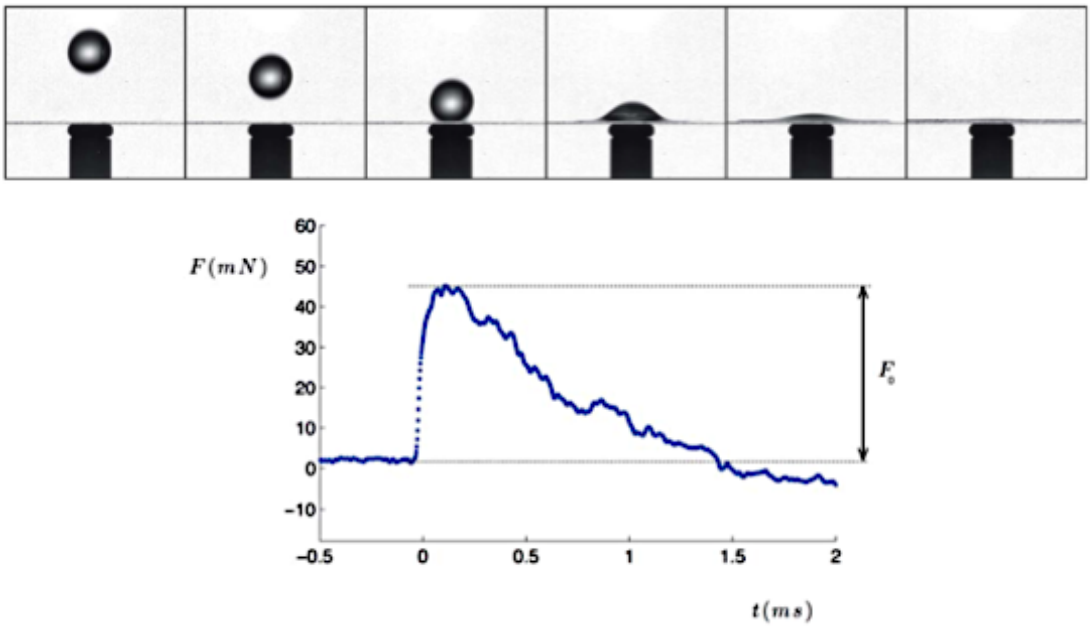

Figure 17 Reprinted and edited from [10]*, upper image series depicts the side view of a water drop of radius R = 1.3 mm hitting a piezoelectric quartz at V = 3 m/s. Successive images occur at a 0.5 ms time scale. Lower graph image displays impact force "F" as a function of time for impact measured by the piezoelectric sensor. The curve is not symmetrical between the beginning and the end of the collision. The maximum force F0 is reached after about a tenth of a millisecond.*

This equation can be used to produce a dynamic estimate of droplet impact force. Studies carried out on the impact force of rain present an equation for the estimated maximum impact force, considering the largest cross-section of the droplet upon impact, as shown in Equation 14 [10], where F_0 is the maximum impact force estimate of falling water droplet, ρ is the fluid density, r is the droplet radius and v is the droplet impact speed.

$$F_0 = \rho v^2 \pi r^2$$

Equation 14

This equation demonstrates the generated impact force as a result of the dynamic pressure "ρv^2" being applied over the droplets centre of axis, cross-sectional surface area "πR^2" [10].

Table 1 displays the range of impact velocities and estimated impact forces for feasible droplet diameters. We see that the range of forces which an impact energy harvesting transducer element may experience is large, spanning potentially 8 magnitudes. It would be impractical to attempt to tailor energy harvesting transducers

to efficiently transfer impact energy for this complete droplet diameter range. As such, it is sensible to target droplets which present an attractive impact energy stimulus. Furthermore, it is shown that the frequency of droplet diameters present during a rain shower are not even – 1 mm diameter droplets tend to occur most frequently, as such it seems to feasible to target such diameters for transducer tailoring [67].

Table 1 Estimated impact velocity and force depending on water droplet diameter

Droplet Diameter / mm	Impact Velocity (Terminal Velocity) / m/s	Estimated Impact Force / N
0.01	0.48	1.78×10^{-8}
0.05	1.07	2.23×10^{-6}
0.1	1.51	1.78×10^{-5}
0.25	2.38	2.79×10^{-4}
0.5	3.37	2.23×10^{-3}
1.0	4.77	1.78×10^{-2}
2.0	6.74	0.143
3.0	8.26	0.482
4.0	9.53	1.14
5.0	10.66	2.23
6.0	11.68	3.85

Whilst it was initially proposed to target incident rain droplets as the primary excitation method for energy harvesting, there are numerous issues with such an approach. From a logical view point, the efficiency of the rain droplet excitation method is sub-optimal for the following reasons:

1. Harvesters exposed to the natural environment must be made durable enough to withstand a wide impact force range, reducing harvester sensitivity. Damage could otherwise be caused by higher impact force droplets, driven by external forces such as high winds.

2. Previous studies regarding piezoelectric energy harvester performance in actual rain conditions note the inconsistency of energy generation, due to the sporadic nature of rainfall events [68]

3. Random, unoptimised droplet impacts upon the harvester surface will result in inefficient straining of the piezoelectric layer

4. Whilst it is possible to estimate the most common droplet diameters likely to be harvested using rain fall drop size distribution (DSD) data for the energy harvester location, such data is not 100% accurate [67][69]. As such, tailoring the energy harvesting transducers to efficiently harvest droplet impact energy, based on estimations of impact force corresponding to droplet diameter, is difficult.

It is therefore deemed necessary to pivot the project's original aim of rainfall droplet energy harvesting, by proposing that it is more beneficial to collect incident droplets first, before guiding them to optimal impact locations on the harvesting transducers in order to achieve a maximal response from the piezoelectric elements. Whilst this approach may compromise on the raw kinetic energy available from a rain droplet travelling at terminal velocity, it is theorised that controlled dispensing of droplets allows for more precise tailoring of the energy harvesting elements, in order to encourage greater energy transfer efficiency.

2.2 Existing Droplet Impact Energy Harvesters Using Piezoelectric Transducers

Research into droplet impact energy harvesting has seen limited progress to-date, with the majority of investigations utilising commercially available sensors to analyse droplet impact mechanics. Whilst good insight has been produced from these analyses, using commercial sensors as the energy harvesting transducer limits the degree to which the transducers can be modified to efficiently harvest the droplet impact stimulus.

A comparison of power outputs achieved by previously reported water droplet energy generators is given in Table 2 [17]. Investigations into water droplet impact energy harvesting appear to have been formally initiated by Guigon *et al* in 2008 , where both the theory and experimental work contributing to efficient mechanical energy harvesting using a piezoelectric PVDF membrane was outlined in a two-part study [9], [12].

Table 2 Adapted from [17]*, a comparison of potential rain droplet energy generators*

Researchers	Year published	Piezoelectric material	Impact droplet diameter and speed	Transducer & dimensions (length/width/thickness) / mm	Peak Instantaneous Output Power
Guigon et al. [52]	2008	PVDF	5 mm, 5.7 m/s	Fixed-fixed beam, (100/3/0.25)	12.5 mW
Alkhaddeim et al. [70]	2012	PZT	0.2 mm, 0.22 m/s	Cantilever, (20/8/0.58)	23 μW
Valentini et al. [71]	2013	PMMA / GO	0.06 mm, 2 m/s	N/A	6 nW
Viola et al. [72]	2013	PVDF	5 mm, 8 m/s	Cantilever, (40/10/0.58)	4.5 μW
Lee et al. [73]	2015	PVDF	<0.1 mm, acoustically vibrated	Cantilever (73/15/0.2)	80 μW
Wong et al. [74]	2017	PZT	2.96 mm, 2.15 m/s	Cantilever (81/38/0.6)	3.47 μW

The initial theoretical investigation illustrated how variation of the harvesting structure width and thickness optimises the transfer of deformation energy from the drop to the piezoelectric polymer, before investigating the structure conversion efficiency through surface contact electrode design. It was concluded that the piezoelectric transducer material must be very thin (μm scale), not be pre-stressed and be of a width slightly smaller than the maximum diameter of the impacting drop for efficient energy harvesting to take place. Additionally, it was considered optimal for the piezoelectric material to be entirely covered with conducting electrodes. Simulations demonstrated a theoretical energy output of 25 μJ and peak instantaneous power output of 12 mW from a "downpour" drop of 5 mm diameter [12].

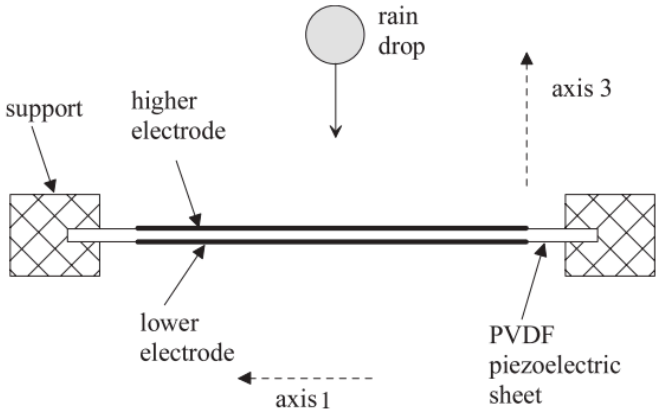

Figure 18 Reprinted from [9]*, diagram to represent a raindrop energy harvesting system*

The corresponding experimental study, illustrated in both Figure 18 and Figure 19, demonstrated how mono-stretched PVDF polymer bands of 10 cm length, 3 mm

width and 25μm thickness demonstrated a peak power output of approximately 1 μW of instantaneous power from a single droplet impact. It was observed that the recovery of electrical energy was maximised when droplet impacts were slightly off-centre from the beam material. This is reported to be due to the rigidity of the material, where the stiffness of the material naturally varies along the beam length. For example, it was found that the beam stiffness is greatest in close proximity to the clamped ends, and less at the beam length centre. Therefore, it is proposed that the effect of applied force at a position of $\frac{Beam\ Length}{4}$ induces greater stress within the piezoelectric layer, compared to forces applied to the beam centre. It is noted that no hydrophobic encapsulation was administered to the bands, therefore the droplet impacts were treated as inelastic.

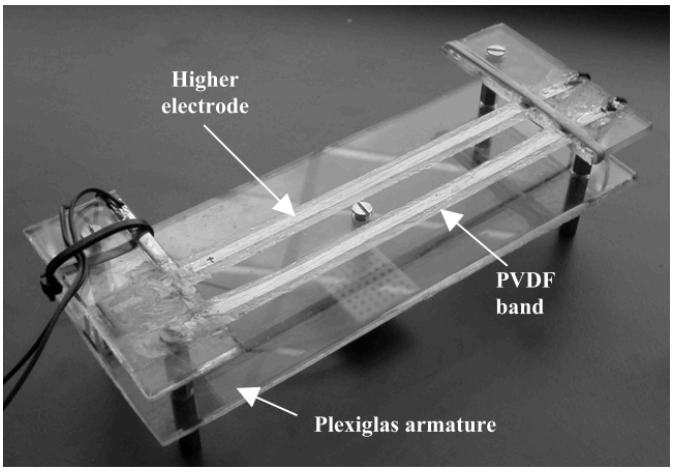

Figure 19 Reprinted from [9]*, photograph of PVDF band experimental setup*

These preliminary investigations led to subsequent investigations using different geometries and materials. Ilyas and Swingler analysed the voltage output profiles produced from droplet impact upon commercially available sensors in detail, identifying two distinct phases in voltage and power output, illustrated in Figure 20; log growth at the initial impact, before exponential decay took place throughout the remainder of the impact event [21][75]. It was demonstrated that the log growth stage significantly contributes to the overall power output of the device.

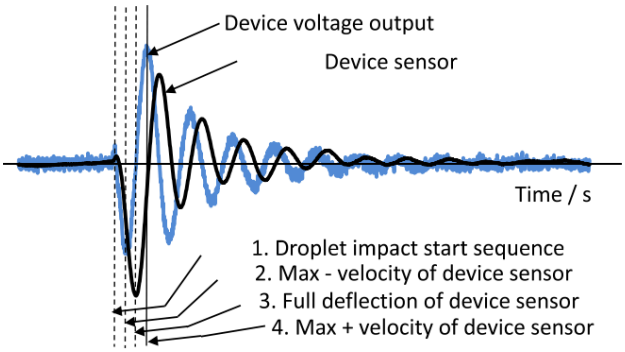

Figure 20 Reprinted from [75]*, voltage output profile of droplet impact illustrating key impact points*

The sensor used for voltage output profile measurements, a Pro-Wave (FS-2513P), utilised a piezoelectric polyvinylidene fluoride layer with an active volume of approximately 0.975 μm^3. A peak instantaneous power output of 2.5 µW was produced from a single droplet impact, which is in-line with previous results. Whilst the insight provided by this research is important, it is noted that the conversion efficiency of such commercial sensors is in the region of 0.12 %, representing a clear opportunity for further improvement of energy transfer efficiency.

A limited number of different harvester configurations have been tested. Research conducted by Viola *et al* has investigated droplet energy output with commercially available piezoelectric sensors, in addition to testing the harvester configurations illustrated in Figure 21[20], [23], [72], [76]. It was found that the cantilever structure achieved the best response to impacting droplets, with LDT1-028K MEAS piezoelectric sensors producing 17 V output from droplets dispensed from a height of 2 m. The active dimensions of the sensor PVDF film used are length 30 mm, width 12.19 mm, thickness 0.028 mm. The performance of various rectification circuits was also investigated, with voltage outputs at each stage shown in Figure 22, highlighting how the useful power output available from droplet impact energy harvesting is significantly lower than expected.

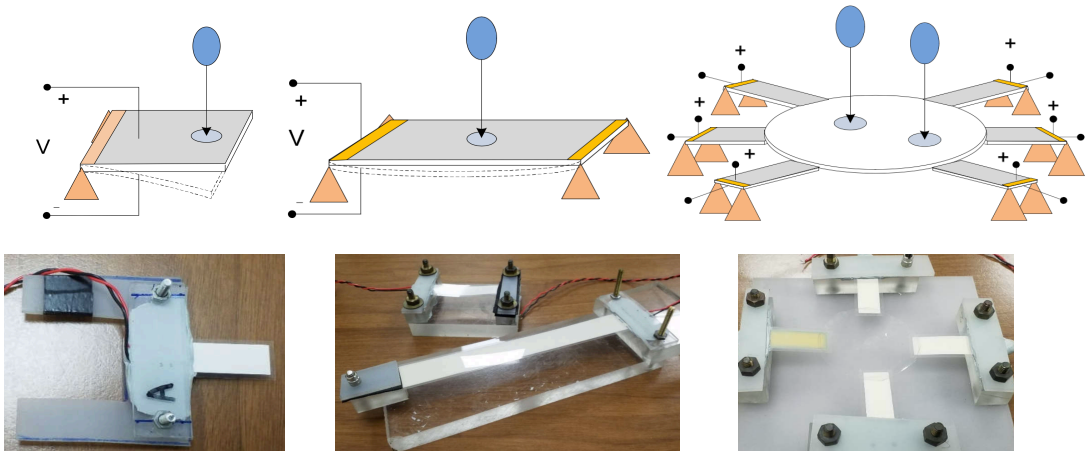

Figure 21 Reprinted from [23], upper row of diagrams illustrating (left to right) piezoelectric cantilever beam, bridge and floating circle energy harvesting structures. Lower row of images represents corresponding experimental setup of these configurations using MEAS LTD PVDF sensors

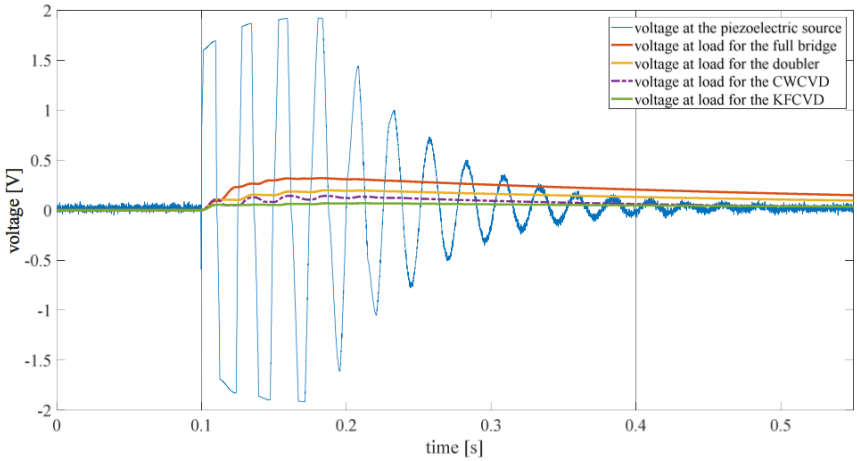

Figure 22 Reprinted from [23]*, voltage output across 10 kΩ load resistor produced by a single water droplet impact upon a LDT1-028K MEAS piezoelectric sensor in cantilever configuration. The voltage output for the instances of no rectifying circuit, full bridge rectifier, Greinacher voltage doubler, Cockcroft Walton Cascade Voltage Doubler (CWCVD) and Karthaus Fisher Cascade Voltage Doubler (KFCVD) rectifying circuits are compared.*

The performance of piezoelectric energy harvesters in both simulated and actual rainfall was evaluated by Wong *et al* [68], [77]. A spray-type rain simulator was used to dispense a range of droplet diameters from a height of 2.5 m onto a PZT piezoelectric beam, with a schematic of the beam composition given in Figure 23. In this case, a Midé Volture™ commercial piezoelectric sensor (model V25W) was used for measurements, composed of two PZT layers of 46 mm length, 33 mm width and 0.6 mm overall sensor thickness [78]. The PZT layers were connected in series across a 15 kΩ load resistor. The simulated rain rates, droplet diameter distribution mean and power outputs generated are displayed in Table 3.

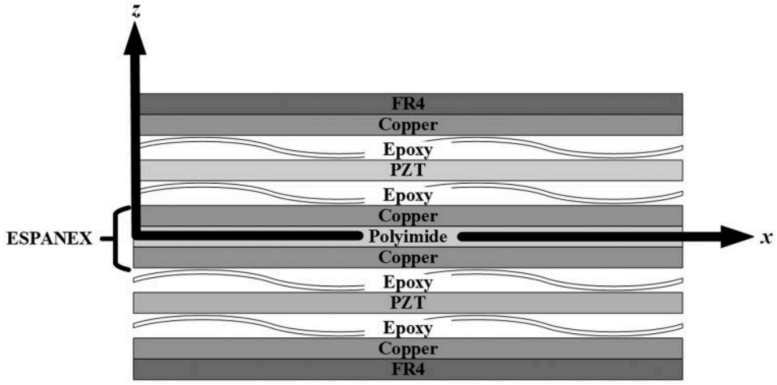

Figure 23 Reprinted from [76], layer composition of the Midé Volture commercial piezoelectric sensor PZT piezoelectric beam used

Table 3 Simulated rainfall experiment settings and results

Simulated Rainfall Setting	Rainfall rate / mm/h	Droplet diameter distribution mean / mm	Total accumulated power from 300 second study duration / μW
1	33	0.77	0.074
2	40	0.81	0.156
3	62	0.80	0.167
4	99	0.73	0.207

Results from field testing of the commercial sensor in three different rainfall events of duration 250, 204 and 301 minutes produced total harvested energies of 155.6 μJ, 438.9 μJ and 2076 μJ respectively. The significantly long time scale required to capture these energies highlights the inefficiency of attempting to harvest energy directly from rainfall droplet impacts.

To conclude this chapter, it is clear that the interaction of an impacting water droplet with a solid surface is non-trivial. A wide variety of factors influence the impact dynamics, ranging from droplet diameter and impact speed, to the transducer elasticity and surface wettability . There is sizeable opportunity for the following key developments to be made in the field :

- Further investigation into energy outputs from harvesters encapsulated in hydrophobic surface treatment

- Investigation of tailor-made piezoelectric transducers, not commercially available sensors, which can be tuned with greater accuracy to increase droplet impact energy transfer efficiency

- Variation of both the geometry and materials used for developing impact energy harvesting transducers

3 Material Selection

"Never memorise something that you can look up."

— Albert Einstein

The harvesting of droplet impact energy requires high mechanical sensitivity in order to harvest impact energy efficiently. In this chapter, the merits of utilising piezoelectric materials as the transducer medium are analysed; such as the strong electromechanical coupling properties, favourable power density scaling, robustness and design flexibility.

3.1 Introduction to Piezoelectricity

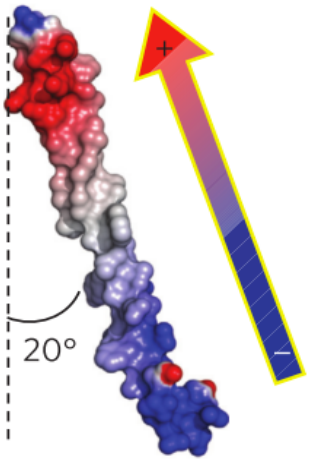

Figure 24 Reprinted from [84]*, side-view representation of the electrostatic potential of a single M13-phage pVIII coat protein.*

The electromechanical phenomenon of piezoelectricity has both intrigued and perplexed researchers since its reported discovery by two scientists, Carl Linnaeus and Franz Aepinus, during the mid 18th century. These scientists discovered the Pyroelectric effect, and it was through this work that subsequent theories predicted the discovery of Piezoelectricity [79]. Later, Pierre and Jacques Curie proved that in known piezoelectric materials, such as quartz or Rochelle salt crystals, suitable compression of the materials caused a mechanical strain, which resulted in the generation of an electrical potential across the material [79][80].

In 1881, a mathematician named Gabriel Lippman theorised that there should be a converse piezoelectric effect, which was soon experimentally proved by the Curie brothers as the "inverse piezoelectric effect" [79][81].

Today, we formally define the piezoelectric effect as the linear, electromechanical interaction between the mechanical and the electrical state in crystalline materials with no inversion symmetry [82]. A surprisingly large range of both natural and synthetic materials exhibit some form of piezoelectricity. For example, collagen

fibrils found in dried bone samples were shown to exhibit piezoelectric properties [83]. Additionally, viral proteins have been demonstrated to possess piezoelectric qualities, such that a piezoelectric energy generator based upon M13 bacteriophage was used to operate a small liquid crystal display [84].

The fundamental relationships used to describe the piezoelectric effect are shown in Equation 15 and Equation 16, which describe the inverse and direct piezoelectric effect respectively [85][86]. Such coupled equations are used to describe both the mechanical and electrical properties that contribute to the piezoelectric effect, where S is the imposed mechanical strain, s^E is the material compliance under a zero or constant electrical field, T is mechanical stress, d_{ij}^t is the inverse piezoelectric effect described in transposed matrix notation, E is the electric field, D is the electrical displacement, or charge density, d_{ij} is the direct piezoelectric effect described in matrix notation and ε^T is the dielectric permittivity under a zero or constant stress.

$$\{S\} = [s^E] \cdot \{T\} + [d_{ij}^t] \cdot \{E\}$$

Equation 15

$$\{D\} = [d_{ij}] \cdot \{T\} + [\varepsilon^T] \cdot \{E\}$$

Equation 16

If we omit the coupling term "$d^t \cdot E$" from Equation 15, we are left with Hooke's law for relating stress and strain. Similarly, if we omit the "$d \cdot T$" term from Equation 16 we are left with the dielectric equation [86].

The properties of a piezoelectric material are typically anisotropic – they are directionally dependent. Directionality of these properties is described using a Cartesian coordinate system, with Figure 25 illustrating this. Of the associated coefficients used to describe piezoelectric material behaviour, this study is particularly interested in [87]:

- The piezoelectric charge constant, or "*d*" coefficients. This coefficient relates the generated charge density to the applied mechanical stress applied to the piezoelectric material, or conversely the developed strain in a piezoelectric material caused by an applied field.

- The piezoelectric voltage constant, or "*g*" coefficients. This coefficient relates to the electric field generated by a piezoelectric material depending on the applied mechanical stress, or conversely the mechanical strain experienced by the piezoelectric material per unit of applied electrical displacement.

- The electromechanical coupling factor, labelled as "*k*", which is used to quantify the effectiveness of a piezoelectric material's ability to convert mechanical energy to electric energy, or vice versa. The dimensions of a piezoelectric material can dictate unique expressions of "*k*".

- Permittivity, "ε", otherwise known as the dielectric constant. This constant is a measure of the materials' dielectric displacement per unit of applied electric field

These constants are both important and interlinked; the charge constant "*d*" is a measure of a piezoelectric material's suitability for strain-dependent applications. The voltage constant "*g*" is important for gauging a piezoelectric material's suitability for sensing applications. "*d*" , "*g*" and "ε" can be used to express the other, as per the relationship outlined in Equation 17.

$$g = \frac{d}{\varepsilon}$$

Equation 17

Of key importance to energy harvesting applications, the output power is proportional to the product of "*g*" and "*d*", shown in Equation 18, as a "Figure of Merit" to gauge the effectiveness of an energy harvester [88].

$$P \propto g \times d$$

Equation 18

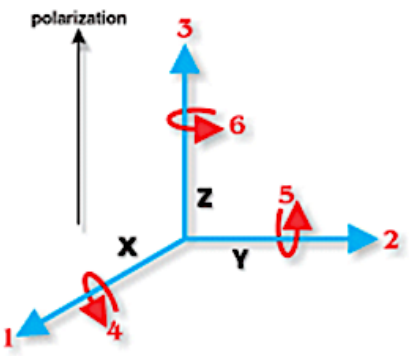

Figure 25 Reprinted from [87]*, diagram to show subscript labelling of forces effecting a piezoelectric material in relation to the direction of polarization*

In order for a material to demonstrate a piezoelectric response, there are two key requirements. Firstly, the atomic structure of the material must be non-centrosymmetric; there must be a symmetry-breaking element in the atomic structure of the material, which ensures that a net polarization is developed when the material is placed under mechanical stress due to formation of dipole moments.

Secondly, the non-centrosymmetric material must undergo a poling process in order to align groups of dipoles with the same alignment, known as Weiss domains, into a uniform direction. In a process analogous to the magnetization of a permanent magnet [89] , the application of a strong electric field, often whilst the material is heated to a critical temperature, allows the dipole groups to align in a desired direction. Once orientated, an observable piezoelectric response can be generated in an expected direction. Figure 26 gives an exaggerated illustration of the effects of the poling process and its influence upon dipole moment orientation. In reality, the dipole regions will align in an average orientation, creating a net polarization. It is very unlikely for all dipoles to align in a uniform direction due to factors such as strong intermolecular forces.

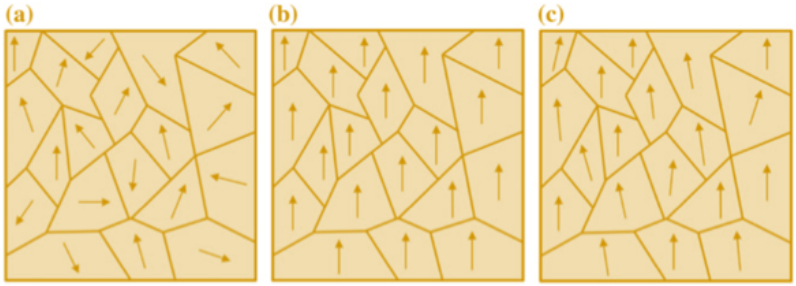

Figure 26 Reprinted and edited from [89]*, A simple diagram to illustrate the orientation of groups of dipoles (Weiss domains) (a) before, (b) during and (c) after the poling process. It must be noted that, diagram (b) is a simplified diagram for understanding purposes, with diagram (c) most likely representing the dipole orientation of a piezoelectric material after successful poling.*

Piezoelectric materials are part of a 32 crystal class and are composed from a number of subset materials, as illustrated by Figure 27. This study will look at utilising Ferroelectric materials, a class of materials that exhibit a spontaneous electric polarisation. This polarisation can be reversed by the application of a suitably strong electric field [90][91]. Ferroelectric materials are ideally suited for piezoelectric applications, as they can be poled by an external field and produce the required break of inversion symmetry [92].

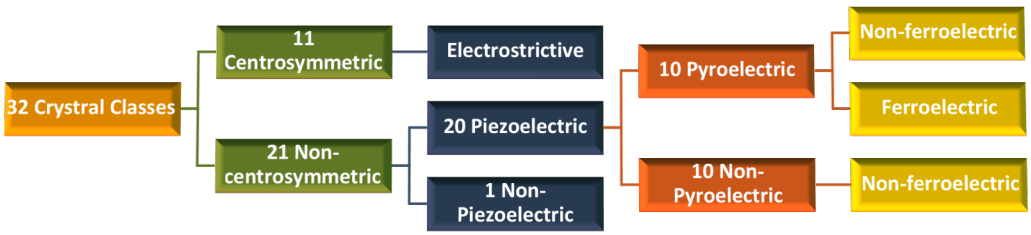

Figure 27 Edited from [93]*, diagram to show classification of 32 crystal class materials*

3.2 Piezoelectric Material Selection

Since the discovery of piezoelectric materials, the international market has long been dominated by the piezoelectric material $Pb(Zr_{1-x}\ Ti_x)O_3$, or PZT. However, since the early 2000's, there has been a sharp increase in research focusing on the synthesis and performance of lead-free piezoelectric materials. This is largely in part due to increased legislation regulating the usage of toxic lead in consumer products [92][94]–[96]. Given that the results of this research may interact with environmental aspects such as rain water, lead-free piezoelectric materials are considered in order to adopt a positive environmental approach.

Potassium Sodium Niobate (KNN) was first reported as a potential lead-free piezoelectric material in 1959, with continued research demonstrating KNN materials with commendable ferroelectric and dielectric properties, yielding much promise for future applications [92], [97]–[102]. Since then, one of the most notable breakthroughs in material development occurred in 2004, where a synthesised KNN solution exhibited piezoelectric properties close to that of PZT [103]. Certain compositions of KNN have been discovered to retain a high mechanical quality factor under increasing vibration levels, proving to be superior to some types of hard PZT. Indeed, it is reported that KNN materials with "giant" d_{33} values of ~390−490 pC/N have been developed using conventional solid-state methods of preparation [104]. Although more recent articles have been published [97], an excellent summary published in 2009 by J. Rödel, W. Jo, K. Seifert *et al* [92] provides a series of informative diagrams explaining the rationale behind lead-free material suitability and selection. Whilst the pricing will alter, Figure 28 shows a comparison of cost and toxicity for elements of interest.

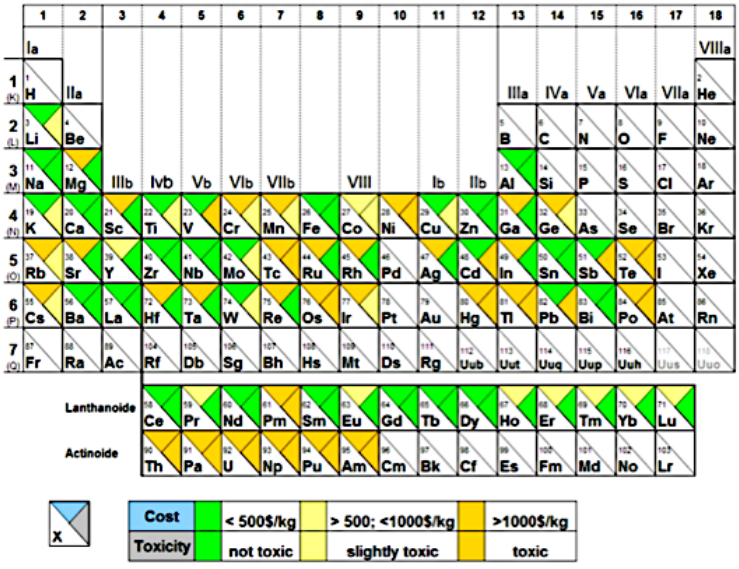

Figure 28 Reprinted from [92]*, diagram to show relative cost and toxicity of elements*

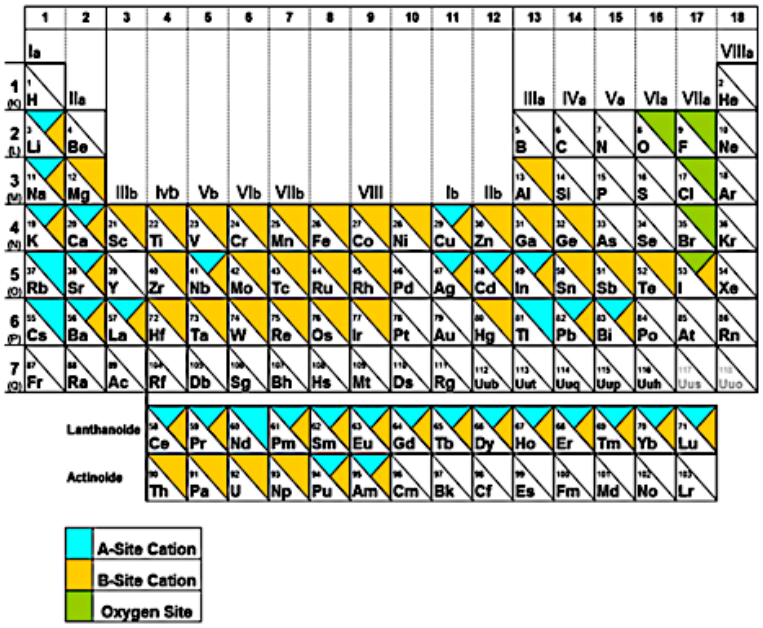

Figure 29 Reprinted from [92]. *Diagram to show possible candidates for A, B and oxygen sites in perovskite type structured piezoelectric materials*

Given that the aim of this study is to ultimately produce a device which will interact with water droplets, it is of paramount importance that all materials used within the harvester are appropriate for use, and are either unreactive with water or can be reliably encapsulated. KNN, containing both potassium and sodium, can be expected to react with high volatility on contact with water, demanding thorough encapsulation. Furthermore, preliminary investigations have shown that although KNN is a desirable lead-free material to utilise, it has proven difficult to deposit KNN over large areas, with current methods restricted to deposition over minimal substrate surface areas through spin-coating. This alludes to future difficulties should the droplet energy harvester require larger surface areas of piezoelectric material than expected.

For the purposes of rapid prototyping the lead-free piezoelectric polymer polyvinylidene fluoride, or PVDF, appears to provide an attractive solution. A clear, elastic polymer, PVDF exhibits a high electromechanical coupling factor. In applications where a sizeable degree of physical motion is expected from the energy source, PVDF's superior mechanical properties make it a better choice for energy harvesting over brittle piezoelectric ceramic materials. However, the piezoelectric properties of PVDF remain inferior to popular piezoelectric materials, with low piezoelectric coefficients of 6-7 pC/N reported. These properties can be improved to reported values of -38 pC/N d_{33}, with modified PVDF copolymers such as polyvinylidene fluoride-trifluoroethylene (P(VDF-TrFE)) exhibiting piezoelectric

coefficients of -50 pC/N for d_{24} at a temperature of 295 K [105][106]. Advantageously, the deposition of P(VDF-TrFE) is achievable through a variety of methods such as spray coating or casting, and it is possible to coat a significantly larger substrate surface area with ease. This property makes P(VDF-TrFE) a very attractive candidate for large scale transducer production. Given that the intended application will see the harvesting elements undergoing multiple "shock" impulse events from droplet impact, P(VDF-TrFE) presents itself as a flexible, elastic material with good resistance to environmental corrosion. Figure 30 demonstrates the successful deployment of P(VDF-TrFE) materials in energy harvesting applications involving water waves as the input vibration stimulus.

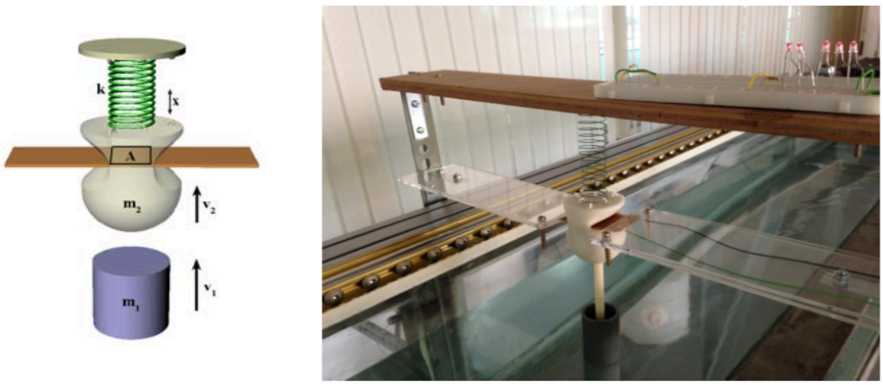

Figure 30 Reprinted from [107]*, illustrations depicting a small elastic floating energy harvester for ocean ripple power harvesting utilising knitted PVDF thin film. Left image depicts knocking structure and beating element, with the PVDF strip labelled "A", whilst right image shows prototype device for experiment in wave maker tank.*

3.3 Substrate Material Selection

Whilst it is the piezoelectric material that generates the electrical power, the substrate that supports it significantly dictates the overall mechanical properties of the system for thin piezoelectric films. Furthermore, the conductivity of the substrate will also significantly influence the electrical power output of the piezoelectric film. A summary of the substrate materials used successfully in the deposition and growth of KNN films, along with some examples of PZT and P(VDF-TrFE) deposition, is shown in the Appendix. For this work, a substrate which can be deformed many times whilst withstanding a range of randomly applied impact forces is desirable. Additionally, we must also consider desirable parameters from a commercial point of view; pricing, availability, toxicity and robustness. A straight forward way of assessing material suitability is to investigate the elastic modulus, or Young's

modulus, denoted using Equation 19, Where Y is Young's modulus, F is the force exerted on an object under tension, A is the cross-sectional area through which the force is applied, ΔL is the amount by which the length of the object changes and L_0 is the original object length.

$$Y = \frac{\sigma(\varepsilon)}{\varepsilon} = \frac{F/A}{\Delta L/L_0} = \frac{FL_0}{A\Delta L}$$

Equation 19

For example; rubber, known for its excellent elastic properties, typically has a very low Young's modulus of 0.01-0.1 GPa [108]. Conversely diamond, known for its extreme hardness, has a Young's modulus of 1050 – 1210 GPa [109]. An extended summary of substrates which have been previously used for the deposition of piezoelectric materials is given in the Appendix.

Table 4 Comparison of Young's moduli for materials previously used in KNN deposition research

Substrate Material	**Piezoelectric Materials Deposited**	**Young's Modulus Range (GPa)**	**References**
Aluminium Oxide	$K_{0.5}Na_{0.5}NbO_3$ (KNN)	215-413	[110] [111]
Inconel 600	$K_{0.88}Na_{0.12}NbO_3$ (KNN)	207	[112] [113]
Glass	$K_{0.5}Na_{0.5}NbO_3$ (KNN)	50-90	[108] [114]
Magnesium Oxide	$K_xNa_{1-x}NbO_3$ (KNN)	270-330	[115] [116]
Polydimethylsiloxane (PDMS)	P(VDF-TrFE)	0.00057 - 0.0037	[117]
Silicon (Single Crystal, Dif. Directions)	PZT $K_xNa_{1-x}NbO_3$ (KNN)	130-185	[111] [118] [119] [120]
Strontium Oxide	$K_xNa_{1-x}NbO_3$ (KNN)	N/A (Shear Modulus = 6.1 GPa)	[121] [122]
Stainless Steel	PZT $K_xNa_{1-x}NbO_3$ (KNN)	180-203	[108] [120] [123] [124]

Silicon is a popular material used to date, however, it is typically very brittle (although development of flexible silicon substrates is progressing) [125][126]. Moreover, silicon wafer prices are quoted as upwards of £135 GBP for wafers of dimensions 2

inch diameter by 0.5 mm thickness [127]. This pricing potentially makes large scale harvester devices economically unfeasible. Brittleness, in conjunction with high cost, make substrates such as aluminium oxide, glass, magnesium oxide, silicon and strontium oxide also unsuitable for this application. In order for the harvesting elements to be sensitive enough to harvest the smallest of droplet impact forces, yet have the potential to withstand the largest of droplet impacts, high elasticity will be required at thicknesses in the millimetre scale and below. In contrast to silicon, PDMS appears to be a potential substrate candidate, having a low Young's Modulus – however, such substrates require additional processing as they are typically non-conductive, and as such require conductive interlayers to be deposited in order to serve as a bottom electrode to the piezoelectric materials. This increases the complexity of fabrication, and is likely to limit scalability of the final device. In light of this, it seems natural to consider a metallic substrate for such an application. Table 5 displays relevant parameters of metals typically used in electronic devices. Stainless steel appears to possess the mechanical qualities desired for a rainfall harvester, in addition to favourable pricing on the global market, due to the abundance of its constituent materials [128]. Stainless steel is also a good conductor of electricity, removing the need to deposit additional interlayer electrodes. However, better conducting materials exist with comparable mechanical properties, such as copper. Copper is widely used in electronic devices for its high conductivity and reasonable cost. With copper sheets of dimensions 300 mm length, 170 mm width and 0.05 mm thickness costing approximately £2 GBP per sheet [129], copper presents an affordable option with attractive mechanical qualities for droplet impact energy harvesting substrates. Both stainless steel and copper are investigated for their suitability in this application, although the corroding nature of copper will require investigation into appropriate encapsulation methods.

Table 5 Relevant material parameters of commonly used electronic device metals

Material	Resistivity / Ω/m	Conductivity S/m	Young's Modulus / GPa	Reference
Aluminium	2.65×10^{-8}	3.77×10^{7}	70	[130]
Copper	1.68×10^{-8}	5.96×10^{7}	110–128	[131][132]
Nickel	6.99×10^{-8}	1.43×10^{7}	200	-
Tin	1.09×10^{-7}	9.17×10^{6}	50	-
Titanium	4.20×10^{-7}	2.38×10^{6}	116	-

Silver	1.59×10^{-8}	6.30×10^{7}	83	[130][133]
Stainless Steel	6.90×10^{-7}	1.45×10^{6}	180-203	[108][123]

To conclude, it is shown that a variety of piezoelectric materials exist, each with its own ideal application. The piezoelectric polymer, P(VDF-TrFE), is identified as a suitable piezoelectric material for usage in the harvesting of water droplet impact energy, given its flexibility and reasonable piezoelectric properties. Furthermore, the substrate chosen to support the piezoelectric material often dictates the mechanical properties of the overall transducer, requiring significant consideration. It is found that either copper or stainless steel present viable options, given their robustness and resilience to sustained mechanical stimuli.

4 Transducer Geometry Investigations

"We shape our buildings; thereafter they shape us"

— Winston Churchill

How to capture, transform and utilise energy as efficiently as possible from a target energy source is the fundamental purpose of an energy harvesting device. In this chapter, the methods of maximising the energy transfer efficiency between the transducer and stimulus are considered. Energy harvesting systems are complex, multiphysics systems, often with several energy transfer stages to be considered for optimisation. Figure 31 illustrates the stages of energy transfer present in a piezoelectric vibrational energy harvester. It is demonstrated that there are 3 distinct phases relating to the matching of both mechanical and electrical impedances throughout the device energy flow [134].

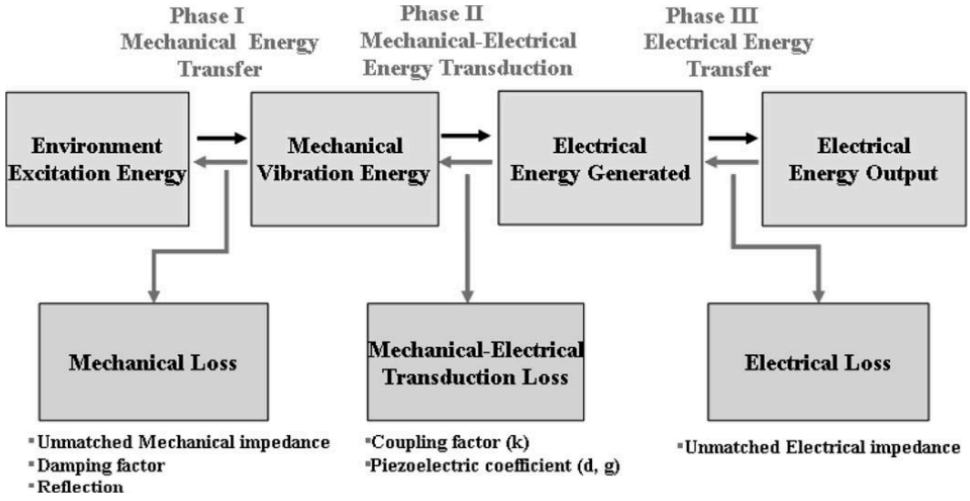

Figure 31 Reprinted from [134] *Diagram illustrating energy flow in a harvester system*

Phase I focuses on the dynamic mechanical response of the system, with a view to match the mechanical impedances of the excitation source and the harvesting element. This is an example of structural optimisation and can be achieved through informed device design, guided by mechanical engineering principles. Considering an impact energy harvesting transducer, Figure 32 highlights parameters necessary to optimise in order to achieve ideal energy transfer efficiency.

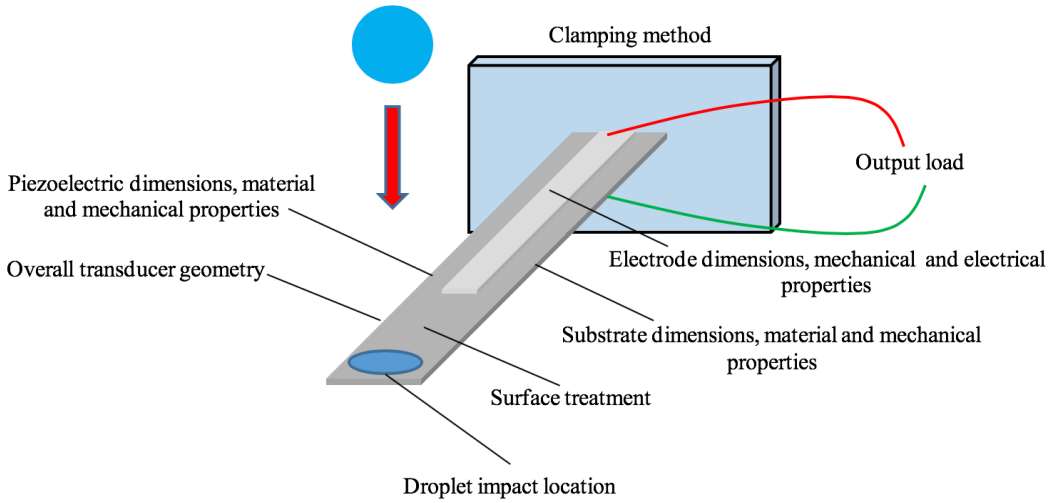

Figure 32 Diagram to illustrate parameters considered to be necessary to optimise in order to encourage efficiency droplet impact energy harvesting

This investigation primarily focuses upon how best to optimise Phase I, considering the mechanical energy transfer between the droplet kinetic impact energy and the transducer harvesting element, in order to achieve maximal electrical energy output from the piezoelectric material.

Whilst optimisation of Phase II is beyond the scope of this research, involving chemical engineering of the piezoelectric material in order to enhance the electromechanical coupling factor, Phase III is considered in part through the process of electrical impedance matching. For power transfer circuits such as piezoelectric energy harvesters, it is necessary to attempt to match the source impedance (the internal impedance of the piezoelectric material) to the load impedance (an output load, such as a resistor) as closely as possible. This is derived from the maximum power transfer theorem, which states that the maximum power which can be transferred from source to load is 50%, which occurs when source impedance is exactly matched to load impedance [135][136]. It is important to not confuse this theorem with the efficiency of the device; the maximum power transfer possible and maximum device efficiency are different entities. For example, should the load resistance be increased, more power is dissipated in the load than in the source impedance – as a result, efficiency is increased [137].

Conveniently for piezoelectric systems, we may analyse a harvester's response to external stimuli by representing a mechanical system with an analogous electrical

system, illustrated in Figure 33. The mechanical system is represented as an electrical system via an impedance or Maxwell analogy [138][139].

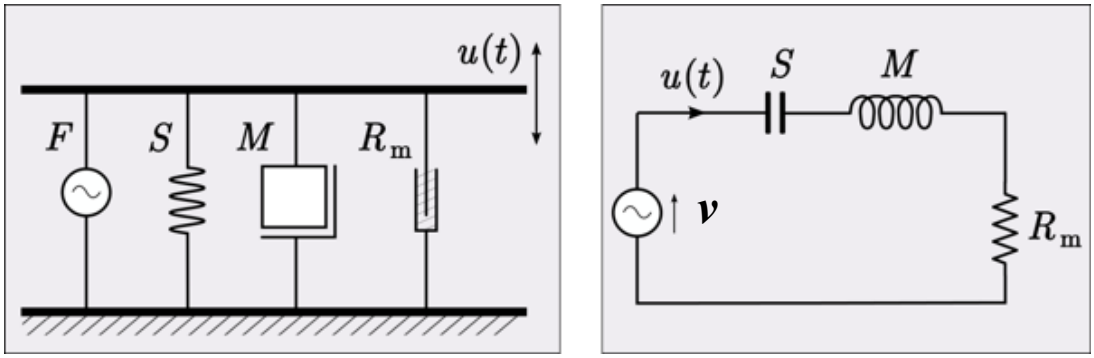

Figure 33 Reprinted from [140]*, based upon work from* [141]–[143] *- diagram to show a simple mechanical resonator (left) with the corresponding impedance analogy electrical circuit (right).*

Figure 33 illustrates the analogy of a mechanical resonator, comparing a constant force generator, stiffness element, mass and damper, to that of an analogous electrical circuit, consisting of a corresponding voltage source, capacitor, inductor and resistor respectively. The comparisons are logical; the force generator drives the system, much like a voltage source. The stiffness of the system, otherwise known as the inverse of mechanical compliance, is analogous to the elastance or inverse capacitance of an electrical circuit. A mass, the movement of which is relative to a frame of reference within the system, could be compared to the impedance imposed by an inductor within an electrical circuit. Finally, a mechanical damper shares similarities to that of an electrical resistor in that both components represent a loss of energy within the system.

In doing so, the analogy between electrical impedance and mechanical impedance is also preserved. As such, it is assumed that both require the same conditions for power transfer to be maximised; that both load and source impedance should be matched. Taking the piezoelectric transducer's stiffness to be the load and the impacting droplet to be the source, this theory suggests that an ideal transducer for harvesting droplet impact energy should resist droplet impact to a similar force magnitude to that of the impacting droplet. It has been shown that increasing the mechanical coupling between the transducer and energy source, thereby reducing the damping factor and reflection ratio, can have a dramatic effect on the energy generation efficiency. A piezoelectric "cymbal" transducer system, illustrated in Figure 34, was found to exhibit approximately 40 times higher effective strain coefficient than piezoelectric ceramics,

when sufficiently pre-stressed to better match the vibration excitation source. The results of this investigation are displayed in Figure 35 [134]. As such, there is indication that an ideal transducer stiffness exists for each excitation source, resulting in maximal power output.

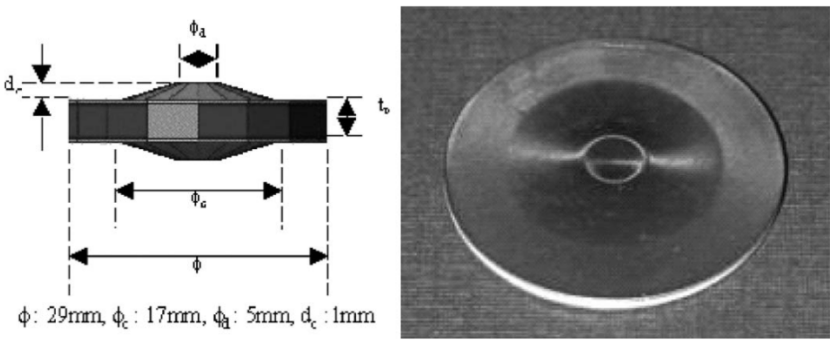

Figure 34 Reprinted from [134] *structure of the cymbal used as a piezoelectric transducer. The presence of cavities in the cymbal allowed the metal end caps to serve as mechanical transformers, which in turn amplified a portion of the incident axial stress.*

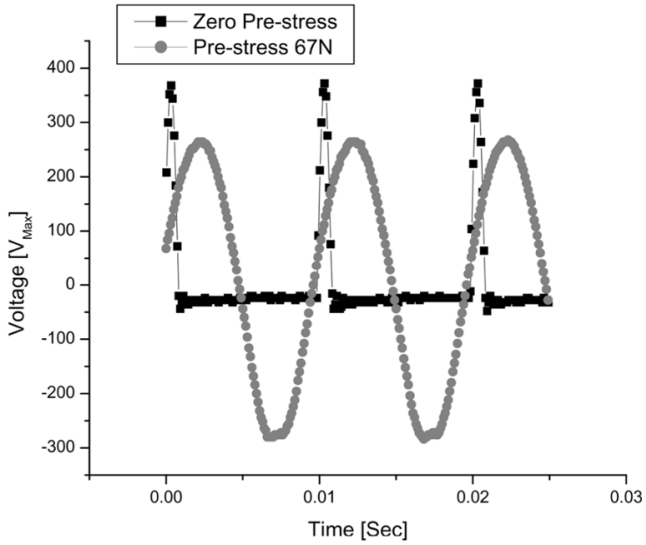

Figure 35 Reprinted from [134] *Graph to show output peak voltage of cymbal transducer depending on pre-stress condition. Force of 8 N and 40 N at 100 Hz were applied for zero stress and pre-stress conditions respectively.*

4.1 Piezoelectric Cantilever Beam Considerations

In this research, practical investigations start with exploring the effect of mechanical stiffness variation on energy conversion efficiency. In order to ensure as fair testing as possible, it is important to vary the stiffness parameter in isolation. It is proposed that the simplest method of observing the effects of stiffness variation is to utilise cantilever beam shaped transducers. The relationship defining cantilever beam

stiffness for a point load deflection applied at the free-end of the cantilever, perpendicular to the beam axis, is given in Equation 20 and illustrated in Figure 36, where k_b is the beam bending stiffness, E is the beam elastic modulus, w is the beam width, t is the beam thickness and L is the beam length.

$$k_b = \frac{Ewt^3}{4L^3}$$

Equation 20

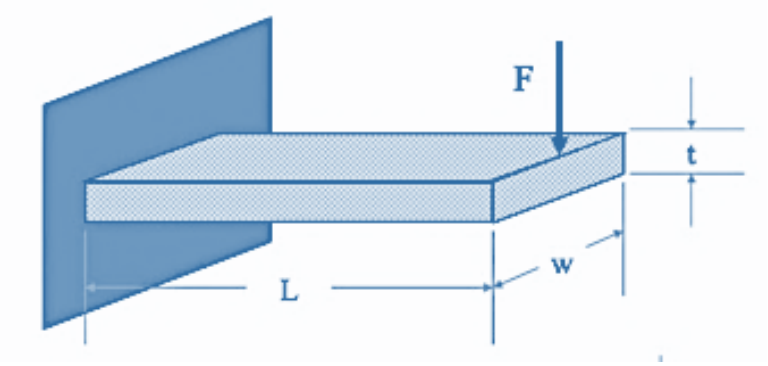

Figure 36 reprinted from [144]*, illustration of single fixed end cantilever beam with applied point load force.*

Moreover, it is found that the stiffness of a cantilever beam geometry may be altered in isolation by varying the width of the beam whilst keeping all other variables constant, without affecting other mechanical parameters such as the beams resonant frequency. The steps shown resulting in Equation 21 [145] illustrate how the natural frequency of a cantilever beam isn't dependent on beam width, where f_b is the beam's resonant frequency, Y is the beam's Youngs modulus, I is the beam's second moment of area $\left(I = \frac{wt^3}{12}\right)$, ρ is the beam density, A is the beam area $(A = wt)$, L is the beam length, w is the beam width and t is the beam thickness.

$$f_b = \left(1.875^2 \sqrt{\frac{YI}{\rho A L^4}}\right) \cdot \frac{1}{2\pi}$$

$$\Downarrow$$

$$f_b = \left(1.875^2 \sqrt{\frac{\left(\frac{Yt^2}{12}\right)}{\rho L^4}}\right) \cdot \frac{1}{2\pi}$$

Equation 21

Research carried out by T.Vasileiou *et al* [146] explored how the tuning of substrate flexibility can work synergistically with surface texture to enhance surface hydrophobicity, resulting in droplet breakup resistance, contact time reduction, and restitution coefficient increase. It was noted that reducing both the mass per unit area, or area density, and bending stiffness imparts immediate acceleration and intrinsic responsiveness of the substrate to impacting droplets, effectively "cushioning" the impact. This results in an increased apparent surface hydrophobicity, whilst raising the droplet splashing threshold. Whilst this study did not focus on obtaining efficient conversion of kinetic to electrical energy using piezoelectric materials, the results outlined that efficient energy conversion from droplet kinetic energy to substrate kinetic and strain energy is more likely to be achieved when the following substrate qualities are imposed:

1) Substrate has low mass per unit area, which is significantly lower than the liquid fluid density multiplied by the droplet diameter:

$$\rho_A \ll \rho D_0$$

Equation 22

2) Substrate stiffness should be low – approximately equivalent to the liquid surface tension of the water droplet. This relates to the mechanical impedance matching between the impacting droplet and the transducer; if the substrate is too stiff, it will resist the impact of the droplet and reduce the stress exerted on the piezoelectric layer, lowering the power output and reducing the energy transfer efficiency:

$$k_b \approx \sigma$$

Equation 23

3) To achieve a high value of substrate downward acceleration on impact, the substrate damping ratio should be minimised, where f_s is the substrates natural frequency of oscillation, c is the damping coefficient and k is the beam stiffness:

$$\zeta = \frac{\pi f_s c}{k} \approx 0$$

Equation 24

It is reported that adhering to these design principles not only maximises the probability of droplet rebound upon impact, but ensures minimal deformation of the droplet-free surface during collision with the substrate. This is considered to encourage efficient energy transfer from the droplet to the beam substrate [146]. Furthermore, the influence of the beam's natural frequency, f_b, and effective mass, m_b, were considered also. It was proposed that tailoring these parameters to the droplet mass, m_d, and the natural oscillation period of the droplet, f_d, had significant effect on the energy transferred during impact. For reference, the proposed relationship for the natural vibration frequency of the droplet is given in Equation 25, where T is the natural oscillation period of a vibrating droplet [147], ρ is the droplet liquid density, D_0 is the droplet diameter and σ is the droplet liquid surface tension.

$$f_d = \frac{1}{T} = \frac{1}{\frac{\pi}{4}\sqrt{\frac{\rho D_0^3}{\sigma}}}$$

Equation 25

Interestingly, it was proposed that depending on the relation between f_b and f_d, and m_b and m_d, the substrate movement can act synergistically, passively or destructively on the droplet kinetic energy after recoil from the substrate, E_{k1} [146]. Moreover, it was found that for substrate beams where $f_b < f_d$, droplet recoil from the substrate occurred during the downward motion of the beam, decreasing E_{k1}. This implies that the elastic strain energy stored in the beam, E_{el}, is increased. Finally, it was reported that E_{k1} can be further minimized by ensuring that $m_b > m_d$. The results from this investigation are displayed in Figure 37, which demonstrate the effect of varying f_b in relation to f_d, and the resulting effect on energy transfer during collision.

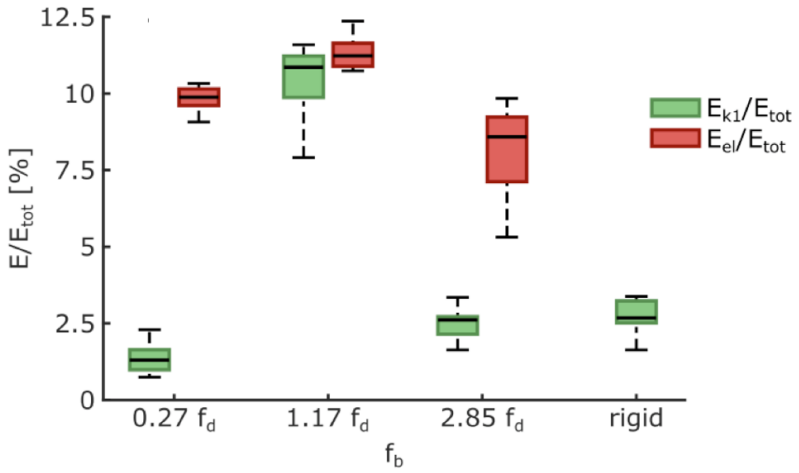

Figure 37 Reprinted and edited from [146]*, graph to show the energy transfer characteristics of an impacting droplet upon a substrate depending on the ratio of beam natural frequency to droplet natural frequency. Values displayed here are a) the residual kinetic energy of the droplet after rebound (E_{k1}, green bars), alongside the strain energy of the substrate beam at maximum deflection (E_{el}, red bars), normalized by the total available energy of the droplet before impact (E_{tot}). Vs. f_b. Droplets of the same size were used for the impact testing in each case.*

To further encourage the optimal stressing of a piezoelectric material under-going droplet impact, the position of the neutral axis is considered. In a beam, the neutral axis runs along the cross section, at which point there are no longitudinal stresses or strains generated when the cantilever is forced to bend. In non-composite material beams, the neutral axis is at the centroid of the beam cross-section. However, in composite beams such as a piezoelectric layer deposited upon a substrate, the induced stress throughout the beam as a result of bending is discontinuous between layers due to the different material properties. Resultantly, the positioning of this neutral axis is critical to the voltage response of the piezoelectric layer; it is desirable to maximise the strain the piezoelectric layer is exposed to in order to maximise the voltage response, by ensuring that the piezoelectric layer is placed in a complete torsional/compression bending regime when the cantilever is stressed [148]. It is worth noting that such approaches are relevant for the design of a unimorph; for bi-morph transducers, the piezoelectric axis can easily be placed in a favourable bending regime by making both the upper and lower piezoelectric layers, enclosing the middle substrate, of the same thickness.

Positioning of the neutral axis is dictated by the relative Young's modulus and thickness of the layers. As the neutral axis is the location of zero induced bending stress, we may place the piezoelectric layer in an advantageous bending regime

though positioning the neutral axis as far away from the piezoelectric material as possible; the piezoelectric layer stiffness must be significantly less than the substrate stiffness.

Thin stainless steel foil of thickness 25 μm is initially considered for usage as a substrate. It is possible to calculate the optimal thickness of piezoelectric material to deposit. In this case, P(VDF-TrFE) is selected for usage given the ease of preparation and characterisation. The relevant properties of both materials are displayed in Table 6.

Table 6 Parameters used to estimate ideal piezoelectric film thickness

Material Parameter	Value
PVDF Film Thickness	N/A
PVDF Density	1780 kg/m^3
PVDF Young's Modulus	4 GPa
Stainless Steel Sheet Thickness	25μm
Stainless Steel Sheet Density	8000 kg/m^3
Stainless Steel Sheet Young's Modulus	190 GPa

The neutral axis location is determined relative to the bottom surface of the harvester. It is assumed that the induced stresses through the cross-section of the beam are in equilibrium, allowing the distance between the neutral axis and the bottom surface of the beam "h" to be defined. From this definition, we may locate the position of the neutral axis, in addition to estimating the ideal layer thickness of the piezoelectric material based upon the Young's moduli of each material.

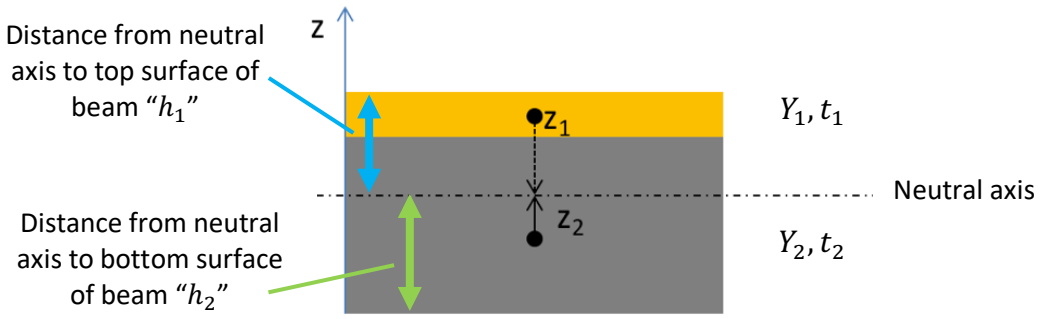

Figure 38 Illustration of composite piezoelectric transducer beam to highlight key parameters required to optimise piezoelectric layer, depicted in yellow here. The substrate layer is depicted in grey colour.

Using Figure 38 to illustrate, Equation 26 and Equation 27 define the distance from the material centroid of each layer to the neutral axis. We manipulate and combine these equations to provide a relationship which gives the distance of the neutral axis from the bottom surface of the transducer, shown in Equation 28, where Y_1 and Y_2 are the Youngs moduli of the piezoelectric and substrate layers respectively, and $t_1$and t_2 are the thicknesses of the piezoelectric and substrate layers respectively. z_1 and z_2 are defined from the middle of layers 1 and 2 respectively.

$$z_1 = \frac{(Y_2 t_2)(t_1 + t_2)}{2(Y_1 t_1 + Y_2 t_2)}$$

Equation 26

$$z_2 = \frac{(Y_1 t_1)(t_1 + t_2)}{2(Y_1 t_1 + Y_2 t_2)}$$

Equation 27

$$\mathrm{h}_1 = \frac{\mathrm{t}_1}{2} + \mathrm{z}_1$$

Equation 28

$$h_2 = \frac{t_2}{2} + z_2$$

Equation 29

We may use this value of h_1/h_2, in addition to Equation 30, which depicts the area moment of inertia for a beam with rectangular cross-section (where I is the second moment of area single layer, b is the beam width and h is the beam cross-section height), in order to solve the relationship shown in Equation 31. Equation 31 is reproduced from literature which investigated the positioning of the neutral axis in multilayer piezoelectric polymer energy harvesting devices [149]. With knowledge of both materials Young's moduli and the thickness of the substrate material, values for possible piezoelectric layer thicknesses are swept through until a maxima is reached, shown in Figure 39.

$$I = \frac{bh^3}{12}$$

Equation 30

$$f(t_1) = \left(\frac{h}{l}\right)^2 \cdot t_1$$

Equation 31

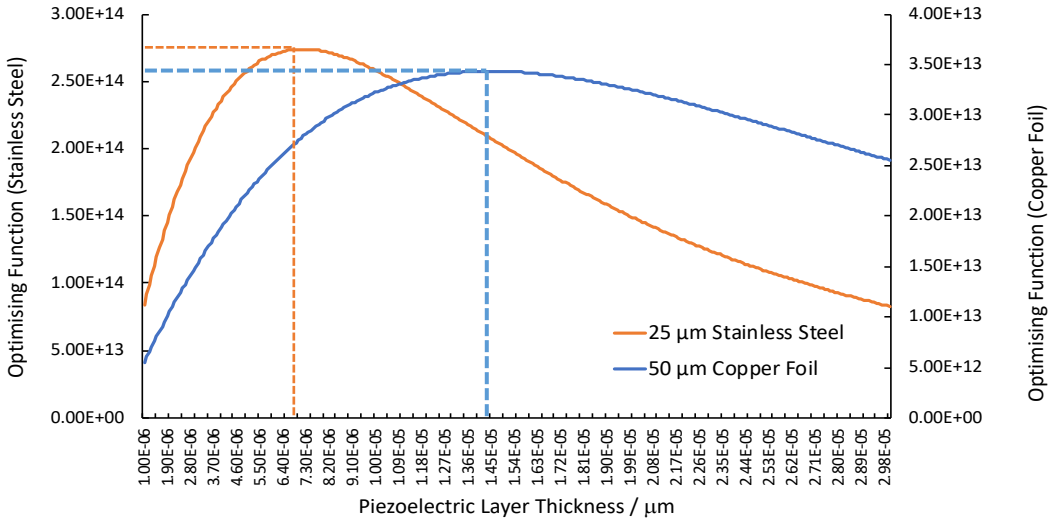

Figure 39 Graph to illustrate optimal piezoelectric layer thickness identification through observation of optimising function maxima for stainless steel and copper substrates

In future testing, a 50 µm thick copper foil substrate will be used –included here for comparison. The optimisation function estimates that a P(VDF-TrFE) layer thickness of approximately 7.2 µm is considered optimal to place the piezoelectric layer in an optimal bending regime through positioning of the neutral axis. This will efficiently stress the piezoelectric layer from bending on the stainless steel substrate, increasing the voltage output. It was also deduced that a 14.5 µm thickness P(VDF-TrFE) layer was optimal in the case of a copper foil substrate being used.

4.2 Further Geometry and Topology Considerations

In addition to cantilever beams, other energy harvester geometries have been investigated. The results demonstrate that the physical shape and topology of the harvester element significantly affects the efficiency of electrical energy generation by piezoelectric elements [150]. It has been shown that a triangular beam shape not only maximizes the material average strain distribution for a given force input, but that it demonstrates superior robustness to classical rectangular designs by reducing the stress concentration on the beam [151]–[153]. When a fixed force is applied to the free end of a cantilever, triangular geometries can improve power density by

approximately 85 % in comparison to a conventional rectangular beams [154]. Similarly, investigations into the effect of geometry on frequency driven energy harvesting elements found that an increased power output per unit volume of up to 30% was achieved with triangular geometries in comparison to rectangular cantilevers [152]. It is important to note that these findings relate to experiments where the force is applied at the end of the cantilever beam only. In situations where the location of force application is varied, harvesters which displayed the greatest strain distribution when the load is applied at their free end may not continue to be optimum.

The Finite Element Analysis (FEA) software COMSOL is utilised in this project to carry out an investigation into optimal geometry shapes for harvesting energy from droplet impacts. Initial simulations studied the induced volume average stress of 525 different geometry variants utilising z-direction loading regimes (parallel to the geometry upper surface). The initial hypothesis behind analysing the induced volume average stress assumes that a larger induced stress throughout the material body of a selected geometry will contribute towards maximizing the electromechanical response of a piezoelectric material, thus increasing the efficiency of mechanical to electrical energy transfer. Some of the geometry variants tested are illustrated in Figure 40, with key simulation parameters displayed in Table 7. Any form of structural damping is not considered at this stage.

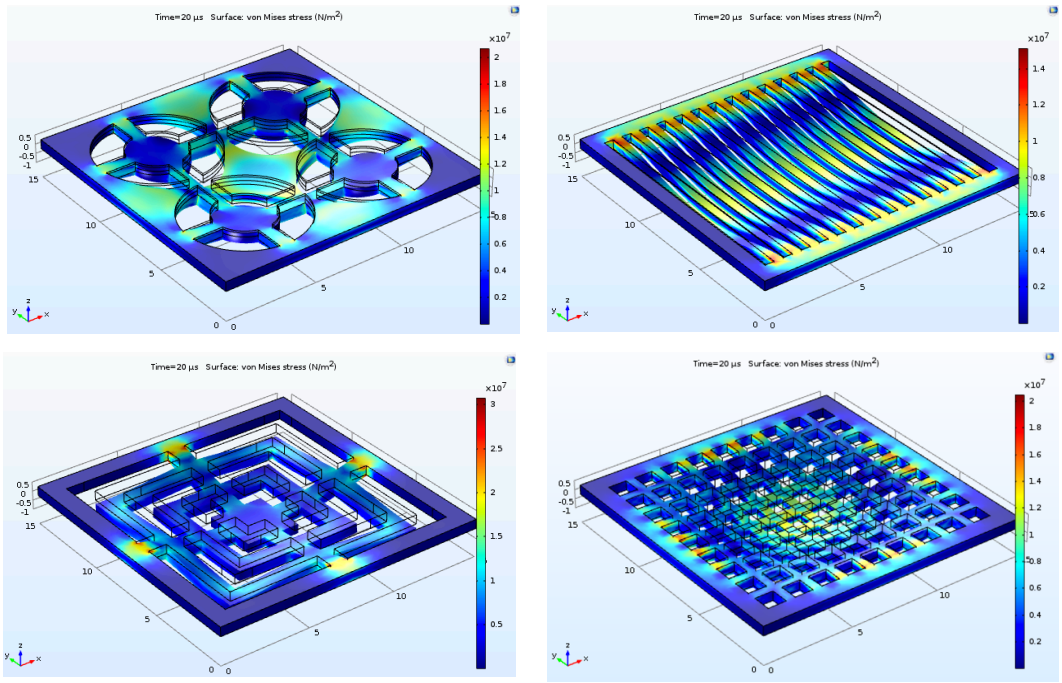

Figure 40 A selection of some geometry configurations tested during the 525 geometry variant loading sweep. The colour gradient indicates induced stress, with red highlighting the areas of greatest induced stress, descending to blue to highlight areas of least induced stress.

Table 7 Simulation sweep material properties, retrieved from COMSOL multiphysics pre-defined material library

Test Sample Dimensions	Length = 15 mm Width = 15 mm Thickness = 0.5 mm
Structural Steel Material Properties	Density = 7850 kg/m^3 Young's Modulus = 200 GPa Poisson's ratio = 0.33

Illustrated in Figure 41, the load is applied as a uniform force per unit area, downwards upon the test geometry upper surface, in an idealized case in which it is considered that all upper facing areas of the harvester undergo an impact event simultaneously. The estimated 33.5 mN force generated by a single impacting 1 mm diameter droplet was extrapolated and applied as an overall force to the upper surface of each harvester geometry, corresponding to a force per unit area of 42, 675 N/m^2. It has been shown that the initial water droplet impact has a significant contribution to the energy output of the device, as the rain droplet kinetic energy will be at a maximum during this time [21]. As such, this study focuses on the initial deflection generated during the 20 μs impact period in isolation, which is in reasonable agreement with relevant studies [155]–[157].

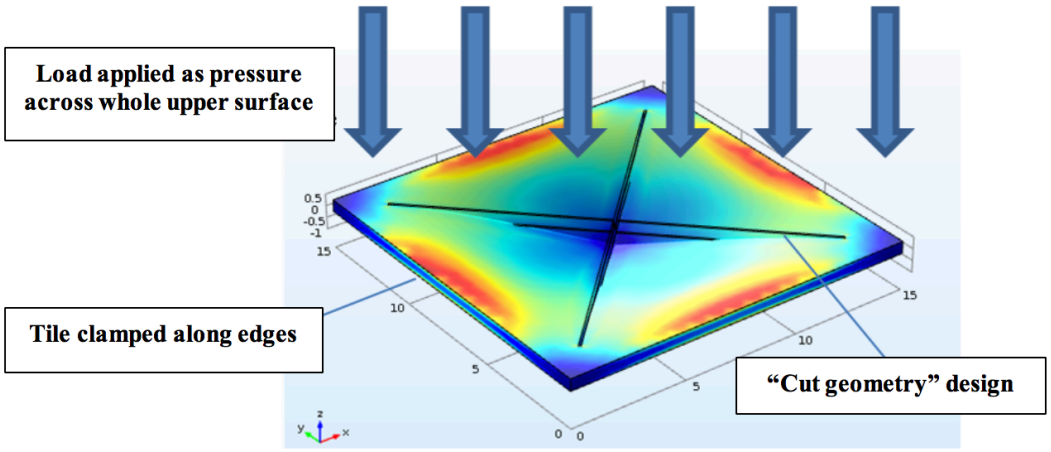

Figure 41 Screenshot of "cross cut" geometry equivalent tensile stress result to illustrate finite element method setup. The colour scale indicates induced stress gradient, with red indicating the areas experiencing the highest induced stress, and blue indicating areas experiencing lower stress levels.

A volume averaging function was utilised to analyse the equivalent von Mises stress

of each geometry at 0.1 μs intervals throughout the loading duration. The stress data returned for each 0.1 μs interval was further averaged, so that each geometry had a single value for the induced stress over the 20 μs simulation period. Of the 525 geometrical variations tested, the ten designs demonstrating the greatest stress output were shortlisted, with their labelled names and associated stress data displayed in Table 10, illustrated in Figure 42 and Figure 43. Further examples of the geometry range tested are displayed in the appendices.

Table 8 Volume average von Mises stress induced by top ten geometries tested under step loading

Geometry name	**Volume average equivalent von Mises stress induced from 20 μs step load / MN/m^2**
9 Spiral	1.5
81 Grid Circle (0.5 mm radius)	1.48
13 Spiral	1.46
30 Cut Hole (0.5 mm radius)	1.456
20 Spiral	1.44
81 Grid Circle (0.25 mm radius)	1.44
30 Cut Hole (0.1 mm radius)	1.44
30 Cut Hole (0.3 mm radius)	1.44
30 Cut Hole (0.2 mm radius)	1.4399
20 Spiral (0.15mm minor radius)	1.438

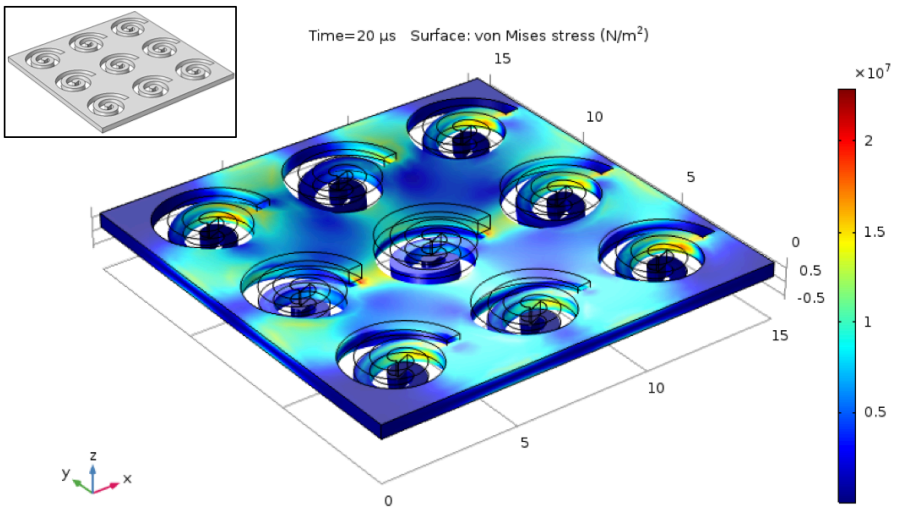

Figure 42 Example of geometry tested, "9 Spiral". Main image displays geometry at 20 μs whilst under loading. The induced surface stress is displayed utilising a colour scheme, indicated in the scale. Inset image depicts geometry without loading.

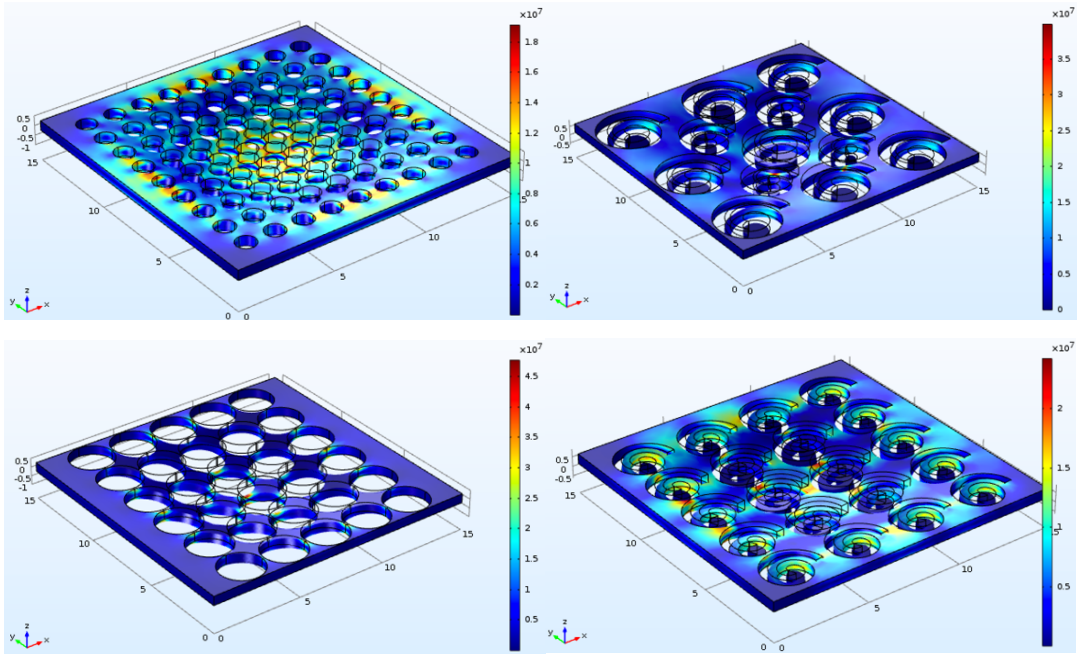

Figure 43 Illustrations of design choices under loading which produced the highest von Mises stress. Clockwise from top – 81 Grid Circle, 13 Spiral, 20 Spiral and 30 Cut Hole.

It was observed that the percentage difference between the highest and lowest induced stress for the tested geometry range is approximately 1160%, clearly underlining the importance of carefully selecting the harvester geometry depending on the intended application. It is proposed that the high % difference in induced stress relates to the influence of design features on stress distribution – for example, the top ten induced stress designs have features which encourage areas of high strain to develop i.e. narrower sections within the transducer geometry. Conversely, designs which produced lower induced stress, such as the designs illustrated in Figure 44, do not provide opportunities for areas of high stress to develop to such an extent.

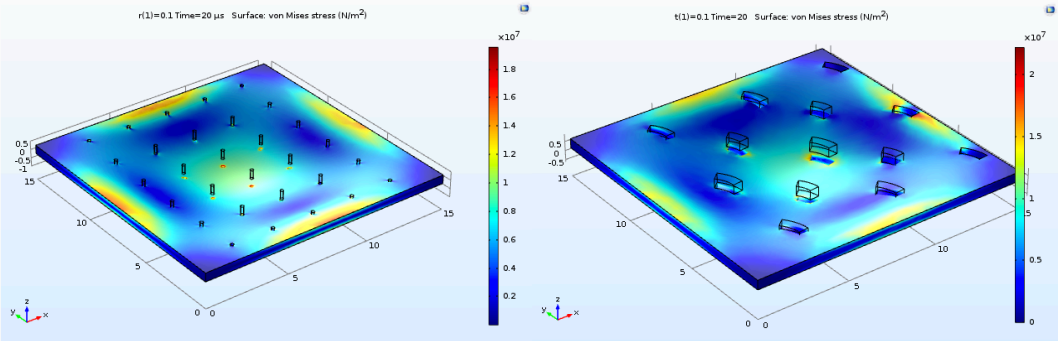

Figure 44 Illustration of 30 Cut hole, 0.1 mm radius geometry (left) and 13 spiral turn variation (right). It is proposed that geometries of this nature produce a lower induced stress under loading, as the minimal design features do not encourage areas of high stress to develop throughout the geometry compared to other designs

To further investigate the results of this uniform step load analysis, the ten designs were subjected to pseudo-random impulse loading in order to closer emulate the conditions of an actual rainfall event in the following manner. Additionally, the ten "runner up designs" were also tested, to highlight any changes in the greatest induced stress ranking:

- Using in-built pseudo random values from the COMSOL software, a set of 50 variables were defined, which applied a 20μs load application at a pseudo-randomly chosen time during the chosen 10 second simulation period. This attempted to reflect the sharp impact force of a 1 mm diameter droplet travelling at a speed of 8m/s, in line with previous approximations.

- The impulse force was applied as a force per unit area, but instead of applying this load to the entire upper surface area of each design, the impulse force would be pseudo-randomly applied to a series of 1 mm diameter circles drawn across the top surface of each design, illustrated upon a plain geometry in Figure 45 . These circles simulated the cross-sectional area of a 1 mm droplet on impact, ignoring compression/expansive collision effects.

- In total, 225 1 mm diameter circles were drawn onto the top layer of the 20 geometries found to exhibit the highest induced stress from the original analysis. This aims to emulate how a physically realized harvesting design may undergo loading during a rainfall event.

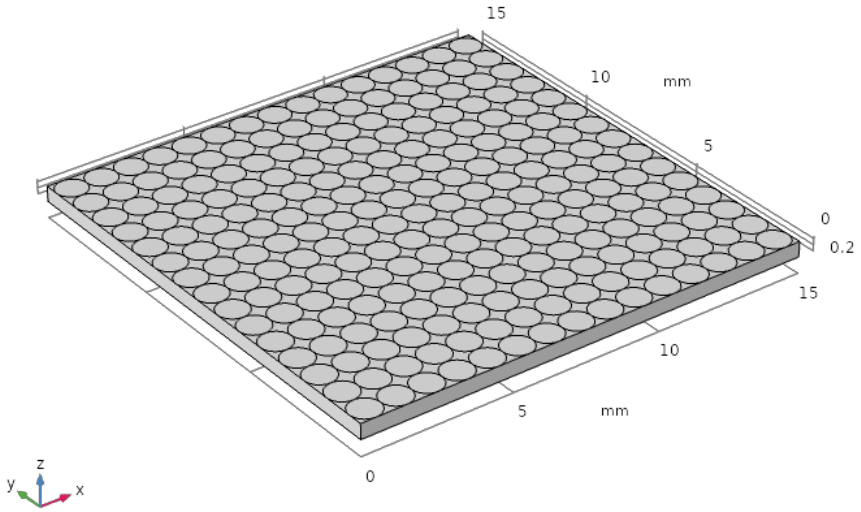

Figure 45 Diagram to demonstrate application pattern of random loading variables upon upper surface of plain geometry

Table 9 Volume average equivalent tensile stress induced by top ten geometries tested under psuedo-random impulse loading

Geometry name	Volume average equivalent von Mises stress induced from 20 μs pseudo-random impulse loading / kN/m^2
9 Spiral	26
13 Spiral	23
20 Spiral	21
0.3mm Radius 4 Cut Hole	20
0.5mm Radius 30 Cut Hole	17.8
0.4mm Radius 30 Cut Hole	17.7
0.2mm Radius 4 Cut Hole	17.6
13 Spiral 0.15mm Minor Radius (Clean Cut)	16.7
81 Grid Triangle	16.3
0.1mm Radius 4 Cut Hole	16.3

It was found that there is some movement with regards to the order of geometries showing the highest strain, however key geometries remain – notably, those encompassing spirals in their design. In light of this, spiral-type geometries were investigated further, with a view to exploring the merits of applying such shapes for water droplet energy harvesting applications.

4.3 Double-Armed Archimedean Spiral Geometry Investigation

The spiral shape is fundamentally a curved cantilever beam. However, the curvature of the spiral shape amplifies both the torsional and bending stresses under impact, making such geometries attractive for usage in piezoelectric transducers due to the coupled mechanical strains in action. As a result of their inherent multiple degrees of freedom, spirals are naturally very sensitive to vibration. This is an attractive characteristic for water droplet harvesting, as it allows a maximal range of droplet diameters to be harvested, without concern over lack of transducer mechanical sensitivity, whilst providing a compliant structure that will react with favourable energy transfer efficiency to impacts across a greater surface area [158][148]. For example, such geometries have harvested mechanical energy from the flight of Green

June Beetles, generating approximately 115μW from the physical contact of the beetle's flapping wings [159].

However, as a result of the exhibited multiple mechanical degrees of freedom, care must be taken over electrode placement - it has been found that charge cancellation can occur if the piezoelectric layers are uniformly polarised. Considering a single top or bottom piezoelectric material layer, it is reported that the polarity of the produced charge changes across an imposed "zero-strain/zero-charge axis" when a static force is applied to the spiral beam tip [159]. Consequently, without modifying the poling process, a spiral shape harvester with a uniformly polarized electrode would suffer charge cancellation during excitation, resulting in reduced electrical power output. As such, in this research shadow masks are used to deposit top electrodes separately onto each arm of the spiral energy harvesters, before length optimisation takes place in order maximise power output.

In addition to vibration sensitivity, spiral shapes can exhibit low resonant frequency (< 10Hz) depending on parameters such as sample thickness, or spiral turn number. This is considered an attractive feature for utilising such designs for droplet energy harvesting; assuming that the likelihood of a harvester of undergoing greater than 10 droplet impacts per second is unlikely [160][161]. Tikani *et al*. proposed a design for a spiral, multimode piezoelectric energy harvester with wide bandwidth at low frequencies. The design, simulated and optimised using the Taguchi method, exhibited its first three natural frequencies at 4.2Hz, 6.2Hz, 10.2Hz [162].

The Archimedean spiral, or arithmetic spiral, is a spiral defined with a polar equation, outlined in Equation 32 and illustrated in Figure 46. Here, r is the radial distance, a and b are real number constants (varying a turns the spiral, whilst varying b controls the distance between successive turnings), θ is the polar angle and n is a constant which determines how tightly the spiral is "wrapped" around the centre point [163]. Such spiral designs have been proven to display high mechanical sensitivity, with arrays of MEMS scale spirals utilised as cochlear multi-electrode implants [164].

$$r = a + b\theta^{\frac{1}{n}}$$

Equation 32

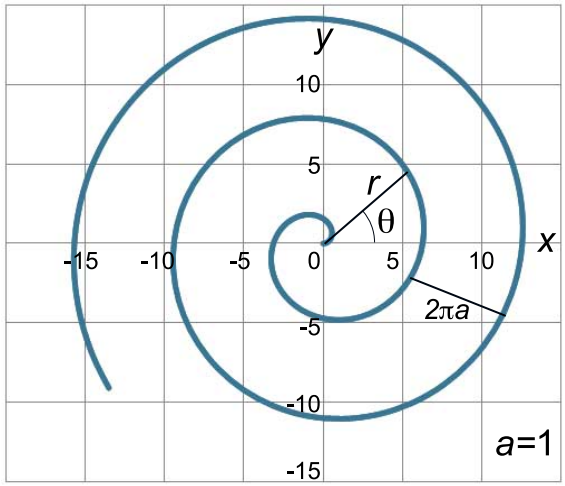

Figure 46 Reprinted from [165]*, diagram to illustrate definition of spiral parameters. Here, a determines the density of spiral turns, with the distance between successive turnings defined using 2πa, represented as b in Equation 32*

A number of analytical investigations into the mechanical behaviours of Archimedean spiral-based springs and bimorphs have taken place [159]. Considering out-of-plane vibration dynamics, the moment-displacement relationships for the curved beam displayed in Figure 47 are shown in Equation 33 and Equation 34, Where M_x is the bending moment, EI_x is the arc bending stiffness, M_z is the twist torque and GJ is the torsional stiffness. κ and τ are defined in Equation 35 and Equation 36, where β is the twist angle, R is the radius of the curved beam, L_{def} is the out of plane deflection and s is the position coordinate along the arc. [166][167].

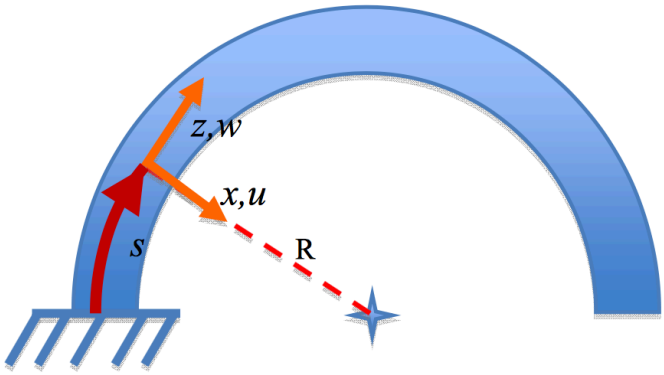

Figure 47 Reprinted from [167]*, curved beam with co-ordinates notation*

$$M_x = EI_x\kappa$$

Equation 33

$$M_z = GJ\tau$$

Equation 34

$$\kappa = \frac{\beta}{R} - \frac{\partial^2 L_{def}}{\partial s^2}$$

Equation 35

$$\tau = \frac{\partial \beta}{\partial s} + \frac{1}{R}$$

Equation 36

The strain energy U_s and the kinetic energy T_{ke} of the curved beam for out-of-plane motion are displayed in Equation 37 and Equation 38, where F_{ext} is the external applied force, i is the mass moment of inertia per unit length of the curved beam and Φ is the twisting moment.

$$U_s = \frac{1}{2}\int_0^{S_L} (M_x \kappa + M_z \tau - F_{ext}\, L_{def} - \Phi\beta) ds$$

Equation 37

$$T_{ke} = \frac{1}{2}\int_0^{S_L} (m \dot{L_{def}}^2 + i\, \dot{\beta}^2) ds$$

Equation 38

An example of the double armed variant is illustrated in Figure 48. A popular design for spiral antennas, the double armed spiral variant combines the benefits of a mechanically sensitive structure with multiple-degrees of freedom, whilst enhancing the induced stress under loading as the structure essentially takes the form of an elongated, double-clamped piezoelectric beam. Initial investigations into the suitability of such a geometry for droplet energy harvesting are carried out using COMSOL Multiphysics simulation software. The objectives of the simulation analysis are to identify the appropriate parameter ranges required to design spirals that demonstrate the following qualities, which are considered desirable for water droplet energy harvesting transducers:

- Spiral resonant frequency should be low (< 20 Hz), in light of the expected maximum droplet impact frequency

- Spiral stiffness should be low, close to the magnitude range of 0.1 N/m [146]

- Spiral initial deflection should be minimal, to allow for as large a bending range as possible, in order to optimally stress the piezoelectric layer – as such, the overall transducer size and spiral turn number are naturally constrained.

- Transducer dimensions are further limited by the piezoelectric layer application method – a doctor blade of width 15 cm

The design of a parameterised, single armed Archimedean spiral is altered accordingly in order to produce a double armed design [168]. Key parameters affecting the energy transfer efficiency between the droplet and the transducer, considered to be the spirals axial/torsional stiffness and resonant frequency, can be precisely tuned depending on a combination of the following parameters, illustrated in Figure 48:

- Spiral final radius – AF
- Spiral initial radius – A1
- No. of turns – n1
- Arm thickness – defined by "Gap", otherwise denoted as *b* in Equation 32

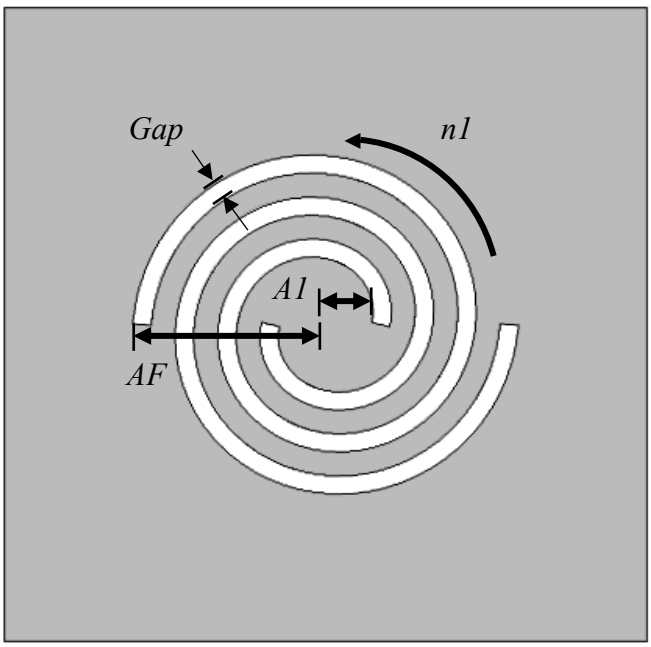

Figure 48 Diagram to illustrate parameters of interest for the finite element analysis upon a 1-turn spiral

The variation of these parameters in order to tailor the spiral's mechanical behaviour does not require a larger surface area to be fabricated. For comparison, to reduce the resonant frequency of a cantilever beam design transducer, the beam length would need to be increased, creating a larger transducer overall. Alternately, a mass could be added to the cantilever beam end, however this would significantly reduce the sensitivity and intrinsic responsiveness of the harvester. As such, it is found that the spiral geometry is both a highly tuneable design that promotes efficient space usage, making it a useful design for applications where space is limited i.e./ drain pipes, or internal water management systems. The simulation material properties used are displayed in Table 10 In each case, the edges of the geometry were clamped, and gravity was applied across the entire volume in the -z axis direction. Copper was chosen as the substrate material of investigation due to its electrical conductivity, favourable mechanical properties and low cost.

Table 10 Simulation parameters of piezoelectric and substrate materials used

Material Parameter	Value
PVDF Film Thickness	15 μm
PVDF Density	1780 kg/m^3
PVDF Young's Modulus	4 GPa
Copper Sheet Thickness	0.05 mm
Copper Sheet Density	8960 kg/m^3
Copper Sheet Young's Modulus	110 GPa
Polyvinylidene fluoride (PVDF) Compliance Matrix strain-charge form [1/Pa] (Ordering *{sE11, sE12, sE22, sE13, sE23, sE33, sE14, sE24, sE34, sE44, sE15, sE25, sE35, sE45, sE55, sE16, sE26, sE36, sE46, sE56, sE66}* ; sEij = sEji)	{4.43e-010, -9.91e-011, 5.04e-10, -3.10e-010, -3.19e-010, 1.14e-9, 0, 0, 0, 1.82e-09, 0, 0, 0, 0, 1.70e-09, 0, 0, 0, 0, 0, 1.45e-09}
Polyvinylidene fluoride (PVDF) Coupling Matrix strain-charge form [C/N] (Ordering *{dET11, dET21, dET31, dET12, dET22, dET32, dET13, dET23, dET33, dET14, dET24, dET34,*	{0, 0, 1.36e-01, 0, 0, 1.94e-011, 0, 0, 2.97e-011, 0, 2.01e-011, 0, 1.93e-011, 0, 0, 0, 0, 0}

dET15, dET25, dET35, dET16, dET26, dET36})	

4.3.1 Key parameter influence on spiral axial stiffness

The effect of varying the aforementioned parameters (AF, A1, n1 and Gap) on axial stiffness is investigated initially. A spiral's inherent multiple degrees of freedom makes gauging the mechanical stiffness a coupled problem, as both direct bending and torsional stiffness contribute. To simplify, each spiral's reaction force to a prescribed displacement applied along the -z-axis to the centre is analysed. Equation 39 is used to calculate the estimated bending stiffness, where "k" is the estimated spiral axial stiffness, "F" is the reaction force, and "δ" is the prescribed displacement.

$$k = \frac{F}{\delta}$$

Equation 39

Using Finite Element Modelling (FEM) software to investigate axial stiffness, a prescribed displacement of 10, 20, 30, 40 and 50 mm was applied to the centre of the spiral downwards along the z axis, as illustrated in Figure 49. The edges of the geometry were clamped, and gravity was applied across the entire volume downwards along the z-axis direction. The resulting z-component reaction force of the spiral resisting each displacement was measured, before being plotted on a reaction force vs. displacement graph, illustrated in Figure 50. The gradient of the line produced was calculated in order to estimate the axial stiffness of each spiral tested. Two studies were carried out – the first studied the effect of varying turn number on estimated stiffness for a variety of spirals with different finial and initial radii, with the second study looking at the effect of varying the "Gap" parameter in isolation. These results are displayed in Figure 51 and Figure 52, with an illustration of spiral design variations for both studies shown in Figure 57 and Figure 54.

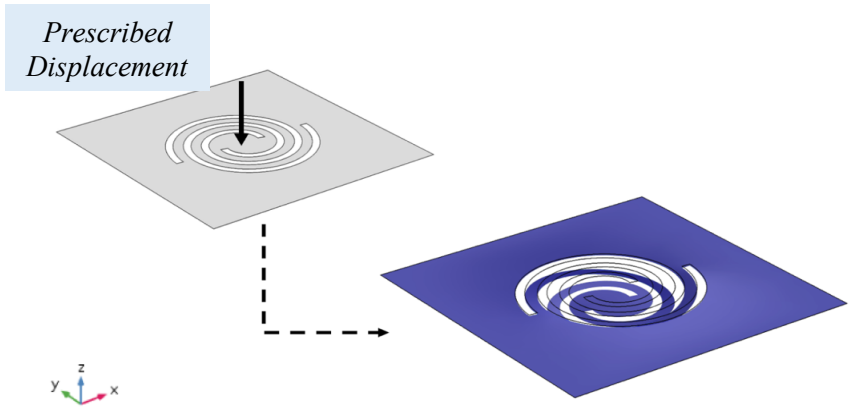

Figure 49 Illustration of prescribed displacement axial stiffness testing

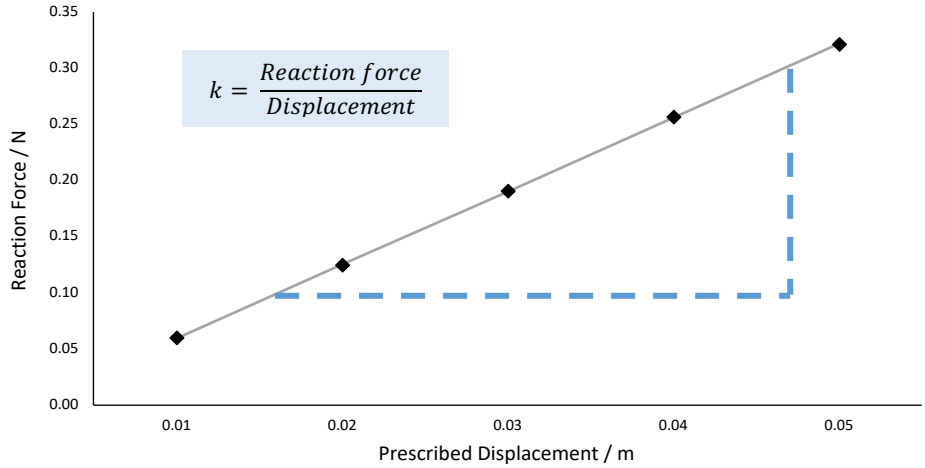

Figure 50 Illustration of estimated stiffness plotting process for an AF = 30 mm, A1 = 6 mm, 1.5 turn spiral

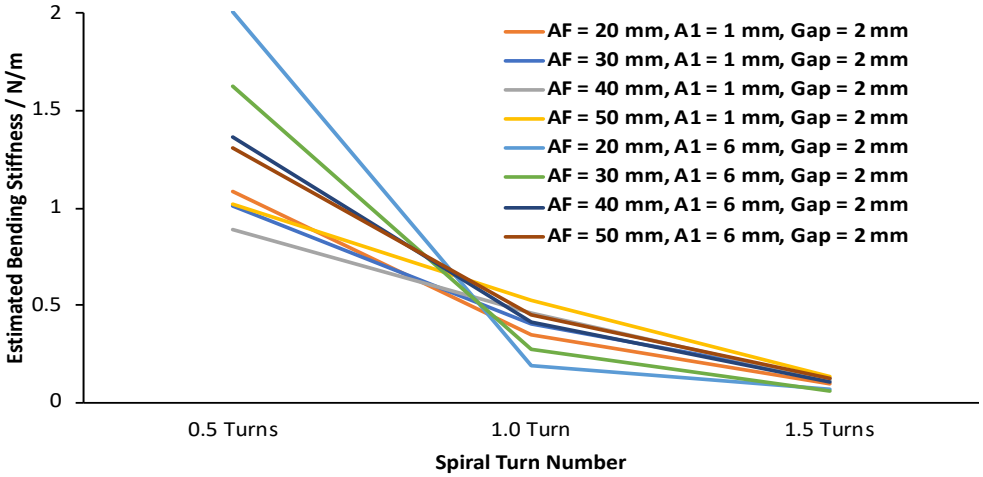

Figure 51 Effect of variation of turn number, spiral final radius and spiral initial radius on estimated axial stiffness

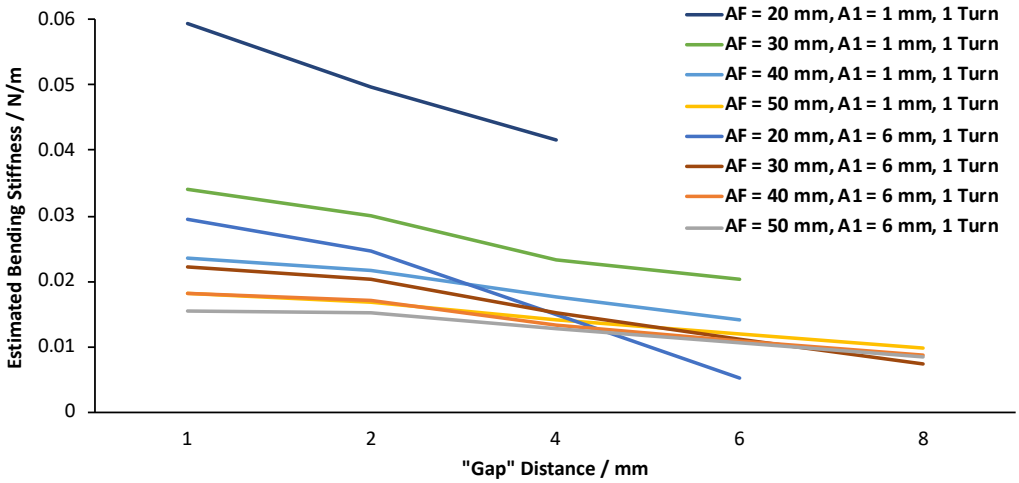

Figure 52 Effect of varying spiral gap distance parameter "Gap" on estimated axial stiffness

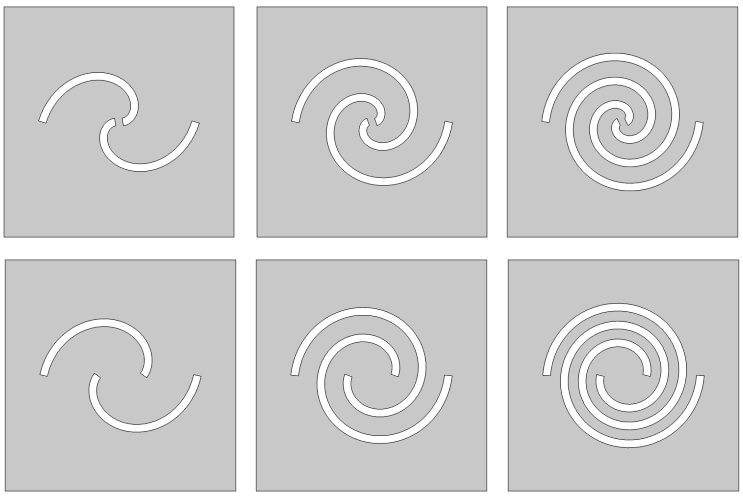

Figure 53 Illustration of spiral design variations for turn number, final and initial radius studies; top row spirals, left to right, 0.5 / 1 / 1.5 turns with AF = 30 mm and A1 = 1 mm. Bottom row, left to right, 0.5 / 1 / 1.5 turns with AF = 30 mm and A1 = 6 mm

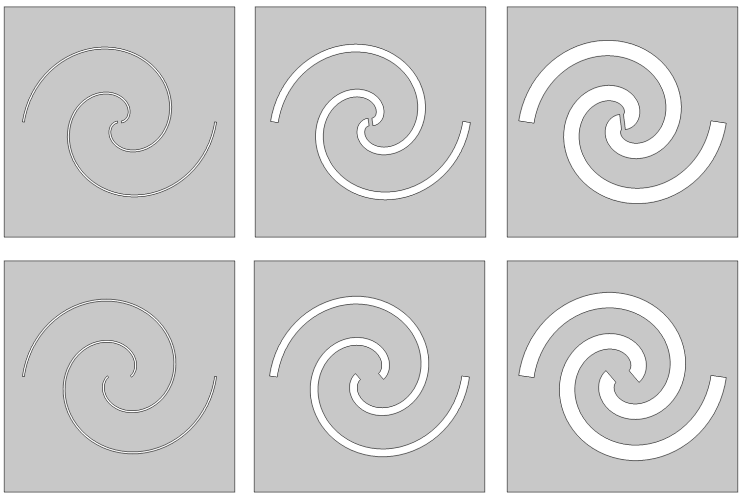

Figure 54 Illustration of spiral designs for spiral gap distance variation; top row spirals, left to right, 1 mm / 4 mm / 8 mm gap distances with AF = 50 mm and A1 = 1 mm. Bottom row, left to right, 1 mm / 4 mm / 8 mm gap distances with AF = 50 mm and A1 = 6 mm

The results of axial stiffness simulations demonstrated that:

- Increasing the turn number "n1" can result in a magnitude change of axial stiffness i.e. The AF = 20 mm, A1 = 6 mm, Gap = 2 mm sample exhibited a stiffness of 2.01 N/m with 0.5 turns, and stiffness of 0.07 N/m with 1.5 turns, representing a difference of 1.94 N/m or approximately 97% decrease in bending stiffness.

- Increasing the spiral initial radius "A1" decreases stiffness to a lesser extent, aside from when the turn number is low. It is hypothesised that this is because, with higher turn number, the spiral arm distance is longer and a larger initial radius acts as a "proof mass" at the centre of the spiral. In the case of low turn number, the spiral distance is short, therefore by increasing initial radius we increase the arm width, resulting in an increase of the axial stiffness, illustrated in Figure 55. For example, the difference in stiffness between the AF = 40 mm, Gap = 2 mm, 0.5 turns sample with A1 = 1 mm (stiffness = 0.89 N/m) and A1 = 6 mm (stiffness = 1.37 N/m) is 0.48 N/m or an increase of approximately 35%. Conversely, the difference in stiffness between the AF = 40 mm, Gap = 2 mm, 1.5 turns sample with A1 = 1 mm (stiffness = 0.12 N/m) and A1 = 6 mm (stiffness = 0.11 N/m) is 0.01 N/m or approximately a decrease of 7.6%.

- Increasing the gap between spiral arms, "*Gap*", also decreases stiffness by decreasing the spiral arm width, illustrated in Figure 56. For example, the AF = 20 mm, A1 = 6 mm, 1 Turn sample has a stiffness of 0.029 N/m with a Gap of 1 mm, compared to 0.0053 N/m with a Gap of 6 mm. This represents a change of 0.024 N/m, or approximately a decrease of 82 %.

It is clear the variation of the spiral turn number has the most significant influence on estimated bending stiffness, with stiffness changes being in the 1 N/m magnitude range. Whilst it is useful to be aware of the impact of varying initial radius or gap distance, stiffness changes from these parameters were in the 0.01 N/m magnitude range

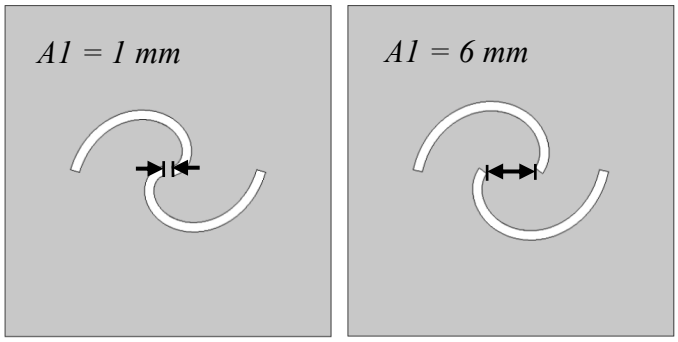

Figure 55 Illustration of geometry changes when increasing the initial spiral radius, "A1", at low spiral turn number

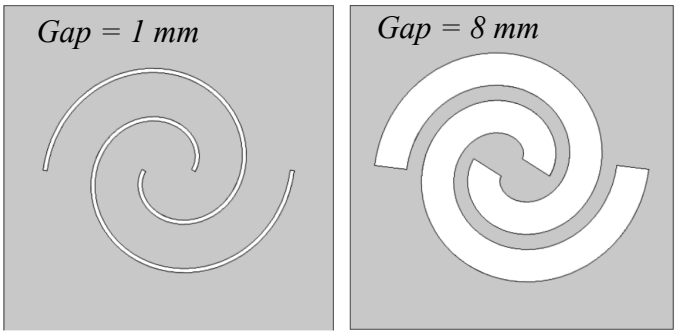

Figure 56 Illustration of geometry with varying arm gap thickness

4.3.2 Key parameter influence on spiral first order resonant frequency

The effect of varying the aforementioned parameters (AF, A1, n1 and Gap) on each spiral's first order resonant frequency is investigated next. Parameters of interest were incrementally varied, with an Eigenfrequency study carried out at each step. As before, two studies were carried out – the first studied the effect of varying turn number on the first order resonant frequency for a variety of spirals with different finial and initial radii, with the second study looking at the effect of varying the "Gap" parameter in isolation. These results are displayed in Figure 57 and Figure 58.

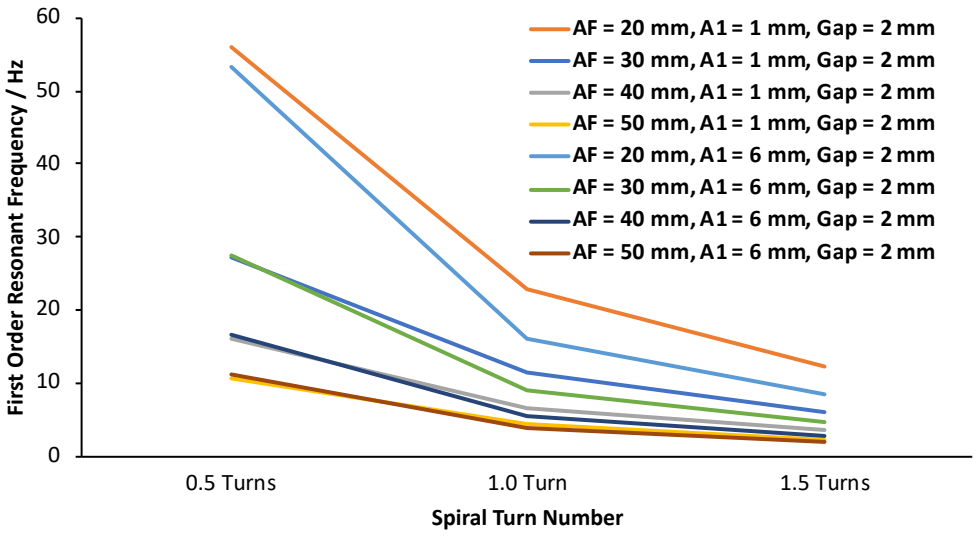

Figure 57 Effect of variation of turn number, spiral final radius and spiral initial radius on spiral first order resonant frequency

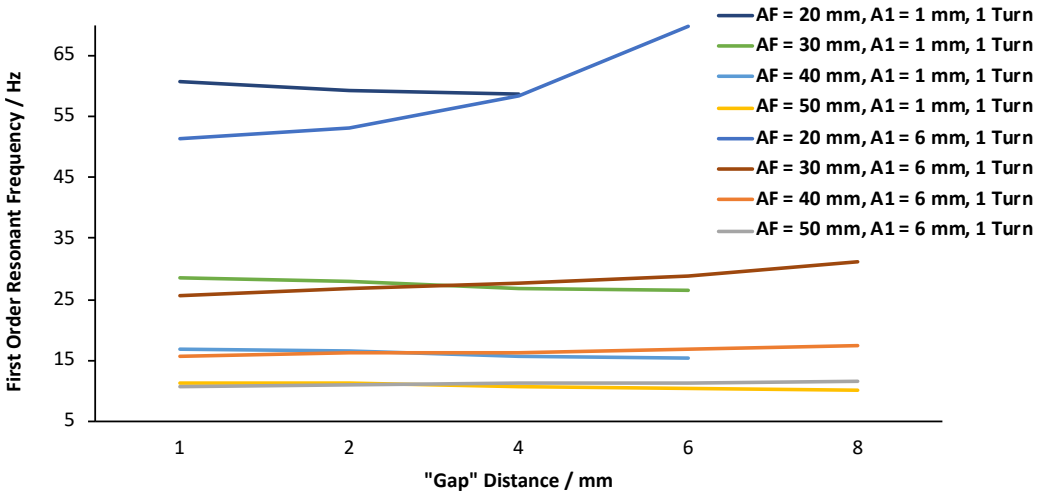

Figure 58 Effect of spiral arm "Gap" distance on spiral first order resonant frequency

The results of the first order resonant frequency simulations demonstrated that:

- Similar to the axial stiffness investigation, altering the spiral turn number can produce the greatest variation in spiral first order resonant frequency. For example, the AF = 20 mm, A1 = 1 mm, Gap = 2 mm sample has a resonant frequency of 55.9 Hz with 0.5 turns, compared to 12.3 Hz with 1.5 Turns.

- Increasing the spiral final radius, *AF*, decreases the spiral's resonant frequency significantly also. For example, the AF = 20 mm, A1 = 1 mm, Gap = 2 mm, 0.5 turns sample has a resonant frequency of 55.9 Hz, compared to the AF =

50 mm, A1 = 1 mm, Gap = 2 mm, 0.5 turns sample of resonant frequency 10.7 Hz.

- Perhaps the most important result was the investigation into Gap variation on spiral first order resonant frequency. As shown in Figure 58, Gap width has little effect on spiral resonant frequency in most cases:

    - For spirals with A1 = 1 mm, increasing the Gap distance results in a decrease of resonant frequency i.e. for the AF = 40 mm, A1 = 1 mm, 1 Turn sample, 1 mm Gap produces first order resonance at 16.9 Hz, compared to 15.3 Hz with a 6 mm Gap distance

    - For spirals with A1 = 6 mm, increasing the Gap distance results in an increase of resonant frequency i.e. for the AF = 40 mm, A1 = 6 mm, 1 Turn sample, 1 mm Gap produces first order resonance at 15.7 Hz, compared to 17.4 Hz with a 6 mm Gap distance

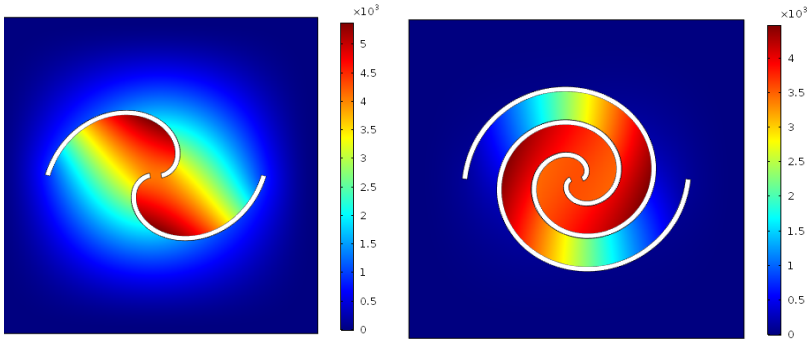

Figure 59 Images of AF = 20 mm, A1 = 1 mm, Gap = 2 mm sample first order modal shapes, with 0.5 turns (left) and 1.5 turns (right). The colour scale chart indicates total displacement, mm

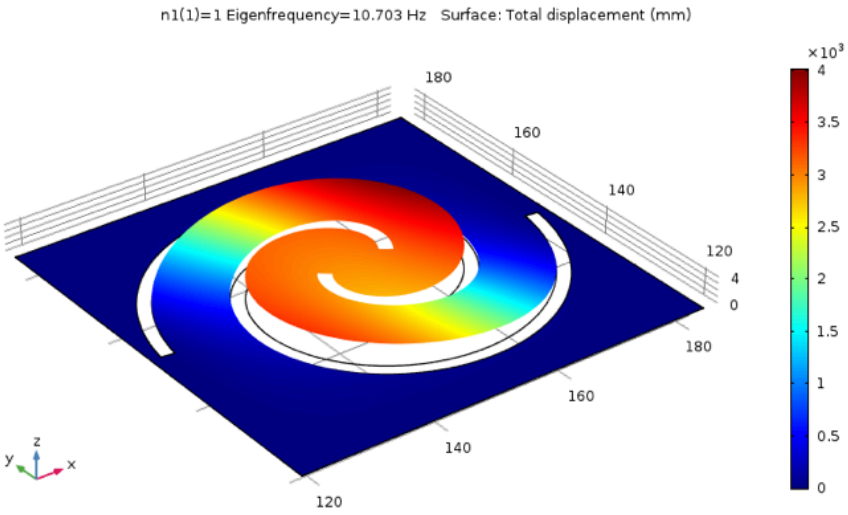

Figure 60 Screenshot of 30 mm spiral final radius Eigenfrequency analysis. Image displays spiral with 1 turn, first order Eigenfrequency of 10.703 Hz. The colour scale indicates surface displacement whilst at resonance.

The significance of these findings relates to the disproportionate change in spiral resonant frequency and stiffness when Gap is varied. It was found that axial stiffness varied at much greater magnitude than resonant frequency; for example, in the case of the AF = 50 mm, A1 = 1 mm, 1 Turn sample, increasing the Gap distance from 1 mm to 8 mm resulted in a change of resonant frequency from 11.4 Hz to 10 Hz, or an approximate 12% decrease.

However, the corresponding change in stiffness for the same sample was an approximate 45.6% decrease, from 0.0182 N/m when gap was 1 mm, to 0.0099 N/m when gap was 8 mm. Such results are noteworthy, as they serve to outline the adaptability and tunability of the Archimedean spiral geometry, allowing the designer to create a structure which can be tuned to meet design requirements without the spiral stiffness and frequency parameters being too directly dependent on each other.

This behaviour follows the same trend of cantilever beams, which allow variation of stiffness through changing the beam width, whilst maintaining a constant resonant frequency as long as the beam length and thickness are not varied. The independence of stiffness and resonant frequency was illustrated previously in Equation 21, which demonstrated how the beam's resonant frequency does not depend on the width term.

In summary, we may colloquially propose that varying the spiral turns is comparable to "coarse" tuning of mechanical behaviour, with any variation of initial radius or gap distance representing a "finer" tuning of spiral mechanical properties.

4.4 Effect of Drainage Holes on Spiral Mechanical Behaviours

In anticipation of a final device, we must consider the flow of water throughout a droplet energy harvester system. It has been shown that the formation of a water layer from successive droplet impacts can detrimentally affect droplet energy harvester efficiency by increasing both the mass and damping [169]. As such, it is useful to briefly investigate how the addition of drainage holes to spiral samples could affect mechanical behaviours.

A finite element model was compiled which studied how the placement of 6 mm diameter holes would affect the mechanical behaviours of each sample, with a focus on sample resonant frequency and axial stiffness. Placement of such drainage holes, illustrated in Figure 61, was decided following observation of water pooling when physical transducers were subjected to drip streams. Naturally, some configurations are only plausible depending on sample electrode lengths, as they would interrupt the connection (1 Arm / 2 Arm). The resulting effect on sample resonant frequency and stiffness is displayed in Figure 62. It was found that drainage hole configuration affected the simulated sample frequency and stiffness by < 1 %. It is proposed that this is due to the very small change in mass and stiffness caused by introducing the drainage holes, resulting in little effect on the overall spiral mechanical properties. This was experimentally verified, illustrated in Figure 63, with test results indicating a first order resonant frequency fluctuation of no greater than $\pm$ 1 Hz and no observable stiffness change for any drainage hole configuration applied.

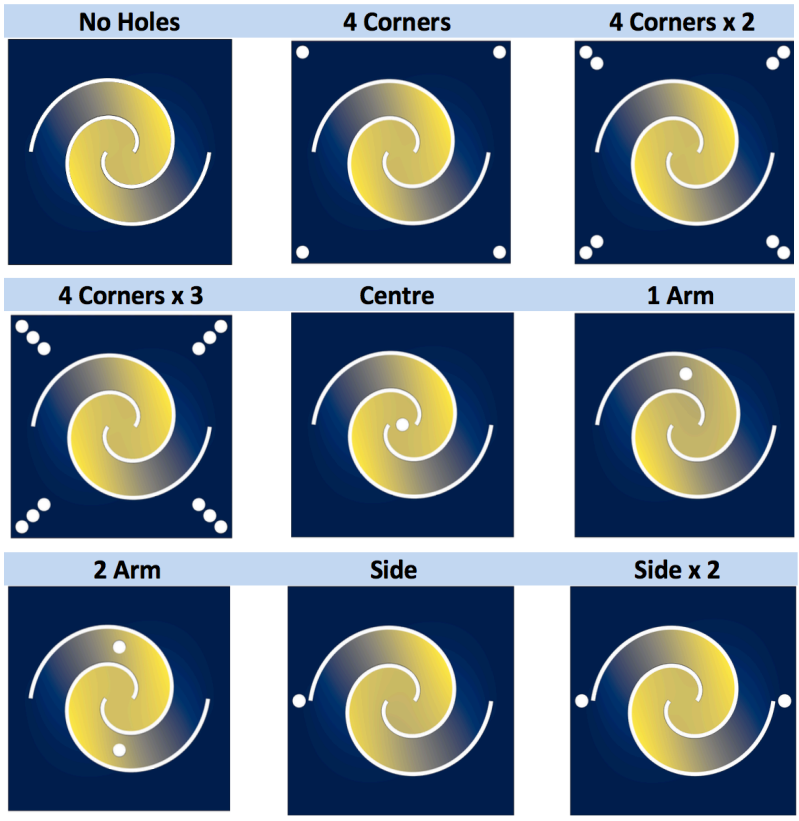

Figure 61 Diagram to illustrate drainage hole configurations analysed

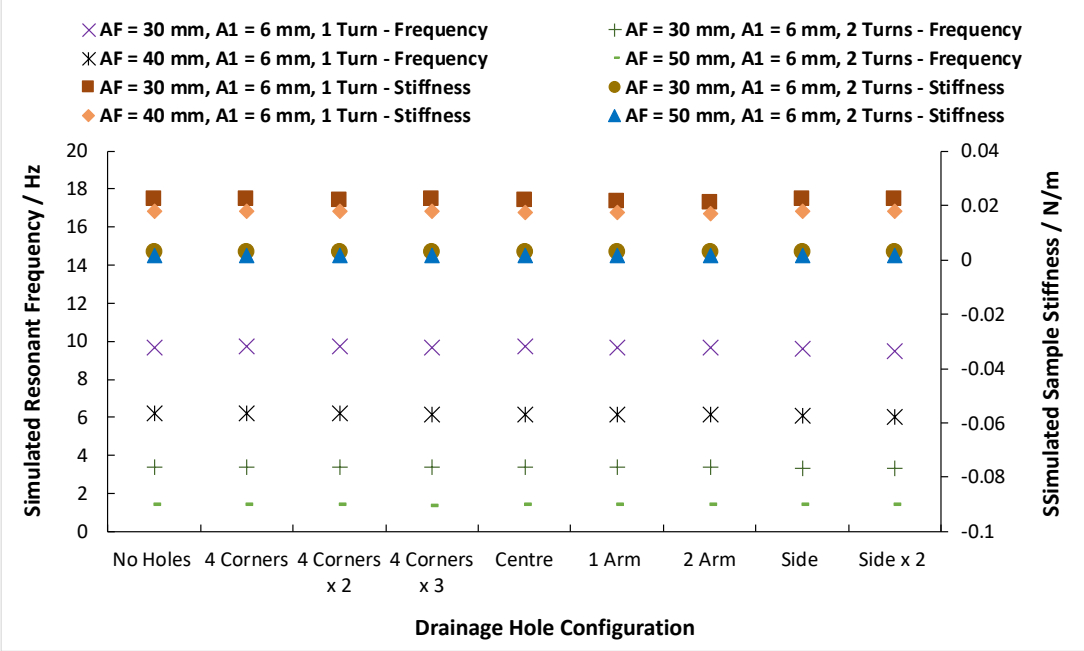

Figure 62 Effect of drainage hole configuration on sample resonant frequency

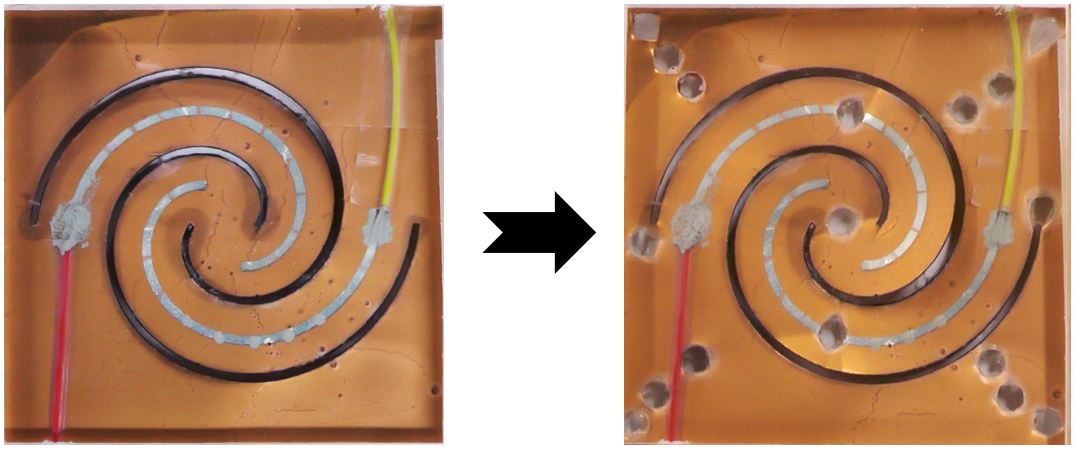

Figure 63 Illustration of drainage hole configuration testing on sample mechanical properties using an AF = 35 mm, 1 turn sample

4.4.1 Electrode Dimension Simulations

It has been reliably shown that the dimensions of the active electrode area used as the top electrode on piezoelectric devices significantly contributes to the device power output [170][171]. Careful consideration of device strain mechanics is required; perhaps counter-intuitively, maximising the active electrode area does not always result in an increase of output power, with power output being detrimentally affected if opposing strain areas are covered [170]. In an experiment which investigated the optimal electrode area for a piezoelectric cantilever beam, an electrode area coverage of approximately 50% generated 30.8% greater power output than 100% electrode coverage [171]. With this in mind, the electrode lengths for each fabricated spiral sample were optimised.

To investigate, the first order resonant frequency of each simulated spiral was identified, before driving the samples at this frequency whilst varying the length of the electrode running along the spiral arm's upper surface. A sweep of electrode length covering a small section at the base of each spiral arm, ranging to the end of the arm, was carried out for each spiral. The electrode width was kept constant throughout this research to allow for variation of spiral arm width, in order to analyse the effect of bending stiffness variation, without altering the electrode area once an ideal length have been identified.

The simulated output impedance was 10 MΩ, to match that of the oscilloscope impedance used in experimental testing (at this stage, the output power is normalized as electrical impedance matching has yet to take place – this step was completed after identifying an ideal electrode length). The normalised output power as a function of

electrode for two sets of spiral samples, each with different varied parameters, are shown in Figure 64 and Figure 65.

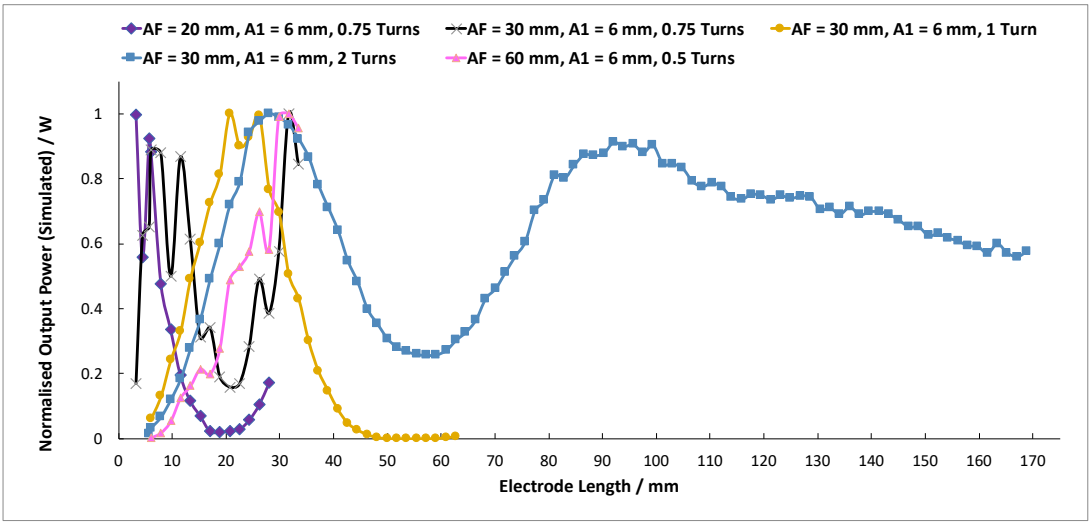

Figure 64 Simulated Normalised output power of samples (mixed radius) as a function of electrode length for comparison

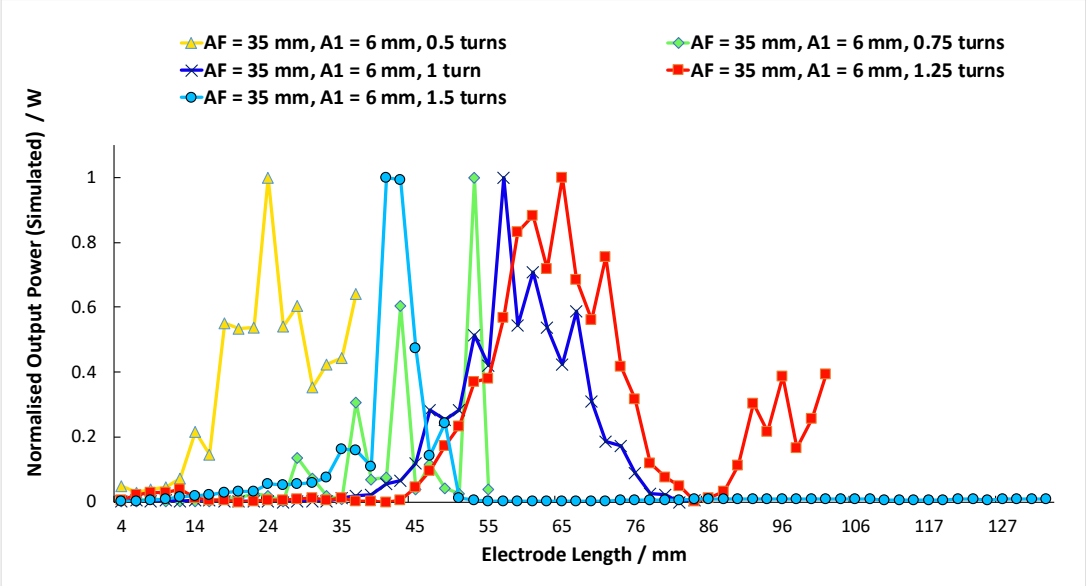

Figure 65 Simulated normalised output power of samples (AF=35 mm radius) as a function of electrode length

It is found that the simulations depict that some results, such as the AF = 35 mm, A1 = 6mm, 0.75 turns trace in Figure 65, vary from 0 to 1 abruptly at times. It is unlikely that the power output magnitude would vary with such frequency in reality; as such it is concluded that a sub-optimal solver configuration has been utilised for such cases. However, for result trends which vary more steadily, these simulation results serve to highlight the importance of optimising electrode length, with the difference between the highest and lowest power output ranging up to 2 magnitudes.

An illustration of the simulated optimal electrode lengths for an assortment of different spiral variants is shown in Figure 66.

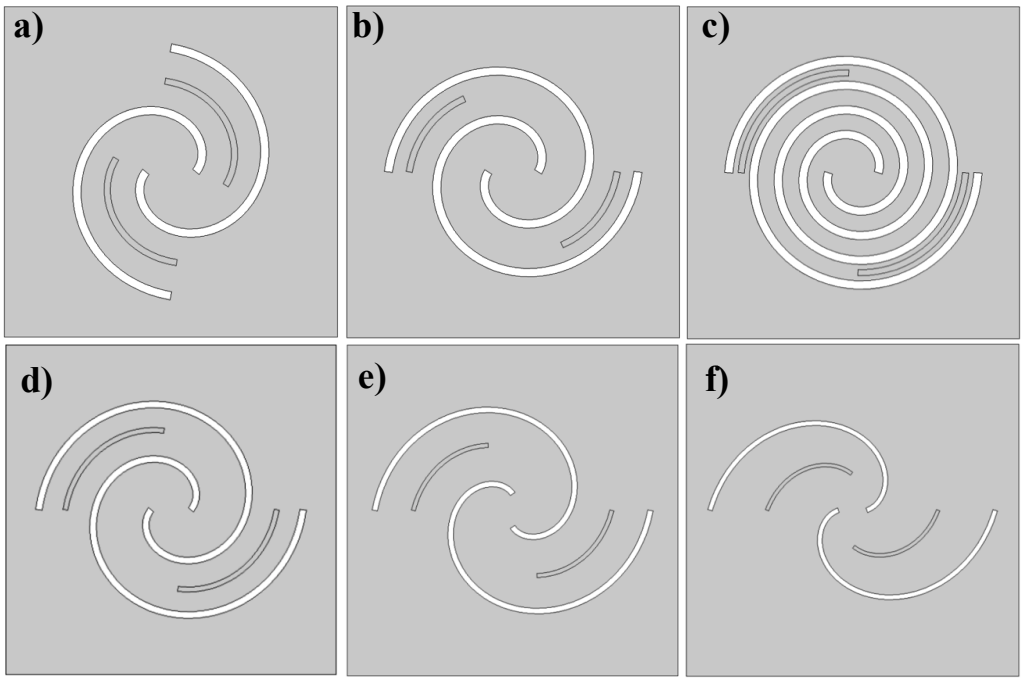

Figure 66 Screenshots of AF = 30 mm spiral geometries displaying electrode lengths which produced the greatest power output for a) AF = 30 mm, A1 = 6 mm, 0.75 turns, b) AF = 30 mm, A1 = 6 mm, 1 turn, and c) AF = 30 mm, A1 = 6 mm, 2 turns, d) AF = 40 mm, A1 = 6 mm, 1 turn, e) AF = 50 mm, A1 = 6 mm, 0.75 turns and f) AF = 60 mm, A1 = 6 mm, 0.5 turns

To conclude, this chapter outlined a variety of approaches available to optimise the mechanical energy transfer efficiency of a piezoelectric energy transducer. It is demonstrated how appropriate tailoring of transducer dimensions, such as layer thickness, can result in high mechanical responsivity to an excitation stimulus. Furthermore, it is also shown how the geometry of the transducer significantly affects the overall mechanical response. Through extensive finite element modelling, it is concluded that double-armed spiral geometry transducers lend themselves well to water droplet energy harvesting, presenting a self-supporting, highly sensitive design.

5 Mechanical Parameters Influencing Energy Transfer Efficiency

"There is no substitute for hard work"

— Thomas A. Edison

Chapter 5 covers the methodology and experimental testing carried out to identify the influence of key parameters on transducer energy harvesting efficiency. A piezoelectric cantilever beam geometry is used, due to both the abundance of existing mathematical formulae enabling straight-forward characterisation, in addition to the ability to test parameters of interest, such as bending stiffness, in isolation.

5.1.1 Transducer Stiffness Variation Experimental Method and Results

In order to investigate the effect of beam stiffness variation on energy transfer efficiency, a custom-built rig consisting of an adjustable clamp (ranging to a height of approximately 2.4 m), base stand and drip tray was fabricated for holding syringes in place to dispense droplets. An illustration of this experimental set-up is shown in Figure 67. Syringes with different aperture dimensions, achieved by cutting at different locations along the nozzle in addition to utilising needle tips, were placed in the clamp and used to dispense droplets of diameter 3.1 mm ± 0.1 mm , 4.4 mm ± 0.1 mm and 5.5 mm ± 0.1 mm from varying heights.

A solution was prepared by dissolving 20% weight P(VDF-TrFE) co-polymer powder (70/30 mol ratio, supplier Piezotech, Arkema Group) in a solvent of dimethylformamide and acetone (volume ratio 20/80). The solution was heated at 55°C in an oil bath and mechanically stirred for approximately 1 hour, before being degassed in an ultrasonic water bath for 1-2 hours. A doctor blade was used to uniformly spread the P(VDF-TrFE) solution onto a stainless steel foil sheet. To accommodate for shrinkage during the annealing process, the applicator was set to produce 25 μm film thickness in order to achieve a final 15 μm film thickness post heat treatment.

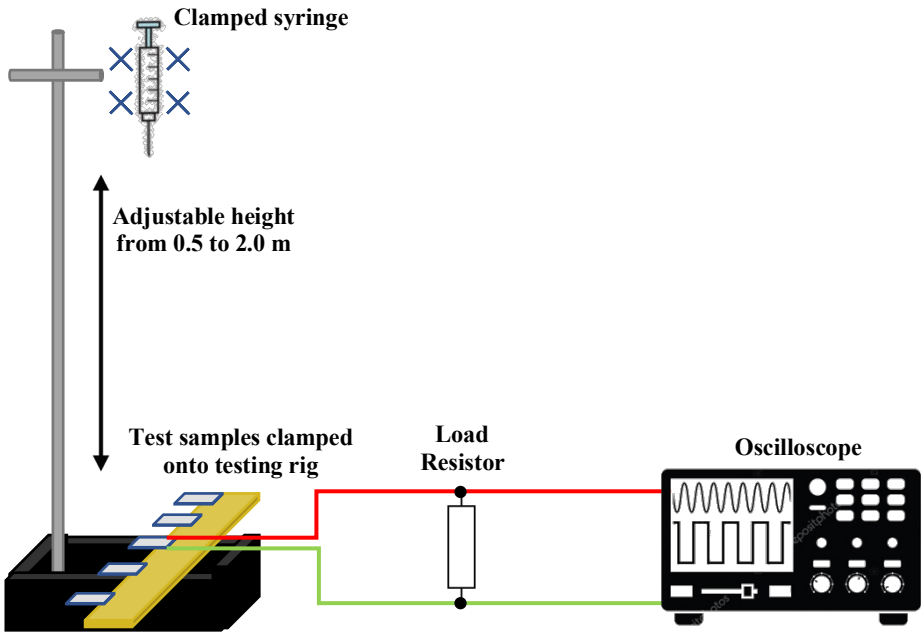

Figure 67 Illustration depicting droplet impact testing setup. Droplets are dispensed from a syringe clamped in an extended clamp stand. The voltage response from the piezoelectric transducers is measured across an electrically impedance matched load using an oscilloscope.

This thickness was found to display good piezoelectric properties; despite theoretical estimates indicating that a 7.2 µm thick film would be optimal in terms of neutral axis positioning, in practice it was found that these films tended to breakdown during the poling process. After deposition, the sheet was placed in an oven at 100°C for 5 minutes to allow the solution to dry, before the temperature was increased to 135°C to anneal the sample. The annealing process took place for 2 hours in order to increase the piezoelectric material's crystallinity. Following the heat treatment, the sheet was poled using a corona poling rig (ENCORE LT Corona gun from Nordson) for 10 minutes at a poling voltage of ~18 kV, with the corona poling tip approximately 10 mm away from the sample surface. Following the poling process, the sample sheets were cut into the desired length and width. Silver electrodes of 32 mm length, 2 mm width, and 200 nm thickness were deposited onto each sample through a shadow mask via e-beam evaporation. The electrode width was kept constant to maintain consistency between samples, in order to observe the variation of stiffness in isolation. Wire connections were attached to the deposited electrode using silver electrode paste, before the samples were encapsulated using NeverWet® superhydrophobic surface treatment in order to isolate all electrical connections from water. An initial sample set of 53 mm length cantilever beams was fabricated, illustrated in Figure 69 and Figure 70.

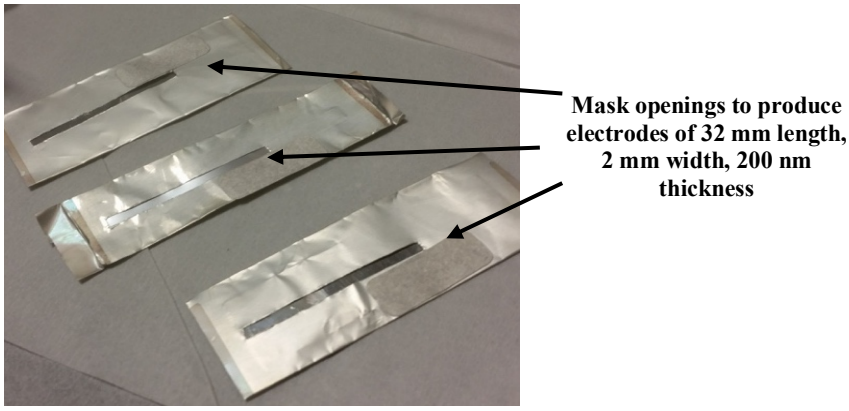

Figure 68 Cantilever beams with P(VDF-TrFE) deposited on stainless steel and poled, prepared for electrode deposition with foil mask

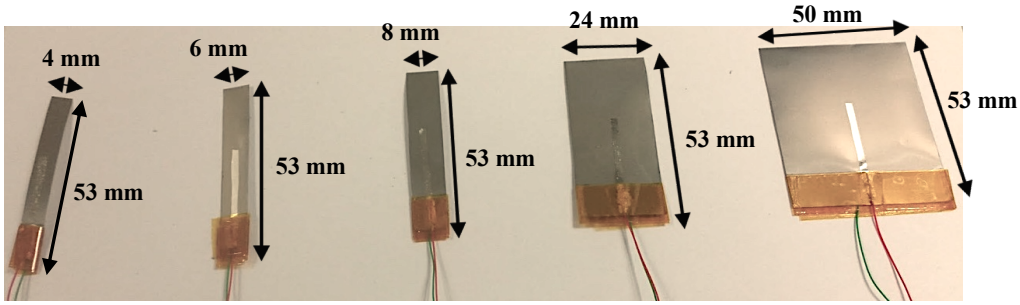

Figure 69 Photograph of a selection of 53 mm length cantilever beam test samples

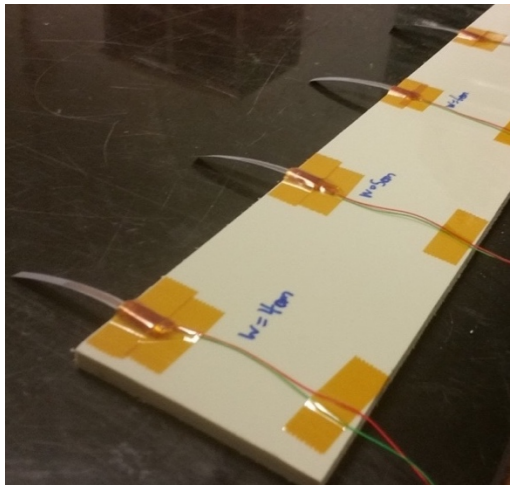

Figure 70 Close up of 53 mm length cantilever beam testing array to highlight mounting/clamping condition

53 mm length cantilever beam design and test details are shown in Table 11 and Table 12. Beam stiffness was calculated by measuring beam end displacement after adhering a series of known masses to the free end of the beam. Electrical impedance matching was carried out using a vibration shaker, with the driving frequency set to the fundamental resonance of each sample respectively. Note that the results here are incomplete due to sample failure of the 8 mm and 50 mm width samples in between testing with the 3.1 mm and 4.4 mm diameter droplets. It is proposed that the

impedance matched load varied between samples due to a combination of P(VDF-TrFE) and electrode layer thickness variation. Furthermore, the cold soldering technique of applying silver adhesive paste to connect the terminal wires may have influenced the impedance between samples.

Table 11 53 mm length piezoelectric cantilever beam experimental parameters

Cantilever total length	53 mm
Length of beam clamped	10 mm
Length of beam free	43 mm
P(VDF-TrFE) layer thickness	15 μm
Stainless steel foil layer thickness	25 μm
Beam widths tested	3 mm, 4 mm, 6 mm, 8 mm, 10 mm, 24 mm, 27 mm, 45 mm, 50 mm
Beam resonant frequency	10 - 15 Hz
Test drop diameters used	3.1 mm, 4.4 mm
Droplet test heights used	0.5 m, 1 m, 1.5 m, 2 m

Table 12 53 mm length piezoelectric cantilever beam mechanical parameters

Cantilever Beam Width / mm	**Resonant Frequency / Hz**	**Impedance Matched Load**	**Actual beam stiffness for point load at beam free-end / N/m**
3	10	3 MΩ	0.0605
4	10	10 MΩ	0.0666
6	10	9 MΩ	0.074
8	10	8 MΩ	0.085
10	11	7.5 MΩ	0.0951
24	10	8.5 MΩ	0.307
27	10	800 kΩ	0.409
45	15	2.5 MΩ	0.491
50	11	400 kΩ	0.5

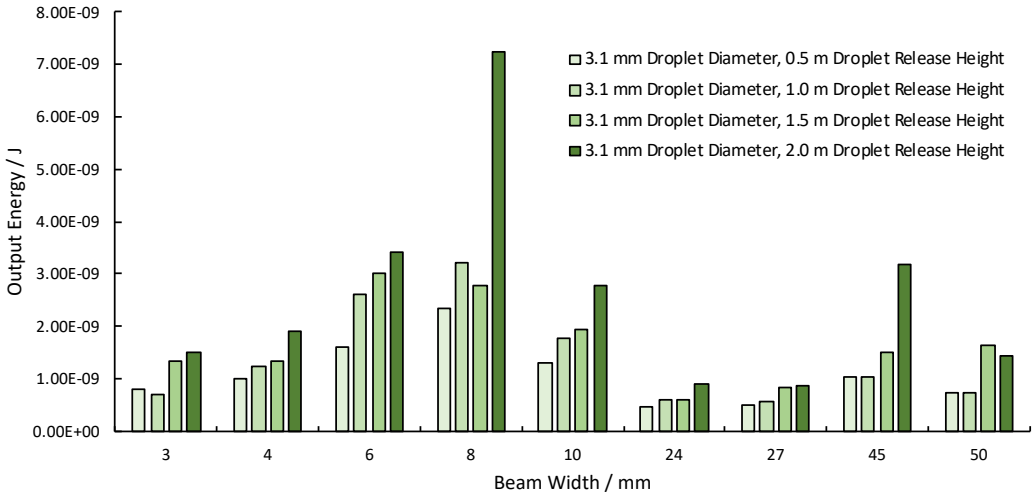

Figure 71 Graph displaying results of 3.13 mm diameter droplet impact testing for length = 53 mm samples

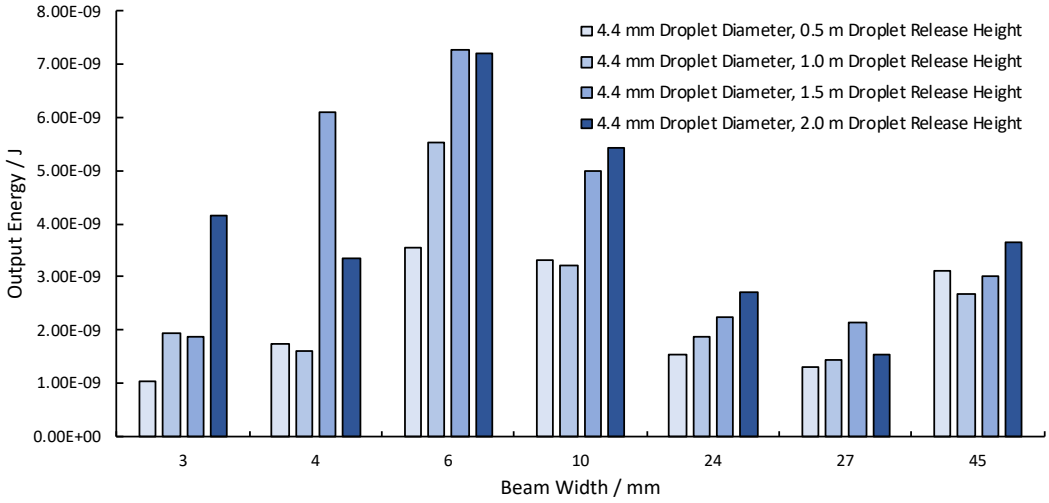

Figure 72 Graph displaying results of 4.4 mm diameter droplet impact testing for length = 53 mm samples

Initial analysis concluded that peak energy transfer efficiency appeared to occur when the beam width was in the 6 to 10 mm width region. To further improve result reliability, the clamping setup of the cantilever beam was altered. It was noted that, in previous testing, the cantilever beams were clamped on top of the connecting wires. This raised concerns regarding uniformity, and whether the non-homogenous surface created by the silver electrode paste contacts could affect results. As such, an alternative clamping setup was utilised, illustrated in Figure 73.

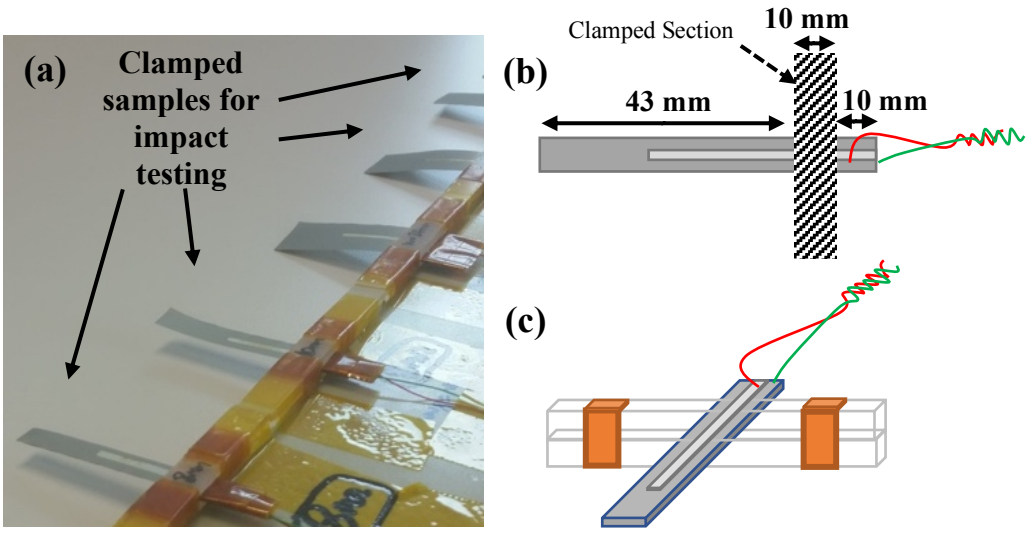

Figure 73 Images to illustrate clamping set-up for 63 mm length samples. (a) depicts a photograph of samples used for testing. (b) illustrates sample dimensions - free beam length is 43 mm, with 10 mm being clamped securely with acrylic supports, and the last 10 mm of the beam reserved for electrode connections. (c) illustrates sample clamping set-up graphically.

In this clamping arrangement, a 20 mm section of the cantilever beam was reinforced and encapsulated with clear tape, after silver electrodes of 32 mm length, 2 mm width, and 200 nm thickness were deposited via e-beam evaporation process. Of this 20 mm section, 10 mm is clamped, whilst the remaining 10 mm is used for adhering wire contacts using silver electrode paste. In this way, the clamped section of the beam is as homogenous as possible. Relevant details for these samples are shown in Table 13.

Table 13 63 mm length piezoelectric cantilever beam experimental parameters

Cantilever total length	63 mm
Length of beam clamped	10 mm
Length of beam free	43 mm
P(VDF-TrFE) layer thickness	15 μm
Stainless steel foil layer thickness	25 μm
Beam widths tested	6 mm, 8 mm, 10 mm, 24 mm, 26 mm, 27 mm
Beam resonant frequency	9 – 10 Hz
Test drop diameter used	3.13 mm, 4.4 mm, 5.47 mm
Droplet test heights used	0.5 m, 1 m, 1.5 m, 2 m

The individual beam characteristics are displayed in Table 14. In this round of testing, both the dielectric loss and capacitance of each sample was measured using an LCR

meter, with a measuring frequency of 1 kHz, in order to investigate sample consistency.

Table 14 63 mm length piezoelectric cantilever beam mechanical parameters

Cantilever Beam Width / mm	**Resonant Frequency / Hz**	**Impedance Matched Load**	**Actual beam stiffness / N/m**	**Sample Capacitance @ 1 kHz / pF**	**Dielectric Loss @ 1 kHz**
6	10	8 MΩ	0.09432	511.7	0.01728
8	10	8 MΩ	0.117	611.7	0.01773
10	10	8 MΩ	0.129	443.2	0.0600
24	9	5 MΩ	0.307	491.5	0.02180
26	9	5 MΩ	0.3067	424.1	0.01527
27	10	8 MΩ	0.3066	676.1	0.01799

The results of testing using all three droplet diameter sizes at the selected heights are displayed in Figure 75. A further round of impact testing was carried out using a single sample which was trimmed in-between testing rounds, with the results displayed in Figure 77. The theory behind this approach assumed that using a single sample would increase test reliability as physical differences between samples which could influence results, such as different initial displacements, would be negated. Additionally, the usage of multiple samples complimented this testing by outlining that any trends achieved were not specific to the trimmed sample. The 27 mm sample used in the previous testing round was utilised. The sample width was progressively cut along each side, as illustrated in Figure 74. Experimental details are shown in Table 15. It is worth noting that impact testing from a height of 2 m was not carried out here, due to concerns over impact location reliability. Interim measurements were made for each sample after cutting, as displayed in Table 16. At widths of 11 mm and 4 mm, the sample was re-impedance matched using a shaker. As it did not appear that the impedance altered by a significant amount in each case, the original matched load of 8 MΩ was used throughout testing.

It was found that, for both rounds of testing, beams with a bending stiffness within the range of 0.067 to 0.134 N/m achieved the best energy transfer efficiency. Despite the electrode area being constrained in order to achieve consistency throughout the sample set, inevitably resulting in sub-optimal energy output, it was calculated that the achieved results of samples represented a significant improvement on energy

transfer efficiency compared to commercially available sensors. The results from previous testing [75] which utilised commercially available piezoelectric sensors (The Pro-Wave (FS-2513P) sensor) indicated an energy output of no more than 90 nJ from droplet impact. With an active volume of approximately 0.975 μm^3, the energy density is calculated as 0.092 J/m^3. In comparison, the peak energy output of 28 nJ achieved from the testing results of this investigation, generated by an active sample volume of 1.76 nm^3, represents an energy density of 15.9 J/m^3. These results exemplify how appropriate transducer mechanical tailoring to the excitation source can result in significant energy transfer efficiency improvement. As such, whilst the peak energy output achieved in this research is not the highest possible, it demonstrates significant energy transfer efficiency for the active electrode areas used. It is proposed that the energy density of the commercial sensors typically utilised in other studies suffers due to the relatively stiff Mylar coating used to encapsulate the sample.

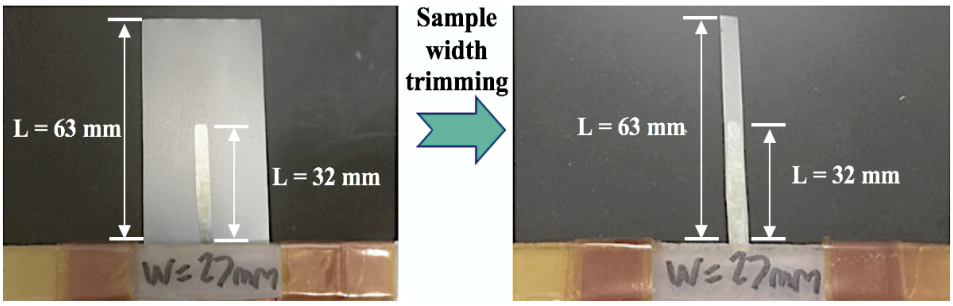

Figure 74 Images to illustrate progressive trim testing of single sample

Table 15 Progressive trim piezoelectric cantilever beam experimental parameters

Cantilever total length	63 mm
Length of beam clamped	10 mm
Length of beam free	43 mm
P(VDF-TrFE) layer thickness	15 μm
Stainless steel foil layer thickness	25 μm
Beam widths tested	4 mm, 7 mm, 11 mm, 15 mm, 19 mm, 25 mm, 27 mm
Beam resonant frequency	10 Hz
Test drop diameter used	3.1 mm, 4.4 mm, 5.5 mm
Droplet test heights used	0.5 m, 1 m, 1.5 m

Table 16 Progressive trim piezoelectric cantilever beam experimental parameters

Cantilever Beam Width / mm	**Resonant Frequency / Hz**	**Impedance Matched Load**	**Actual beam stiffness / N/m**	**Sample Capacitance @ 1 kHz / pF**	**Dielectric Loss @ 1 kHz**
4	10	8 MΩ	0.067	657 pF	0.01677
7	10	8 MΩ	0.094	620 pF	0.13
11	10	8 MΩ	0.134	621 pF	0.14
15	10	8 MΩ	0.188	619 pF	0.15
19	10	8 MΩ	0.188	660.6 pF	0.02
25	10	8 MΩ	0.23535	661 pF	0.022
27	10	8 MΩ	0.23535	663 pF	0.02

The energy output results shown in Figure 75 and Figure 77 are averaged from the impacts of at least 5 droplets in each case.

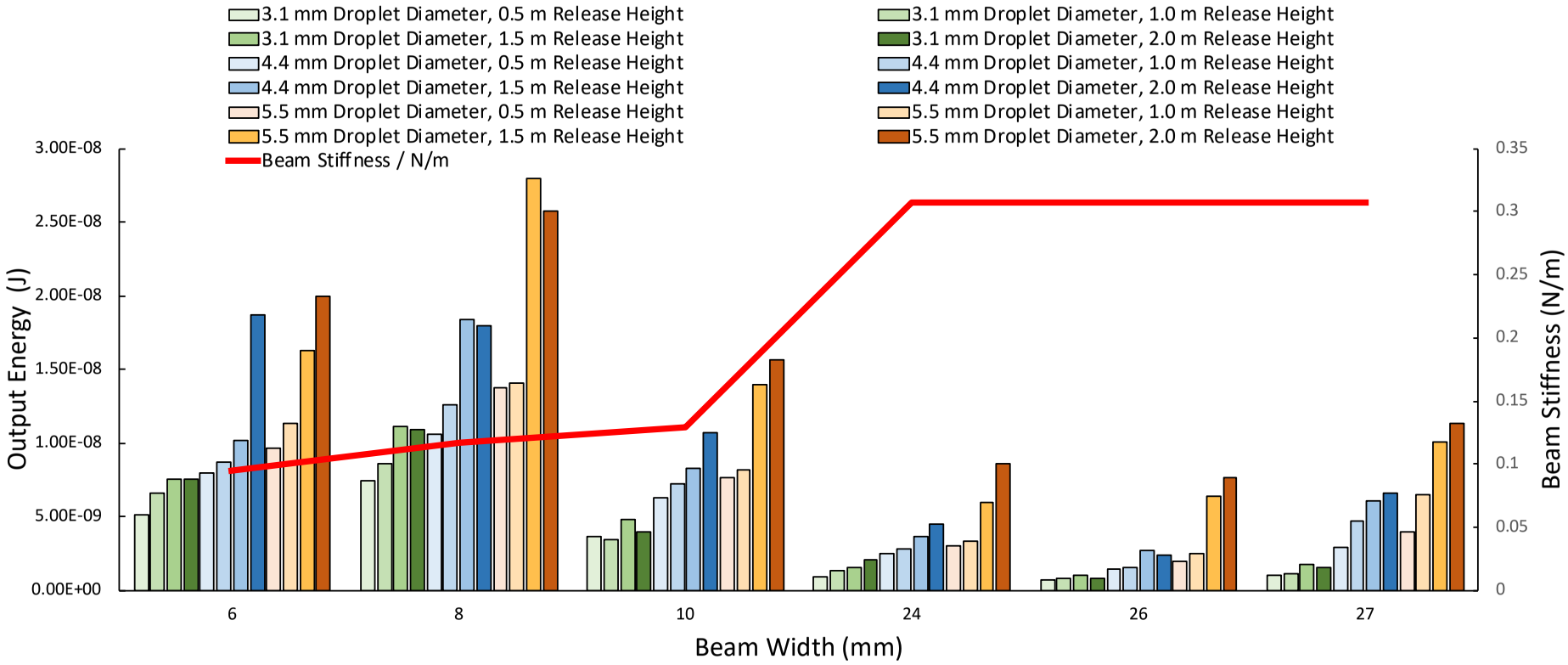

Figure 75 Graph displaying results of 3.13 mm, 4.4 mm and 5.47 mm diameter droplet impact testing from 0.5 m, 1 m, 1.5 m and 2 m heights onto length = 63 mm samples

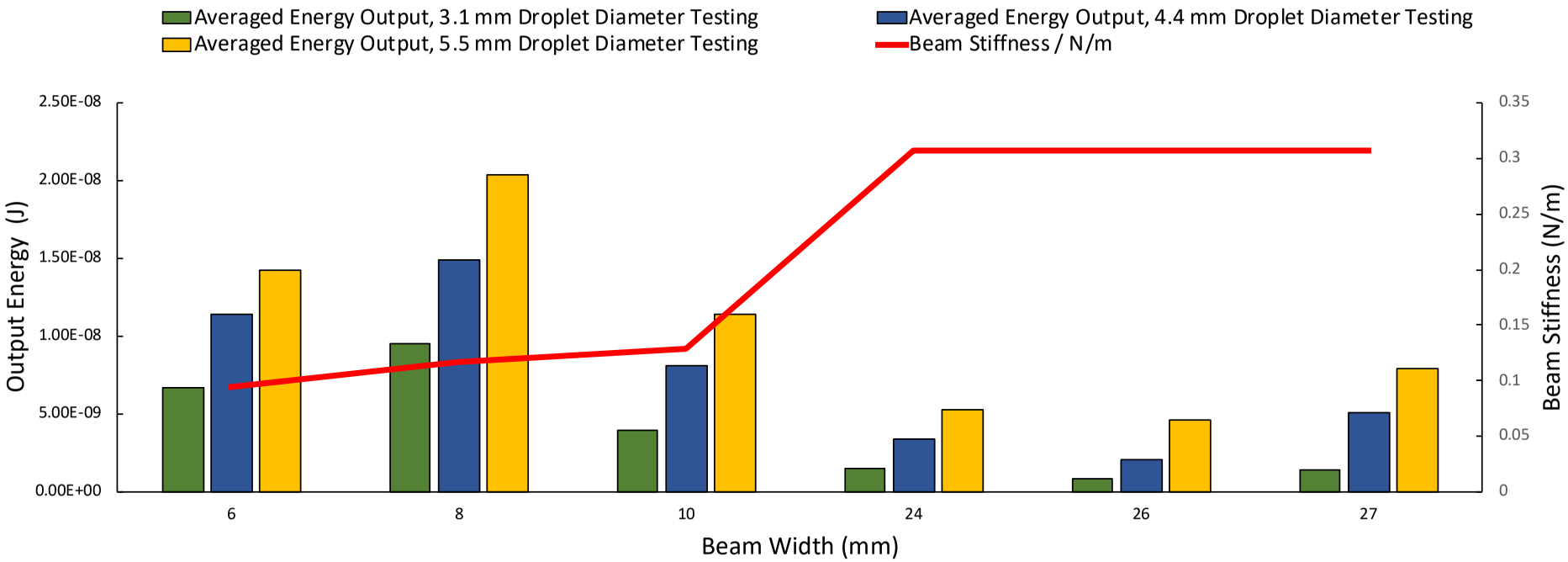

Figure 76 Graph displaying all droplet release height results from Figure 75 (multiple test samples) averaged to give a single output energy, per beam width, for each droplet diameter tested

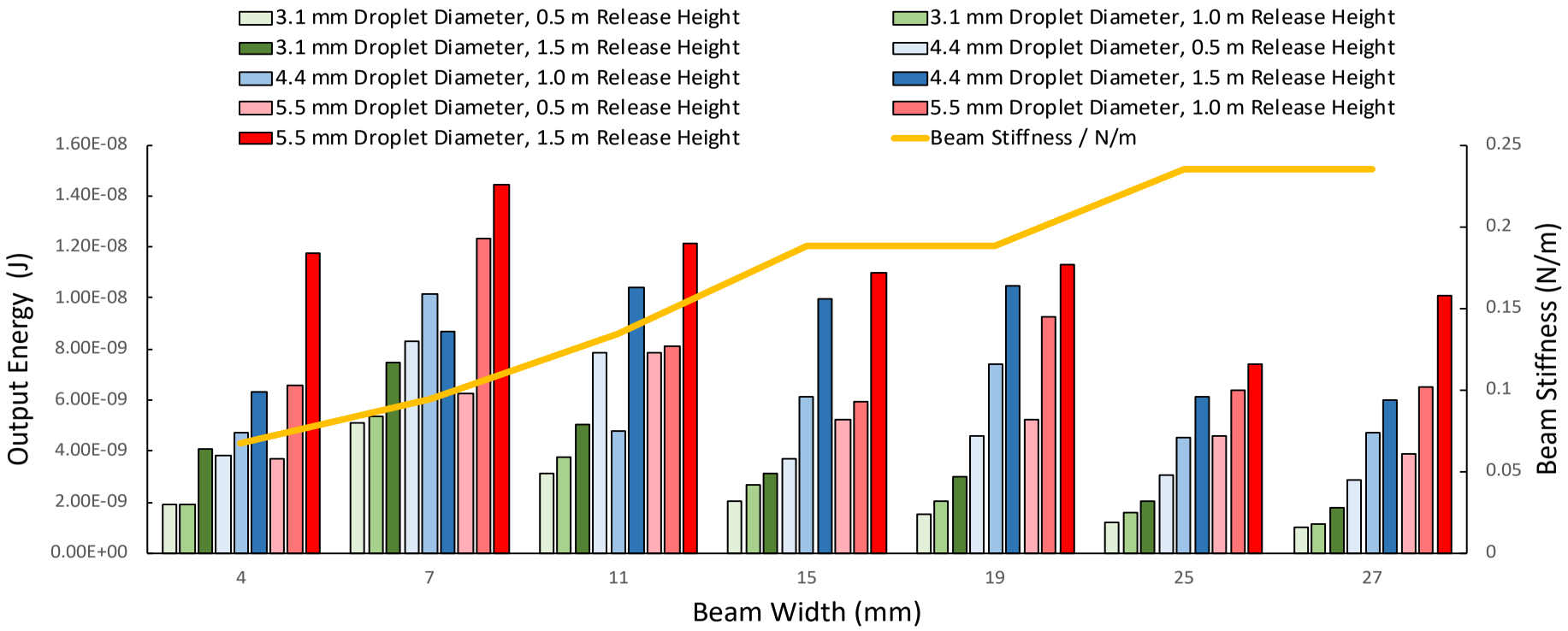

Figure 77 Average output energy per beam width as a function of impacting droplet diameter and release height, progressive trim testing

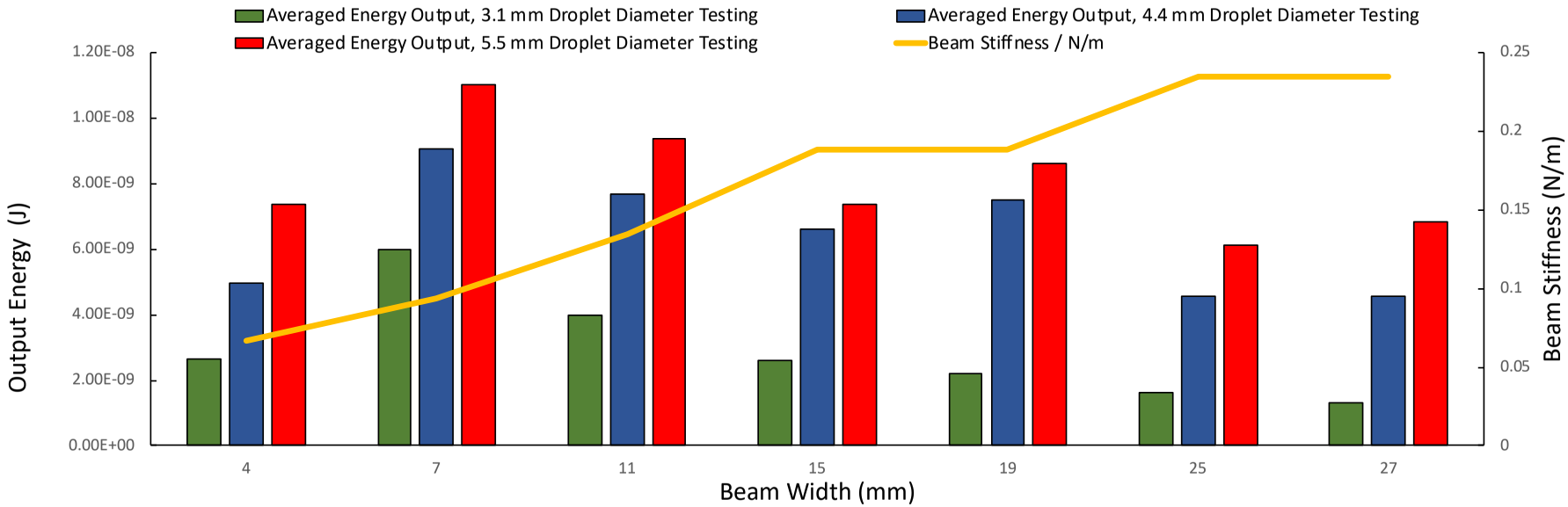

Figure 78 Graph displaying all droplet release height results from Figure 77 (progressive trim testing) averaged to give a single output energy, per beam width, for each droplet diameter tested

5.1.2 Droplet Impact Frequency Variation Experimental Method and Results

An investigation into the energy transfer efficiency depending on droplet impact frequency is carried out. Whilst it is rational to assume that driving an energy harvester at its resonant frequency will result in maximised power output, it has been reliably demonstrated that droplet-surface interactions are not trivial, given the elastic nature of droplets upon impact. It has been proposed that, depending on the relation between the beam resonant frequency and the natural vibration frequency of the impacting droplet, illustrated in Equation 40, the reactive transducer movement to impact can synergistically, passively or destructively contribute towards the droplet kinetic energy after recoil from the substrate [146]. As such, this work seeks to validate the effect of impact frequency upon the energy transfer efficiency, as this has yet to be explicitly demonstrated elsewhere.

$$f_d = \frac{1}{t} = \frac{1}{\frac{\pi}{4}\sqrt{\frac{\rho D_0^3}{\sigma}}}$$

Equation 40

This investigation began by simulating the length = 63 mm samples tested previously in the COMSOL modelling software. Simulations investigated sample power output whilst being driven by a range of frequencies. In addition to simulation analysis, a practical test was carried out using an Alaris IVAC P7000 syringe driver to dispense 3 mm-diameter droplets at a range of drip frequencies onto each sample beam end from a distance of 30 cm. This test round utilised the samples used in previous tests (widths of 4, 6, 8, 10, 24 and 26 mm). An IR detector was used to measure the drip frequency rate of the droplets, outputting a negative spike each time a droplet broke the IR beam. This signal was measured using an oscilloscope and used to calculate drip frequency. Measured drip frequencies ranged from 1 Hz to at least 30 Hz for all samples.

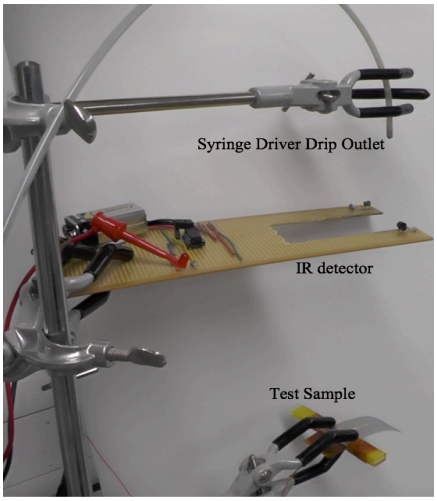

Figure 79 Photograph to illustrate impact frequency effect on power output test setup

The impact frequency testing results in Figure 80 demonstrate that, despite the non-trivial behaviour of droplet-surface impact interactions, sample output power was better when the frequency of incident impacting droplets onto the sample beam ends' was close to/at the samples resonant frequency. The simulated results, although displaying power output levels a couple magnitudes greater than the practical results, support the conclusion that driving the samples at their resonant frequency achieves optimal power output. It is noted that there is a difference between the simulated and experimental result peaks. This is considered to be due to the disparities between the simulation and experimental environments; for example, in the simulation the samples are driven with a periodic impulse, which does not account for fluid dynamics. Additionally, it is likely that that the material properties for the fabricated samples would differ from the simulated samples. In each case, the power output was maximised when the simulated/practical sample was driven by impacts matching its resonant frequency.

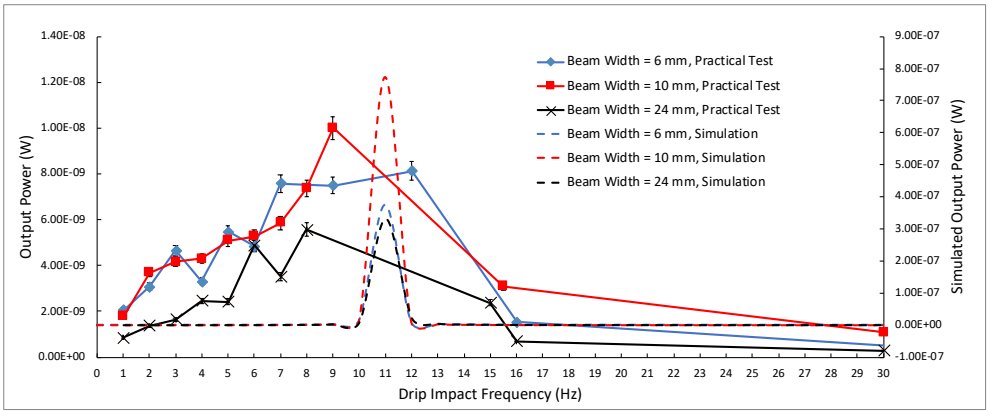

Figure 80 Sample output power as a function of droplet impact frequency, simulation and practical test results

To conclude, it is found that in the case of water droplets of diameter 3.3 – 5.5 mm, falling from a height of 0.5 to 2.0 m, piezoelectric cantilever beams of bending stiffness within the range of 0.067 to 0.134 N/m achieved the best energy transfer efficiency.

Additionally, it was proven that droplets impacting upon the cantilever beams with a frequency which was close to the beam resonant frequency elicited the greatest energy output. Whilst perhaps intuitive, the impact of a droplet upon a solid surface is a highly dynamic, non-trivial event; these results demonstrate that the micro-scale mechanical dynamics can be ignored in favour of the macro-scale driving frequency.

6 Archimedean Spiral Transducer Fabrication and Testing

"Noli turbare circulos meos!"

— Archimedes

In this chapter, aspects relating to optimal design and implementation of spiral transducers into an energy harvesting system are investigated practically. From FEM geometric investigations, it was observed that double-armed Archimedean spiral-type geometries held inherent mechanical behaviours which lend themselves favourably to droplet impact energy harvesting. A brief summary of the spiral characterisation carried out is as follows:

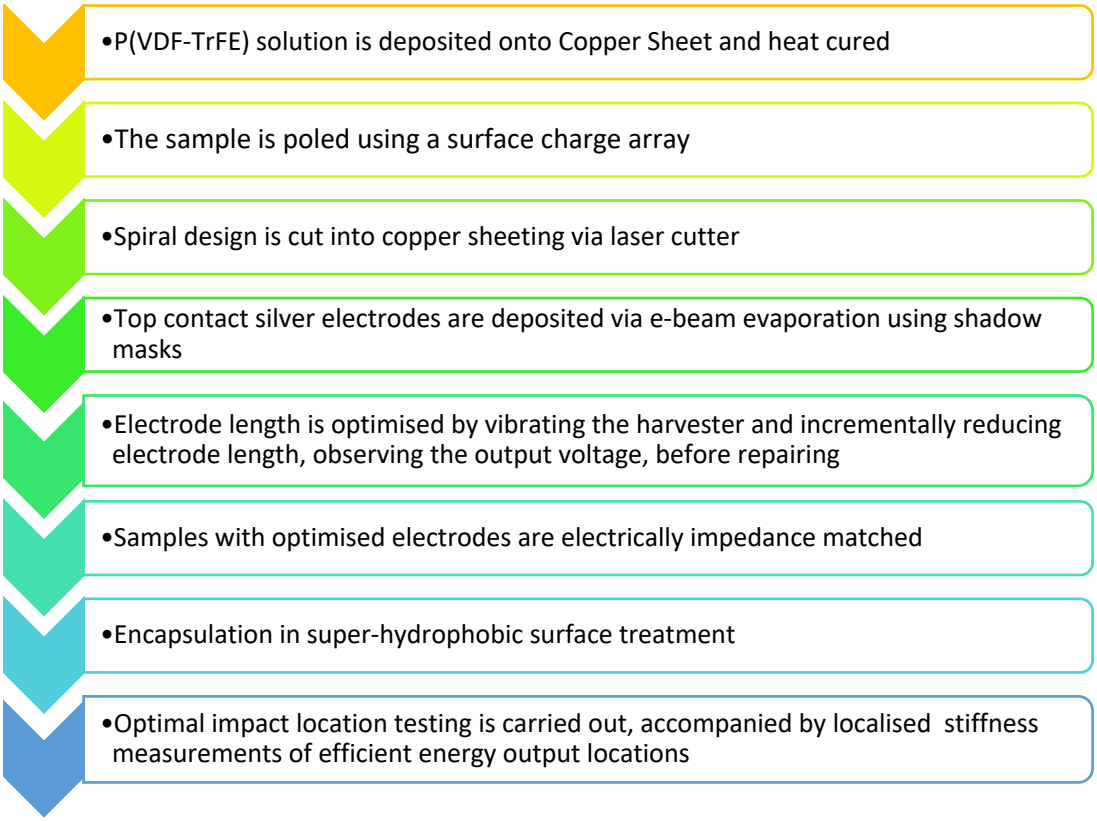

Figure 81 Diagram to illustrate spiral sample fabrication, characterisation and optimisation process

6.1 Sample Fabrication

2 different sample sets were initially fabricated – 5 samples composed of spirals with mixed final radii and turn number, and 5 samples with AF = 35 mm, A1 = 6

mm, Gap = 2 mm and turn number ranging from 0.5 to 1.5 in 0.25 turn increments. A solution was prepared by dissolving 20% weight P(VDF-TrFE) co-polymer powder (70/30 mol ratio) in a solvent of dimethylformamide and acetone (volume ratio 20/80). The solution was heated at 55°C in an oil bath and mechanically stirred for approximately 1 hour, before being degassed in an ultrasonic water bath for 1-2 hours. A doctor blade was used to uniformly spread the P(VDF-TrFE) solution onto 50 μm thick copper foil sheets. Following issues with sample short circuiting, it appeared that too thin film thickness results in perforation during the drying process. It was proposed that this occurred due to thermal expansion coefficient mismatch between the polymer and substrate layers; the thermal expansion coefficient of copper is approximately 17 μK^{-1}, compared to that of PVDF polymers which are typically in the region of 120 μK^{-1} [172]. Such mismatch would introduce additional mechanical strain on the deposited P(VDF-TrFE) film during the heat process, potentially thinning the layer to the point of perforation, which would result in short circuiting post electrode deposition.

Consequently, to avoid this it was found that films of at least 50 μm thickness should be deposited, producing an estimated 20-25 μm thick film post heat treatment. After deposition, the sheet was placed in an oven at 100°C for 5 minutes to allow the solution to dry. The sheet was then annealed for 2-3 hours at a temperature of 135°C in order to increase the piezoelectric material's crystallinity. Following the heat treatment, the sheet was poled using a custom built surface charge poling rig, which consisted of an array of brass pins to create an evenly distributed poling field, illustrated in Figure 82.

Positioned parallel to the P(VDF-TrFE) upper surface, the distance between the sample and the pin tips was approximately 20 mm. A poling voltage of ~13-13.5 kV was applied for 5 minutes to each sample, with the surface charge measured after each poling period to check that adequate poling had occurred.

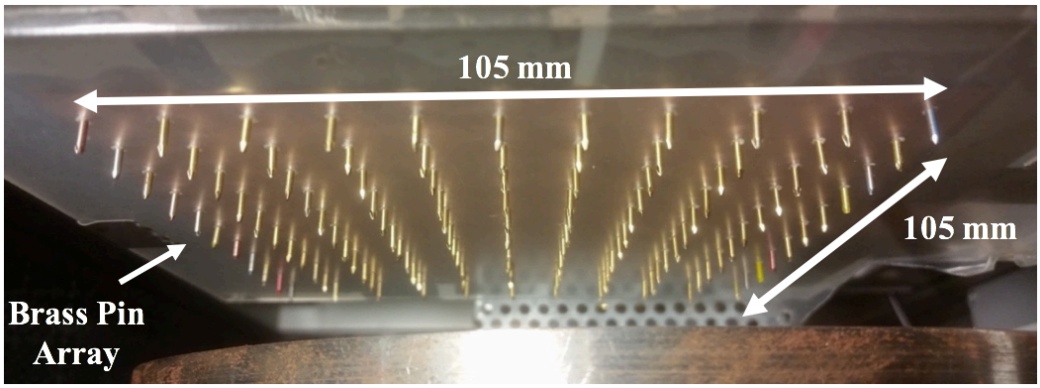

Figure 82 Photograph of custom built surface charge array used to polarize P(VDF-TrFE) on copper foil samples. Samples were positioned underneath the array in order to experience an evenly distributed poling field across the upper surface

In order to prevent charge cancellation during oscillation, shadow masks were used to deposit individual silver electrodes on each spiral arm, instead of carrying out variable zone polarisation. The electrodes were 200 nm thick, 2 mm width, and initially ran the full spiral arm length for each design. A thin electrode width was chosen so that it could be kept constant whilst sample turn number was increased (spiral arm width decreases with increasing turn number when the final and initial spiral radii are kept constant). It is noted that this electrode arrangement is perhaps not a true reflection of the greatest available power output - future work looks to optimise the active area further. Wire connections were attached using silver conductive paint, before each sample was securely clamped along the edges in an acrylic frame. After electrode optimisation took place, the samples were encapsulated using NeverWet® superhydrophobic surface treatment in order to isolate all electrical connections from water, with the resulting difference in water droplet contact angle illustrated in Figure 83. A selection of successfully fabricated spiral samples is shown in Figure 84. The parameters' physical expression is displayed in Figure 85 for reference. Optimal impact location testing is carried out, before the bending stiffness of the impact location which produces the highest energy output is calculated.

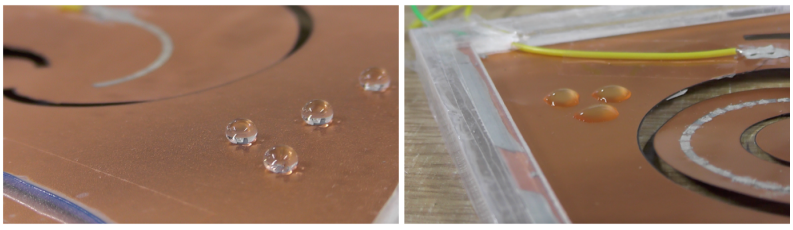

Figure 83 Photographs to illustrate the effect of NeverWet® superhydrophobic surface treatment on water droplet contact angle, post-treated sample (left) and pre-treated sample (right)

Figure 84 Photographs displaying some of the fabricated spirals

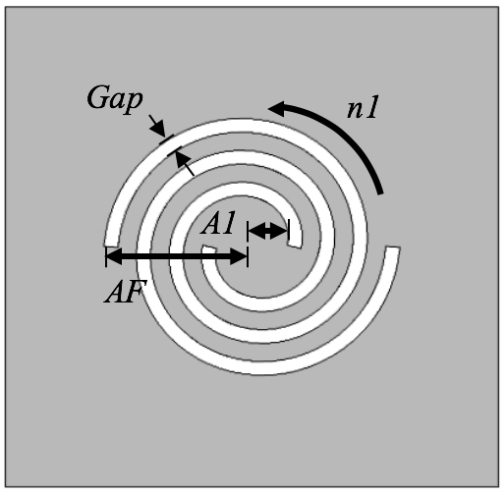

Figure 85 Varied spiral parameters

6.2 Spiral Electrode Optimisation and Impedance Matching

Experimental variation of electrode length was carried out. Each sample was driven at resonance, with 0.5 cm sections of the electrodes disconnected at intervals through mechanical abrasion, in order to measure the effect on the output voltage with shortening electrode length. Once an optimal electrode length is identified, the sample electrodes are repaired using silver conductive paint. The electrodes are optimised with the samples being driven at resonance due to the anticipated sample post-impact mechanics – after the droplet collides with the sample upper surface, it rolls off the sample due to the hydrophobic coating, leaving the sample to oscillate at its natural frequency. The electrode length variation results are shown in Figure 86 for the mixed radii spirals, and in Figure 87 for the AF=35 mm radius spirals with turn number varied in isolation.

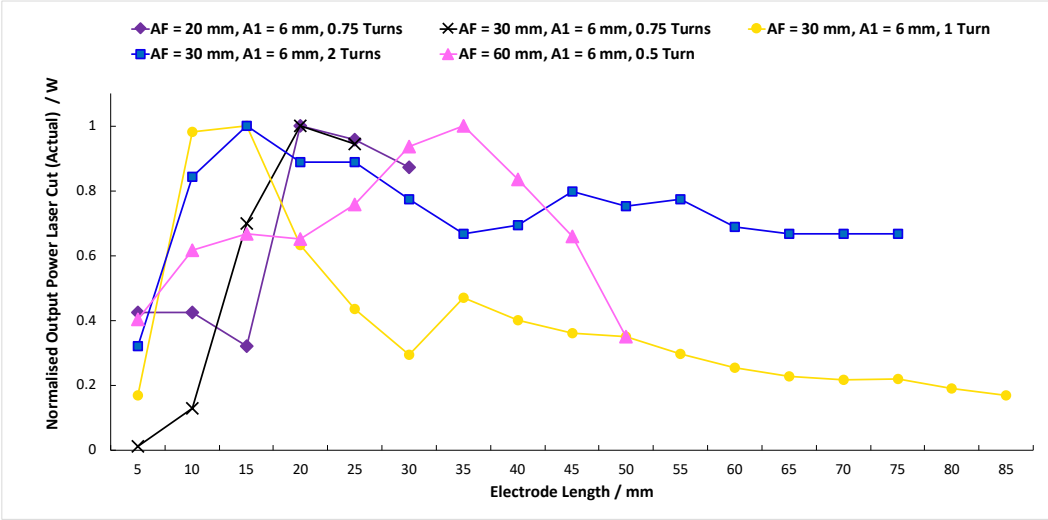

Figure 86 Actual normalised output power of samples (mixed radius) as a function of electrode length

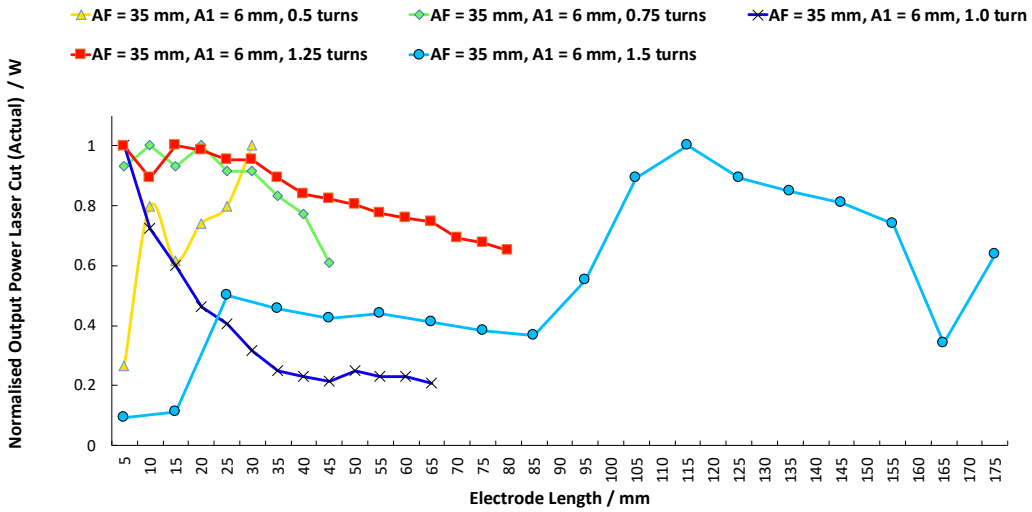

Figure 87 Actual normalised output power of samples (AF=35 mm radius) as a function of electrode length

The variation in power output with electrode length is noteworthy – it is demonstrated that, for samples such as the "AF = 60 mm, A1 = 6 mm, 0.5 Turn", power output decreases with decreasing electrode length. However, the power output for the "AF = 30 mm, A1 = 6 mm, 2 Turns" sample peaks at two distinct locations in both the simulated and practical results. This highlights the complex stress/strain distribution throughout the spiral arms during bending, which is pronounced in this geometry likely due to axial/torsional stresses being greater in longer spiral arms. Relevant parameters for all fabricated samples post-optimisation are displayed in Table 17.

Table 17 Relevant parameters of fabricated spiral sample sets

	Sample Parameters	Sample Thickness / mm	Resonant Frequency / Hz	Active Electrode Length/Width/ Depth (per arm) / mm^2	Electrically Impedance Matched Load / MΩ
Laser Cut (Mixed Radii)	AF = 20 mm, A1 = 6mm, 0.75 Turns	0.07-0.09	16	17 mm / 1.5 mm / 200 nm	5
	AF = 30 mm, A1 = 6mm, 0.75 Turns	0.05-0.08	16	30 mm / 1.5 mm / 200 nm	2
	AF = 30 mm, A1 = 6mm, 1 Turn	0.07-0.08	18	17 mm / 1.5 mm / 200 nm	5
	AF = 30 mm, A1 = 6mm, 2 Turns	0.07-0.09	8	34 mm / 1.5 mm / 200 nm	3.5
	AF = 60 mm, A1 = 6mm, 0.5 Turns	0.06-0.07	20	35 mm / 1.5 mm / 200 nm	4
Laser Cut (Increasing Turn)	AF = 35 mm, A1 = 6mm, 0.5 Turns	0.09-0.12	20	37.5 mm / 1.5 mm / 200 nm	6.7
	AF = 35 mm, A1 = 6mm, 0.75 Turns	0.08-0.17	16	27.5 mm/ 1.5 mm / 200 nm	4
	AF = 35 mm, A1 = 6mm, 1 Turn	0.08-0.10	15	14 mm/ 1.5 mm / 200 nm	8.7
	AF = 35 mm, A1 = 6mm, 1.25 Turns	0.08-0.11	15	26 mm / 1.5 mm / 200 nm	8.7
	AF = 35 mm, A1 = 6mm, 1.5 Turns	0.10-0.14	8	92.5 mm / 1.5 mm / 200 nm	6.7

The optimal electrode length for each sample was selected from the experimental testing results, with electrical impedance matching taking place subsequently. The samples were driven at a steady vibration frequency and the output voltage was measured across a variety of resistances. The resulting power output was calculated and plotted to produce a peaked curve. From this curve, a value for max power output depending on output load was found for each sample.

6.3 Effect of Droplet Impact Location on Energy Output

The effect of droplet impact location variation on each sample was studied. A selection of locations were chosen for each sample, with multiple 5 mm diameter droplets being released from a height of 0.5 and 1.0 metre onto each position. For each sample, the normalised average energy output of each location from the perspective of one arm connection was calculated, indicating the impact location

which produced the greatest energy output at unity. Subsequently, the bending stiffness of the impact location producing the greatest energy output was found.

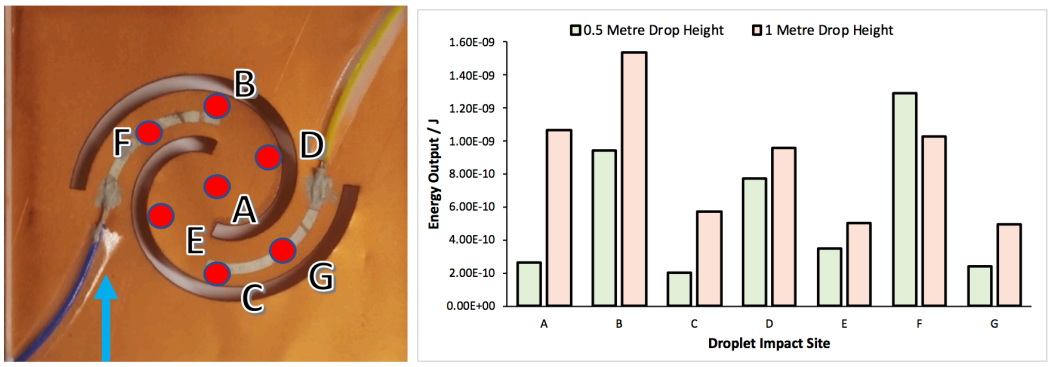

Figure 88 AF = 20 mm, A1 = 6 mm, 0.75 Turns – Output Energy from Blue Arm Connection

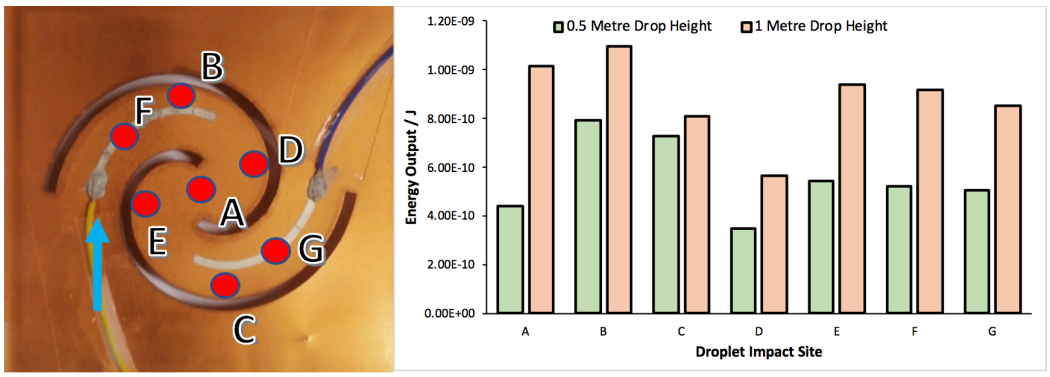

Figure 89 AF = 30 mm, A1 = 6 mm, 0.75 Turns – Output Energy from Yellow Arm Connection

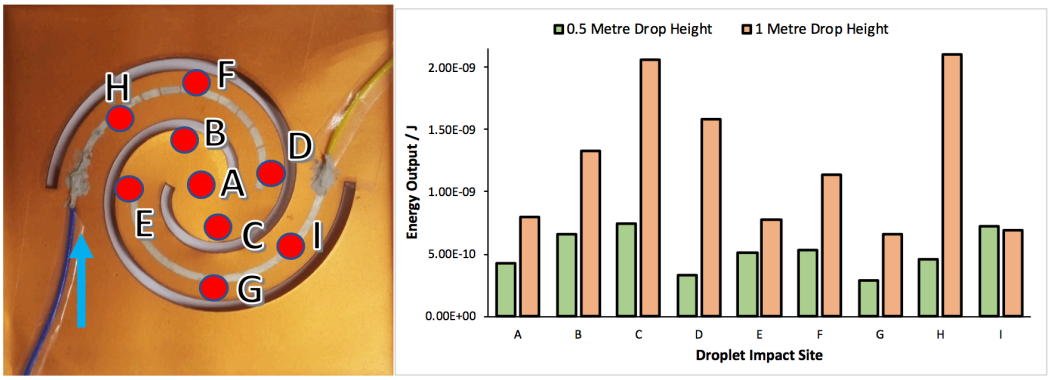

Figure 90 AF = 30 mm, A1 = 6 mm, 1 Turns – Output Energy from Blue Arm Connection

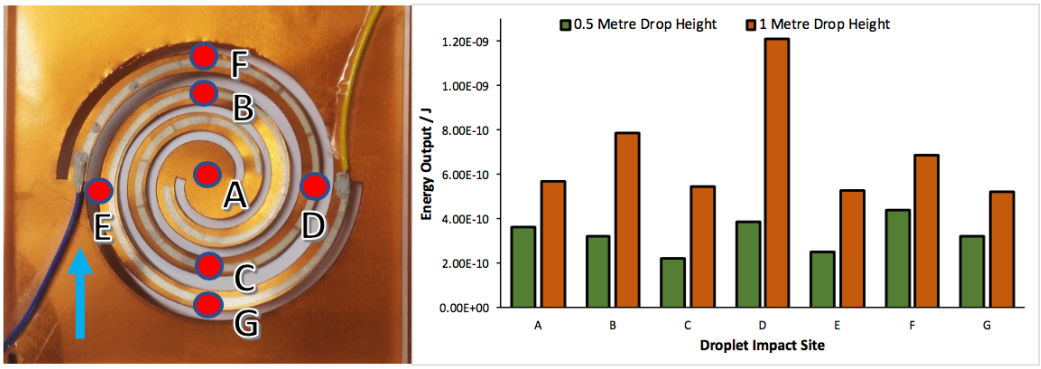

Figure 91 AF = 30 mm, A1 = 6 mm, 2 Turns – Output Energy from Blue Arm Connection

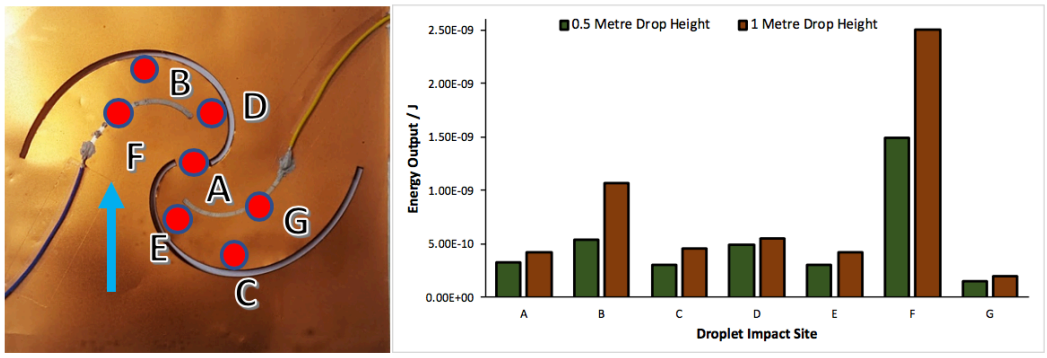

Figure 92 AF = 60 mm, A1 = 6 mm, 0.5 Turns – Output Energy from Blue Arm Connection

Graphs displaying the impact location which produced the greatest energy output, and the overall average energy output of all impact locations on each sample, are shown in Figure 93 and Figure 94. In Figure 93 error bars are used to illustrate the highest to lowest range in energy output from all droplet impacts used to test the samples. Following the identification of impact locations which produced a peak energy output for each sample, the axial stiffness of these locations was measured. The results appear to demonstrate that increasing stiffness results in greater energy transfer to a certain threshold, although there is some variation which suggests that gauging energy transfer efficiency by stiffness in isolation is not sufficient. The spiral geometry also appears to influence energy transfer efficiency, with the AF = 30 mm, 1 turn sample producing a jump in energy output compared to spirals with similar dimensions but different turn number.

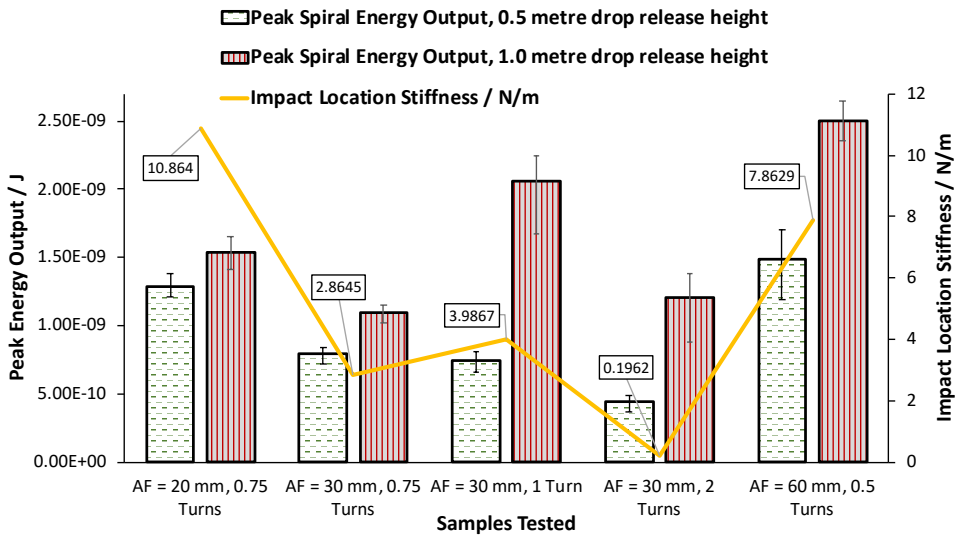

Figure 93 Laser cut sample (mixed radius) peak energy output data compared to bending stiffness at the impact location (bending stiffness values shown beside trend line)

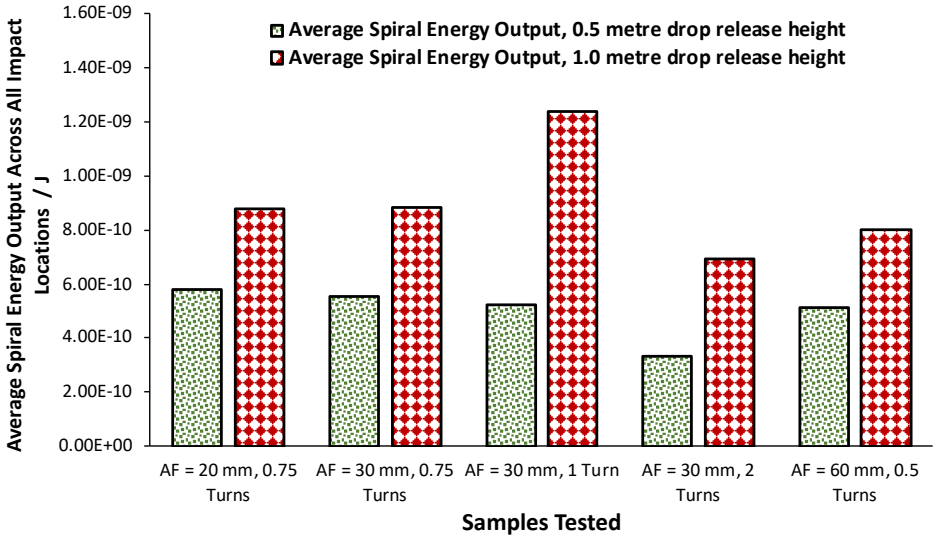

Figure 94 Graph displaying average energy output from all tested impact locations for each sample, giving an overall display of energy output for each sample.

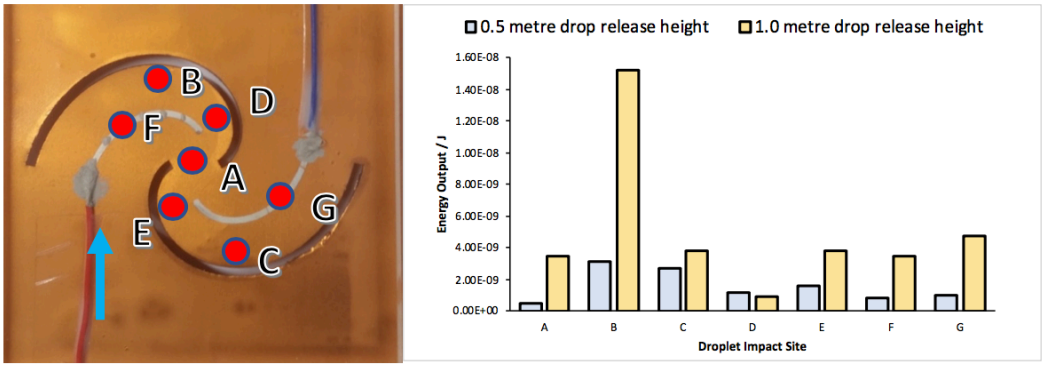

Figure 95 AF = 35 mm, A1 = 6 mm, 0.5 Turns – Output Energy from Red Arm Connection

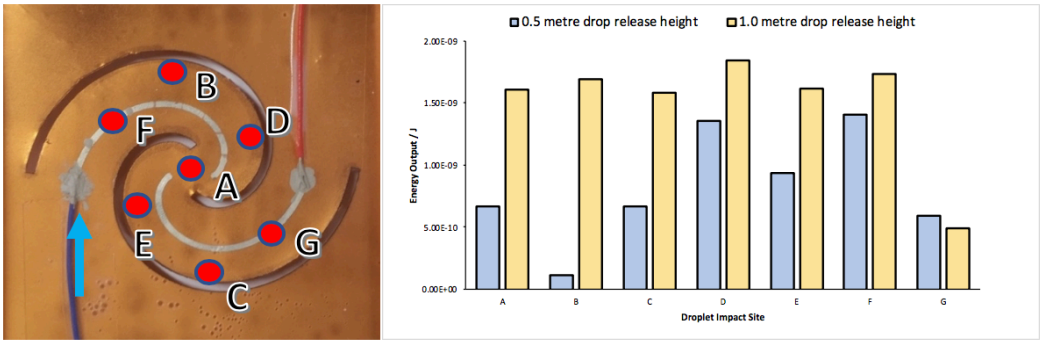

Figure 96 AF = 35 mm, A1 = 6 mm, 0.75 Turns – Output Energy from Blue Arm Connection

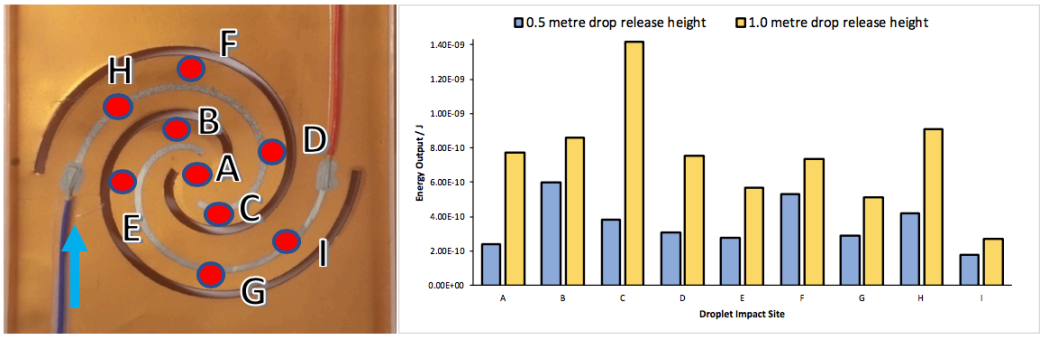

Figure 97 AF = 35 mm, A1 = 6 mm, 1 Turns – Output Energy from Blue Arm Connection

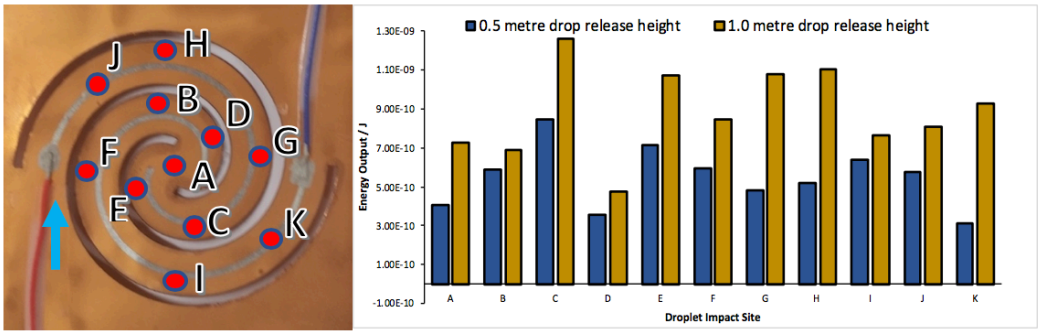

Figure 98 AF = 35 mm, A1 = 6 mm, 1.25 Turns – Output Energy from Red Arm Connection

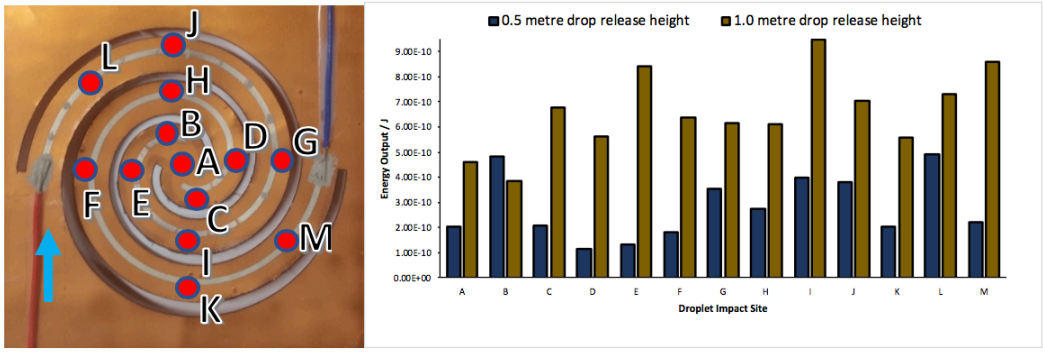

Figure 99 AF = 35 mm, A1 = 6 mm, 1.5 Turns – Output Energy from Red Arm Connection

Graphs displaying the impact location which produced the greatest energy output, and the overall average energy output of all impact locations on each sample, are

shown in Figure 100 and Figure 101. In Figure 100 error bars are used to illustrate the highest to lowest range in energy output from all droplet impacts used to test the samples. Following the identification of impact locations which produced a peak energy output for each sample, the axial stiffness of these locations was measured. It was found that the energy output typically increased with increasing sample impact location stiffness for the range tested, peaking significantly with the peak energy output of the 0.5 turn sample, at impact location B. Additionally, an analysis of the overall average energy output from the samples, covering all energy outputs from all impact locations, further demonstrated that the samples with an overall greater bending stiffness produced a greater output energy.

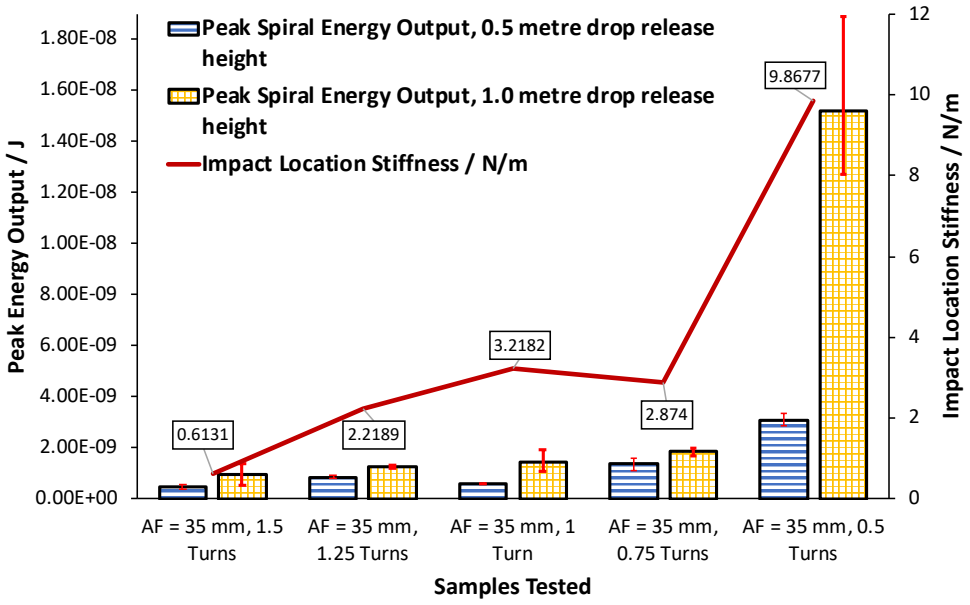

Figure 100 Graph displaying peak energy output from the tested impact locations for all samples

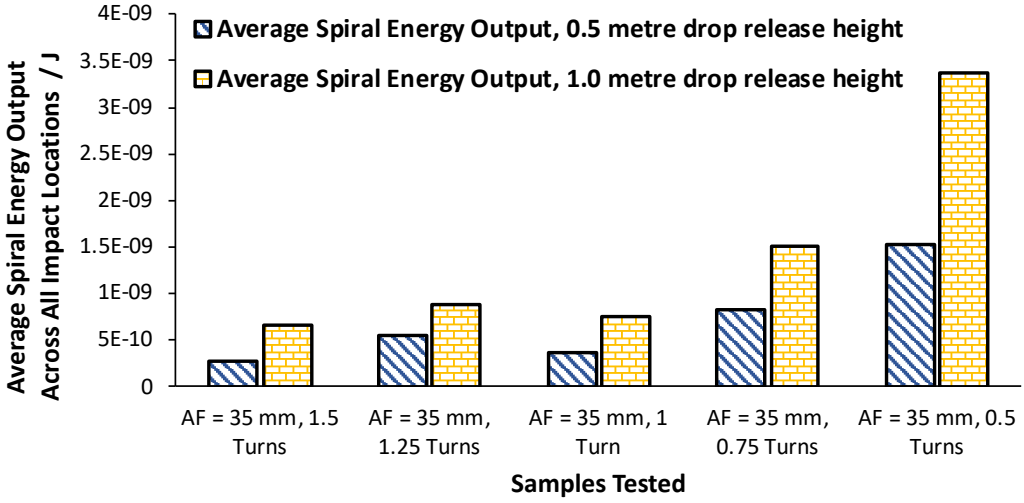

Figure 101 Graph displaying average energy output from all tested impact locations for each sample, giving an overall display of energy output for each sample.

6.3.1 Effect of Droplet Impact Location on Energy Output Result Discussion

The original guiding hypothesis behind these experiments was that a lower stiffness would result in greater energy transfer efficiency, as was found in the testing of cantilever beam energy harvesters demonstrated previously in this research. From simulation and experimental work, in the case of spiral shape transducers it is concluded that the overall bending stiffness of the spiral is reduced as turn number increases. As such, the results appear to demonstrate that the energy output of each spiral actually increases with increasing overall spiral stiffness, although it is unknown to what limit from this result set.

It is concluded that the extent to which the samples resist the impact of the droplet, relating to the bending stiffness and otherwise represented as the mechanical impedance of the sample, affects the energy transfer efficiency through varying the degree to which the piezoelectric layer is placed under stress. For example, the impact voltage vs. time profiles for the AF = 30 mm, 2 turns sample and the AF = 60 mm, 0.5 turns sample are shown in Figure 102 and Figure 103 respectively. The AF = 60 mm sample is significantly stiffer than the AF = 30 mm sample in this case; we observe that the voltage vs. time outputs of each sample undergoing a single droplet impact are considerably different, with the AF = 60 mm sample indicating a much higher voltage output across a shorter time frame.

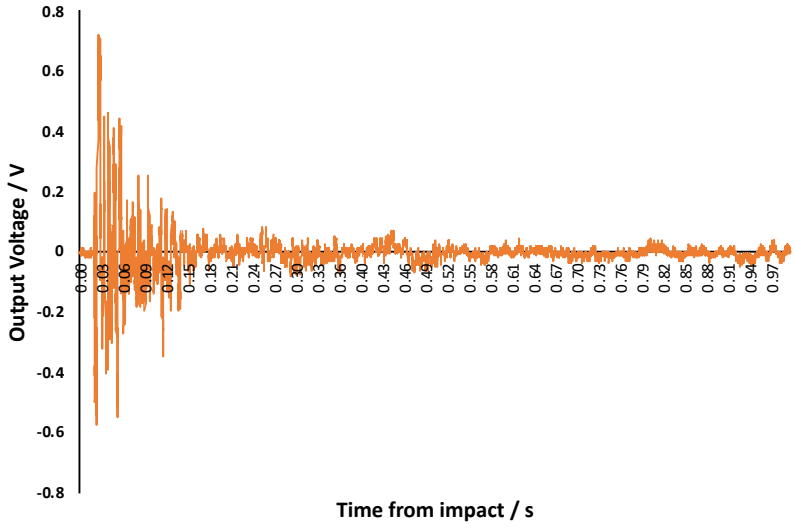

Figure 102 Voltage vs. Time for droplet impact upon impact location A for AF = 30 mm, 2 turns sample

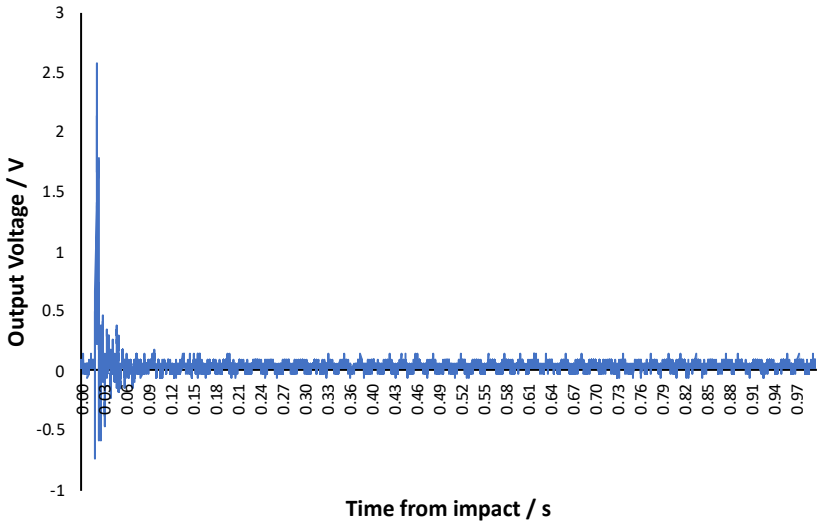

Figure 103 Voltage vs. Time for droplet impact upon impact location F for AF = 60 mm, 0.5 turns sample

Quantitatively, the impact upon the AF = 30 mm, 2 turn sample produced an energy output of 1.4 nJ, compared to 2.6 nJ produced by the AF = 60 mm, 0.5 turn sample. We surmise that the bending stiffness of the AF = 60 mm sample was better matched to the impact force of the droplet than the AF = 30 mm sample, resulting in increased stressing of the piezoelectric layer and thus greater energy output.

However, it is also proposed that considering the mechanical impedance matching of the sample in isolation is insufficient for obtaining ideal energy transfer efficiency. It is proposed that achieving high energy output from droplet impact using spiral shaped transducers is also influenced by factors such as:

- **Spiral Arm Thickness** – If two extreme sample cases are considered, 0.5 and 1.5 turns, illustrated in Figure 104, it is shown that the 0.5 turn sample provides a greater area for initial droplet impact energy transfer to take place. Given that the surface is coated in superhydrophobic coating, droplets are very likely to slide off the surface shortly after impact, particularly given a droplet's tendency to spread during impact, as shown in Figure 105– if the spiral arm width is comparable to the droplet diameter, the likelihood of droplets sliding off the arm during impact is increased, particularly if the initial droplet impact location was not precisely aimed onto the centre of the spiral arm. This will undoubtedly affect the useful energy transferred by the impacting droplet.

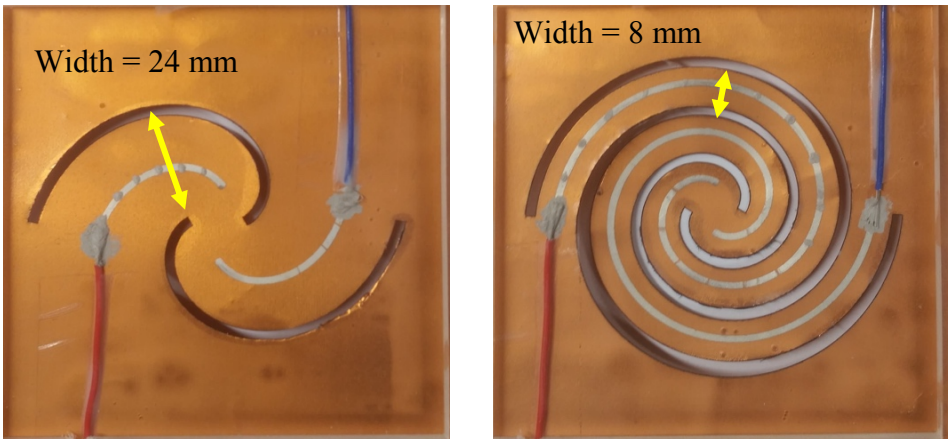

Figure 104 Comparison of arm width in regard to energy transfer for AF = 35 mm samples – (left) 0.5 turn sample, (right) 1.5 turn sample

Figure 105 Reprinted from [49]*, image illustrating droplet spreading on impact*

- **Geometry Strain Distribution** – With changing spiral final radius, initial radius and turn number, the strain distribution of each sample will differ. As such, this will have an effect on the level of induced strain in the piezoelectric material connected by electrodes, influencing the energy output. Furthermore, strain distribution influences the active area size of the top electrode used, in order to avoid charge cancellation through opposing bending regimes. As such, samples with long arms, such as the AF = 35 mm, 1.5 turns sample, may experience charge cancellation and require shorter electrode lengths than possible, whereas shorter, stiffer armed samples such as the AF = 35 mm, 0.5 turns sample may experience a uniform bending regime across a greater sample area. To illustrate this from Figure 93 and Figure 94 it was shown that, despite samples like the AF = 60 mm, 0.5 turns sample producing the greatest peak energy output, the overall energy output from the same sample set was produced by the AF = 30 mm, 1 turn sample.

6.4 Variation of "Gap" Parameter Testing

Simulation results and previous experimental testing in section 4.3 - 4.3.2 has reliably demonstrated that decreasing the spiral arm width results in a decrease of axial stiffness, with little effect on other parameters such as the spiral resonant frequency. In light of this, further experiments were carried out to explore the effect of axial stiffness on energy transfer efficiency.

Samples with 0.5 and 1.0 turn numbers, prepared in the same method as previously outlined, were selected for testing following previous experimental evidence of greater energy output for such dimensions. 5 mm diameter droplets were dispensed onto the spiral centre, with the average energy output recorded, before the spiral arm widths were progressively trimmed using a laser cutter, as illustrated in Figure 106.

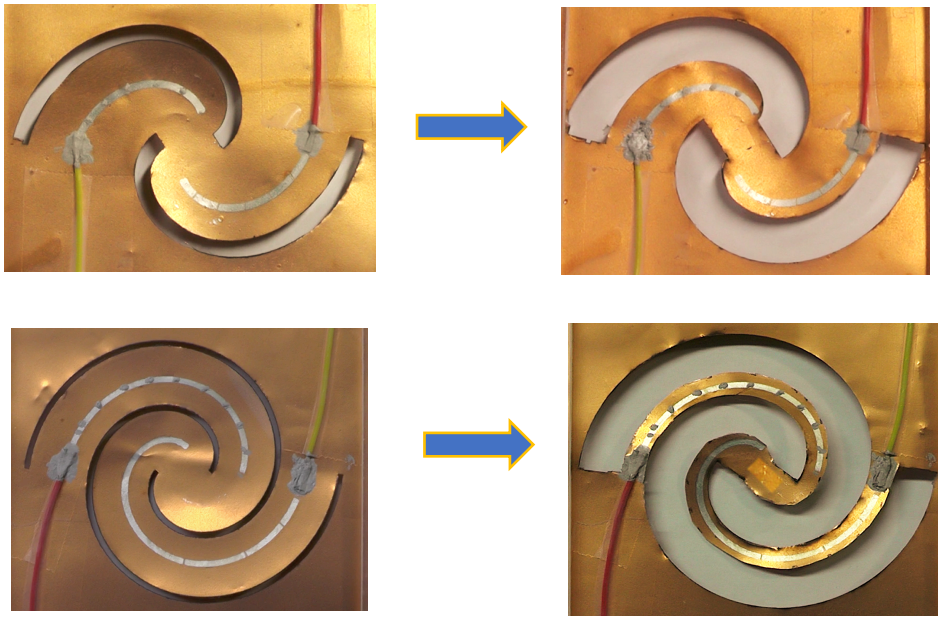

Figure 106 Photograph to illustrate sample trimming process, AF = 35 mm, 0.5 turns (top) and AF = 35 mm, 1.0 turns (bottom). The 0.5 turn sample had an active electrode length of 35 mm, width 15 mm and thickness 200 nm, with an electrically impedance matched load of 8 MΩ. The 1.0 turn sample had an active electrode length of 59 mm, width 15 mm and thickness 200 nm, with an electrically impedance matched load of 7 MΩ.

Simulation results depicting the influence of Gap width on spiral axial stiffness for 0.5 and 1.0 turn samples are displayed in Figure 107 and Figure 108, with experimental testing results displayed in Figure 109 and Figure 110

The 0.5 turn sample's initial resonant frequency, 28 Hz, varied from 26-30 Hz, whilst the 1.0 turn sample's initial resonant frequency, 13 Hz, varied from 12-14 Hz, supporting the theory that variation of Gap does not largely influence resonant frequency, despite an approximate 50 % stiffness variation.

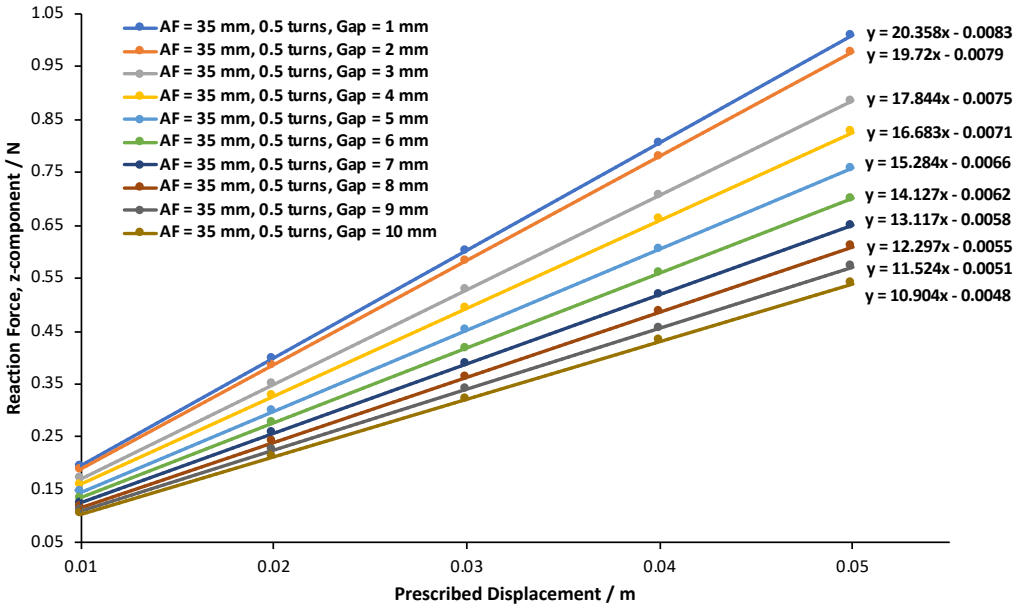

Figure 107 Influence of Gap distance on spiral stiffness for AF = 35 mm, 0.5 turn sample. The line equation for each Gap state is provided to illustrate spiral stiffness variation.

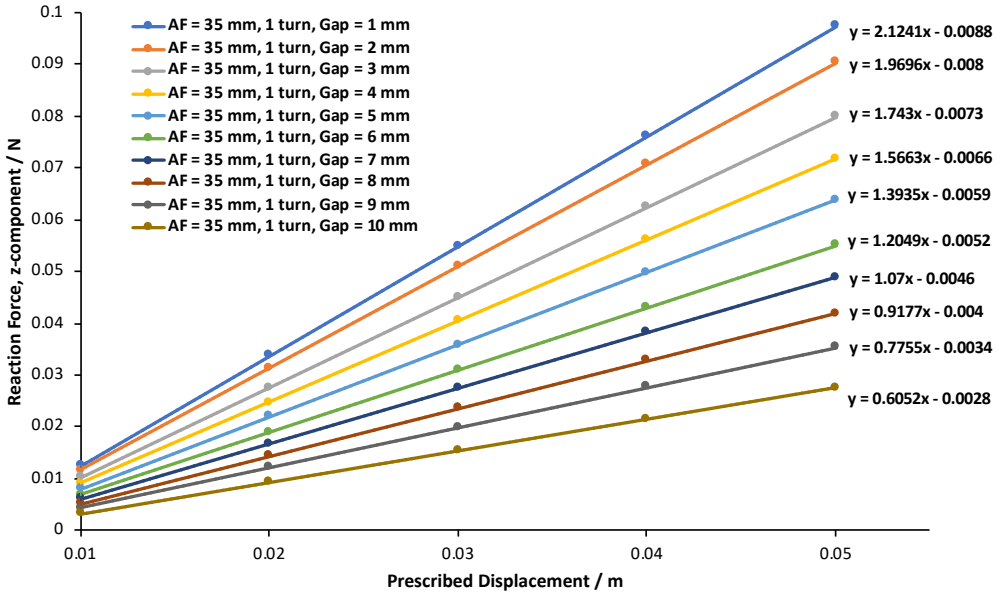

Figure 108 Influence of Gap distance on spiral stiffness for AF = 35 mm, 1 turn sample. The line equation for each Gap state is provided to illustrate spiral stiffness variation.

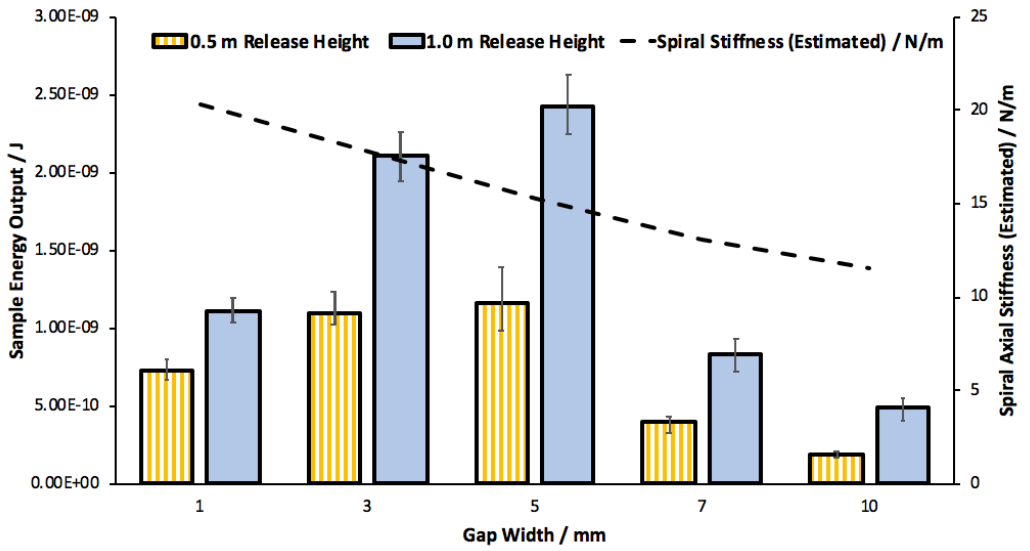

Figure 109 Result of progressive arm width trim testing for AF = 35 mm, 0.5 turn sample. Due to sample stiffness, it was not possible to physically test the axial stiffness without damaging the contact electrodes – as such, the simulated stiffness is illustrated here. Error bars illustrate the difference between highest and lowest energy output for each arm width tested. Each gap width configuration was tested with at least 8 droplet impact repetitions, the average energy is displayed here.

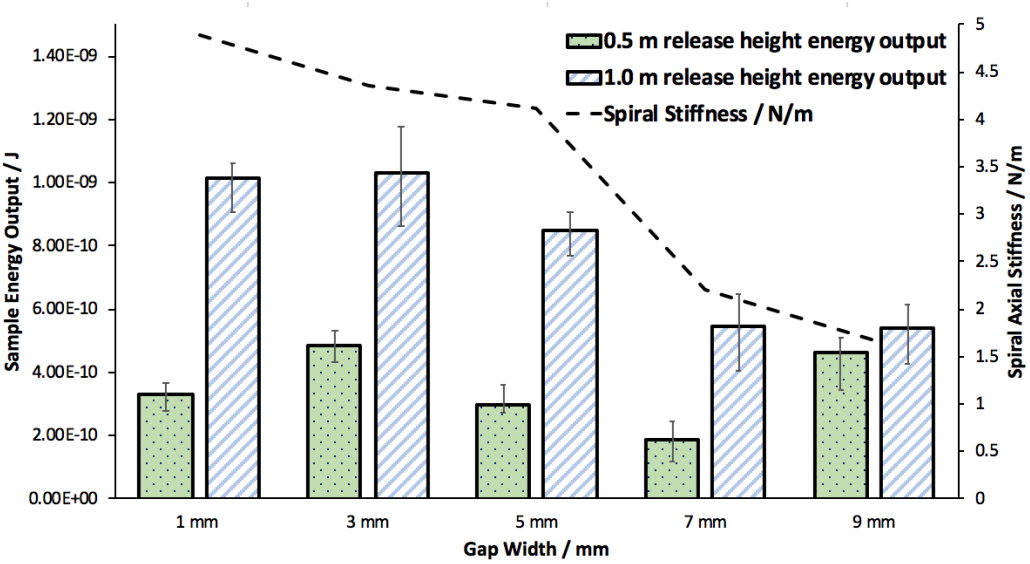

Figure 110 Result of progressive arm width trim testing for AF = 35 mm, 1.0 turn sample. Error bars illustrate the difference between highest and lowest energy output for each arm width tested. Each gap width configuration was tested with at least 8 droplet impact repetitions, the average energy is displayed here.

6.5 Fixed-Fixed Beam Comparison Testing

Following the spiral sample results, it was felt necessary to compare the results of the AF = 35 mm spiral transducers to equivalent fixed-fixed cantilever beams, given their geometrical similarity. The effective length of the spiral sample was measured, as illustrated in Figure 111, in addition to arm width in order to fabricate equivalent fixed-fixed beam samples for comparison. A selection of beams were fabricated from the same deposited P(VDF-TrFE) on copper sheeting used in the

production of the spiral samples, ensuring experimental reliability. Due to raw material dimensions constraints it wasn't possible to produce a 1/1.5 turn spiral sample equivalent, so a shorter 0.25 turn spiral sample equivalent was fabricated.

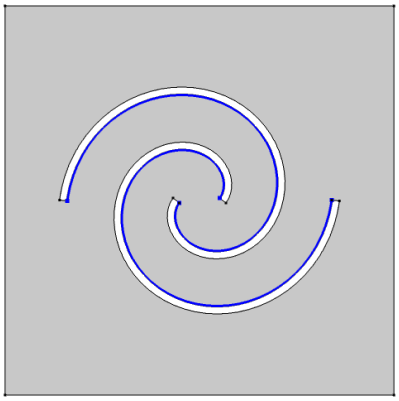

Figure 111 Image illustrating the effective length for the 1 turn spiral sample. In this example, the equivalent fixed-fixed beam length is approximately 251.84 mm, with arm width measured as 14 mm.

Sample electrode dimensions were kept consistent with the dimensions used for the equivalent spiral samples, although each sample was electrically impedance matched. Relevant parameters for the fabricated fixed-fixed beams are displayed in Table 18. After impedance matching, the samples were encapsulated in superhydrophobic surface coating, before 5 mm droplets were impacted upon the surface in an identical testing set-up to the previous spiral optimal impact location testing.

Figure 112 Photograph of AF = 35 mm spiral equivalent length fixed-fixed beams. Beams represent spiral arm width and length in a straight, fixed-fixed beam format. From left to right, fixed-fixed beam equivalent of a 0.25, 0.5, 0.75 and 1 turn samples

Table 18 Fixed-fixed beam sample parameters

Fixed-Fixed Beam Spiral Sample Equivalent	Fixed-Fixed Beam Length and Width / mm	Active Electrode Area (L/W/T)	Resonant Frequency / Hz	Electrically Impedance Matched Load / MΩ
AF = 35 mm, 0.25 Turns	Length = 83.9 Width = 24	37.5 mm / 1.5 mm / 200 nm	50	3
AF = 35 mm, 0.5 Turns	Length = 135.55 Width = 24	37.5 mm / 1.5 mm / 200 nm	38	3
AF = 35 mm, 0.75 Turns	Length = 192.75 Width = 16	27.5 mm/ 1.5 mm / 200 nm	22	3
AF = 35 mm, 1.0 Turns	Length = 251.84 Width = 12	14 mm/ 1.5 mm / 200 nm	25	5

The impact locations and energy outputs for each beam are illustrated in Figure 113, Figure 114 and Figure 115 and 122! with a summary of results depicted in Table 19.

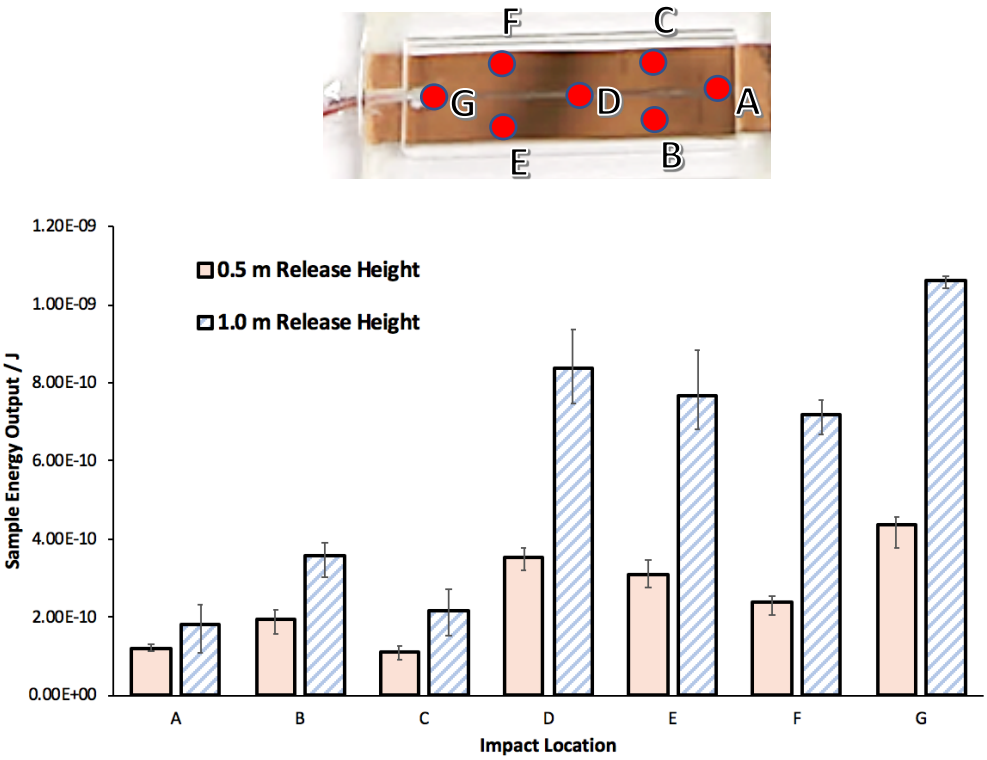

Figure 113 0.25 turn equivalent fixed-fixed beam energy output depending on droplet impact location, illustrated in upper image

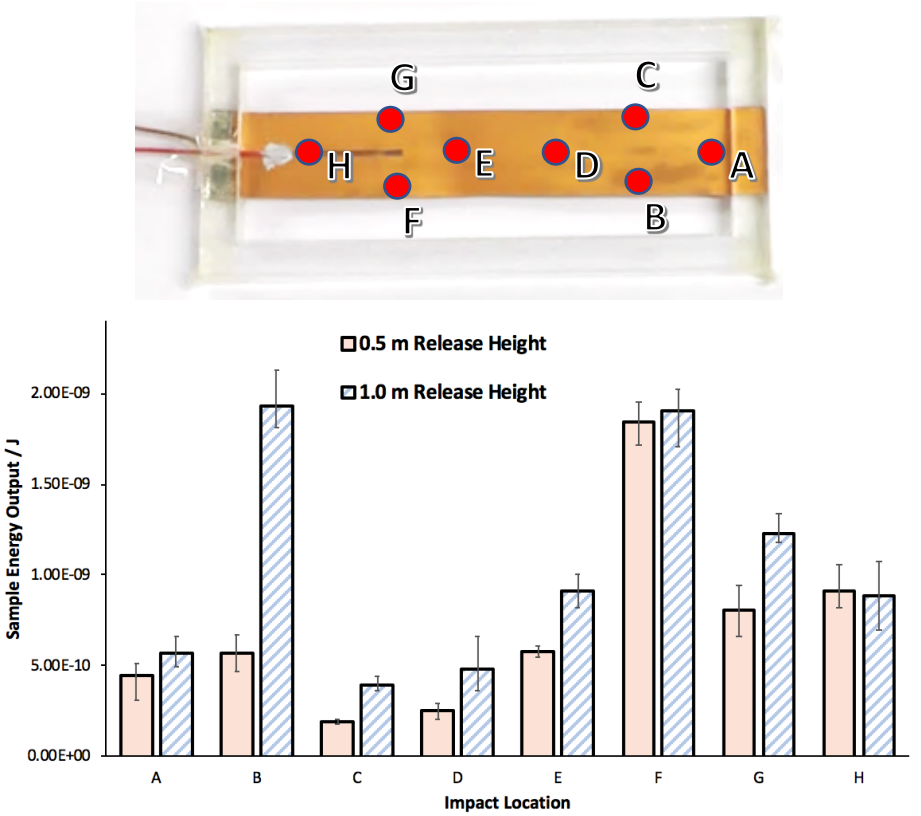

Figure 114 0.5 turn equivalent fixed-fixed beam energy output depending on droplet impact location, illustrated in upper image

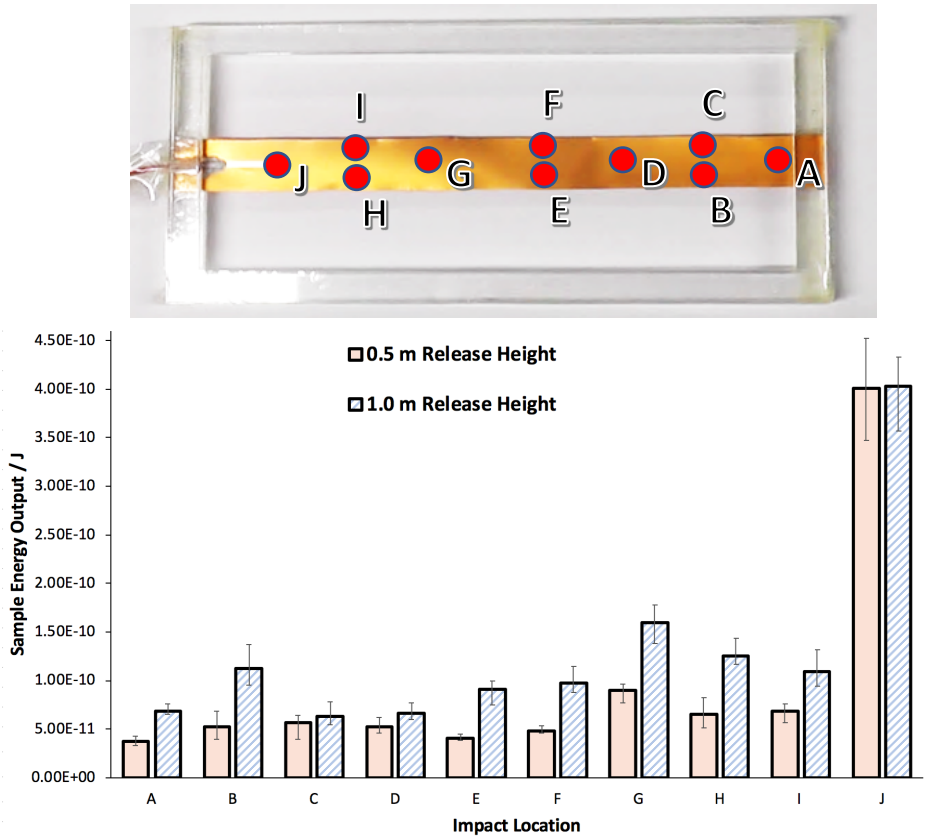

Figure 115 0.75 turn equivalent fixed-fixed beam energy output depending on droplet impact location, illustrated in upper image

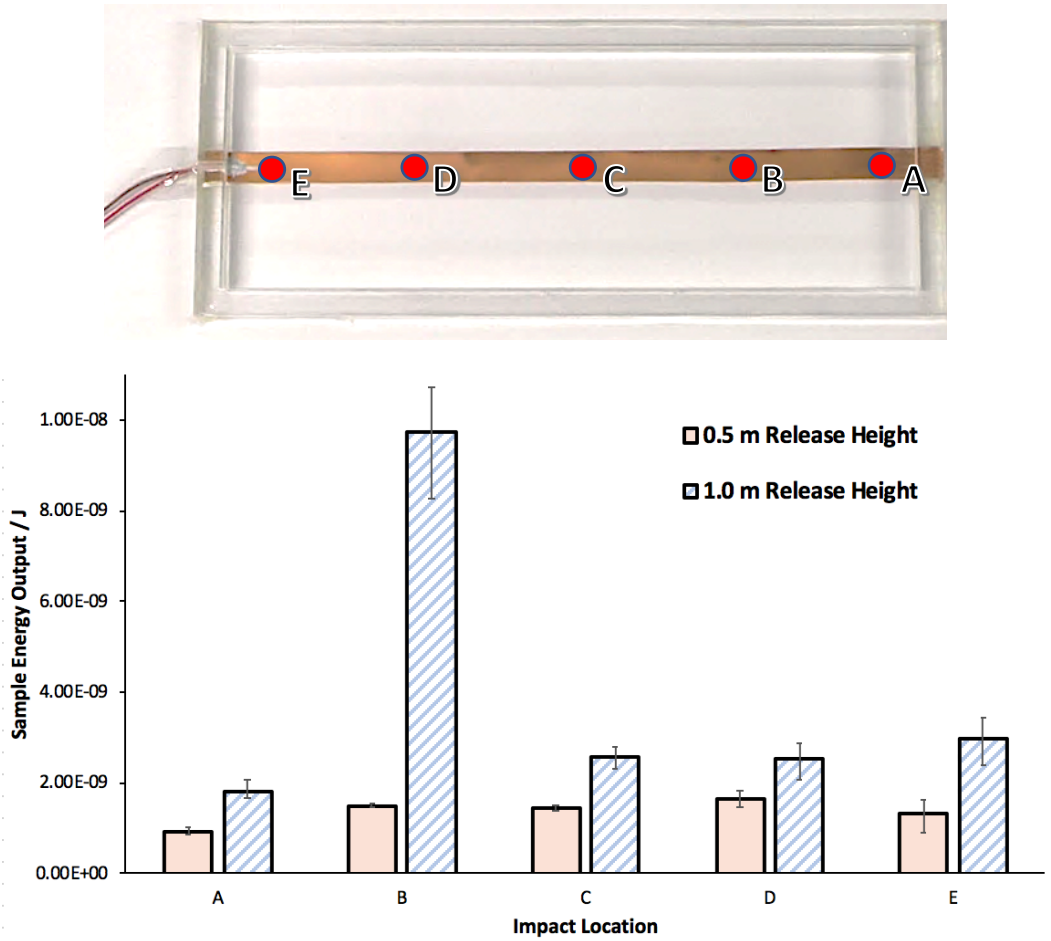

Figure 116 1.0 turn equivalent fixed-fixed beam energy output depending on droplet impact location, illustrated in upper image

Table 19 Results of fixed-fixed beam experimental testing

Fixed-Fixed Beam Spiral Sample Equivalent	Peak energy output 0.5 m droplet release height and location	Peak energy output 1.0 m droplet release height and location	Overall average energy output 0.5 m droplet release height	Overall average energy output 1.0 m droplet release height
0.25 Turns	0.44 nJ, location G	1.06 nJ, location G	0.25 nJ	0.59 nJ
0.5 Turns	1.8 nJ, location F	1.9 nJ, location B	0.7 nJ	1.0 nJ
0.75 Turns	0.4 nJ, location J	0.4 nJ, location J	0.06 nJ	0.1 nJ
1.0 Turns	1.63 nJ, location D	9.8 nJ, location B	1.36 nJ	3.93 nJ

The results indicate that the energy output from a fixed-fixed beam is typically less than that of their spiral equivalents. For example, the peak energy output of the 0.5 turn equivalent fixed-fixed beam was 1.8 nJ with a droplet release height of 0.5 m and 1.9 nJ with a droplet release height of 1.0 m. Conversely, the AF = 35 mm, 0.5 turn spiral sample produced 3.1 nJ with a droplet release height of 0.5 m and 15.2 nJ with a droplet release height of 1.0 m.

However, the energy output achieved by the 1.0 turns equivalent beam is superior to its spiral equivalent, with a peak energy output of 9.8 nJ achieved with a droplet

release height of 1.0m, compared to the AF = 35 mm, 1 turn sample peak energy output of 1.4 nJ with the same droplet release height. Whilst this impact energy is promising, it is important to note that depending on the desired application it may be unpractical to implement such a fixed-fixed beam transducer, given its length of 251.84 mm. In general, it was noted that the fixed-fixed beam equivalents have higher first order resonant frequencies than their spiral sample counterparts, and are also significantly stiffer. It is proposed that fixed-fixed beams experience coupled axial-torsional bending stress to a lesser extent due to their design, resulting in lesser straining of the piezoelectric P(VDF-TrFE) layer.

To conclude this chapter, the fabrication process required to produce double-armed spiral energy harvesters is outlined. The importance of droplet impact location is shown, with specific, localised regions of each harvester producing a peak energy output upon impact depending on the spiral design. These results emphasise the attractiveness of controlling the droplet impact location in terms of energy transfer efficiency.

It is additionally demonstrated how the energy output is not only reliant on the stiffness of the spiral, but upon the geometry also. This result is obtained through analysis of each spiral's peak energy output, compared to the average energy output calculated from a series of droplet impacts across each design.

Finally, an experimental comparison of spiral transducers to their fixed-fixed beam equivalents (in terms of "untwisted" length and width) illustrates how the spiral design encourages higher energy output through promoting both an axial and torsional bending regime under impact. Furthermore, fixed-fixed beams tend to be stiffer, and as a result have higher resonant frequency.

7 Tiered Droplet Impact Control System

"Start with the end in mind."

— Stephen R. Covey

Attempting to harvest rain droplet impact energy through direct exposure of harvesting transducers is an inefficient process. Is this chapter, the design and testing of a tiered system to control droplet diameter, impact frequency and location is presented.

Random impacts of incident water droplets will result in an inefficient energy output. Furthermore, in order to protect transducer elements from damage caused by higher impact force droplets driven by external forces such as high winds, it is necessary to increase the transducer durability. However, it is likely that such designs will produce an unacceptable loss of mechanical sensitivity, with the efficiency of harvesting smaller droplet impact energy being significantly reduced.

It is proposed more beneficial to collect incident droplets first, before guiding them to optimal impact locations on the harvesting transducers in order to achieve an energy efficient response. Whilst this compromises the raw kinetic energy available from a droplet travelling at terminal velocity, it is theorised that controlled dispensing of droplets allows for more precise tailoring of the energy harvesting elements. It is possible to control the droplet diameter dispensed from a nozzle by controlling the nozzle aperture diameter. Droplet diameter can be estimated by using the relation shown in Equation 41, where $R_{droplet}$ is the formed droplet radius, $R_{capillary}$ is the radius of the capillary, or syringe tip opening, γ is the water surface tension at the liquid/vapour interface, g is the gravitational constant and ρ is the water density [15].

$$R_{droplet} = \left(\frac{3R_{capillary}\gamma}{2g\rho_{water}}\right)^{\frac{1}{3}}$$

Equation 41

Initial investigations into droplet parameter control focused on how variation of the stream outlet diameter influenced the drip frequency of the formed droplets. An acrylic box was laser cut to have outlets along its bottom, ranging from 1 mm to 6 mm in diameter in 0.5 mm increments. Dyed water was pumped into the acrylic box in order to produce continuous water streams from the outlets. An Infra-Red detector circuit was used to measure the frequency of droplets passing by as the jet transitioned from a continuous stream to dripping. It was found that :

- The frequency of droplets was quite variable at all measurement points along the stream, with the IR detector circuit measuring drip frequency in the region of 80-200 Hz.

- It appeared that the only effect different diameter outlets had was to vary at what distance from the outlet the stream transitioned from a steady jet to drips – the larger the outlet, the further the distance from the outlet hole was required for this transition to occur, illustrated in Figure 118. It is likely that this related to the surface tension of the water; a larger stream will take longer to break-up into droplets, as its cross-section has the largest distance to recede before break-up.

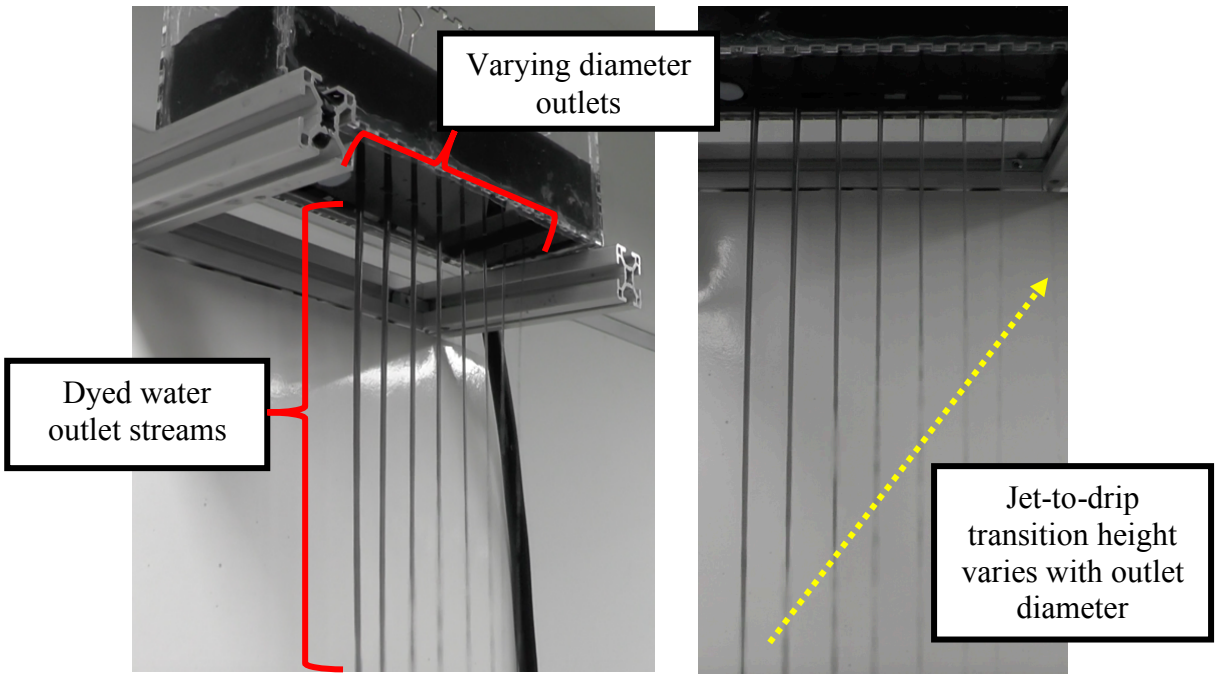

Figure 118 (left) Photograph of acrylic container with varied bottom outlet diameters, (right) photograph to illustrate variation of Jet-to-drip transition state depending on outlet diameter (6.0 mm to 1.0 mm from left to right, only streams from outlet diameters of 1.0 mm to 4.5 mm are displayed in this image as water would otherwise drain too quickly with all outlets open for reasonable observation to take place).

Observing that the drip frequency was both high and uncontrollable when allowed to freely flow from a single outlet, further investigations were carried out in an attempt to devise a method for producing controllable, lower drip frequency droplets.

It was found that when the box was allowed to run dry, eventually the water level resembled a thin film across the bottom floor of the box. At this point, drips formed directly at the outlets and fell with significantly lower frequency than observed previously (<10 Hz). In light of this, a droplet dispensing system comprised of two stacked acrylic tanks was fabricated and is illustrated in Figure 119. This consisted of an upper storage stage, which dispensed 1 litre of water through an array of 1 mm diameter outlets laser cut into its base. Beneath this tank is a lower stage with a single 6 mm diameter outlet laser cut into its base.

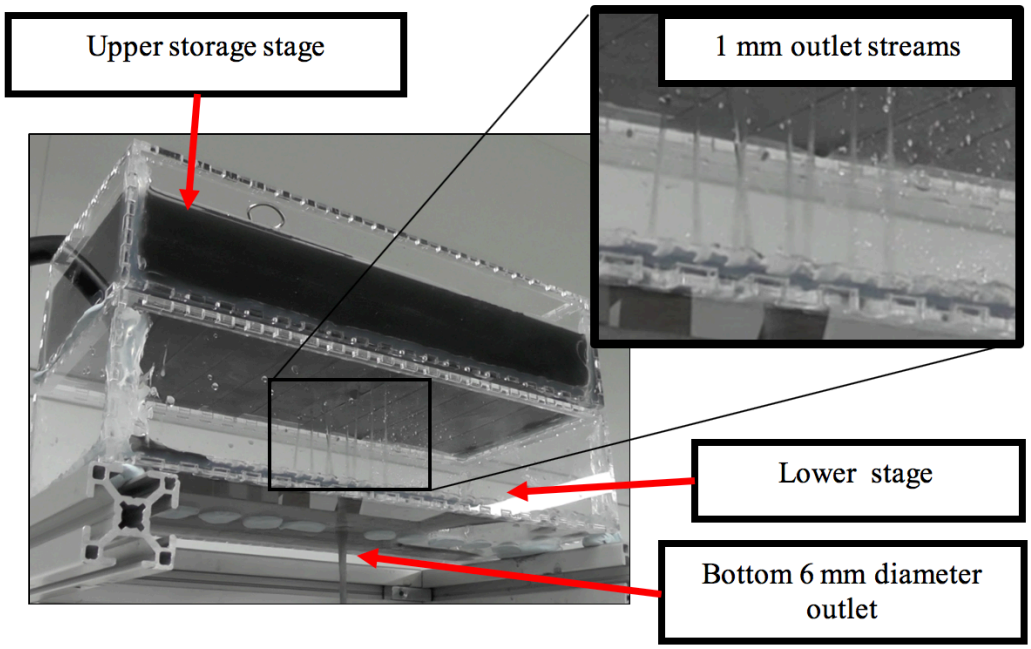

Figure 119 Tiered tank stages to control droplet formation and impact frequency. The tank liquid is de-ionised water dyed with black food colouring.

This encouraged droplets to form and fall from the 6 mm outlet with predictable frequency, providing an opportunity to increase energy transfer efficiency through matching the resonant frequencies of the samples being driven by the droplet stream. Additionally, it was found that modifying the ratio of open upper stage 1 mm diameter outlets to the lower stage 6 mm diameter outlet controlled the volume flow of the droplets, altering both the drip frequency and time scale with which the stored water was dispensed, illustrated in Figure 120. The scenario where no upper

stage is used, whereby the water is added directly to the lower stage, is given for comparison. It is proposed that the frequency decreased over time for each outlet ratio tested as the water level in the upper stage decreased, resulting in a decrease of pressure, which lowered the 1 mm outlet stream flow rate.

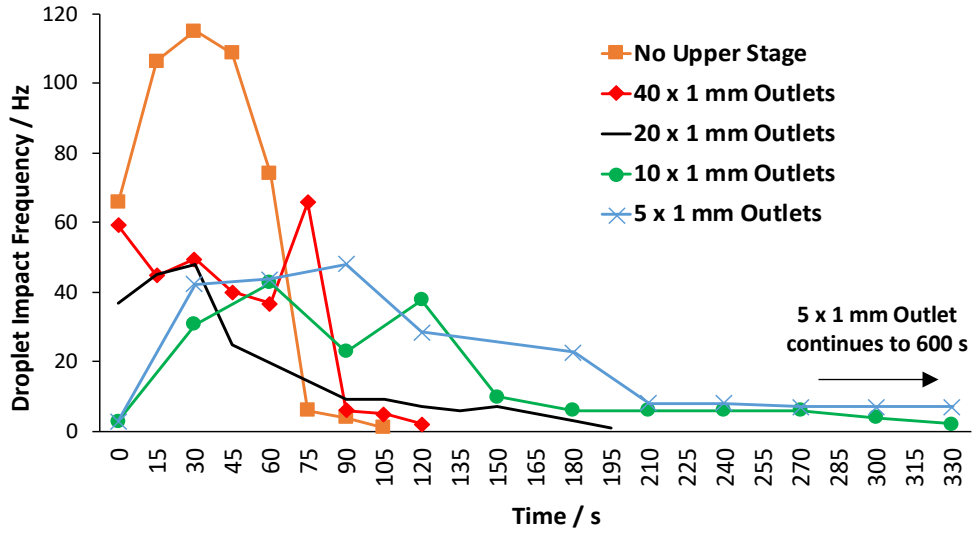

Figure 120 Tiered system drip frequency rates for AF = 60 mm, 0.5 turns sample depending on number of open upper stage 1 mm outlet

The samples fabricated previously were orientated beneath the 6 mm outlet so that the droplets impacted upon locations shown to produce the largest energy output from previous testing. It was found that, at a position of 1.0 m below the 6 mm outlet, the AF = 60 mm, 0.5 turns sample produced the greatest power output for the ratios of open upper 1 mm diameter outlets tested, with the power output over time displayed in Figure 121.

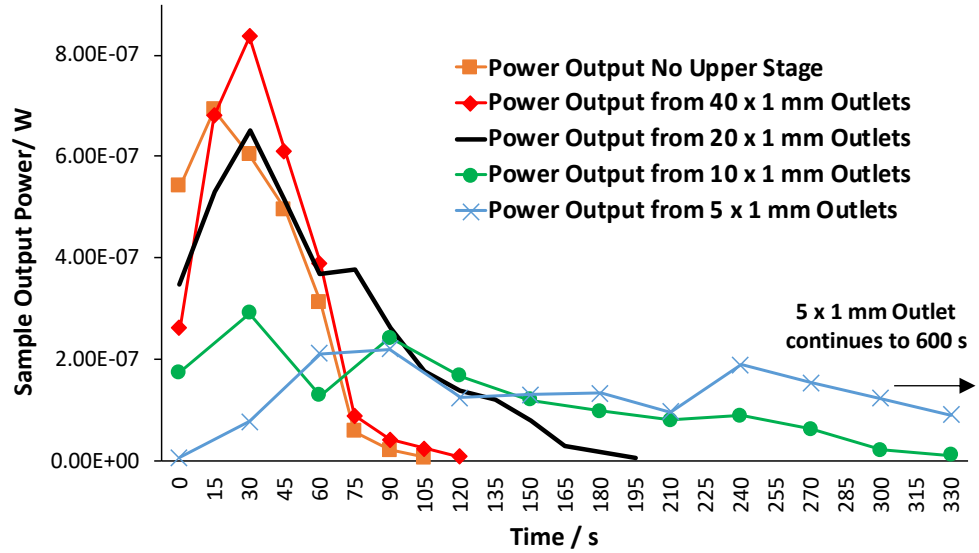

Figure 121 Power output for the AF = 60 mm, 0.5 turns sample driven with a variety of different upper stage outlets open at a position of 1.0 m beneath the lower 6 mm outlet. Sample power output is derived from voltage signal traces captured at regular time intervals.

The AF = 60 mm, 0.5 turns sample achieved a peak, total accumulated power output of 58.9 μW, relating to a power density of 16 mW/cm^3 considering the piezoelectric material covered by the top surface electrode. The accumulated output power generated for 1 litre of water dispensed as droplets upon the AF = 60 mm, 0.5 turns sample from heights of 0.3 and 1.0 m for each 1 mm outlet ratio tested is given in Table 20. The dimensions of the AF = 60 mm, 0.5 turn sample, illustrated in Figure 122, are likely larger than typical rain gutter down spout dimensions. However, it is assumed that a typical two-storey building with downspout gutter length of 5.7 m [173] could contain a system of 13 stacked stages, which accounts for the 0.12 mm two stage system and 0.3 m droplet fall height between the bottom stage system outlet and the sample. Based upon the power output results achieved here, if a tiered tank configuration of 20 × 1 mm outlets was used, such a system could produce a total output power of 0.33 mW for every litre of water which drains through the system, considering the output from one spiral arm only.

We compare this energy output to theoretical estimates regarding the gravitational potential energy of a litre of water positioned at 5.7 m above the ground, which equates to approximately 55.9 J, or 55.9 W of instantaneous power if it is assumed that this body of water takes 1 second to descend to the ground. This estimate outlines the efficiency of the stacked droplet energy harvesting system as 0.00001 %, highlighting the clear opportunities for energy transfer efficiency improvement in future work through development of transducer mechanical, chemical and power management aspects.

It is important to note that the electrode dimensions used, illustrated in Figure 122, are significantly thinner than the spiral arm width (for consistency between samples with varying arm widths, as outlined previously). As such, a straight forward method of increasing energy transfer efficiency would be to increase the electrode width to that of the spiral arm, which could potentially result in a 10-20x improvement with minimal transducer modification.

Table 20 Sample output power depending on tiered tank upper to lower outlet ratio

Outlet Ratio	Total Output Power From One Sample Arm, Generated From 1 Litre of Water Dispensed as Droplets from a height of 0.3 m / µW	Total Output Power From One Sample Arm, Generated From 1 Litre of Water Dispensed as Droplets from a height of 1.0 m / µW
No Upper Stage	6.3	36.9
40 x 1 mm Outlets	15.4	42.2
20 x 1 mm Outlets	25.4	51.7
10 x 1 mm Outlets	21.5	42.1
5 x 1 mm Outlets	17.1	58.9

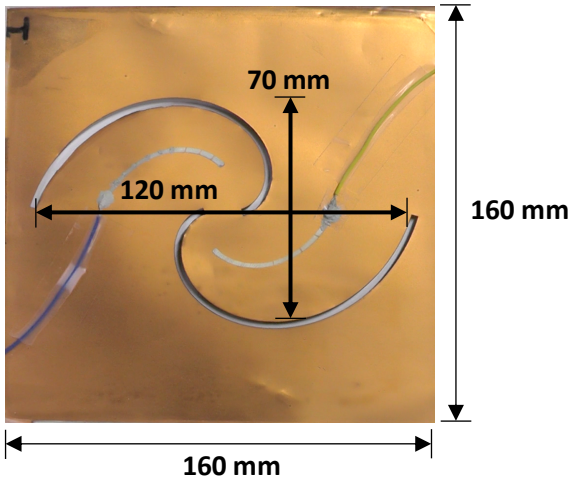

Figure 122 Dimensions of AF = 60 mm, 0.5 turns sample illustrated

To conclude, it is demonstrated how dispensing a water volume in the form of a controlled droplet stream can result in greater energy transfer efficiency. This is shown by evaluating the case where no upper stage is used, meaning that the water volume is dispensed through a single outlet at the bottom of the tank, in comparison to using a two tiered system with varying ratios of outlet diameters. A peak, total accumulated power output of 58.9 µW is achieved from one arm of the AF = 60 mm, 0.5 turns sample, using of ratio of 5 x 1 mm diameter outlets compared to one single 6 mm diameter outlet. This relates to an approximate 63 % increase in total accumulated power compared to when no upper stage is used.

8 Conclusion

8.1 Achievement Summary of Research Work

A summary of the novel research outcomes achieved in this work are presented here.

An initial investigation took place to determine which mechanical parameters have significant influence on the resulting energy output for impact energy harvesters. Piezoelectric cantilever beams consisting of P(VDF-TrFE) solution deposited via micrometre adjustable film applicator onto stainless steel foil were prepared. Using these transducers, it was demonstrated how bending stiffness and resonant frequency have a notable influence on the energy transfer efficiency, through variation of the cantilever beam width in isolation. A peak energy output of 28 nJ was achieved when the transducer bending stiffness was within the range of 0.067 to 0.134 N/m, generated from the impact of a 5.5 mm diameter droplet at the beam end.

Although this energy output represents a theoretical energy transfer efficiency of approximately 0.0013%, it is important to consider that the electrode area was constrained in order to retain experimental consistency across the sample set. Furthermore, a comparison of transducer energy densities highlights the benefits of mechanical tailoring to the excitation source. Results from previously published literature [75], which utilised commercially available piezoelectric sensors for impact energy harvesting, indicate an energy density of 0.092 J/m^3. In comparison, the peak energy output of 28 nJ achieved in this work represents an energy density of 15.9 J/m^3.

As such, whilst the peak energy output achieved in this research is not the highest possible, it demonstrates significant energy transfer efficiency for the active electrode areas used. It is proposed that the energy density of the commercial sensors typically utilised in other studies is notably lower due to the relatively stiff Mylar coating used to encapsulate the sample. This further supports the claim that appropriate tailoring of transducer bending stiffness significantly affects energy transfer efficiency.

The results of the piezoelectric cantilever beam testing also validated that energy output was increased when the beam resonant frequency was close to/at the droplet impact frequency. Whilst this result appears to be intuitive, it has been reliably demonstrated that droplet-surface interactions are not trivial, being proposed elsewhere that energy transfer efficiency is more dependent on the relation between the beam resonant frequency and the natural vibration frequency of the impacting droplet.

However, it has been reliably demonstrated that cantilever beam geometries are not the most efficient design for energy harvesting. With the key mechanical parameters dictating energy transfer efficiency outlined for cantilever beams, an attempt to extrapolate these guiding principles to superior geometries for energy harvesting was conducted. An extensive simulation investigation utilising COMSOL multiphysics was carried out to explore the stress distributions of over 525 different potential transducer geometries. On comparison of the induced stress produced in each geometry under a pulse loading regime, spiral shape geometry configurations appeared to demonstrate a significant induced stress throughout their volume, prompting further investigation.

Research into spiral shape geometries identified that such configurations exhibited favourable mechanical behaviours for droplet impact energy harvesting, such as low bending stiffness and low resonant frequencies. Double-armed spiral geometries in particular presented a balanced, self-supporting structure with multiple degrees of freedom, encouraging high sensitivity to droplet impact.

Additionally, it was found that spiral designs are inherently adaptable, providing the opportunity for mechanical properties to be tuned according to the excitation source without need for additional surface area. For example, increasing the number of spiral turns whilst keeping the final radius constant lowers the spirals resonant frequency, allowing for precise tailoring to an excitation source within a confined area.

A variety of spirals with different final radius, initial radius and turn number were selected for fabrication. P(VDF-TrFE) solution was deposited via micrometre

adjustable film applicator onto copper foil, before being laser cut into the desired geometry. Whilst spiral designs have been previously demonstrated in the literature as antennas, research has yet to investigate the usage of such designs for impact energy harvesting. It was found that spiral designs with greater bending stiffness, demonstrated here in the form of 0.5 turn samples with localised bending stiffness in the range 7.8 – 9.9 N/m, produced the highest peak energy outputs. However, on consideration of the overall average energy output measured from impacts across the entire sample upper surface, it was found that designs with lesser bending stiffness, such as the AF = 30 mm, 1 turn sample, could produce a greater energy output on average. This led to the conclusion that it is important to consider a wide range of design aspects in addition to the geometry design, such as spiral arm thickness and the strain distribution throughout the geometry, in order to fabricate samples with optimal impact energy transfer efficiency.

Furthermore, an investigation that compared spiral designs (which are in essence curved fixed-fixed beams) to equivalent fixed-fixed straight beam transducer designs found that the spiral designs had lower resonant frequency and typically produced greater energy output. It is proposed that the curvature of the spiral design encourages both axial and torsional bending stresses to occur throughout the piezoelectric layer, resulting in higher voltage output, compared to straight fixed-fixed beams which promote torsional bending stresses to a lesser extent.

Finally, it was concluded that attempting to harvest rain droplet impact energy through direct exposure of harvesting transducers is an inefficient process, due to the randomness of droplet impact in terms of both periodicity and impact location. In light of this, a tiered tank system was developed which passively controls the diameter, impact frequency and impact location of dispensed droplets from a stored water volume. It was found that the controlled dispensing of a stored litre of water could significantly affect the total energy output achievable by the spiral transducers; a total peak output power of 58.9 μW was achieved by a single spiral transducer arm driven by 1 litre of water dispensed as droplets, relating to a power density of 16 mW/cm^3.

This power output demonstrates how an array of stacked harvesters could produce a theoretical output power of 0.33 mW for every litre of water which descends

through the guttering of a two storey building (estimated 5.7 m vertical height). With a suitable energy accumulation and management system, it is feasible to use this for powering applications such as low-power sensor systems.

8.2 Future Work

The following areas represent potential directions of future work:

Variable Surface Wettability - It has been demonstrated that wettable droplet energy harvesters generate a greater energy output than non-wettable devices due to increased torque created by droplet cohesion on impact. However, wettable surfaces inevitably become water logged with successive impacts, which introduces significant damping and decreases harvester mechanical sensitivity. It is proposed that an ideal harvester surface would be wettable during the impact event and non-wettable at the conclusion of the impact. The solution to this issue of actively varying the harvester surface wettability may be found in the field of electrowetting theory. The field of electrowetting investigates the variation of surface wettability as a function of an applied electric field. As well as electrically modifying the surface wettability, other methods of electrowetting include magnetic, mechanical, chemical, magnetic and temperature-driven techniques [174]. It has been shown that superhydrophobic surfaces can have their hydrophobicity reduced, even decreased to the point of being hydrophilic, using such techniques. For example, it has been demonstrated that polyamide film with a triangular net-like structure, illustrated in Figure 123, switches between superhydrophobic and superhydrophilic surface wettability when it is bi-axially extended and unloaded [175].

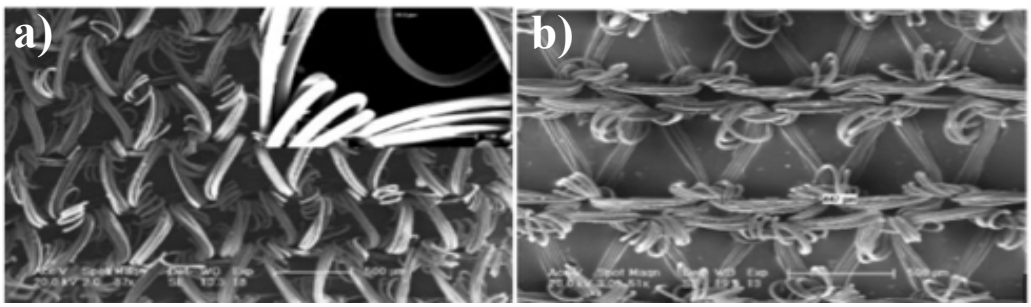

Figure 123 Reprinted and edited from [175] *FESEM images of the triangular net-like structure of the elastic polyamide film. Image a) shows film before biaxial extension in its superhydrophobic state, with the average side length of the triangle approximately 200 mm. The average size of the polyamide elastic fibre is 20 mm. Image b) shows structure of film in its superhydrophilic state, with applied extension ratio of near to 120%. In this case, average side length of the triangle is around 450 mm.*

Care would be required to ensure that the material could return to an unloaded state after the impact event in order to achieve the beneficial superhydrophobic state at rest, with such properties dictated by the restoring force of the cantilever. Such smart surfaces may prove to be a significant contributing asset to the efficiency of a rainfall energy harvester.

Further investigation into tiered droplet control system - The water flow velocity and flow volume from an outlet at the bottom of tank, otherwise known as a base aperture, can be calculated using Equation 42 and Equation 43. Here, v_{outlet} is the outlet velocity, C_v is the velocity coefficient (0.97 for water), g is the acceleration due to gravity, H is the height of the water from the base aperture, V_{flow} is the volume flow, $C_{discharge}$ is the discharge coefficient and $A_{aperture}$ is the area of the bottom aperture. $C_{contraction}$ is the contraction coefficient, which is a measure of the aperture rim sharpness – the coefficient for a sharp edged aperture, obtained through precise manufacturing methods such as laser cutting, is 0.62 [176].

$$v_{outlet} = C_v(2gH)^{1/2}$$

Equation 42

$$V_{flow} = C_{discharge}\, A_{aperture}(2gH)^{1/2}$$

Equation 43

$$C_{discharge} = C_{contraction} C_v$$

Equation 44

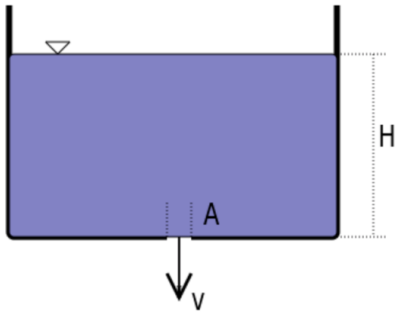

Figure 124 Reprinted [176] *from A tank with base aperture containing water*

As such, the droplet impact frequencies achieved here could likely be adjusted further by varying the height of the upper storage tank. For example, a narrower

tank of the same volume would increase the water pressure above the 1 mm diameter outlets, encouraging a greater water volume flow rate for a longer time period. Further experimental testing is required to find the ideal dimensions of the tiered droplet control system in order to promote the most efficient droplet dispensing system.

Bubble Energy Harvesting: The devices exhibited in this report may have useful applications for harvesting energy from bubble flows; where gravity is the driving force for water droplets falling from the sky, air bubbles rise through a liquid medium driven by buoyancy force. As such, there may be further applications for the technology outlined in this research regarding aquatic environments, for example in applications such as aquarium or aquaponics systems.

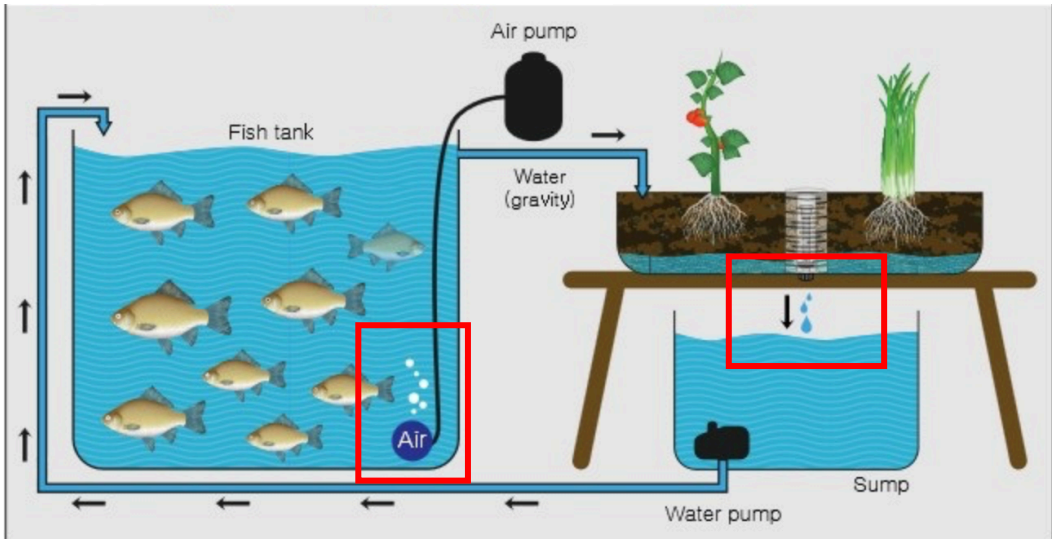

Fig. 125 Reprinted from [177]*, a diagram detailing a basic aquaponic system set-up. Opportunities for implementation of the transducer devices fabricated in this report, to harvest both droplet and air bubble energy, are highlighted with the red squares.*

Appendices

Examples of substrates successfully utilised for deposition of piezoelectric material

Substrate Material /Thickness	Interlayers /Thickness	Piezoelectric Material Deposited	Deposition Method of Piezoelectric Layer	Reference
Aluminium Oxide (Al_2O_3)/ 630μm	• Platinum (Pt)/ 50 nm	$K_{0.5}Na_{0.5}NbO_3$ (KNN)	Modified Sol-Gel / Spin Coating	[111]
Inconel 600 (Nickel based alloy) / 300μm	• Strontium Ruthenate ($SrRuO_3$)/ 50 nm	$K_{0.88}Na_{0.12}NbO_3$ (KNN)	Hydrothermal Method /	[113]
Inconel 600 (Nickel based alloy) / 300μm	• Strontium Ruthenate ($SrRuO_3$)/ 50 nm • Lanthanum Nickel Oxide ($LaNiO_3$)/ 50 nm	$K_{0.88}Na_{0.12}NbO_3$ (KNN)	Hydrothermal Method /	[113]
Glass	N/A	$K_{0.5}Na_{0.5}NbO_3$ (KNN)	Pulsed Laser Deposition	[114]
Magnesium Oxide (MgO)/0.3mm	• Strontium Ruthenate ($SrRuO_3$)/ N/A Platinum (Pt)/ N/A	$K_xNa_{1-x}NbO_3$ (KNN)	RF-Magnetron Sputtering	[116]
Polydimethylsiloxane (PDMS)/1.5mm	• Titanium (Ti) / 30 nm • Nickel (Ni) / 150 nm	P(VDF-TrFE)	Spin Coating	[117]
Silicon (Si)/ 5μm	• Platinum (Pt)/ 220 nm	PZT	Aerosol Deposition	[120]

	• Titanium (Ti)/ 30 nm			
Silicon (Si)/ N/A	• Platinum (Pt)/ 150 nm • Titanium Oxide (TiO_x)/10 nm Silicon Dioxide (SiO_2)/ N/A	$K_{0.48}Na_{0.48}Li_{0.06}NbO_3$ (KLNN)	Chemical Solution Deposition (Spin Coated)	[178]
Silicon (Si)/ 270µm	• Platinum (Pt) / 50 nm • Silicon Dioxide (SiO_2) / 250 nm	$K_{0.5}Na_{0.5}NbO_3$ (KNN)	Modified Sol-Gel / Spin Coating	[111]
Silicon (Si)/ N/A	• Platinum (Pt)/ N/A • Titanium (Ti)/ N/A • Silicon Dioxide (SiO_2)/ N/A	$K_xNa_{1-x}NbO_3$ (KNN)	Sol-Gel Method/ Spin Coating	[179]
Strontium Oxide ($SrTiO_3$) / N/A	• Strontium Ruthenate ($SrRuO_3$)/ N/A	$K_xNa_{1-x}NbO_3$ (KNN)	RF-Magnetron Sputtering	[122]
Strontium Oxide ($SrTiO_3$) / N/A	• Strontium Ruthenate ($SrRuO_3$)/ 200nm	$K_xNa_{1-x}NbO_3$-$LiTaO_3$-$LiSbO_3$ (KNN-LT-LS)	Pulsed Laser Deposition	[180]
Stainless Steel/ 30µm	• Platinum (Pt)/ N/A • Titanium (Ti)/ N/A • Silicon Dioxide (SiO_2)/ N/A	$K_xNa_{1-x}NbO_3$ (KNN)	RF-Magnetron Sputtering	[124]
Stainless Steel/ 20µm	• Platinum (Pt)/ 220nm • Titanium (Ti)/ 30nm	PZT	Aerosol Deposition	[120]

Screenshots of Geometries Tested in COMSOL for ideal stress distribution

For reference, the following screenshots display a selection of the geometries initially tested which led to the further investigation into spiral geometries. The geometries displayed are under stress to illustrate stress distribution, depicted by a colour scale to the right of each diagram :

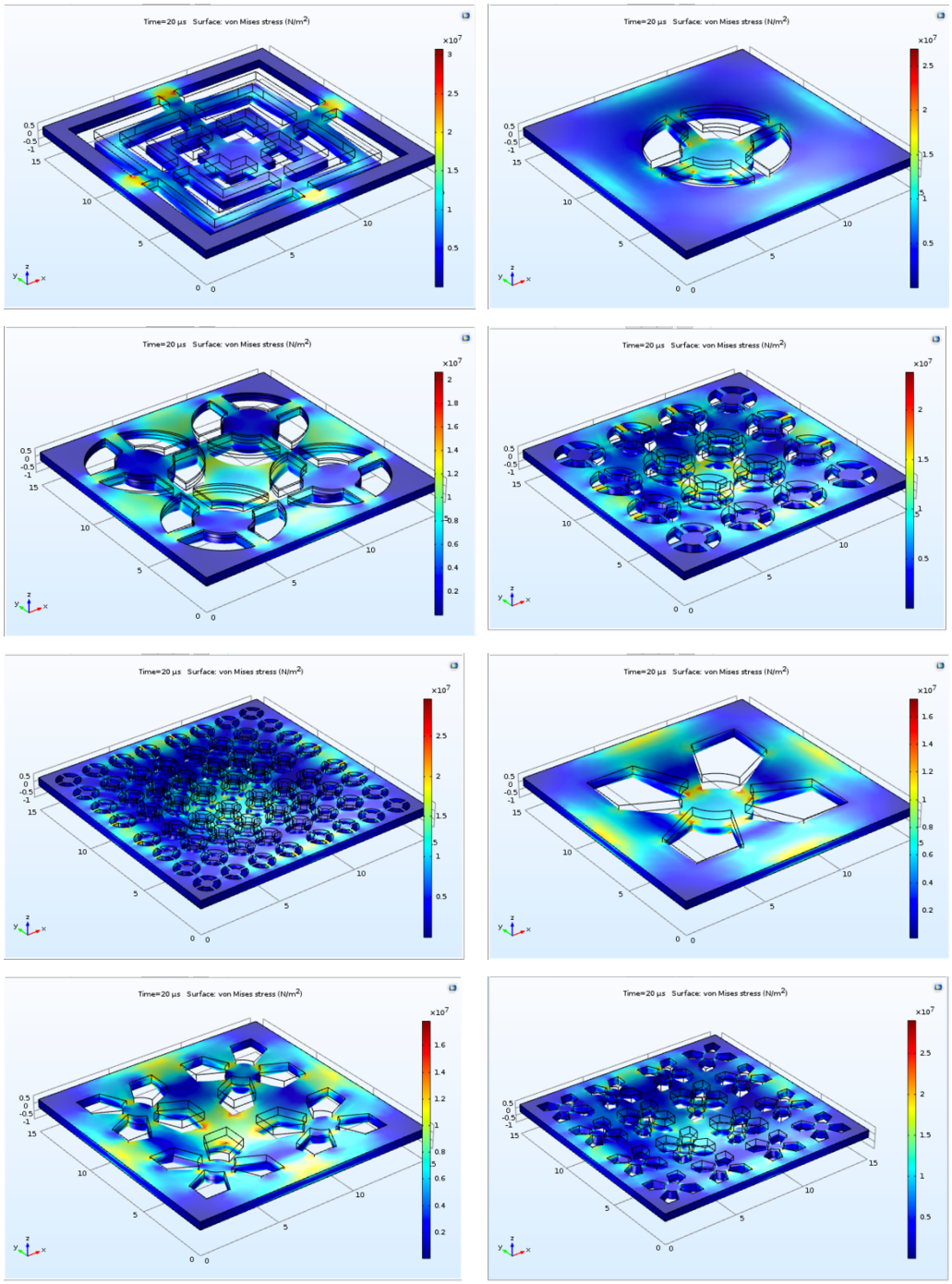

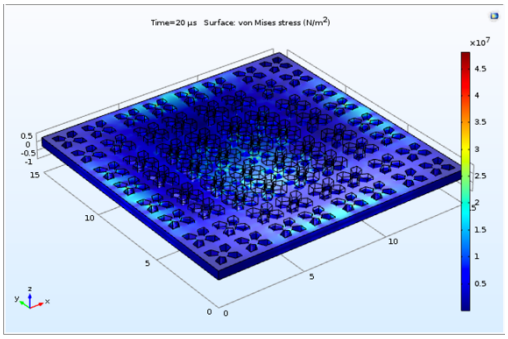
Time=20 µs Surface: von Mises stress (N/m²)
×10⁷
4.5
4
3.5
3
2.5
2
1.5
1
0.5

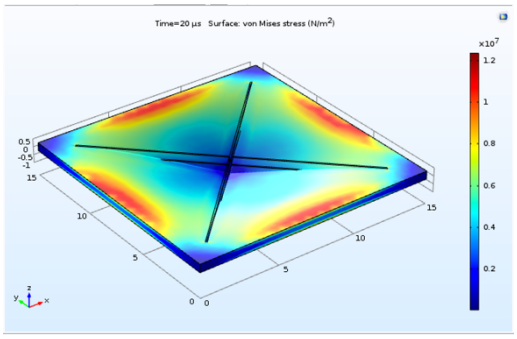
Time=20 µs Surface: von Mises stress (N/m²)
×10⁷
1.2
1
0.8
0.6
0.4
0.2

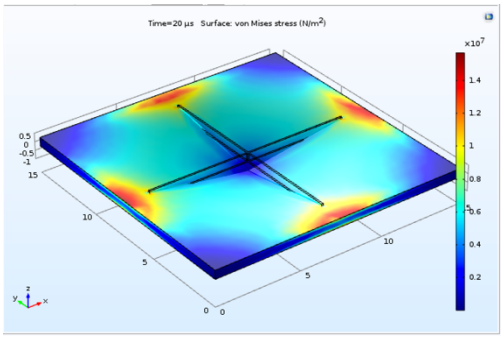
Time=20 µs Surface: von Mises stress (N/m²)
×10⁷
1.4
1.2
1
0.8
0.6
0.4
0.2

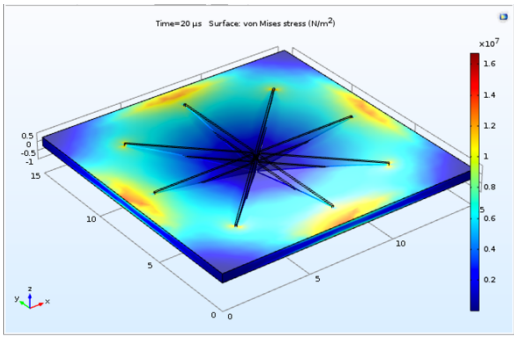
Time=20 µs Surface: von Mises stress (N/m²)
×10⁷
1.6
1.4
1.2
1
0.8
0.6
0.4
0.2

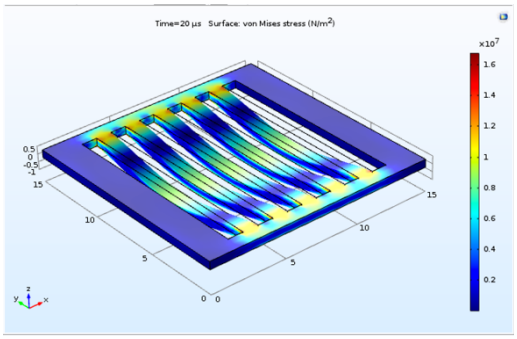
Time=20 µs Surface: von Mises stress (N/m²)
×10⁷
1.6
1.4
1.2
1
0.8
0.6
0.4
0.2

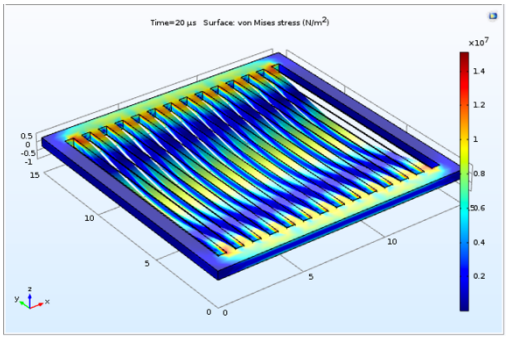
Time=20 µs Surface: von Mises stress (N/m²)
×10⁷
1.4
1.2
1
0.8
0.6
0.4
0.2

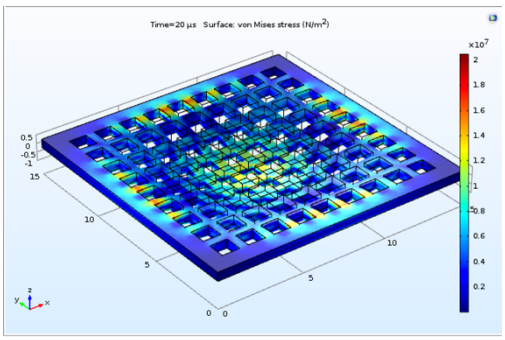
Time=20 µs Surface: von Mises stress (N/m²)
×10⁷
2
1.8
1.6
1.4
1.2
1
0.8
0.6
0.4
0.2

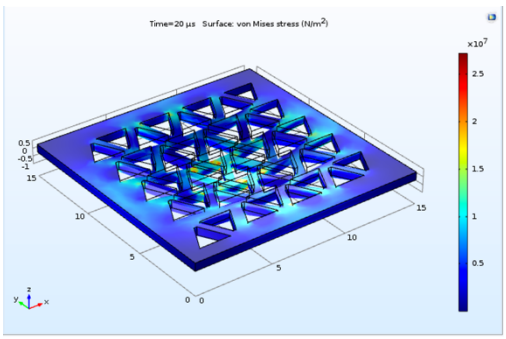
Time=20 µs Surface: von Mises stress (N/m²)
×10⁷
2.5
2
1.5
1
0.5

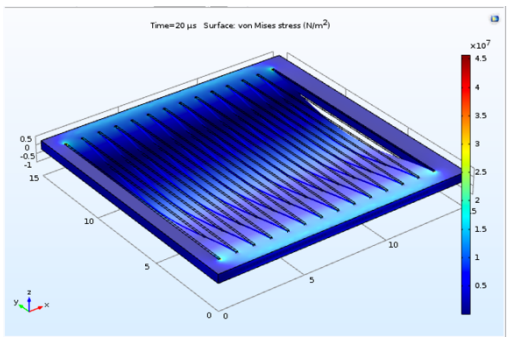
Time=20 µs Surface: von Mises stress (N/m²)
×10⁷
4.5
4
3.5
3
2.5
2
1.5
1
0.5

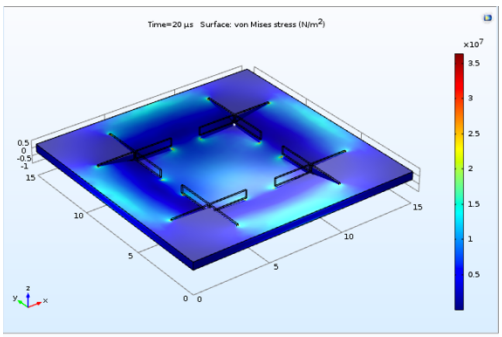
Time=20 µs Surface: von Mises stress (N/m²)
×10⁷
3.5
3
2.5
2
1.5
1
0.5

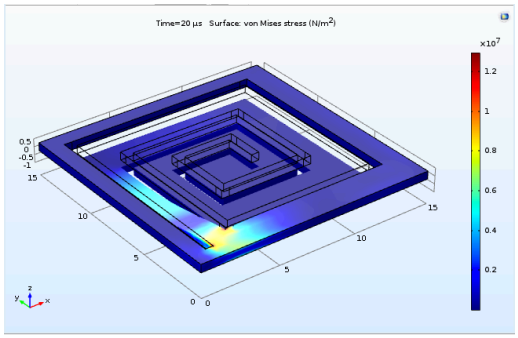
Time=20 µs Surface: von Mises stress (N/m²)
×10⁷
1.2
1
0.8
0.6
0.4
0.2

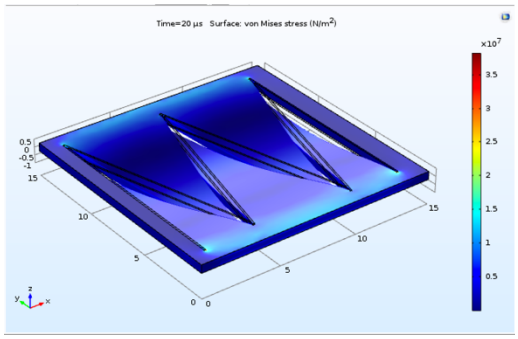
Time=20 µs Surface: von Mises stress (N/m²)
×10⁷
3.5
3
2.5
2
1.5
1
0.5

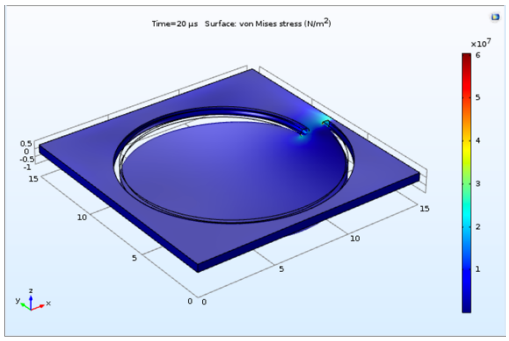
Time=20 µs Surface: von Mises stress (N/m²)
×10⁷
6
5
4
3
2
1

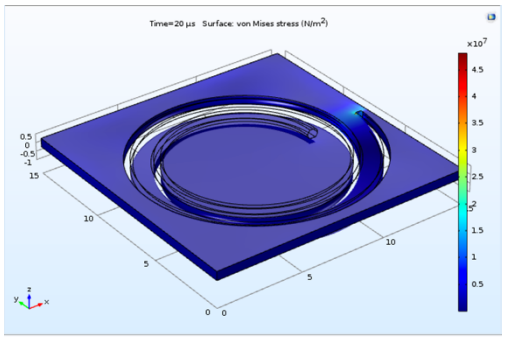
Time=20 µs Surface: von Mises stress (N/m²)
×10⁷
4.5
4
3.5
3
2.5
2
1.5
1
0.5

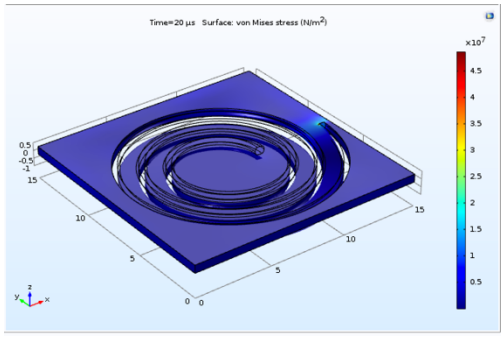
Time=20 µs Surface: von Mises stress (N/m²)
×10⁷
4.5
4
3.5
3
2.5
2
1.5
1
0.5

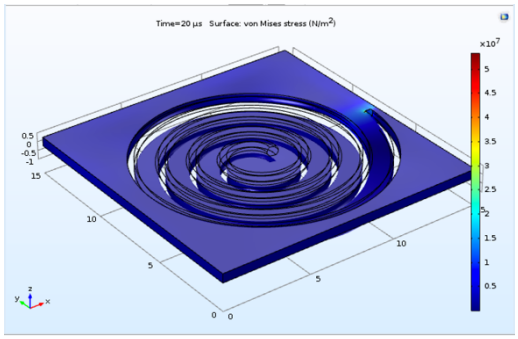
Time=20 µs Surface: von Mises stress (N/m²)
×10⁷
5
4.5
4
3.5
3
2.5
2
1.5
1
0.5

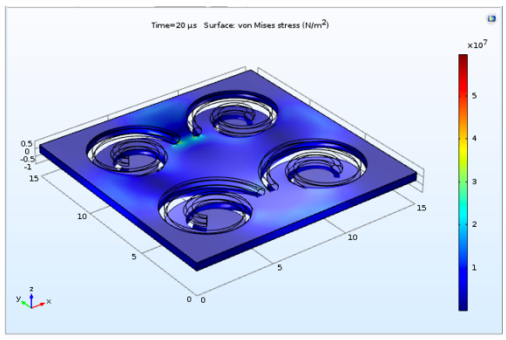
Time=20 µs Surface: von Mises stress (N/m²)
×10⁷
5
4
3
2
1

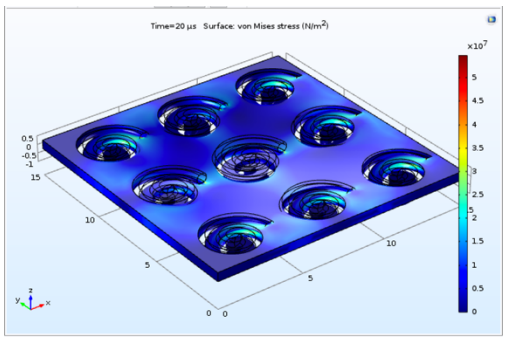
Time=20 µs Surface: von Mises stress (N/m²)
×10⁷
5
4.5
4
3.5
3
2.5
2
1.5
1
0.5
0

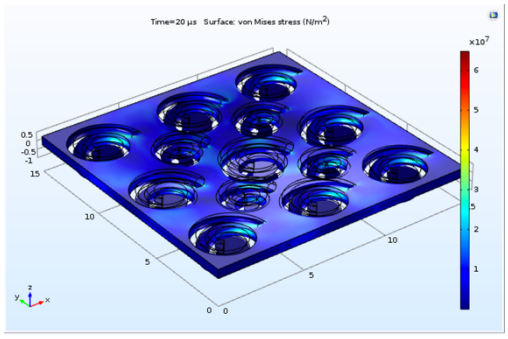
Time=20 µs Surface: von Mises stress (N/m²)
×10⁷
6
5
4
3
2
1

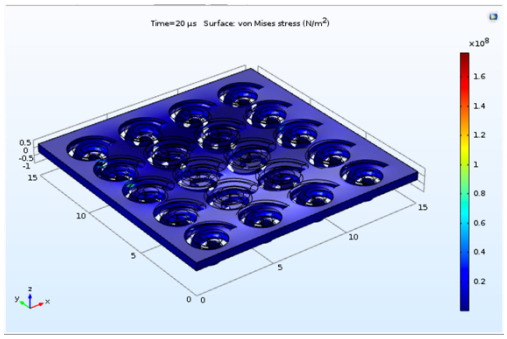
Time=20 µs Surface: von Mises stress (N/m²)
×10⁸
1.6
1.4
1.2
1
0.8
0.6
0.4
0.2

References

[1] "Water - Density Viscosity Specific Weight," *Engineers Edge*. .

[2] N. R. Pallas and Y. Harrison, "Colloids and Surfaces," vol. 43, pp. 169–194, 1990.

[3] Yashwant Singh Sahu, "Solar Energy Market," *Allied Market Research*, 2017. [Online]. Available: https://www.alliedmarketresearch.com/solar-energy-market. [Accessed: 17-Feb-2018].

[4] G. J. Snyder and E. S. Toberer, "Complex thermoelectric materials," *Nat. Mater.*, vol. 7, no. 2, pp. 105–114, 2008.

[5] Y. Zhang, T. Wang, A. Luo, Y. Hu, X. Li, and F. Wang, "Micro electrostatic energy harvester with both broad bandwidth and high normalized power density," *Appl. Energy*, vol. 212, no. September 2017, pp. 362–371, 2018.

[6] L. Zheng, Z. H. Lin, G. Cheng, W. Wu, X. Wen, S. Lee, and Z. L. Wang, "Silicon-based hybrid cell for harvesting solar energy and raindrop electrostatic energy," *Nano Energy*, vol. 9, pp. 291–300, 2014.

[7] H. Nguyen, A. Navid, and L. Pilon, "Pyroelectric energy converter using co-polymer P(VDF-TrFE) and Olsen cycle for waste heat energy harvesting," *Appl. Therm. Eng.*, vol. 30, no. 14–15, pp. 2127–2137, 2010.

[8] A. M. Hawkes, A. R. Katko, S. A. Cummer, A. M. Hawkes, A. R. Katko, and S. A. Cummer, "A microwave metamaterial with integrated power harvesting functionality," vol. 163901, no. 2013, pp. 2011–2014, 2014.

[9] R. Guigon, J. Chaillout, and T. Jager, "Harvesting raindrop energy : experimental study," *Smart Mater. Struct.*, vol. 17, no. 1, p. 015039, 2008.

[10] D. Soto, A. B. De Larivière, X. Boutillon, C. Clanet, and D. Quéré, "The force of impacting rain," *Soft Matter*, vol. 10, no. 27, pp. 4929–4934, 2014.

[11] "Top 10 World's Highest Rainfall Countries 2018," *World's Top*, 2019. [Online]. Available: https://top10-world.org/top-10-worlds-highest-rainfall-countries-2018/. [Accessed: 13-Jan-2019].

[12] R. Guigon, J.-J. Chaillout, T. Jager, and G. Despesse, "Harvesting raindrop energy: theory," *Smart Mater. Struct.*, vol. 17, no. 1, p. 015038, 2008.

[13] F. Viola, P. Romano, and R. Miceli, "Rainfall Energy Harvester," *Innov.*

Mater. Syst. Energy Harvest. Appl., no. February, pp. 116–142, 2016.

[14] V. Wong, J. Ho, and A. Chai, "PIEZOELECTRIC ENERGY HARVESTING IN VARYING SIMULATED," vol. 11, no. 1, pp. 110–114, 2016.

[15] I. Journal and M. Engineering, "Harnessing of Kinetic Energy of Raindrops," *Int. J. Recent Res. Civ. Mech. Eng.*, vol. 2, no. 1, pp. 192–199, 2015.

[16] K.C.R. Perera, B. G. Sampath, V. P. C. Dassanayake, and B. M. Hapuwatte., "Harvesting of Kinetic Energy of the Raindrops," *World Acad. Sci. Eng. Technol. Int. J. Math. Comput. Phys. Quantum Eng.*, vol. 8, no. 2, pp. 325–330, 2014.

[17] C. H. Wong, Z. Dahari, A. Abd Manaf, and M. A. Miskam, "Harvesting raindrop energy with piezoelectrics: A review," *J. Electron. Mater.*, vol. 44, no. 1, pp. 13–21, 2015.

[18] V. K. Wong, J. H. Ho, and H. K. Sam, "On accumulation of water droplets in piezoelectric energy harvesting," *J. Intell. Mater. Syst. Struct.*, vol. 28, no. 4, pp. 521–530, 2017.

[19] C. H. Wong, Z. Dahari, A. Abd Manaf, O. Sidek, M. A. Miskam, and J. J. Mohamed, "Simulation of piezoelectric raindrop energy harvester," *IEEE 2013 Tencon - Spring, TENCONSpring 2013 - Conf. Proc.*, pp. 465–469, 2013.

[20] C. Spataro, F. Viola, P. Romano, and R. Miceli, "Performances of rainfall energy harvester," *Res. Electr. Electron. Meas. Econ. Upturn*, pp. 467–472, 2014.

[21] M. A. Ilyas and J. Swingler, "Towards a prototype module for piezoelectric energy harvesting from raindrop impacts," *Energy*, vol. 125, pp. 716–725, 2017.

[22] R. D. I. Leo, M. Viscardi, G. Ferrini, L. Lecce, and V. J. F. Kennedy, "Preliminary theoretical study about a " Piezoelectric Shingle " for a piezoelectric energy harvesting system in presence of rain," pp. 9–17.

[23] F. Viola, "Comparison Among Different Rainfall Energy Harvesting Structures," *Appl. Sci.*, vol. 8, no. 6, p. 955, 2018.

[24] R. Gunn and G. D. Kinzer, "the Terminal Velocity of Fall for Water Droplets in Stagnant Air," *Journal of Meteorology*, vol. 6. pp. 243–248, 1949.

[25] P. M. Whelan and M. J. Hodgeson, *Essential Principles of Physics, Second Edition*. John Murray, 1978.

[26] V. G. Krishnan, V. Romanin, V. P. Carey, and M. M. Maharbiz, "Design and scaling of microscale Tesla turbines," *J. Micromechanics Microengineering*, vol. 23, no. 12, 2013.

[27] L. E. Helseth and H. Z. Wen, "Evaluation of the energy generation potential of rain cells," *Energy*, vol. 119, pp. 472–482, 2017.

[28] "Climate of Singapore," *Singapore, Meteorological Service*. [Online]. Available: http://www.weather.gov.sg/climate-climate-of-singapore/. [Accessed: 17-Feb-2016].

[29] "Statistics Singapore – Latest Data – Population & Land Area (Mid-Year Estimates)," *Statistics Singapore*, 2014. .

[30] "Clouds," *Meteorological Service Singapore*. [Online]. Available: http://www.weather.gov.sg/learn_clouds/. [Accessed: 03-May-2016].

[31] B. Fischer, "How much does it cost to charge an iPhone 6? A remarkably slender $0.47 per year," *Opower Blog*. [Online]. Available: https://blog.opower.com/2014/09/iphone-6-charging-47-cents/. [Accessed: 03-May-2016].

[32] D. Quéré, "Non-sticking drops," *Reports Prog. Phys.*, vol. 68, no. 11, pp. 2495–2532, 2005.

[33] T. Young, "An Essay on the Cohesion of Fluids," *Philos. Trans. R. Soc. London*, vol. 95, no. 0, pp. 65–87, 1805.

[34] P. S. Laplace, "Œuvres de Laplace," *Impr. R.*, vol. Tome VII, 1847.

[35] J. Rowlinson and B. Widom, *Molecular Theory of Capillarity*. Oxford University Press, 1982.

[36] K. Kles, "Contact Angles," *LibreTexts, Chemistry*. [Online]. Available: https://chem.libretexts.org/Core/Physical_and_Theoretical_Chemistry/Physical_Properties_of_Matter/States_of_Matter/Properties_of_Liquids/Contact_Angles. [Accessed: 29-Mar-2017].

[37] H. Wang, P. J. Mucha, and G. Turk, "Water drops on surfaces," *ACM Trans. Graph.*, vol. 24, no. 212, p. 921, 2005.

[38] R. Förch, H. Schönherr, A. Tobias, and A. Jenkins, *Surface design: applications in bioscience and nanotechnology*. Wiley-VCH, 2009.

[39] S. Wang and L. Jiang, "Definition of Superhydrophobic States," *Adv. Mater.*, vol. 19, pp. 3423–3424, 2007.

[40] C. Neinhuis, “Characterization and Distribution of Water-repellent, Self-cleaning Plant Surfaces,” *Ann. Bot.*, vol. 79, no. 6, pp. 667–677, 1997.

[41] A. Lafuma and D. Quéré, “Superhydrophobic states.,” *Nat. Mater.*, vol. 2, no. 7, pp. 457–60, 2003.

[42] L. E, “THE LOTUS EFFECT,” *futureprospects*, 2010. [Online]. Available: https://futureprospects.wordpress.com/2010/05/17/the-lotus-effect/. [Accessed: 18-May-2016].

[43] M. Nosonovsky and B. Bhushan, “Multiscale effects and capillary interactions in functional biomimetic surfaces for energy conversion and green engineering.,” *Philos. Trans. A. Math. Phys. Eng. Sci.*, vol. 367, pp. 1511–1539, 2009.

[44] I. P. Lipscomb, P. M. Weaver, J. Swingler, and J. W. McBride, “The effect of relative humidity, temperature and electrical field on leakage currents in piezo-ceramic actuators under dc bias,” *Sensors Actuators, A Phys.*, vol. 151, no. 2, pp. 179–186, 2009.

[45] C. Dagdeviren, B. Duk, Y. Su, P. L. Tran, P. Joe, E. Anderson, and J. Xia, “Conformal piezoelectric energy harvesting and storage from motions of the heart , lung , and diaphragm,” vol. 111, no. 5, 2014.

[46] NeverWet LLC, “Product Characteristics,” *NeverWet*, 2016. [Online]. Available: https://www.neverwet.com/applications/product-characteristics.php. [Accessed: 15-Apr-2019].

[47] B. Stern, “Results! | Experimenting with NeverWet + Electronics,” *adafruit*, 2015. [Online]. Available: https://learn.adafruit.com/neverwet-electronics/results. [Accessed: 19-May-2016].

[48] Rioboo, Romain, C. Tropea, and M. Marengo, “Outcomes from a drop impact on solid surfaces,” *At. Sprays 11.2*, 2001.

[49] R. Keedy, “Droplet Impact, Multiphase & Cardiovascular Flow Lab.” [Online]. Available: http://depts.washington.edu/fluidlab/droplet-impact.shtml. [Accessed: 28-Mar-2017].

[50] A. Frohn and N. Roth, *Dynamics of Droplets*. Springer Science & Business Media.

[51] G. Falkovich, *Fluid Mechanics*. Weizmann Institute of Science, Israel: Cambridge University Press.

[52] G. H. McKinley and M. Renardy, “Wolfgang von Ohnesorge,” *Phys. Fluids*, vol. 23, no. 12, 2011.

[53] A. L. Yarin, “DROP IMPACT DYNAMICS: Splashing, Spreading, Receding, Bouncing…,” *Annu. Rev. Fluid Mech.*, vol. 38, no. 1, pp. 159–192, 2006.

[54] P. Tsai, S. Pacheco, C. Pirat, L. Lefferts, and D. Lohse, “Drop impact upon micro- and nanostructured superhydrophobic surfaces,” *Langmuir*, vol. 25, no. 20, pp. 12293–12298, 2009.

[55] D. Richard and D. Quéré, “Bouncing water drops,” *Europhys. Lett.*, vol. 50, no. 6, p. 769, 2000.

[56] R. E. Pepper, L. Courbin, H. A. Stone, R. E. Pepper, L. Courbin, and H. A. Stone, “Splashing on elastic membranes : The importance of early-time dynamics,” *Am. Inst. Phys.*, vol. 20, no. 2008, 2009.

[57] C. J. Howland, A. Antkowiak, J. R. Castrej, D. Sam, J. M. Oliver, R. W. Style, and A. A. Castrej, “It’s harder to splash on soft solids,” *Am. Phys. Soc.*, pp. 1–5, 2016.

[58] P. B. Weisensee, J. Tian, N. Miljkovic, and W. P. King, “Water droplet impact on elastic superhydrophobic surfaces,” *Sci. Rep.*, vol. 6, no. July, p. 30328, 2016.

[59] J. Liu, H. Vu, S. S. Yoon, R. Jepsen, and G. Aguilar, “SPLASHING PHENOMENA DURING LIQUID DROPLET IMPACT,” vol. 20, no. 4, pp. 297–310, 2010.

[60] D. L. Chandler, “Explained: Hydrophobic and hydrophilic,” *MIT News*. [Online]. Available: http://news.mit.edu/2013/hydrophobic-and-hydrophilic-explained-0716. [Accessed: 31-Mar-2017].

[61] V. Wong, J. Ho, and H. Sam, “On accumulation of water droplets in piezoelectric energy harvesting,” *J. Intell. Mater. Syst. Struct.*, vol. 28, no. 4, pp. 521–530, 2017.

[62] S. Gart, J. E. Mates, C. M. Megaridis, and S. Jung, “Droplet Impacting a Cantilever: A Leaf-Raindrop System,” *Phys. Rev. Appl.*, vol. 3, no. 4, pp. 1–8, 2015.

[63] Y. Miao and Y. Jia, “Hybrid Decentralised Energy for Remote Communities : Case Studies and the Analysis of the Potential Integration of Rain Energy,” vol. 2, no. 3, pp. 243–258, 2014.

[64] E. Villermaux and B. Bossa, “Single-drop fragmentation determines size distribution of raindrops,” *Nat. Phys.*, vol. 5, no. 9, pp. 697–702, 2009.

[65] R. Allain, “How fast is falling rain ?,” *WIRED*, 2011. [Online]. Available:

https://www.wired.com/2011/08/how-fast-is-falling-rain/. [Accessed: 15-Apr-2016].

[66] M. a. Nearing, J. M. Bradford, and R. D. Holtz, "Measurement of Force vs. Time Relations for Waterdrop Impact," *Soil Science Society of America Journal*, vol. 50, no. 6. p. 1532, 1986.

[67] W. Asen and C. J. Gibbins, "A comparison of rain attenuation and drop size distributions measured in Chilbolton and Singapore," *Radio Sci.*, vol. 37, no. 3, pp. 1–15, 2002.

[68] V. Wong, J. Ho, and A. Chai, "Performance of a piezoelectric energy harvester in actual rain," *Energy*, vol. 124, pp. 364–371, 2017.

[69] L. S. Kumar, "Accurate Rain Drop Size Distribution Models for the Tropical Region Statement of Originality," *Sch. Electr. Electron. Eng. Nanyang Technol. Univ.*, 2011.

[70] T. Alkhaddeim, A. Boshra, W. Albeiey, F. Alneyadi, and A. Ahmad, "Piezoelectric Energy y Droplet Harvesting an nd Modeling," pp. 0–3, 2012.

[71] L. Valentini, S. . Bon, and J. Kenny, "L. Valentini, S.B. Bon, and J. Kenny, J. Polym. Sci. Part B 51, 1028 (2013).," *J. Polym. Sci. Part B*, vol. 51, no. 1028, 2013.

[72] F. Viola, P. Romano, R. Miceli, and G. Acciari, "On the harvest of rainfall energy by means of piezoelectric transducer," *Proc. 2013 Int. Conf. Renew. Energy Res. Appl. ICRERA 2013*, no. October, pp. 1133–1138, 2013.

[73] Y. R. Lee, J. H. Shin, I. S. Park, K. Rhee, and S. K. Chung, "Sensors and Actuators A : Physical Energy harvesting based on acoustically oscillating liquid droplets," *Sensors Actuators A. Phys.*, vol. 231, pp. 8–14, 2015.

[74] V. Wong, J. Ho, and H. Sam, "On accumulation of water droplets in piezoelectric energy harvesting," vol. 28, no. 4, pp. 521–530, 2017.

[75] M. A. Ilyas and J. Swingler, "Piezoelectric energy harvesting from raindrop impacts," *Energy*, vol. 90, pp. 796–806, 2015.

[76] F. Viola, P. Romano, R. Miceli, G. Acciari, and C. Spataro, "Piezoelectric model of rainfall energy harvester," *2014 9th Int. Conf. Ecol. Veh. Renew. Energies, EVER 2014*, 2014.

[77] V. Wong, J. Ho, E. H. Yap, and A. B. Chai, "Dynamics of a piezoelectric energy harvester in a simulated rain environment," vol. 232, no. 15, pp.

2642–2654, 2018.

[78] ., “PIEZOELECTRIC ENERGY HARVESTERS,” *Midé Volture*, 2013. [Online]. Available: https://media.digikey.com/pdf/Data Sheets/Mide Technology PDFs/Volture.pdf. [Accessed: 14-Mar-2019].

[79] “March 1880: The Curie Brothers Discover Piezoelectricity,” *American Physical Society*, 2014. .

[80] J. Curie and P. Curie, “Development, via compression, of electric polarization in hemihedral crystals with inclined faces,” *Bull. la Soc. Minerol. Fr.*, vol. 3, pp. 90–93, 1880.

[81] P. Curie and J. Curie, “Contractions and expansions produced by voltages in hemihedral crystals with inclined faces,” *Comptes Rendus*, vol. 93, pp. 1137–1140, 1881.

[82] G. Gautschi, “Piezoelectric Sensorics: Force, Strain, Pressure, Acceleration and Acoustic Emission Sensors, Materials and Amplifiers.,” *Springer*, 2002.

[83] E. Fukada and I. Yasuda, “On the Piezoelectric Effect of Bone,” *J. Phys. Soc. Japan*, vol. 12, no. 10, p. 1158, 1957.

[84] B. Y. Lee, J. Zhang, C. Zueger, W.-J. Chung, S. Y. Yoo, E. Wang, J. Meyer, R. Ramesh, and S.-W. Lee, “Virus-based piezoelectric energy generation,” *Nat. Nanotechnol.*, vol. 7, no. 6, pp. 351–356, 2012.

[85] D. Damjanovič, “Ferroelectric, dielectric and piezoelectric properties of ferroelectric thin films and ceramics,” *Reports Prog. Phys.*, vol. 61, no. 9, pp. 1267–1324, 1998.

[86] T. Hehn and Y. Manoli, “CMOS Circuits for Piezoelectric Energy Harvesters: Efficient Power Extraction, Interface Modeling and Loss Analysis,” p. 204, 2014.

[87] “PIEZOELECTRIC CONSTANTS,” *APC International Ltd.* [Online]. Available: https://www.americanpiezo.com/knowledge-center/piezo-theory/piezoelectric-constants.html. [Accessed: 16-May-2016].

[88] K. Uchino and T. Ishii, “Energy Flow Analysis in Piezoelectric Energy Harvesting Systems,” vol. 0193, 2010.

[89] T. Hehn and Y. Manoli, “CMOS Circuits for Piezoelectric Energy Harvesters - Efficient Power Extraction, Interface Modeling and Loss Analysis,” *Springer Ser. Adv. Microelectron.*, vol. 38, 2015.

[90] W. Känzig, *Ferroelectrics and Antiferroelectrics*. 1957.

[91] M. Lines and A. Glass, *Principles and applications of ferroelectrics and related materials*. Clarendon Press, Oxford, 1979.

[92] W. Jo, K. T. P. Seifert, E. Anton, and T. Granzow, "Perspective on the Development of Lead-free Piezoceramics," vol. 1177, pp. 1153–1177, 2009.

[93] E. Defaÿ, Ed., *Integration of Ferroelectric and Piezoelectric Thin Films*, no. November. Wiley, 2003.

[94] "EU-Directive 2002/95/EC: restriction of the use of certain hazardous substances in electrical and electronic equipment (RoHS)," *Off J Eur Union*, vol. 46, pp. 19–37, 2003.

[95] "EU-Directive 2011/65/EC: restriction of the use of certain hazardous substances in electrical and electronic equipment (RoHS)," *Off J Eur Union*, vol. 54, pp. 88–110, 2011.

[96] European Chemicals Agency, "Inclusion of substances of very high concern in the candidate list," vol. ED/169/201, 2012.

[97] J. Rödel, K. G. Webber, R. Dittmer, W. Jo, and M. Kimura, "Feature Article Transferring lead-free piezoelectric ceramics into application," *J. Eur. Ceram. Soc.*, vol. 35, no. 6, pp. 1659–1681, 2015.

[98] P. C. Goh, K. Yao, and Z. Chen, "Reaction Mechanisms of Ethylenediaminetetraacetic Acid and Diethanolamine in the Precursor Solution for Producing (K , Na) NbO 3 Thin Films with Outstanding Piezoelectric Properties," *J. Phys. Chem.*, no. 116, pp. 15550–15556, 2012.

[99] B. Zhang and J. Zhu, "New Potassium − Sodium Niobate Ceramics with a Giant d 33," *ACS Appl. Mater. Interfaces*, pp. 8–11, 2014.

[100] X. Cheng, J. Wu, X. Lou, X. Wang, X. Wang, D. Xiao, and J. Zhu, "Achieving Both Giant d 33 and High Tc in Patassium-Sodium Niobate Ternary System," *ACS Appl. Mater. Interfaces*, vol. 6, pp. 750–756, 2014.

[101] S.-H. Lee, S.-G. Lee, and Y.-H. Lee, "Electrical properties of lead-free 0.98(Na0.5K0.5)NbO3-0.02Ba(Zr0.52Ti0.48)O3 piezoelectric ceramics by optimizing sintering temperature.," *Nanoscale Res. Lett.*, vol. 7, no. 1, p. 15, 2012.

[102] L. Egerton and D. M. Dillon, "Piezoelectric and Dielectric Properties of Ceramics in the System Potassium—Sodium Niobate," *J. Am. Ceram. Soc.*, vol. 42, no. 9, pp. 438–442.

[103] Y. Saito, H. Takao, T. Tani, T. Nonoyama, K. Takatori, T. Homma, T. Nagaya, and M. Nakamura, “Lead-free Piezoceramics,” *Lett. to Nat.*, vol. 432, no. November, pp. 1–4, 2004.

[104] X. Wang, J. Wu, D. Xiao, J. Zhu, X. Cheng, T. Zheng, B. Zhang, X. Lou, and X. Wang, “Giant Piezoelectricity in Potassium − Sodium Niobate Lead-Free Ceramics,” vol. 5, pp. 3–8, 2014.

[105] H. Kawai, “The Piezoelectricity of Poly (vinylidene Fluoride,” *Jpn. J. Appl. Phys.*, vol. 8, no. (7), p. 975, 1969.

[106] K. Omote and H. O. Koga, “Temperature dependence of elastic, dielectric, and piezoelectric properties of ‘“single crystalline”’ films of vinylidene fluoride trifluoroethylene copolymer,” vol. 2760, no. 1997, 2008.

[107] C. W. Tsai, S. C. Shen, S. J. Chang, Y. C. Chen, and M. J. Fang, “A small elastic floating energy harvester for ocean ripple power using knitted PVDF thin film,” *2015 IEEE 10th Int. Conf. Nano/Micro Eng. Mol. Syst. NEMS 2015*, pp. 461–465, 2015.

[108] “Elastic Properties and Young Modulus for some Materials,” *The Engineering ToolBox*. [Online]. Available: http://www.engineeringtoolbox.com/young-modulus-d_417.html. [Accessed: 02-Apr-2017].

[109] K. E. Spear and J. P. Dismukes, *Synthetic Diamond: Emerging CVD Science and Technology*. Wiley.

[110] “Alumina - Aluminium Oxide - Al2O3 - A Refractory Ceramic Oxide,” *AZO Materials*. [Online]. Available: http://www.azom.com/properties.aspx?ArticleID=52. [Accessed: 02-Apr-2017].

[111] H. Bruncková, Ľ. Medvecký, and P. Hvizdoš, “Effect of substrate on phase formation and surface morphology of sol-gel lead-free KNbO3, NaNbO3, and K0.5Na0.5NbO3 thin films,” *Chem. Pap.*, vol. 66, no. 8, pp. 748–756, 2012.

[112] “INCONEL 600 TECHNICAL DATA,” *HIGH TEMP METALS*, 2015. [Online]. Available: http://www.hightempmetals.com/techdata/hitempInconel600data.php. [Accessed: 03-Apr-2017].

[113] T. Shiraishi, H. Einishi, S. Yasui, H. Funakubo, T. Hasegawa, M. Kurosawa, M. Ishikawa, H. Uchida, and Y. Sakashita, “Ferroelectric and

piezoelectric properties of (K,Na)NbO3 thick films prepared on metal substrates by hydrothermal method," *J. Korean Phys. Soc.*, vol. 62, no. 7, pp. 1055–1059, 2013.

[114] W. Zhou, F. Liu, C. He, and J. Chen, "Fabrication of Na0.5K0.5NbO3 thin film on glass substrate by pulsed laser at room temperature," *Beijing Univ. Technol.*, pp. 3–5, 2012.

[115] "Magnesia - Magnesium Oxide (MgO) Properties & Applications," *AZO Materials*. [Online]. Available: http://www.azom.com/properties.aspx?ArticleID=54. [Accessed: 03-Feb-2017].

[116] I. Kanno, T. Mino, S. Kuwajima, T. Suzuki, H. Kotera, and K. Wasa, "Piezoelectric Properties of (K , Na)NbO3 Thin Films Deposited on (001) SrRuO3/Pt/MgO," *IEEE Trans. Ultrason. Ferroelectr. Freq. Control*, vol. 54, no. 12, pp. 2562–2566, 2007.

[117] S. Kim, I. Towfeeq, Y. Dong, S. Gorman, A. M. Rao, and G. Koley, "P(VDF-TrFE) film on PDMS substrate for energy harvesting applications," *Appl. Sci.*, vol. 8, no. 2, 2018.

[118] "Si - Silicon," *Ioffe Institute Database*. .

[119] E. J. Boyd and D. Uttamchandani, "Measurement of the Anisotropy of Young ' s Modulus in Single-Crystal Silicon," *J. Microelectromechanical Syst.*, vol. 21, no. 1, pp. 243–249, 2012.

[120] S.-C. Lin and W.-J. Wu, "Fabrication of PZT MEMS energy harvester based on silicon and stainless-steel substrates utilizing an aerosol deposition method," *J. Micromechanics Microengineering*, vol. 23, no. 12, p. 125028, 2013.

[121] "Strontium," *New World Encyclopedia*. [Online]. Available: http://www.newworldencyclopedia.org/entry/Strontium. [Accessed: 03-Apr-2017].

[122] T. Li, G. Wang, K. Li, G. Du, Y. Chen, Z. Zhou, and D. Rémiens, "Electrical properties of lead-free KNN fi lms on SRO / STO by RF magnetron sputtering," *Ceram. Int.*, vol. 40, no. 1, pp. 1195–1198, 2014.

[123] "Stainless Steel - Grade 304 (UNS S30400)," *AZO Materials*. .

[124] Y. Tsujiura, E. Suwa, H. Hida, K. Suenaga, K. Shibata, and I. Kanno, "LEAD-FREE PIEZOELECTRIC MEMS ENERGY HARVESTERS OF STAINLESS STEEL CANTILEVERS Kobe University , Kobe , JAPAN

Hitachi Cable , Ltd ., Tokyo , JAPAN," no. June, pp. 474–477, 2013.

[125] J. N. Burghatz, "Make Way for Flexible Silicon Chips," *IEEE Spectrum*, 2013. [Online]. Available: http://spectrum.ieee.org/semiconductors/materials/make-way-for-flexible-silicon-chips. [Accessed: 06-Jul-2016].

[126] K. Greene, "High-Performance Flexible Silicon," *MIT Technology Review*, 2006. [Online]. Available: https://www.technologyreview.com/s/406183/high-performance-flexible-silicon/. [Accessed: 06-Jul-2016].

[127] Sigma-Aldrich, "Silicon Wafers." [Online]. Available: http://www.sigmaaldrich.com/materials-science/material-science-products.html?TablePage=105273466. [Accessed: 02-Aug-2016].

[128] "Stainless Steel Sheet - 304," *Metals Depot International*. [Online]. Available: https://www.metalsdepot.com/products/stainless2.phtml?page=sheet. [Accessed: 03-Apr-2017].

[129] "Extra Thin Copper Foil 0.05mm," *Amazon*. [Online]. Available: https://www.amazon.co.uk/Extra-Thin-Copper-Foil-0-05mm/dp/B0027IZ2DI/ref=pd_bxgy_21_2?_encoding=UTF8&pd_rd_i=B0027IZ2DI&pd_rd_r=05357d56-2998-11e9-b867-f73deaabb510&pd_rd_w=XfTLM&pd_rd_wg=YnXIr&pf_rd_p=a0365e62-3353-40ad-91cf-d4ca762b18a7&pf_rd_r=A7FGBCG5WA44BPWF4CVD&psc=1&refRID=A7FGBCG5WA44BPWF4CVD. [Accessed: 05-Feb-2019].

[130] R. A. Serway, *Principles of Physics*. Fort Worth, Texas: Saunders College Pub., 1998.

[131] D. Giancoli, "25. Electric Currents and Resistance," in *Physics for Scientists and Engineers with Modern Physics (4th ed.)*, Upper Saddle River, New Jersey, 2009, p. 658.

[132] R. A. Matula, "Electrical resistivity of copper, gold, palladium, and silver," *J. Phys. Chem. Ref. Data*, vol. 8, 1979.

[133] D. Griffiths, "7. Electrodynamics," in *Introduction to Electrodynamics*, Upper Saddle River, New Jersey: Alison Reeves, 1999, p. 286.

[134] H. K. H. Kim, S. Priya, H. Stephanou, and K. Uchino, "Consideration of Impedance Matching Techniques for Efficient Piezoelectric Energy

Harvesting," *IEEE Trans. Ultrason. Ferroelectr. Freq. Control*, vol. 54, no. 9, pp. 1851–1859, 2007.

[135] T. Phillips, *Dynamo-Electric Machinery; A Manual for Students of Electrotechnics*. Bibliobazaar, 2009.

[136] L. Frenzel, "Back to Basics: Impedance Matching (Part 1)," *Electronic Design*, 2011. [Online]. Available: http://electronicdesign.com/communications/back-basics-impedance-matching-part-1. [Accessed: 12-Apr-2017].

[137] B. Dull, "Understanding the Maximum Power Theorem," *Triad Magnetics Blog*. [Online]. Available: https://info.triadmagnetics.com/blog/maximum-power-theorem. [Accessed: 15-Jun-2019].

[138] Busch-Vishniac and J. Ilene, *Electromechanical Sensors and Actuators*. Springer Science & Business Media, 1999.

[139] R. W. B. Stephens and A. E. Bate, *Acoustics and vibrational physics*, 2nd ed. Edward Arnold, 1966.

[140] "Impedance analogy," *Wikipedia*, 2014. [Online]. Available: https://en.wikipedia.org/wiki/Impedance_analogy. [Accessed: 28-Apr-2017].

[141] J. Eargle, *Loudspeaker Handbook*. Kluwer Academic Publishers, 2003.

[142] M. Kleiner, *Electroacoustics*. CRC Press, 2013.

[143] L. L. Beranek and T. J. Mellow, *Acoustics: Sound Fields and Transducers*. Academic Press, 2012.

[144] M. Gedeon, "Cantilever Beams Part 1 - Beam Stiffness," *TECHNICAL TIDBITS, BRUSH WELLMAN ALLOY PRODUCTS*, 2010. [Online]. Available: https://materion.com/-/media/files/pdfs/alloy/newsletters/technical-tidbits/issue-no-20--cantilever-beams---part-1-beam-stiffness.pdf. [Accessed: 19-Apr-2017].

[145] "Free Vibration of a Cantilever Beam (Continuous System)," *VALUE @ Amrita*. [Online]. Available: http://vlab.amrita.edu/?sub=3&brch=175&sim=1080&cnt=1. [Accessed: 29-Mar-2019].

[146] T. Vasileiou, J. Gerber, J. Prautzsch, T. M. Schutzius, and D. Poulikakos, "Superhydrophobicity enhancement through substrate flexibility," *Proc. Natl. Acad. Sci.*, vol. 113, no. 47, pp. 13307–13312, 2016.

[147] H. Lamb, *Surface Waves*, vol. 26. Cambridge University Press, 1895.

[148] L. Zhang, S. R. Oh, T. C. Wong, C. Y. Tan, and K. Yao, “Piezoelectric polymer multilayer on flexible substrate for energy harvesting,” *IEEE Trans. Ultrason. Ferroelectr. Freq. Control*, vol. 60, no. 9, pp. 2013–2020, 2013.

[149] L. Zhang, S. R. Oh, T. C. Wong, and C. Y. Tan, “Piezoelectric Polymer Multilayer on Flexible Substrate for Energy Harvesting,” *IEEE Trans. Ultrason. Ferroelectr. Freq. Control*, vol. 60, no. 9, pp. 2013–2020, 2013.

[150] J. M. Dietl and E. Garcia, “Beam Shape Optimization for Power Harvesting,” *J. Intell. Mater. Syst. Struct.*, vol. 21, no. 6, pp. 633–646, 2010.

[151] F. Goldschmidtboeing and P. Woias, “Characterization of different beam shapes for piezoelectric energy harvesting,” *J. Micromechanics Microengineering*, vol. 18, no. 10, p. 104013, 2008.

[152] J. Baker, “Alternative Geometries for Increasing Power Density in Vibration Energy Scavenging,” *3rd Int. Energy Convers. Eng. Conf. 15 - 18 August 2005, San Fr. Calif.*, no. August, pp. 1–12, 2005.

[153] P. Glynne-Jones, S. P. Beeby, and N. M. White, “Towards a piezoelectric vibration-powered microgenerator,” *Sci. Meas. Technol. IEE Proc. -*, vol. 148, no. 2, pp. 68–72, 2001.

[154] B. L. Ooi, J. M. Gilbert, and A. R. A. Aziz, “Analytical and finite-element study of optimal strain distribution in various beam shapes for energy harvesting applications,” *Acta Mech. Sin.*, pp. 1–14, 2016.

[155] P. Winder and K. S. Paulson, “An Acoustic Disdrometer: The measurement of rain kinetic energy and rain intensity using an acoustic disdrometer,” *15th Symp. Meteorol. Obs. Instrum.*, 2010.

[156] T. K. Mani and P. R. S. Pillai, “Drop parameter estimation from underwater noise produced by raindrop impact,” *Acoust. Res. Lett. Online*, vol. 5, no. 3, p. 118, 2004.

[157] H. Medwin, A. Nystuen, P. W. Jacobus, L. H. Ostwald, and D. E. Snyder, “The anatomy of underwater rain noise,” *Phys. Dep. Nav. Postgrad. Sch. Monterey, Calif.*, 1992.

[158] W. J. Stronge, *Impact Mechanics*. Cambridge University Press, 2000.

[159] E. E. Aktakka, H. Kim, and K. Najafi, “Energy scavenging from insect flight,” *J. Micromechanics Microengineering*, vol. 21, no. 9, p. 095016, 2011.

[160] A. W. Jayawardena and R. B. Rezaur, “Drop size distribution and kinetic energy load of rainstorms in Hong Kong Abstract :,” vol. 1082, no. August 1999, pp. 1069–1082, 2000.

[161] Y. Jiuqin, L. Yin, and C. Longxi, “Preliminary study on mechanics-based rainfall kinetic energy,” *Int. soil water Conserv. Res.*, vol. 2, no. 3, pp. 67–73, 2014.

[162] R. Tikani, L. Torfenezhad, and M. Mousavi, “Optimization of spiral-shaped piezoelectric energy harvester using Taguchi method,” no. September 2016, 2017.

[163] E. W. Weisstein, “Archimedean Spiral,” *Mathworld--A Wolfram Web Resource*. [Online]. Available: http://mathworld.wolfram.com/ArchimedeanSpiral.html.

[164] P. Udvardi and J. Ferencz, “Spiral-Shaped Piezoelectric MEMS Cantilever Array for Fully Implantable Hearing Systems.”

[165] “Derivatives of Polar Functions,” *Math24*. [Online]. Available: https://www.math24.net/derivatives-polar-functions/. [Accessed: 29-Mar-2019].

[166] A. E. H. Love, “A Treatise on the Mathematical Theory of Elasticity,” *HAL*, vol. 1, 1892.

[167] M. A. Karami, B. Yardimoglu, and D. J. Inman, “Coupled out of plane vibrations of spiral beams,” *Struct. Struct. Dyn. Mater. Conf.*, no. May, pp. 1–17, 2009.

[168] Y. Zheng, X. Wu, M. Parmar, D. Lee, Y. Zheng, X. Wu, M. Parmar, and D. Lee, “High-efficiency energy harvester using double-clamped piezoelectric beams,” vol. 026101, pp. 2–5, 2014.

[169] V. K. Wong, J. H. Ho, and E. H. Yap, “Dynamics of a piezoelectric beam subjected to water droplet impact with water layer formed on the surface,” *J. Intell. Mater. Syst. Struct.*, vol. 26, no. 16, pp. 2170–2180, 2015.

[170] S. Du, Y. Jia, and A. Seshia, “Maximizing Output Power in a Cantilevered Piezoelectric Vibration Energy Harvester by Electrode Design,” *J. Phys. Conf. Ser.*, vol. 660, no. 1, 2015.

[171] S. Du, Y. Jia, S. T. Chen, C. Zhao, B. Sun, E. Arroyo, and A. A. Seshia, “A new electrode design method in piezoelectric vibration energy harvesters to maximize output power,” *Sensors Actuators, A Phys.*, vol. 263, pp. 693–701, 2017.

[172] "PVDF," *Holscot Fluoroplastics Ltd*. [Online]. Available: https://holscot.com/glossary/pvdf/. [Accessed: 15-Jun-2019].

[173] S. Smith, "How to clean gutters using a ladder safely," *Ladderstore*. [Online]. Available: https://www.ladderstore.com/blog/gutter-clearing-ladder-advice. [Accessed: 03-Mar-2019].

[174] N. Verplanck, Y. Coffinier, V. Thomy, and R. Boukherroub, "Wettability Switching Techniques on Superhydrophobic Surfaces," *Nano Rev.*, pp. 577–596, 2007.

[175] J. Zhang, X. Lu, W. Huang, and Y. Han, "Reversible Superhydrophobicity to Superhydrophilicity Transition by Extending and Unloading an Elastic Polyamide Film," pp. 477–480, 2005.

[176] Engineering Toolbox, "Flow of Liquids from Containers - Volume Flow and Emptying Time Calculator," 2011. .

[177] Leo, "What is Aquaponics System?," *Aquaponics System Reviews*, 2015. .

[178] H. Maiwa, K. Ohashi, and T. Hayashi, "Preparation and Properties of Lithium-doped K0.5Na0.5NbO3 Thin Films by Chemical Solution Deposition," *Shonan Inst. Technol.*

[179] X. Yan, W. Ren, X. Wu, P. Shi, and X. Yao, "Lead-free (K , Na) NbO 3 ferroelectric thin films : Preparation , structure and electrical properties," *J. Alloys Compd.*, vol. 508, no. 1, pp. 129–132, 2010.

[180] M. Abazari, E. K. Akdogan, and A. Safari, "KNaNbO3-LiTaO3-LiSbO3 Thin Films by Pulsed Laser Deposition," *Glenn Howatt Electron. Ceram. Lab. Rutgers Univ.*